# 論文 / 著書情報
# Article / Book Information

| | |
|---|---|
| 題目(和文) | |
| Title(English) | High-χ Parameter Diblock Copolymers with Fluorinated Side Chains for Next Generation Lithography |
| 著者(和文) | DongLei |
| Author(English) | Lei Dong |
| 出典(和文) | 学位:博士(工学),<br>学位授与機関:東京工業大学,<br>報告番号:甲第11609号,<br>授与年月日:2020年9月25日,<br>学位の種別:課程博士,<br>審査員:早川 晃鏡,扇澤 敏明,松本 英俊,道信 剛志,戸木田 雅利 |
| Citation(English) | Degree:Doctor (Engineering),<br>Conferring organization: Tokyo Institute of Technology,<br>Report number:甲第11609号,<br>Conferred date:2020/9/25,<br>Degree Type:Course doctor,<br>Examiner:,,,, |
| 学位種別(和文) | 博士論文 |
| Type(English) | Doctoral Thesis |

**Doctoral Dissertation**

# High-χ Parameter Diblock Copolymers with Fluorinated Side Chains for Next Generation Lithography

**Lei Dong**

**Supervisor: Teruaki Hayakawa, Dr. Eng**

**July 13th, 2020**

*Department of Materials Science and Engineering*

*School of Materials and Chemical Technology*

*Tokyo Institute of Technology*

# Contents

**Chapter 1 General Introduction ..... 5**

1.1 Diblock copolymers ..... 5

1.2 Self-assembly of diblock copolymers ..... 6

1.3 High χ block copolymers ..... 8

1.4 Block copolymers with fluorinated side chains ..... 13

1.5 Surface properties of BCPs with fluorinated side chains ..... 17

1.6 Micelles self-assembly of BCPs with fluorinated side chains ..... 18

1.7 Thin film self-assembly of BCPs with fluorinated side chains ..... 23

1.8 SCLC self-assembly ..... 32

1.9 Block copolymer lithography ..... 34

1.10 Composition of this dissertation ..... 36

1-11. References ..... 38

**Chapter 2 The Role of Liquid Crystalline Side Chains for Long-range Ordering in the Block Copolymer Thin Films ..... 51**

2-1. Introduction ..... 51

2-2. Experimental Section ..... 53

2-2-1. Materials ..... 53

2-2-2. Methods ..... 53

2-2-3. Synthesis of homopolymer ..... 54

2-2-4. Estimating the surface free energies of the homopolymers ..... 55

2-2-5. Synthesis of PS-*b*-PGMA ..... 55

2-2-6. Synthesis of PS-*b*-P8FMA through the post-functionalization of PS-*b*-PGMA with 1H,1H,2H,2H-Perfluorodecanethiol ..... 56

2-2-7. Detailed information about the estimation of $\chi_{eff}$ ..... 58

2-2-8. Synthesis of PTFEMA-*r*-PMMA-*r*-PMAAs ..... 59

2-2-9. Bulk sample preparation ..... 60

2-2-10. Thin film preparation ..... 60

2-2-11. Etch contrast in $O_2$-RIE ..... 60

2-3. Results and Discussion ..... 61

2-3-1. Synthesis and characterization of the homopolymers ..... 61

2-3-2. Synthesis and characterization of the BCPs ..... 63

2-3-3. Morphologies in the bulk ..... 66

2-3-4. Estimation of $\chi_{eff}$ ..... 73

2-3-5. Nanostructure and domain orientation in thin films ..... 77

2-3-6. Quantitative analysis on thin film patterns ..... 85
2-4. Conclusion ..... 90
2.5 References ..... 91
**Chapter 3 Study on Effects of Semifluorinated Side Chains with Varied Lengths on Self-assembly Morphology of Diblock Copolymer ..... 95**
3-1. Introduction ..... 95
3-2. Experimental Section ..... 97
3-2-1. Materials ..... 97
3-2-2. Methods ..... 97
3-2-3. Synthesis of ,3,4,4,5,5,6,6,6-nonafluoro-1-hexanethiol ..... 98
3-2-4. Synthesis of homopolymer ..... 99
3-2-5. Synthesis of PS-*b*-PGMA ..... 101
3-2-6. Synthesis of PS-*b*-PXFMA (X=1 or 4 or 6 or 8) through the post-functionalization of PS-*b*-PGMA with 2,2,2-Trifluoroethanethiol or 3,3,4,4,5,5,6,6,6-Nonafluoro-1-hexanethiol or 3,3,4,4,5,5,6,6,7,7,8,8,8-Tridecafluoro-1-octanethiol or 1H,1H,2H,2H-Perfluorodecanethiol ..... 102
3-2-7. Estimating the surface free energies of the homopolymers ..... 103
3-2-8. Detailed information about the estimation of $\chi_{eff}$ ..... 103
3-2-9. Bulk sample preparation ..... 104
3-3. Results and Discussion ..... 105
3-3-1. Synthesis and characterization of the homopolymers ..... 105
3-3-2. Synthesis and characterization of the BCPs ..... 108
3-3-3. Morphologies in the bulk ..... 112
3-3-4. Estimation of $\chi_{eff}$ ..... 121
3-4. Conclusion ..... 125
3-5. Reference ..... 126
**Chapter 4 Adjusting Thin Film Domain Spacings of Side-Chain Liquid Crystalline Semi-fluorinated Block Copolymers with Elliptical Cylinders with Anisotropic Hexagonal Packing ..... 128**
4-1. Introduction ..... 128
4-2. Experimental Section ..... 130
4-2-1. Materials ..... 130
4-2-2. Methods ..... 130
4-2-3. Synthesis of PS-*b*-PGMA ..... 131

4-2-4. Synthesis of PS-*b*-P8FMA through the post-functionalization of PS-*b*-PGMA with 1H,1H,2H,2H-Perfluorodecanethiol ..... 131
4-2-5. Synthesis of PMMA-*r*-PTFEMA-*r*-PMAAs ..... 133
4-2-6. Thin film preparation ..... 135
4-3. Results and Discussion ..... 135
4-3-1. Synthesis and characterization of the BCPs ..... 135
4-3-2. Domain orientation control in thin film ..... 136
4-3-3. Effects of side chain length on thin film morphology ..... 144
4-4. Conclusion ..... 146
4-5. Reference ..... 146
**Chapter 5 A High-χ Silicon-backbone in Combination with Fluorinated Side Chains Block Copolymer of Ultra-fast Thermal Annealing for Forming Perpendicular Pattern ..... 149**
5-1. Introduction ..... 149
5-2. Experimental Section ..... 152
5-2-1. Materials ..... 152
5-2-2. Methods ..... 152
5-2-3. Synthesis of homopolymer homo-PMVS ..... 153
5-2-4. Synthesis of homopolymer homo-PSi8F ..... 153
5-2-5. Synthesis of poly(styrene-*b*-methyl vinyl siloxane) (PS-*b*-PMVS) ..... 154
5-2-6. Synthesis of side chain modified PS-*b*-PSi8F ..... 155
5-2-7. Estimating the surface free energies of the homopolymer Homo-PSi8F ..... 155
5-2-8. Detailed information about the estimation of $\chi_{eff}$ ..... 158
5-2-9. Bulk sample preparation ..... 159
5-2-10. Synthesis of PTFEMA-*r*-PMMA-*r*-PMAAs ..... 159
5-2-11. Synthesis of top coat TC ..... 160
5-2-12. Thin film preparation ..... 161
5-3. Results and Discussion ..... 162
5-3-1. Synthesis of PS-*b*-PMVS ..... 162
5-3-2. Synthesis of PS-*b*-PSi8F ..... 163
5-3-3. Bulk Morphology ..... 163
5-3-4. Estimation of $\chi_{eff}$ ..... 169
5-3-5. Morphologies Predictions by Self-consistent field theory (SCFT) ..... 173
5-3-6. Perpendicular Lamellae in Thin Film ..... 178
5-4. Conclusion ..... 183

5-5. Reference ..... 183

**Chapter 6 Downsizing the Thin Film Domain of Poly-(styrene-*block*-methyl methacrylate) by Introducing Fluorine to Randomly Pre-polymerized Functional Units ..... 187**

6-1. Introduction ..... 187

6-2. Experimental Section ..... 188

6-2-1. Materials ..... 188

6-2-2. Methods ..... 189

6-2-3. Synthesis of PS-*b*-(PGMA-*r*-PMMA) ..... 189

6-2-4. Synthesis of PS-*b*-(PHFMA-*r*-PMMA) via thiol-epoxy reaction ..... 190

6-2-5. Detailed information about the estimation of $\chi_{eff}$ ..... 192

6-2-6. Bulk sample preparation ..... 192

6-2-7. Thin film preparation ..... 192

6-3. Results and Discussion ..... 193

6-3-1. Synthesis and characterization of the BCPs ..... 193

6-3-2. Estimation of $\chi_{eff}$ ..... 198

6-3-3. Morphologies in the bulk ..... 204

6-3-4. Morphologies Predictions by Self-consistent field theory (SCFT) ..... 208

6-3-5. Perpendicular Lamellae in Thin Film ..... 212

6-4. Conclusion ..... 219

6-5. Reference ..... 220

**Chapter 7 General Conclusions ..... 224**

**List of Publications and Presentations ..... 229**

**Acknowledgements ..... 231**

# Chapter 1
# General Introduction

## 1.1 Diblock copolymers

Block copolymers are made up of a number of different various segments, which are connected by covalent bonds. As the simplest AB diblock copolymer, two segments A and B are connected by covalent bonds to form the polymer chain. Moreover, ABC or ABA type triblock copolymer of more complex segments structure was recently discovered and studied. From the aspect of topology of polymer molecule, linear[1], rings[2], star[3], miktoarm[4] type were synthesized and studied for diblock copolymer. For triblock ABC, besides the traditional linear type, some more complex topology, such as miktoarm stars[5 6 7], were also reported.

The block copolymer can be synthesized by multiple methods, including anionic/cationic living polymerization[8], atom-transfer radical-polymerization (ATRP)[9] and reversible addition-fragmentation chain-transfer polymerization (RAFT)[10], and ring opening metathesis polymerization[11]. Among them, the anionic living polymerization exhibits the advantages of well-controlled polydispersity on product. Another great advantage of anionic polymerization is that it allows a very straightforward synthesis of block copolymers, which is free from the usage of additional catalyst or special agent compared with ATRP and RAFT. Since monomer batches are completely consumed, one can simply add a different comonomer to the polymerization mixture. The only concern is that sometimes the sequential monomer technique does not work, due to the difference in the reactivity of monomers their carbanion species. Thus, the sequence design of blocks is of great importance in anionic living polymerization. In the anionic living polymerization, the second block of AB type diblock copolymer is polymerized after the polymerization of the first block. As sometimes the reactivity of B comonomer with A carbanion specie is not adequate, the end-capping regent, such as (derivatives of) diphenylethylene (DPE)[12], which can end-cap the anionic species, is added to modify the reactivity mentioned above. The first synthesis of a diblock copolymer by living anionic polymerization was reported by Szvarc et al[13]. In fact, since the discovery of block copolymer, the development of synthetic methods had always been associated with the characteristics of the synthesized block copolymers. As discussed in the following introduction part, the self-assembly behavior of block copolymers, as one important characteristic, had been widely studied due to the potential application in industry. And according to the characteristics of the designed block copolymers, distinctive synthetic methods were utilized.

## 1.2 Self-assembly of diblock copolymers

Due to the fundamental incompatibility between the blocks of distinctive chemical structures, the self-assembly of block copolymers can occur, yielding ordered structure in a wide range including sphere, cylinder, lamella, bicontinuous structures and other complex or hierarchical assembly. The self-assembly of block copolymers could result in valuable technological applications; thus, the relationship between the chemical structure of block copolymers and the self-assembled morphology have been widely studied. To understand the phenomena, the microphase separation statistical theory of phase equilibrium in bulk[14] (or later mean field theory[15]) was developed for A-B type diblock copolymer.

In general, the self-assembly behaviors is driven by an unfavorable mixing enthalpy, together with a small mixing entropy. And the covalent bond connecting the blocks effectively prevents the macroscopic phase separation, which is different from homopolymer blending systems. As the self-assembly process is driven by repulsion interactions between A and B blocks, the weak repulsion led to the miscible phases based upon the minimization of free energy. In a system with weak repulsion, the increase in entropy is higher than that in enthalpy, which leads to a spontaneous miscible process. However, if the repulsion interaction between A and B blocks becomes strong, the increment in entropy becomes lower than that in enthalpy resulting from this miscibility. To minimize the free energy, the microphase separation between A and B domains becomes preferable rather than a homogenous phase The microphase separation of an A-B diblock copolymer is dependent on the following three parameters: (1) the volume fractions of the A and B blocks ($f_A$ and $f_B$, with $f_A+f_B = 1$), (2) the total degree of polymerization ($N = N_A + N_B$), and (3) the Flory-Huggins interaction parameter, $\chi_{AB}$. Herein the $\chi$ parameter specifies the degree of incompatibility between the A and B blocks, which result from the chemical properties of repeating units. The degree of microphase separation of diblocks is determined by the segregation product, $\chi N$. According to the mean field theory, the symmetrical block copolymer can be microphase separated and form a self-assembly morphology when $\chi N > 10.5$. Otherwise, the symmetrical two blocks will be miscible.

Furthermore, as shown in Equation 1-1, the interaction parameter $\chi_{AB}$ exhibits temperature dependence:

$$\chi_{AB} = \alpha/T + \beta \qquad \text{Equation 1-1}$$

where $\alpha$ and $\beta$ are constants and $T$ is temperature.

Therefore, based upon the above theory, the repulsion between two blocks can be enhanced by a higher $\chi$ resulting from lower temperature and a higher degree of polymerization $N$, which both contribute to a higher product of $\chi N$. As $\chi N$ becomes higher than 10.5, in theory, the incompatibility between the constituent blocks increases to a critical point in which the microphase separation will occur as to minimize the free energy of the system. Accordingly, a

periodic self-assembled structure will be formed as the periodic interface can minimize the interfacial area in order to minimize the total interfacial energy.

For a particular A-B type block copolymer, as $\chi$ is fixed under constant temperature, the morphology resulting from self-assembly will depend on the volume fraction of each block ($f_A$ and $f_B$), and the periodic dimension will depend principally on the degree of polymerization $N$. A phase diagram such as Figure 1-1 is quite useful to describe the self-assembly behavior affected by the volume fraction and degree of polymerization. Moreover, as mentioned above, the segregation limits can be divided into two: weak segregation limit (WSL) ($\chi N < 100$) and the strong segregation limit (SSL) ($\chi N > 100$) with regards to the magnitude of $\chi N$. The self-consistent mean-field (SCMF) theory[16 17 18] is often used to describe the whole range. as shown in Figure 1-1(a). The experimental phase diagram is also shown Figure 1-1(b) for comparison. With increasing $f_A$ at a fixed $\chi N$, the self-assembly nanostructure starts from closely packed spheres and body-centered cubic spheres (S), passing through hexagonally packed cylinders (C) and bicontinuous gyroids (G), to lamellae (L). The mechanism of the morphology transition is highly dependent on two competing factors: interfacial energy between the two blocks and chain stretching. The two factors represent the enthalpic and entropic contribution, respectively. To minimize the interfacial energy, the two blocks separated in a pattern of the minimized interface area. However, the microphase separation induced the stretching of the polymer chain, which was previously of a preferred coil conformation. And the stretching degree is dependent on the volume ratio of two blocks. As $f_A$ increases in Figure 1-1, the A domain gradually prefer to surround the B domain as the majority. The change of A block volume faction leads to the change of morphology, as the new morphology needs to be adapted to the lowest interfacial area and increased configurational entropy characteristics, based upon the former morphology. Also the stretching of chain conformation will be reduced as the two blocks become equal, leading to the morphology change from sphere of high curved interface to lamella of low curved interface. The morphology transitions were also verified by the experiments.

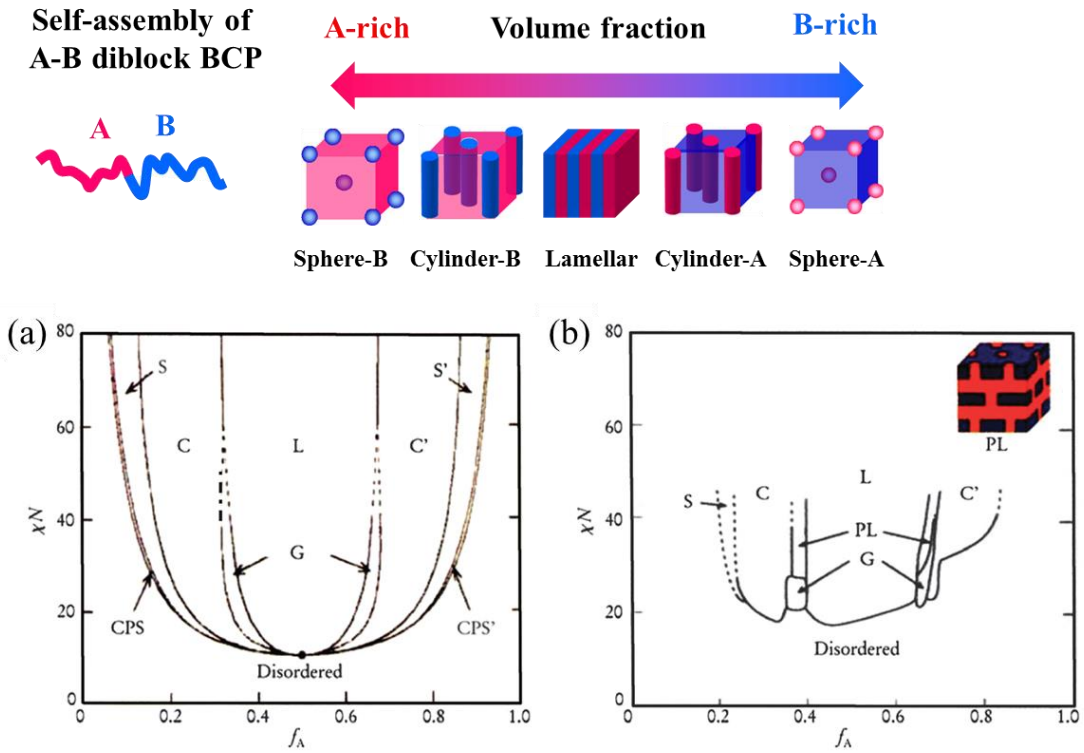


**Figure 1-1**. Schematic self-assembly morphologies and phase diagram of linear A-B diblock copolymers[19], comparing theory and experiment, (a): Self-consistent mean-field theory predicts four equilibrium morphologies: spherical (S), cylindrical (C), gyroid (G) and lamellar (L), depending on the composition and product of $\chi N$. (b): Experimental phase portrait for poly(isoprene-styrene) diblock copolymers.

For symmetric A-B diblock copolymer, the domain space size can be described by equation 1-2 and 1-3, in correspondence with a strong and weak segregation limit, respectively.

$d \propto aN^{2/3}\chi^{1/6}$ Equation 1-2

$d \propto aN^{1/2}$ Equation 1-3

Where in both equations *a* denotes the statistical segment length.

### 1.3 High χ block copolymers

The ability to self-assemble into 1-100 nm scale regular patterns gives block copolymers (BCPs) great potential in various industrial applications. Especially, perpendicularly-oriented lamellae with sub-10 nm feature sizes can be applied to next-generation lithography for semiconductor manufacturing. However, numerous issues including increasing the strength of segregation ($\chi_{eff}$), lowering the defectivity of the nanostructures, and inducing perpendicular orientation on thin films, are required to be addressed simultaneously before any practical applications.

At first, to obtain the sub-10 nm or smaller featured size from BCP self-assembly, a high

Flory-Huggins interaction parameter χ of BCP, which describes the driving force for microphase separation, was predicted by the earliest theory proposed by Leibler in 1980[14]. Since high-χ BCPs exhibited higher degree of chemical repulsion between the counter-blocks and thus enable the self-assembly of BCPs at low molecular weight, a smaller feature size of BCP self-assembly domains with higher domain density will be achieved. In theory for obtaining the self-assembly feature size of sub-10 nm, the relationship between the domain spacing and χ parameter values are expressed by equation 1-2 in strong segregation regime. Based on the equation, the domain spacing of self-assembly nanostructure is reversely proportional to the value of χ parameter.

Secondly, the defects of BCPs self-assembled nanostructure are undesirable for nanolithographic applications. The defect population is also related to the Flory-Huggins interaction parameter χ and a higher χ was considered capable of effectively reducing defects density.

In addition, the interface between two blocks in microphase separation is of great importance. In terms of the interface which delineates the two blocks, intermaterial dividing surface (IMDS) was exactly applied. The geometry of IMDS is determined by the conditions that the interfacial energy is minimized and the chain conformation entropy is maximized. And the thickness of IMDS was believed to scale with the edge roughness[20]. Thus, based upon equation 1-2, higher χ parameter between two blocks can lead to a thinner IMDS and a low edge roughness.

Based on the chemical properties of blocks, the reported block copolymers with high χ parameters can be categorized into two parts: hybrid organic-inorganic and wholly organic blocks types. In terms of organic-inorganic, inorganic usually refers to the siloxane-based segment. Among the traditional block copolymers, polystyrene-block-polydimethylsiloxane (PS-*b*-PDMS) exhibits a high χ parameter ($\chi_{PS\text{-}PDMS}\sim 0.27$)[21], and its hydrophobic characteristic is only second to the fluorine-containing block. The high χ parameter between inorganic PDMS and organic PS provides the driving force for microphase separation in 8 nm length scale. Additionally, inorganic siloxane-based segments exhibit tend to show higher etch resistance, which provide the chemical etch selectivity for the potential sub-10 nm length scale nanolithography application[22]. Currently, in many literatures, PDMS-based block copolymers[23] [24] (mainly PS-*b*-PDMS, PMMA-*b*-PDMS and P2VP-*b*-PDMS) were widely applied to form nanoscale patterns over a large area in a fast, low cost process. Highly ordered sub-10 nm width lines[25] [26] [27] [28] [21], dots[29] [30], and complex patterns[31] [32] [33] have been demonstrated and further nanopost templates[34] were reported on guiding the self-assembly. Recently Gopalan group developed a PDMS-based diblock copolymer poly(3-hydroxystyrene)-*b*-poly(dimethylsiloxane) (P3HS-*b*-PDMS)[35] of ultrahigh χ parameter.

However, due to the low surface tension ( or called surface free energy, SFE) of PDMS (19.9 mN/m)[36], PDMS preferentially segregates at the air/polymer interface. Thus, the desired perpendicular orientation control on PDMS based block copolymers was difficult. In addition, another drawback of PDMS block was attributed to the low glass transition temperature ($T_g$) that affects pattern stability. Moreover, a wide range of other silicon-containing block copolymers were developed and further utilized in self-assembly study for exploring next-generation block copolymer lithography materials. For example, polyhedral oligomeric silsesquioxane (POSS)-containing block copolymers poly(polyhedral oligomeric silsesquioxane methacrylate-*b*-methyl methacrylate) (PMAPOSS-*b*-PMMA)[37], poly(polyhedral oligomeric silsesquioxane methacrylate-*b*-styrene) (PMAPOSS-*b*-PS)[38] and poly(polyhedral oligomeric silsesquioxane methacrylate-*b*-2,2,2-trifluoroethyl methacrylate) (PMAPOSS-*b*-PTFEMA) [39] [40] [41], polytrimethylsilylstyrene-containing block copolymers poly-(trimethylsilylstyrene-*b*-*D,L*-lactide) (PTMSS-*b*-PLA)[42] [43], poly-(trimethylsilylstyrene-*b*-styrene) (PTMSS-*b*-PS)[44] [45] [46] [47], poly(trimethylsilylstyrene-*b*-*p*-methoxystyrene) (PTMSS-*b*-PMOST)[48], and poly(5-vinyl-1,3-benzodioxole-*b*-pentamethyldisilylstyrene) (PVBD-*b*-PDSS)[49]. Besides, tin-containing block copolymers poly(4-trimethylstannylstyrene-*b*-styrene) (PSnS-*b*-PS) and poly(4-trimethylstannylstyrene-*b*-4-methoxystyrene) (PSnS-*b*-PMOST)[50] were investigated as materials for nanolithographic applications.In addition, triblock copolymers poly(lactide-*b*-dimethylsiloxane-*b*-lactide) (PLA-*b*-PDMS-*b*-PLA)[51], poly(styrene-*b*-trimethylsilylstyrene-*b*-styrene) (PS-*b*-PTMSS-*b*-PS)[43] [52] or even triblock oligo(dimethylsiloxane) liquid crystals[53] capable of forming sub-5 nm patterns were investigated.

Recently, our research group reported a newly designed poly(styrene-*b*-substituted siloxane), (PS-*b*-PMHxOHS)[54]. In which the previously hydrophobic siloxane-based block possess the side chains ended by the hydrophilic groups as to balance the previously large SFE gap between the two blocks. Besides the tuning of SFE from the chemical structure design, top-coating[43]/bottom surface layer (neutral layer)[54] techniques can also assist the formation of perpendicularly orientation of lamella structure. Because the SFE gap resulting from the previous interface with air/substrate will be tuned by the new interface between block copolymers and top-coating/ bottom surface layers.

As for the wholly organic blocks type, poly(styrene-*b*-2-vinylpyridine) (PS-*b*-P2VP)[55], Poly(styrene-*b*-4-vinylpyridine) (PS-*b*-P4VP)[56] and Poly(styrene-*b*-lactide) (PS-*b*-PLA)[57] were widely used to achieve a nano-pattern of around 10 nm feature size. High $\chi$ parameter BCPs consisted of novel moiety structure, for example, poly(cyclohexylethylene)-*b*-poly(methyl methacrylate) (PCHE-*b*-PMMA)[58] was also reported.

Recently, BCPs containing rich hydrophilic hydroxyl groups polydihydroxystyrene-*b*-polystyrene (PDHS-*b*-PS)[59] or small brush molecules[60] [61] were reported for extremely narrow sub-3 or 1 nm domain feature size. Besides, a variety of fluorine-containing block copolymers with poly(styrene-*b*-2,2,2-trifluoroethyl methacrylate) (PS-*b*-PTFEMA)[62] as an example were developed and utilized to form highly ordered self-assembled structures. More details will be included in the following introduction section. Except for commonly used diblock copolymers, ABA triblock (MH-*b*-PCL-*b*-MH) and $A_2B$ star-branched copolymers ($(MH)_2$-*b*-PCL) consisting of maltoheptaose (MH, as the A block) and polycaprolactone (PCL, as the B block) were also synthesized for obtaining different self-assembled nanostructures[63]. Moreover, as organic blocks usually exhibit comparable etch rates, which is different from the case of organic-inorganic type, an additional metal-assisted process[64] is needed to vary the etch rates.

In summary, although high $\chi$ parameter block copolymers can form self-assembled nano-pattern of minimized domain size, the orientation control will be a key factor for the potential nanolithography. Therefore, new molecular design for balancing surface free energy of counter-block and additional orientation techniques including top coating or solvent annealing were widely studied in both academia and industry. The chemical structures of the mentioned high $\chi$ block copolymers were presented in Figure 1-3(a)-(b).

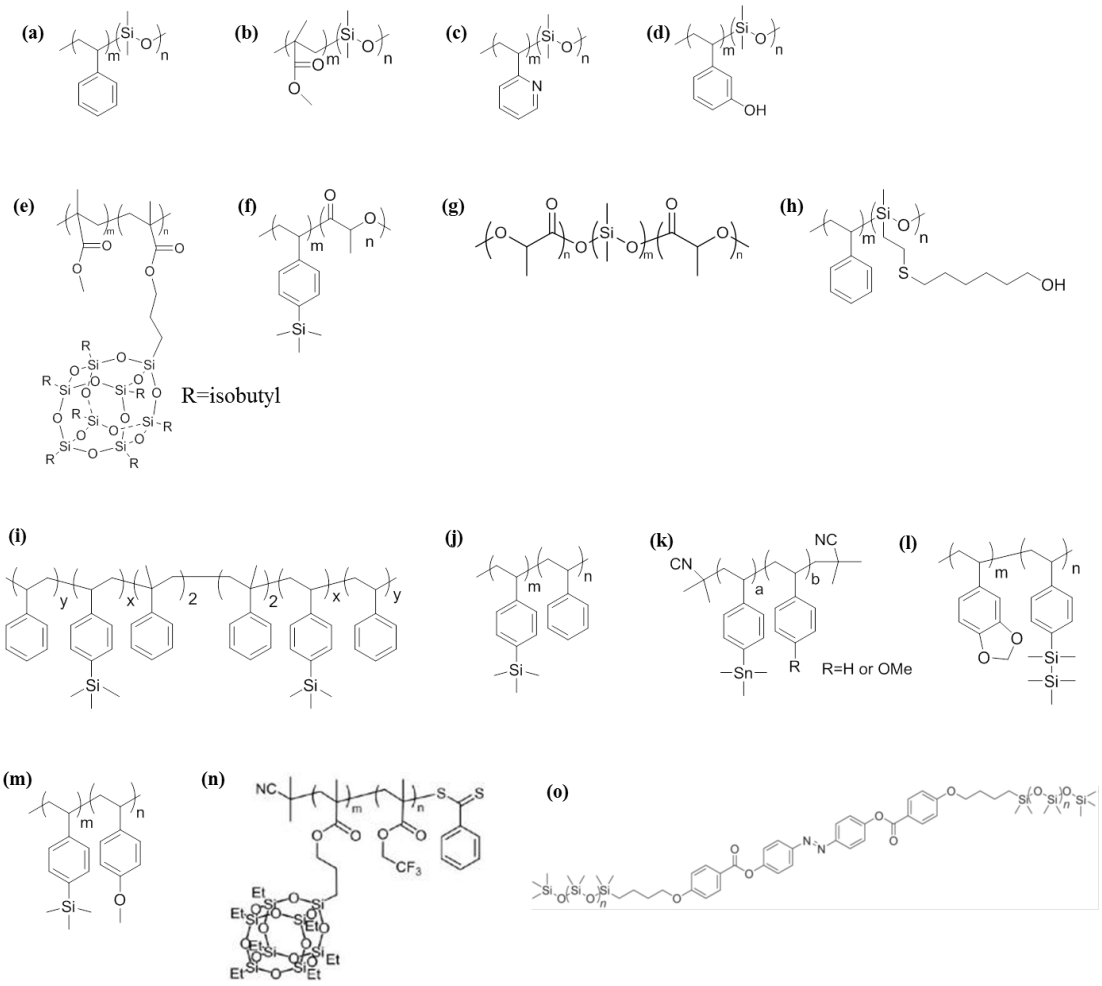


**Figure 1-3(a)**. Chemical structures of hybrid organic-inorganic type BCPs of high χ parameters: (a) PS-*b*-PDMS, (b) PMMA-*b*-PDMS, (c) P2VP-*b*-PDMS, (d) P3HS-*b*-PDMS, (e) PMAPOSS-*b*-PMMA, (f) PTMSS-*b*-PLA, (g) PLA-*b*-PDMS-*b*-PLA, (h) PS-*b*-PMHxOHS, (i) PS-*b*-PTMSS-*b*-PS, (j) PTMSS-*b*-PS, (k) PSnS-*b*-PS or PSnS-*b*-PMOST (l) PVBD-*b*-PDSS, (m) PTMSS-*b*-PMOST, (n) PMAPOSS-*b*-PTFEMA and (o) oligo(dimethylsiloxane) liquid crystal.

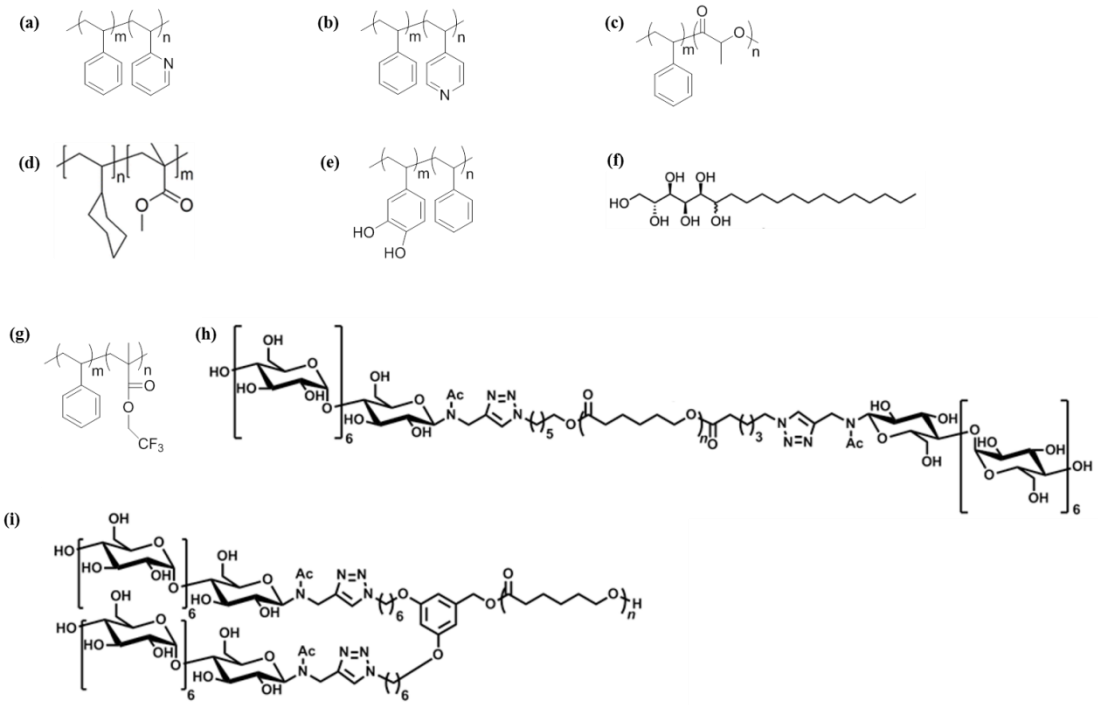

**Figure 1-3(b)**. Chemical structures of wholly organic type BCPs of high χ parameters: (a) PS-*b*-P2VP, (b) PS-*b*-P4VP, (k) PS-*b*-PLA, (d) PCHE-*b*-PMMA, (e) PDHS-*b*-PS, (f) brush molecule, (g) PS-*b*-PTFEMA, (h) MH-*b*-PCL-*b*-MH and (i) $(MH)_2$-*b*-PCL.

### 1.4 Block copolymers with fluorinated side chains

Fluorinated BCPs are reported to have high χ because of their intrinsic low surface energy, which is extremely incompatible with organic carbon/hydrogen-based segments. In 2005, Marc A. Hillmyer and Timothy P. Lodge reported an unusually high Flory-Huggins interaction parameter χ of polybutadiene-*block*-poly-(hexafluoropropylene oxide) by SAXS[65]. The extraction of χ value from the order-disorder transition gave a large order of 1, indicating a high degree of incompatibility between the two immiscible blocks, which is hardly described by mean-field theory.

Additionally, a special class of BCPs, called side chain liquid crystalline (SCLC) block copolymer has been shown various potential applications in the field of nanotechnology. For example, SCLC BCP is reported capable of controlling the orientation of the BCP domains in thin film. In SCLC BCPs self-assembly process, their microstructure will be influenced by two driving forces, side-chain crystalline LC ordering and mirco-phase separation, which is different from other BCPs as only mirco-phase separation was involved. Two periodicities of distinctive scales from side chain LC ordering and microphase separation of the counter-blocks will be co-existed and hence material properties (for instance, the BCP domain orientation in thin film) could be tailored by the hierarchical system. According to the earliest study on the

effect of semifluorinated side chain on surface properties and liquid crystalline structure[66], a long fluorocarbon side chain exhibited a typical smectic A or smectic B LC phase, depending on the number of fluorocarbon. The correlation between fluorocarbon number and LC phase was summarized in Table 1. Another paper later [67] reported BCPs with semifluorinated monodendron side groups, which were synthesized by attachment of a first generation 2- or 3-armed monodendron acid chloride to a hydroxylated poly(styrene-*b*-1,2/3,4-isoprene). The study found that the transition temperatures, mesophase range, and enthalpy of the smectic B-isotropic transition were all affected by side-group structural factors such as flexible spacer length, mesogen length, and monodendron core.

In addition to the bulk study, Atsushi Takahara [68] investigated the effects of fluorinated side chain length on the molecular aggregation states and surface properties thin films. Homopolymer poly(fluoroalkyl acrylate) (PFA-Cy, where y is the fluoromethylene number of the Rf groups) was used in the study. It was revealed that PFA-Cy with y > =8 was crystallized and formed ordered structures, as shown in Figure 1-5. Later Ober studied the supramolecular self-assembly within a liquid crystalline block copolymer thin film with mesogenic semifluorinated alkyl side groups[69]. The horizontal smectic layers takes in-plane direction and amorphous polystyrene block formed vertical domains interspersed in the liquid crystalline matrix, resulting in out-of-plane direction. The study showed similar results with an earlier paper[70].

Since then, morphology studies on the BCP containing fluorinated side chain began emerging till nowadays.

**Table 1-1**. Relationship between the semifluorinated side chain structures and their LC phases.

| BCP | $F(CF_2)k$ | $(CH_2)l$ | Phase | Critical Surface Tensions (mN/m) |
|---|---|---|---|---|
| poly(styrene-*b*-semifluorinated side chain) | k>10 | l>4 | Crystalline | 6 |
| | k=8 | l>4 | Smectic B | 8-9 |
| | k=6 | l>4 | Smectic A | 10-11 |
| | k<6 | l>4 | Isotropic | 12-16 |

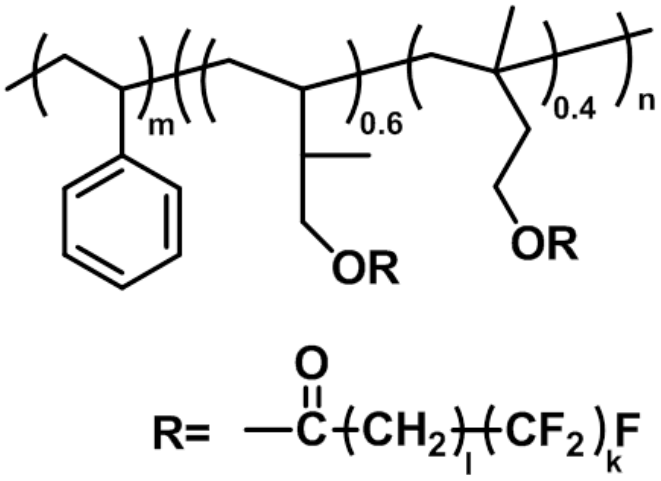


**Figure 1-4.** The chemical structure of studied poly(styrene-*b*-semifluorinated side chain).

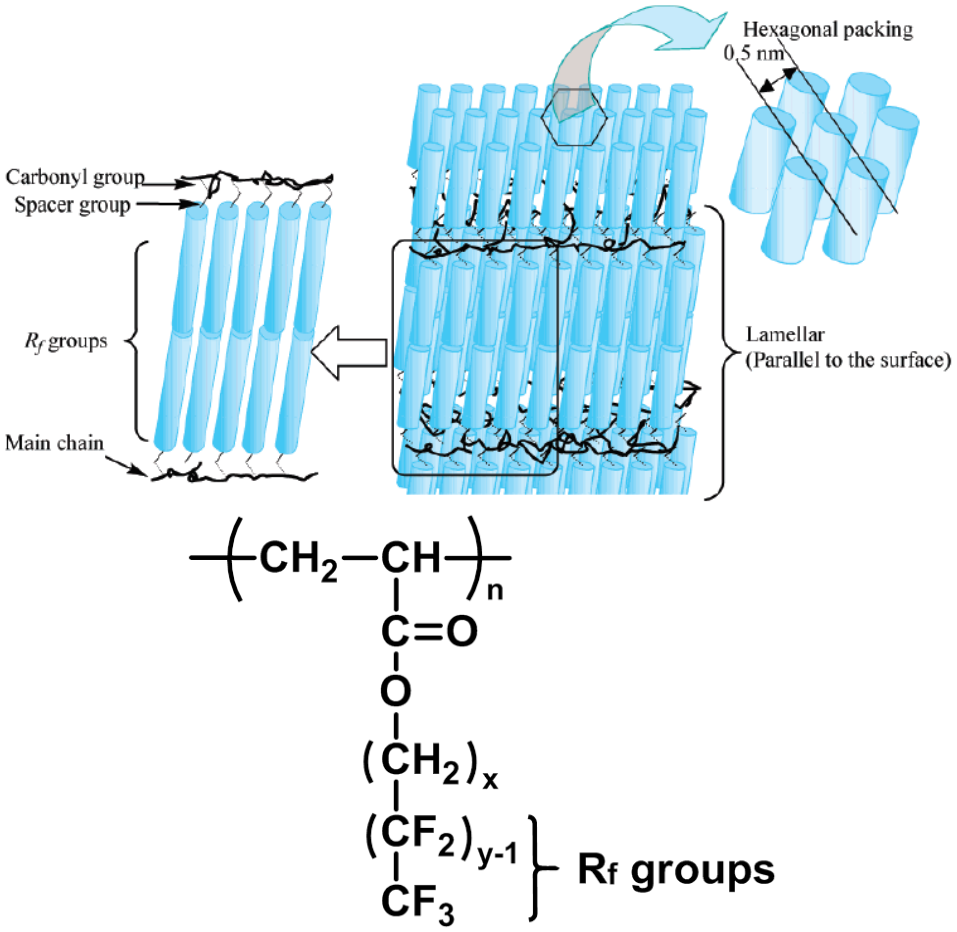


**Figure 1-5**. Schematic representation of molecular aggregation structure for the spin-coated PFA-Cy with y > =8 thin films and chemical structure of poly(fluoroalkyl acrylate).

## 1.5 Surface properties of BCPs with fluorinated side chains

As block copolymers can exhibit micro-phase separation to forme microstructures, the incorporated low surface energy blocks (fluorinated blocks) will segregate at interfaces and create further organization in the region of the low-energy surface. Therefore, the early study on BCPs of fluorinated side chain focused on the BCP architecture on the surface properties[71 72 73]. A representative fluorinated side chain BCP used in these studies is Poly(methyl methacrylate)-*block*-Poly(2-perfluorooctylethyl methacrylate) (PMMA-*b*-PFEMA)[74].

The early applications of BCPs with fluorinated side chains can be divided into marine antifouling coating[75 76 67], patterning of surface functionality[77], switching surface polarity[78], imaging in supercritical carbon dioxide technology[79 80] and polymer resists for 157 nm lithography [81 82 83 84] because fluorine-containing polymers are highly transparent at 157 nm.

Chistopher K. Ober at Cornell University contributed a lot to these mentioned fields. For example, Ober developed a family of fluoropolymers [81 82 83 84] that contain lithographically patternable, photoacid cleavable tetrahydropyranyl (THP-) groups. Because the hydrophobic acid groups are formed in the nonfluorinated block, the chemical changes in lithographical process and its effect on surface behavior are of paramount importance.

Another application example is fabrication super-hydrophobic surface with extremely low SFE. The mechanism is due to the BCPs with semifluorinated side groups, show an ordered arrangement at the air-polymer interface, resulting in low-energy surfaces. A mesomorphic surface was created with highly oriented perfluorinated chains (~1 nm thick) and tilted at certain angle to the surface normal[85]. The averaged tile angle of fluorinated chains at surface increases with increasing the length of the carbon spacer but decreases with increasing the length of -($CF_2$)- units in semi-fluorinated side chain[86]. The chemical composition of the surface-segregated nanostructure of the films was also affected by external environment like water[87]. Additionally, the surface organization of the semifluorinated LC mesogens was found correlated with the LC phase transition at varied temperatures[88].

Although most early studies focused on the surface structure, there are few studies[89] on the self-assembly structure of BCP in bulk sample. The semifluorinated side chains were found to self-assemble into liquid crystalline smectic layers within the microphase domains and an unexpected enhancement of surface organization by the aromatic group was observed. The orientational coupling between the -$CF_2$- helix and the aromatic ring at the surface was found to depend on the length of the fluorocarbon substituent.

In 2004, Ober [90] summarized the previous works on synthesis and characterization of block copolymers with fluorinated side chains, with special emphasis on surfaces formed using these polymers. The chemical structures of some representative BCPs and random copolymers with fluorinated side chains mentioned in this paragraph are summarized in **Figure 1-6**.

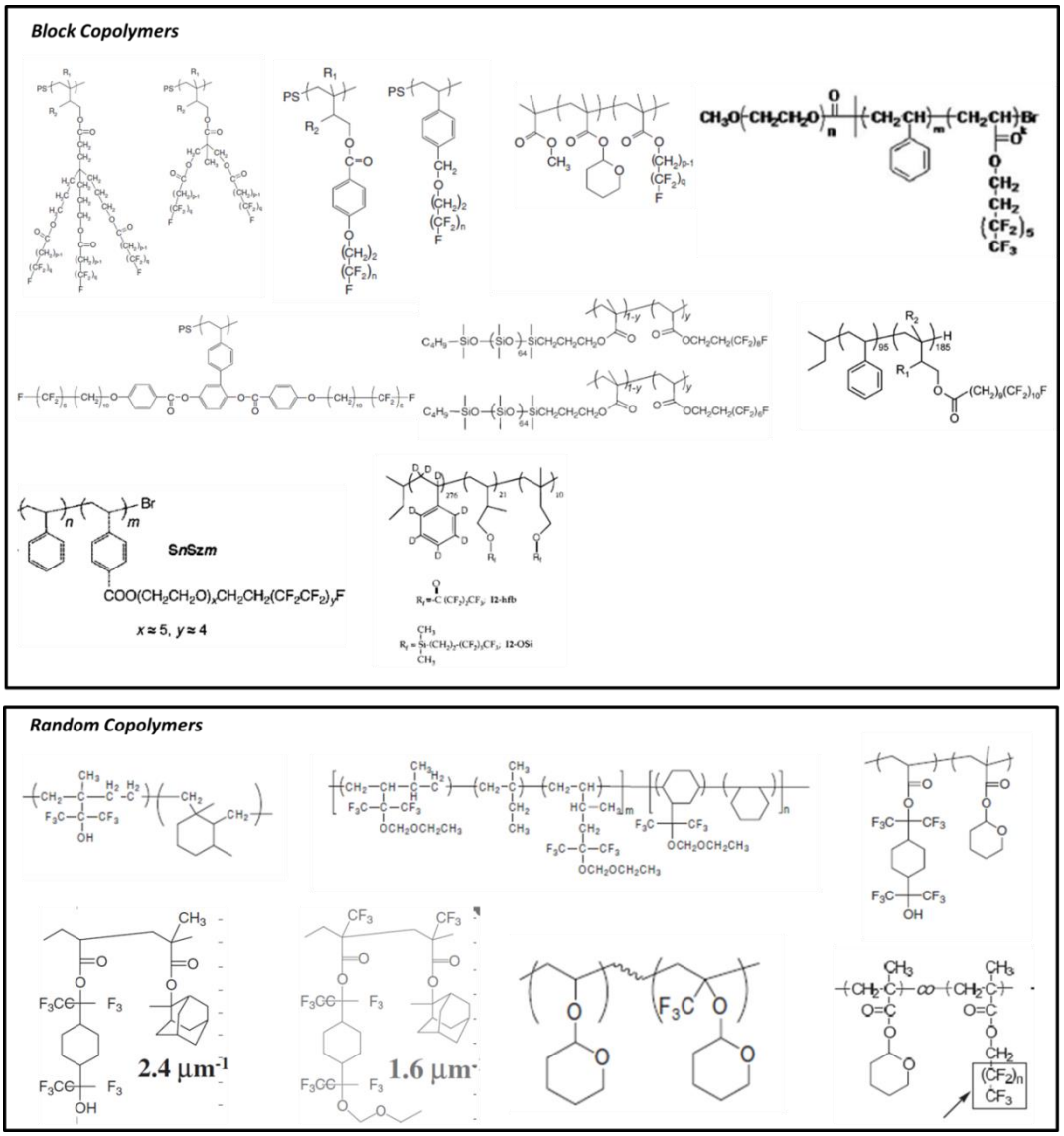


**Figure 1-6**. The chemical structures of some representative BCPs and random copolymers with fluorinated side chains.

## 1.6 Micelles self-assembly of BCPs with fluorinated side chains

Block copolymers containing fluorinated blocks have been widely studied on the solution self-assembly in nano-scale. The intensive incompatibility between the fluorinated and non-fluorinated segments strongly promotes phase segregation in these systems. When the amphiphilic block polymer is placed in a selective solvent preferential to one of the blocks, micelles structure will be formed in the self-assembly process. According to the solvent used, two routines including the fluorinated polymers as the insoluble core block with water or other common organic solvents as the self-assembly media[91 92 93 94 95 96 97 98 99 100 101 102 103], and usage

of fluorous solvents as self-assembly media[104].

A variety of micelles morphology based on fluorinated block copolymer were hence prepared including cylinders, toroids, disks, vesicles, wormlike micelles, and compartmentalized cylinders. The illustrative micelles morphology from self-assembly in solvents and corresponding chemical structure of fluorinated block copolymer were summarized in Table 2. The preferential solvents used for inducing self-assembly in these studied were also noted.

Marc A. Hillmyer and Timothy P. Loge F firstly reviewed the role of fluorination in determining block copolymer thermodynamics in both the solid state and solution state[105]. In this study, the selective and tunable incorporation of difluorocarbene and perfluoroalkyliodide additions to polydiene of model block copolymer was carried out. By increasing the incorporation of fluorinated groups, low-surface-energy polymers were yielded and the incompatibility between count-blocks was also significantly increased, which is quantified by $\chi$ parameter. The phase behaviors of block copolymers are generally categorized into weak, intermediated and strong segregation, depending on the magnitude of $\chi N$. In strong segregation regime, energetic roles begin to play more compared to the dominating entropic role in the weak segregation. The interfacial energy favors well-separated interfaces and stretched chain, meanwhile conformational entropy favors coiled blocks with more interfaces in fixed volume. In super-strong segregation regime of fluorinated BCP with extreme high $\chi$ parameter, the interfacial tensions dominates and therefore minor block has to be stretched out completely. Therefore, the domain size $d_{spacing}$ will linearly scale with $N$, which is different with the predicted $N^{2/3}$ scale dependence in strong segregation regime by Leibler's theory. Herein, as the interfacial tension rises, a transition from the initially spherical micelles to an oblate disk, a hairy hockey puck, and eventually a flat sheet are anticipated whether in bulk solid state or in solution.

As for the exploration on theory, Alimet Sema O¨zen [106] reported a multiscale computational approach employing quantum mechanical, atomistic, and coarse-grained simulations, which is adapted to reveal the self-assembly patterns of a styrene-co-fluorinated acrylate oligomer. As the oligomer concentration is increased, a transition from spherical micelles to hexagonal cylinders and lamella was predicted. The reverse-mapping of the morphologies gives the position information on styrene rings and the fluorinated segments in certain morphology.

**Table 1-2.** The illustrative micelles morphology from self-assembly in solvents and corresponding chemical structure of fluorinated block copolymer.

| BCP Chemical Structure | Micelles Self-assembly Model in Solvent | Solvent | Reference |
|---|---|---|---|
| 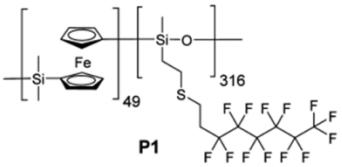  | 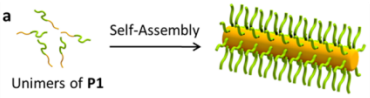  | 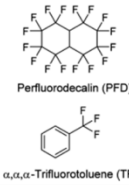  | [104] |
| 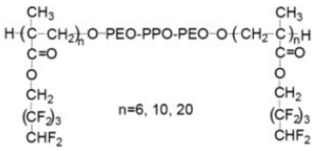  | 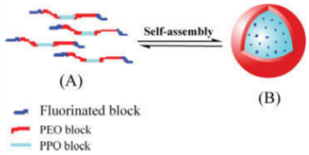  | Water | [91] |
| 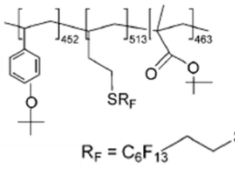  | 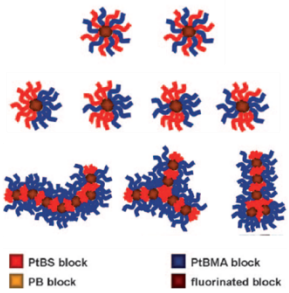  | Dioxane or ethanol | [92] |
| 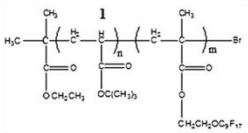  | 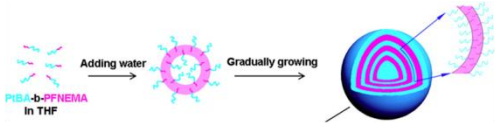  | THF/water | [93] |
| 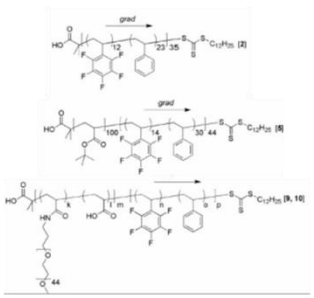 | 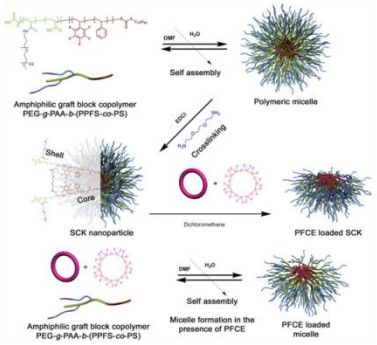  | DMF/water | [94] |
| 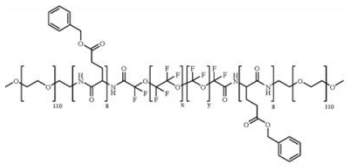 | 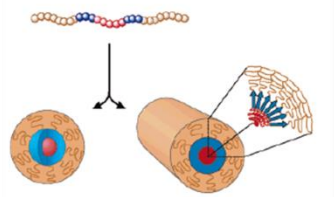 | Water | [95] |

| | | | |
|---|---|---|---|
| 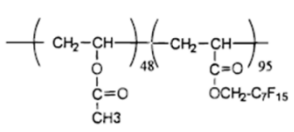 | Micelles (NG) | Carbon dioxide | [96] |
| 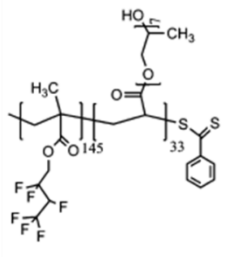 | Micelles (NG) | Water | [97] |
| 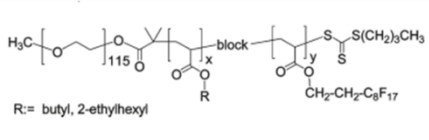 | Micelles (NG) | Water | [98] |
| 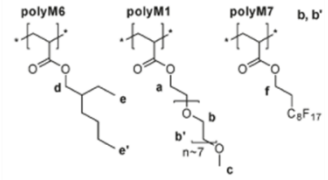 | Multicompartment Cores | Water | [99] |

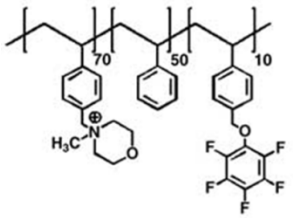


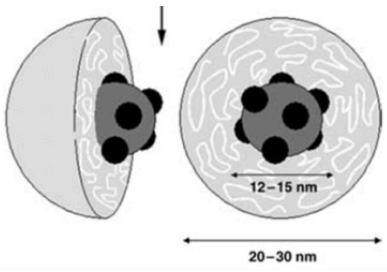


Water [102]

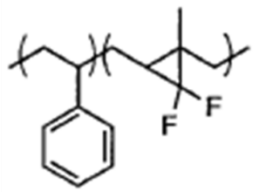


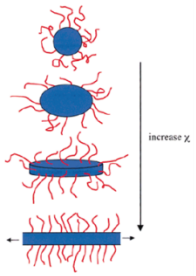


NG [105]

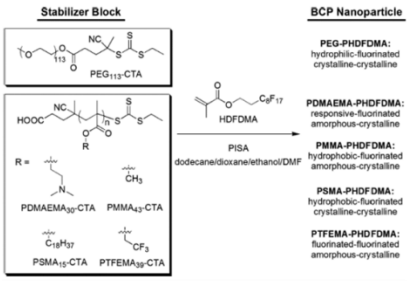


Fusiform nanoparticle
Elongated/fused vesicle
Porous nonspherical particle
Irregular solid particle

Ethanol [103]

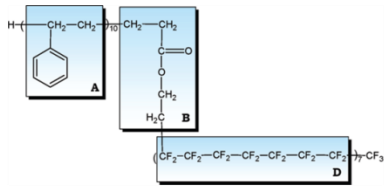


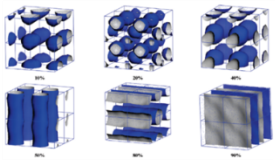

THF [106]

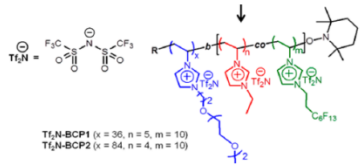


Water [100]

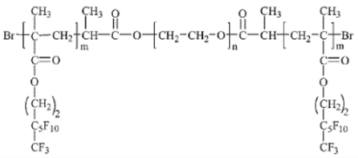

Single micelles, fibrous networks, some irregular morphology

Water [101]

## 1.7 Thin film self-assembly of BCPs with fluorinated side chains

The self-assembly of block copolymers (BCPs) could form pattern in 1-100 nm scale and the feature enable the potential application in industry, especially in next-generation lithography field. Generally, lithography demands BCPs of high χ parameter, high etching contrast and orientation control. Till now, molecular self-assembly of symmetric diblock copolymer had been well studied and understood in bulk such as the formed morphologies of cylinder and lamella. However, in thin film state more factors will contribute to the formation of morphology. Variation in BCP film thickness and substrate interfacial tension had been exploited to direct the orientation of self-assembly of BCPs. As for lamella-forming BCPs in bulk, paralleled and perpendicular orientation of molecular self-assembly could be existed in equilibrium arrangements. The paralleled orientation consists of symmetric and non-symmetric types, depending on the thickness of BCP film. Upon thermal annealing, BCPs will self-assemble into the equilibrium orientation of minimal free energy state. To determine the energy of three orientations, three governing equation were proposed as shown in Figure 1-8 [43]. Where *t* is the BCP film thickness, *n* is an integer, and *γ* represents a measure of the surface interactions of the components (A and B blocks) with the substrate and top interfaces (labeled Btm and Top, respectively). The system is defined such that $\gamma_A < \gamma_B$, and $\gamma_{AB}$ represents the interaction between the two blocks. The driving force for perpendicular orientation is represented by the difference between the horizontal and vertical free energy curves $F_H$-$F_V$. In the literature[107], algebraic models were also used to predict conditions that are favorable for perpendicular versus parallel domain orientation in films confined between two interfaces. The free energy of each orientation could be evaluated, yielding a function of film thickness and the preferential interaction strength at each interface. According to the equations, the possible minimal energy state is highly dependent on the four pairs of interfacial tensions between A/B block and top/bottom interface. To be specific, balanced interfacial tensions of A and B block at top/bottom interface are in demand for achieving perpendicular orientation. Unfortunately, due to the intrinsic difference in block polarity, high χ-BCPs are inclined to take the paralleled orientation as to minimize the interfacial energy. To solve the problem, solvent annealing was widely exploited to induce the perpendicular orientation. However, due to the shortcoming such as long-time annealing, deformation of morphology and incompatibility with current nanomanufacturing process, the process is less advantageous in comparison with thermal annealing.

An ideal solution to archive perpendicular orientation of high χ BCPs will be to confine the BCP between neutral bottom and top interfaces. Hence, top coat is a promising technique due to the following advantages: 1) spin-coating process enables it to be coated as BCPs. 2) the technique is compatible with thermal annealing. 3) processability enables large area of uniform

coverage. The neutral top coat will dissolve at least one block of BCPs in spin coating process due to the similar polarity. Usage of a solvent that does not interact with BCPs is preferred. However, extremely polar solvent such as water can only dissolve very polar polymer which can not be neutral to hydrophilic block of BCPs. Grant Willson group[43 52 45 46 47 50 49] firstly introduced top coat materials with polarity switch ability under thermal treatment. In polar form, top coat materials can be soluble in polar solvent such as methanol. After spin-coating on BCPs, thermal treatment will lead to a chemical transformation and convert top coat into a less polar state, which modulate the interfacial tension and is employed as neutral top interface. Furthermore, as the annealing temperature goes beyond glass transition temperature ($T_g$) of BCPs, perpendicular orientation will be obtained. The top coat can be removed by rinse using aqueous base or direct oxygen plasma etching.

The concepts on interfacial design via top coat materials and optimization on thin film orientation can be concluded as following three aspects: (1) The tuning on composition of top coat (TC) or substrate surface treatment (XST) in synthesis. (2) Salts transformation of TC for improvement solubility in polar solvent. (3) A "confined" island and hole test that precisely identifies preferential wetting at the top coat/bottom interface, which depends on composition of TC. (4) Optimization on perpendicular orientation of BCPs in thin film. The concept for hole/island test was expressed in Scheme1-1 and Figure 1-7(a)-(b).

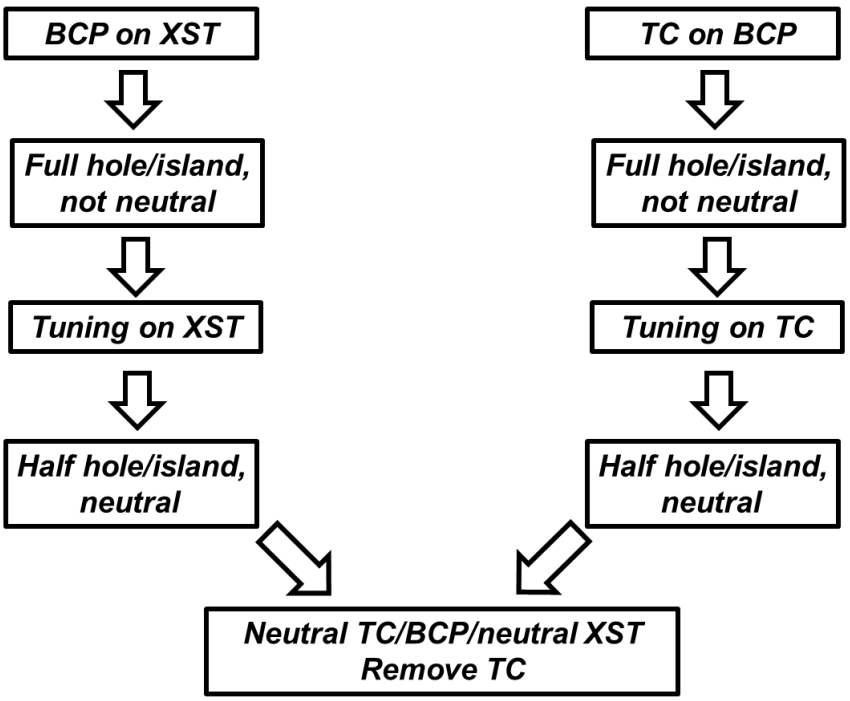


**Scheme 1-1.** Flowchart of refined hole/island tests for exploring neutral TC/XST materials.

**(a)**

| | Interface conditions | | | |
|---|---|---|---|---|
| Top interface | P | N | P | N |
| Btm interface | P | P | N | N |
| Surface topology | $1L_0$ | $0.5L_0$ | $0.5L_0$ | Flat |

P: Preferential N: Neutral

$1.0\ L_0 < L_{avg} < 1.5\ L_0$

Which block wets?

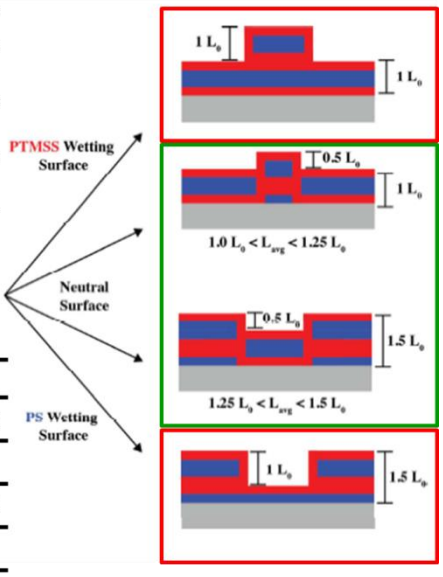


| BCP thickness range | | Top | Btm | Topology |
|---|---|---|---|---|
| $1L_0<L<2L_0$ | $1L_0<L<1.25L_0$ | P | N | $0.5L_0$ island |
| | $1.25L_0<L<1.5L_0$ | P | N | $0.5L_0$ hole |
| | $1.5L_0<L<1.75L_0$ | P | N | $0.5L_0$ island |
| | $1.75L_0<L<2L_0$ | P | N | $0.5L_0$ hole |

**(b)**

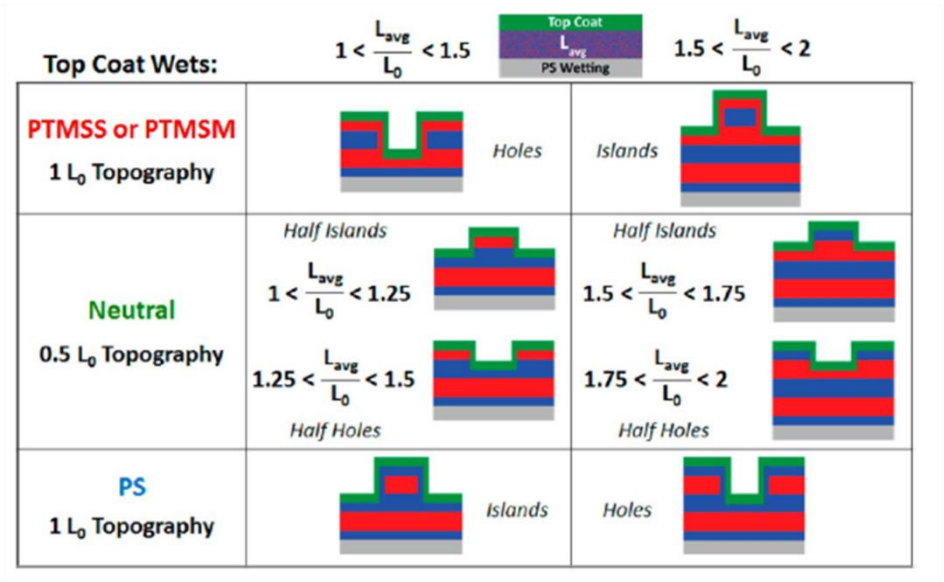


| BCP thickness range | | Top/Btm wetting | Topology |
|---|---|---|---|
| $1L_0<L<2L_0$ | $1L_0<L<1.5L_0$ | Sym | $1L_0$ island |
| | | Assym | $1L_0$ hole |
| | $1.5L_0<L<2L_0$ | Sym | $1L_0$ hole |
| | | Assym | $1L_0$ island |

**Figure 1-7.** Illustration on the relationship between thin film surface topology and block wetting in neutral materials exploration for (a) bottom substrate surface treatment (XST) and (b) top coat (TC) via hole-island test. The red, blue and green denotes PTMSS, PS and TC domain of an illustrative BCP PS-*b*-PTMSS[45], respectively.

As illustrated in the previous introduction, fluorinated BCPs with high χ meets the requirements of minimized domain size, reduced defect density, sharp interface with lower edge roughness. Additionally, the lower resistance of fluorinated block to oxygen plasma etching compared to commonly used building blocks gives fluorinated BCPs the selective etching properties, which facilitate the following pattern transfer to underlying Si substrate. The difficulty seemingly comes from the orientation control of BCP domain in thin film, as super-hydrophilic fluorinated segments of intrinsic lower SFEs were inclined to occupy the free air interface. One solution may be the introduction of side-chain liquid crystal (SCLC) fluorinated functionality.

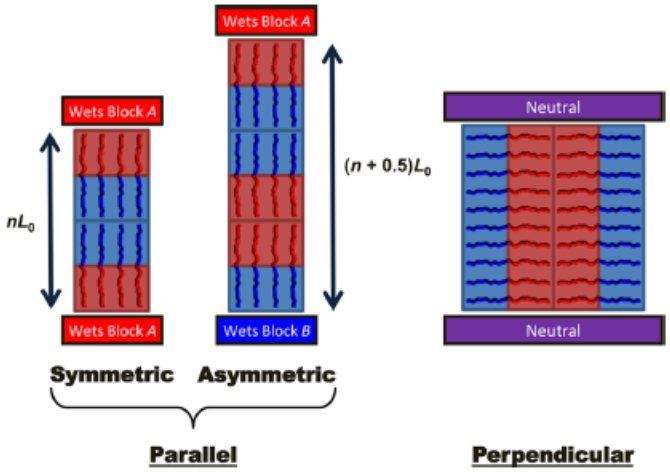


$$\frac{F_{H-SYM}}{F_0} = \frac{1}{3}\left[\left(\frac{t}{n}\right)^2 + \frac{2n}{t} + \frac{1}{t}\left(\frac{r_{A-Top}+r_{A-Btm}}{r_{AB}}\right)\right] \quad \text{Equation 1-4}$$

$$\frac{F_{H-ASYM}}{F_0} = \frac{1}{3}\left[\left(\frac{t}{n+0.5}\right)^2 + \frac{2(n+0.5)}{t} + \frac{1}{t}\left(\frac{r_{A-Top}+r_{A-Btm}}{r_{AB}}\right)\right] \quad \text{Equation 1-5}$$

$$\frac{F_V}{F_0} = \frac{1}{3}\left[3 + \frac{1}{2t}\left(\frac{r_{A-Top}+r_{B-Top}+r_{A-Btm}+r_{B-Btm}}{r_{AB}}\right)\right] \quad \text{Equation 1-6}$$

**Figure 1-8.** Three types of thin-film orientations of lamellae-forming symmetric AB diblock copolymer and energy governing equation for each orientation, denoted as H-SYM for symmetric parallel, H-ASYM for asymmetric parallel and V for vertical/perpendicular orientation, respectively.

Dated back to 2005, W. H. de Jeu [108] focused on the role of mesogen anchoring in the structure formation of a SCLC-BCP. The system studied is a diblock copolymer made of a poly-(methyl methacrylate) (PMMA) block and a poly(acrylate) block bearing semifluorinated alkyl side chains (PMMA-*b*-PF82A). The bulk investigations indicate that the two polymers strongly

microphase segregate into a cylindrical and a lamellar morphology, respectively. Inside the liquid-crystal block, the cylinder-forming block copolymer shows both a crystalline-B and a smectic-A phase, whereas the lamellae forming polymer gives only a smectic-A phase in double layers with a spacing of 3.33 nm. In thin film studies, the smectic layering and the orientational wetting properties of the fluorinated side chains stabilize the minority PMMA cylindrical domains normal to the substrate. In contrast, the lamellae-forming BCP reveal an evolved structure with block lamellae parallel to the substrate in combination with anchoring of the fluorinated chains at the surface of the film. Almost at the same time, a similar study[109] using the diblock copolymers comprise a polystyrene block and a block of poly(methyl methacrylate) bearing a chiral biphenyl ester mesogenic unit linked to the backbone by a dodecyloxy spacer was reported. The role of biphenyl ester mesogen units is found similar to that of fluorinated mesogen in thin self-assembly.

Similar studies [110] on interplayed hierarchical fluorinated LC side chain and self-assembly structures were also reported. In contrast, amorphous fluorinated side chain BCP was also reported[111] for potential lithographic application. Besides the A-B diblock copolymer, the thin film self-assembly behaviors of fluorinated A-B-A triblock copolymer [112] was studied later. Additionally Martin Moeller[113] gave an insight into the structure of supported monolayer of $F(CF_2)_{14}(CH_2)_{20}H$, which is small molecule instead of BCP. Well-defined nanoscopic ribbon and spiral or toroidal superstructures were observed. The fluorinated chains are oriented normal to the surface layer and where the alkyl segments are tilted with a 122 °angle between the two segments and this angle allows a dense packing of the alkyl segments compensating for the larger cross-section of the fluorocarbon segment.

In 2008, Paula T. Hammond group[114] reported a series of SCLC BCPs with LC fluorinated side chain. A simple chemistry route for precisely tuning the LC functionalization was provided. The LC content significantly affects the morphology and properties of the LC mesophase and the self-assembled morphology of the block copolymer. Numerous morphologies, including LCP cylinders, lamellae, PS cylinders, and coexistence of lamellae and cylindrical morphologies were obtained from a single polymer backbone. Therefore, the self-assembled morphologies could be tailored by the precise control on the LC fraction of functionalization. Recently Deng hai group reported several BCPs with fluorinated side chain for potential application in BCP lithography. In these studies, PS-typed[115], PMMA-typed[116] and Poly-(hydroxystyrene)-typed[117] fluoro-containing BCPs were synthesized and used as directed self-assembly materials. The finest half pitch of these BCPs is less than 5 nm. Additionally, the thermal annealing at mild temperature for a short time (e.g. 80 ℃ for 1 min) enables the practical application, which is attributed to the low-friction/high mobility of fluorinated segments.

Recently our group [39] [118] [40] developed a perpendicular lamellae-forming poly(polyhedral oligomeric silsesquioxane methacrylate-*block*-2,2,2-trifluoroethyl methacrylate)s (PMAPOSS-*b*-PTFEMAs). The use of silicon (Si)-containing hybrid high-χ BCPs provides easy access to sub-10 nm feature sizes. More importantly, through the use of fluorinated poly(2,2,2-trifluoroethyl methacrylate) (PTFEMA) segments, an balanced SFEs between PTFEMA and Si-containing polymers was achieved and perpendicular orientation of the BCP domains in thin films can be easily achieved without any interface modification. Direct Anionic polymerization or atom transfer radical polymerization (ATRP) was also utilized to synthesize the fluorine-containing block copolymers of poly(styrene-*block*-2,2,2-trifluoroethyl methacrylate) (PS-*b*-PTFEMA) and poly[styrene-*block*-(methyl methacrylate-*co*-2,2,2-trifluoroethyl methacrylate)] (PS-*b*-(PMMA-*co*-PTFEMA))[62], which are capable of both top-down and bottom-up lithography of lateral ordering of arrays of dots. These thin films were subjected to conventional lithographic processing using e-beam and deep-UV radiation to create integrated patterns such as "dots in lines". Besides the direct polymerization of PTFEMA-based BCPs, our group [119] also introduced 2,2,2-trifluoroethanethiol to glycidyl moieties in BCPs for tailoring SFEs of counter-blocks and chemical incompatibilities for engineering perpendicular lamellae in thin film.

In addition to the potential in lithographic application, other thin film-based applications, for instance, preparation of porous film[120] [121], nanoscopic cylindrical polymer brush[122], fouling release application[76] and organic field-effect transistors of high-mobility[123] were also carried out using BCPs with fluorinated side chain. Additionally, BCP nanoscale features afforded by BCP lithography were reported used for study on cell adhesion phenomena[124]. Similar application of selective binding of nano-particles onto specific regions of the microphase-separated fluorinated BCP via hydrogen bonds interaction [125] was reported as well.

In fact, instead of fluorinated LC side chain, other LC side chain systems[126] [127] [128] [129] [130] [131] [132] [133] [134], mainly azobenzene -containing mesogens, were widely reported to realize the similar effects on domain orientation control and long-ranged orders in thin film. LC main chain attached to polysiloxane segments [53] was also reported to achieve sub-5 nm pattern of long-ranged orders in thin film.

The chemical structures of reported BCPs with amorphous fluorinated side chain, for instance, Polystyrene-*b*-poly-(2,2,2-trifluoroethyl acrylate)s (PS-*b*-PTFEAs)[135] [62], thin film self-assembly and other important parameters of self-assembly were all summarized in **Table 1-3(a).** Besides, the information on BCPs with liquid crystalline fluorinated side chains with a typical example of polystyrene block and polyisoprene block to which perfluoroalkyl groups were attached through a flexible hydrocarbon spacer [69], were summarized in **Table 1-3(b)**. Some BCPs with unverified but quasi-liquid crystalline semi-fluorinated side chains [136] were

also included in this table.

**Table 1-3(a)**. The chemical structures of reported BCPs with amorphous fluorinated side chain, thin film self-assembly model, thin morphology type, BCP domain spacing, the expression of estimated effective χ parameter using random phase approximation and the typical χ parameter value at 150 ˚C annealing temperature.

| BCP Chemical Structure | Thin Film Self-assembly Model | Thin Film Morphology | BCP domain spacing | χ parameter | χ parameter at 150 °C | Reference |
|---|---|---|---|---|---|---|
| 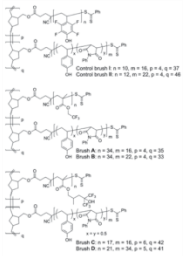 | 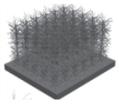 | Perpendicular CYL | NG | NG | NG | [122] |
| 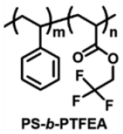 PS-*b*-PTFEA | 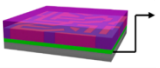 | Perpendicular LAM | Min 10.6 nm | χ = 30.86/T + 0.160 | χ = 0.233 | [135] |
|  pChNDI$_{50}$-*b*-pNB8F$_n$ | 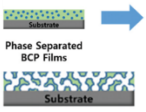 Phase Separated BCP Films Substrate | Pores | NG | NG | NG | [120] |
| blending 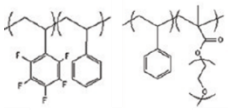 | 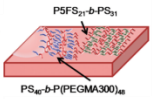 | Perpendicular LAM | NG | NG | NG | [121] |
| 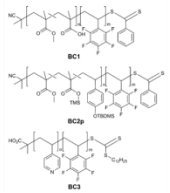 | NG | Parallel HEX | 35/62 nm | NG | NG | [111] |

| | | | | | | |
|---|---|---|---|---|---|---|
| 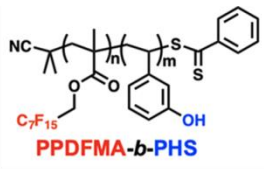 | NG | Perpendicular LAM | 9.8-19.5 nm | $\chi = 4.4/T + 0.4742$ | $\chi = 0.485$ | [117] |
| 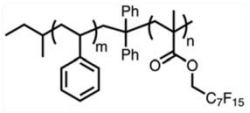 | NG | Perpendicular LAM<br>or Parallel HEX | 8.7-14.3 nm | $\chi = 78.51/T + 0.167$ | $\chi = 0.353$ | [115] |
| 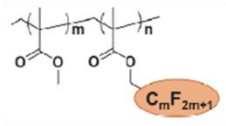 <br>m=3 or 7 | NG | LAM in bulk | 14 nm | NG | NG | [116] |
| 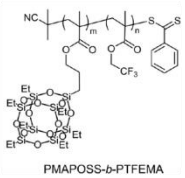 <br>PMAPOSS-*b*-PTFEMA | 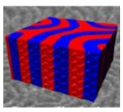 | Perpendicular LAM | 11.0-21.6 nm | $\chi = 27.4/T + 0.383$ | $\chi = 0.448$ | [118]<br>[39] |
| 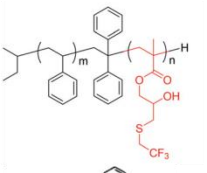 | NG | Perpendicular LAM | 9.6-26.0nm | $\chi = 19.4/T + 0.126$ | $\chi = 0.172$ | [119] |
| 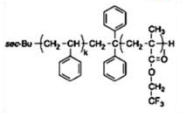 <br> 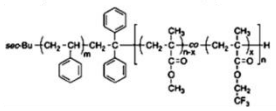 | 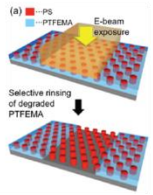 | Perpendicular HEX | ~30 nm | NG | NG | [62] |
| 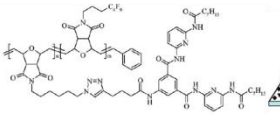 | 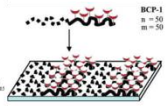 | Particle | 15-30 nm | NG | NG | [125] |

**Table 1-3(b)**. The chemical structures of reported BCPs with liquid crystalline fluorinated side chain, thin film self-assembly model, thin morphology type, LC ordering length, BCP domain spacing, and the expression of estimated effective χ parameter using random phase approximation.

| BCP Chemical Structure | Thin Film Self-assembly Model | Thin Film Morphology | LC ordering length | BCP domain spacing | χ parameter | Reference |
|---|---|---|---|---|---|---|
| 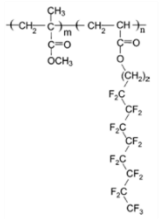 | 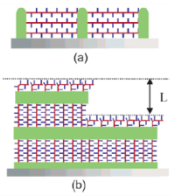 | Perpendicular Cyl or Parallel LAM | 3.3 nm | 30/20 nm | NG | [108] |
| 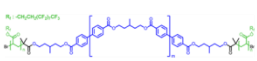 | 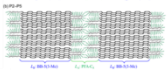 | Perpendicular LAM | 3.2 nm | 24.2-31.5 nm | NG | [112] |
| 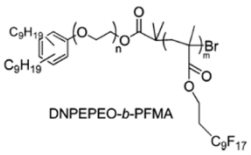 DNPEPEO-*b*-PFMA | NG | Perpendicular CYL | 3.2nm | 21 nm | NG | [110] |
| 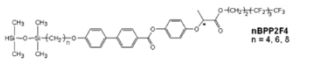 | 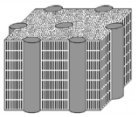 | CYL<br>LAM<br>CYL coexisting with LAM | 3.4/3.6/3.8nm<br>6.4/6.6/6.8nm | NG | NG | [109] |
| 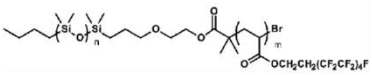 | NG | Spheres | 3.25 nm | NG | NG | [85] |
| 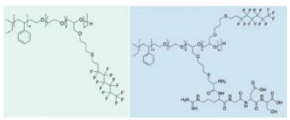 | 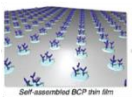 | Perpendicular HEX | NG | 25 nm | NG | [124] |
| 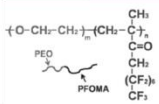 | NG | Spherical micelles<br>Parallel Cyl | NG | 20/30 nm | NG | [136] |
|  | NG | Perpendicular LAM or Dots | NG | 24-29 nm Dot<br>50-100 LAM | NG | [76] |
| 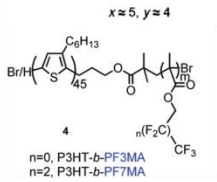 | 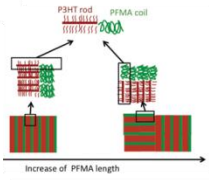 | Perpendicular LAM | 1.63 nm | NG | NG | [123] |
| 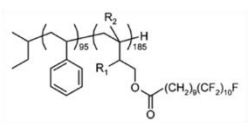 | 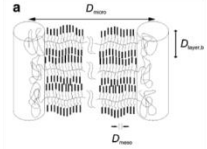 | Perpendicular Cyl | 27.2nm | 4.4 nm | NG | [68] |

## 1.8 SCLC self-assembly

Although the sophisticated use of hierarchical self-assembly materials, which include liquid crystal molecule, SCLC BCP, hydrogen- and p-bonded complexes is in demand in industry, the macromolecular systems with orders in materials over multiplied length scales is still challenging for further study. As people has been trying to understand the balancing organizing forces accounted for the hierarchical orders in one system since 1990s, SCLC BCP of semi-fluorinated side chain became a good solid-state structure for study[137] because of the competing interplay of phase separation and liquid crystallinity.

Compared to structure formed in bulk, the morphology in thin film is even more complex. The previous simulation study[107] predicts that non-preferential interaction at both top and bottom interfaces are required for perpendicular orientation of domains. Therefore, BCPs of balanced SFEs are in demand for perpendicular orientation in thin film, because the top free surface in this case will be air interface. However, the prediction is based on the approximation of flexible BCP in coil-coil model, the additional entropy contributor from SCLC is not concluded in enthalpy-driven equation. Therefore, despite the unbalanced SFEs of counter-blocks, SCLC BCP sometimes can lead to perpendicular orientation of BCP domain in thin film with another co-existed LC periodicity aligned to some certain direction with BCP domain.

To address the problem, modified models were developed. Different from flexible coil-coil diblock copolymer, the mean-field phase behavior for rod-coil or semiflexible-flexible diblock copolymers [138] [139] [140] [141] had been widely studied by applying self-consistent field technique. Based on these previous studies, in 2008 Manas Shah [142] presented a new model based on self-consistent field theory (SCFT) approach and complement it by strong segregation theory (SST) based calculations, as to characterize the self-assembly behavior in SCLC BCP. The micromechanic architecture of model is based on flexible coil-coil diblock copolymers, with rod-like units grafted to one of the blocks. The simulation results indicated that the self-assembly arises from the interplay between block copolymer microphase separation and the orientational ordering of the rod segments. The previous predicted microphases for flexible diblock copolymer also occur with accompanying smectic ordering. The predicted microphases in SCLC BCP are dependent on a variety of parameters, including molecular weight of the copolymer, the length of the rod units, the relative volume fractions of each block, and the energetic and orientational interactions between different components. Remarkably, the simulation results revealed that microphase separation is essential for developing orientational ordering between mesogenic unit. The generated phase diagram from this simulation method was shown in Figure 1-9.

Another approach is to describe the polymeric chains explicitly as collections of beads connected by springs, and incorporates the effects of fluctuations. The dissipative particle dynamics (DPD) simulations was used in these studies[143 144 145 146]. In this model, the block copolymer monomer consists of flexible A segments and flexible B segments grafted by rigid C side chains, where the A, B and C blocks are incompatible with each other. By controlling A and C block lengths and the graft number, various mesophases similar to flexible coiled BCP were found. All performed simulations are claimed to be consistent with vailable experimental observations.

Interestingly, different from SCLC BCPs, a comb-coil diblock formed by the selective complexation of the poly(4-vinylpyridine) (P4VP) block in a linear PS-*b*-P4VP with the surfactant dodecylbenzenesulfonic acid (DBSA) exhibited a tetragonal packing of the cylindrical microdomains[147], which is similar to the morphology observed in some SCLC BCP. Compared to the commonly observed hexagonal lattice, tetragonal lattice is another type of packing symmetry which is rarely observed unless some special factors are introduced to modify the intermicellar interaction, for instance, the interaction from entropy-confined side chain. In this study, the difference in packing symmetry is found to stem from the different relative orientation of the two structural entities with different length scales. Similar dissipative particle dynamics (DPD) simulations[148 149 150]were used to predict the unique self-assembly phase behaviors of rod (rigid side chain)-coil (flexible block) block copolymers in solution or thin film.

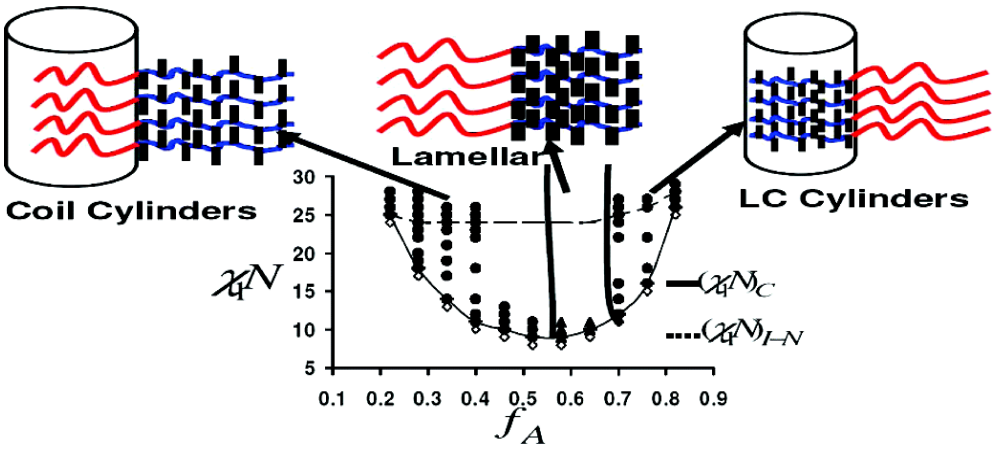


**Figure 1-9.** The self-assembly phase diagram obtained from 2D calculations. The solid line represents the transition from disordered phase to microphase separation, and the dashed line represents the transition to smectic ordering. Open diamonds represents disordered phase, while triangles represent lamellar phases and the circles represent the cylindrical morphologies discussed in the upper notes.

## 1.9 Block copolymer lithography

Lithography refers to the technology for creating extremely small pattern, which can be as small as a few nanometers, on the silicon-based substrate. Currently, the mainstream lithography process for semiconductors is known as photolithography, which is based on the projection optic for transferring pattern onto a substrate. According to the Rayleigh scaling equation, the resolution limit of the technique is proportional to the wavelength of light source. To date, photolithography using extreme ultraviolet (EUV) light source of 13.5 nm wavelength has demonstrated the capacity to form 13nm half pitch pattern with a single exposure.

Recently, people have discovered that the microphase separation of block copolymer could be utilized to fabricate the pattern of sub-20 nm. The advantages of the technique are the improvement of resolution and the simplification of process. However, due to the issue of orientation control, only a minority of block copolymer could be applied to lithography. In the lithography, both the free surface and the substrate surface could contribute to the orientation of micro-domains. To meet the requirements of the subsequent etching process, a perpendicular orientation is necessary instead of a horizontal orientation. Thus, the two blocks of copolymers were expected to exhibit similar affinity to both surfaces. Otherwise, a treatment of the bottom substrate surface, known as the neutralization layer, is adopted to diminish the affinity gap between the two blocks and induce the perpendicular orientation of microdomains. Additionally, the two blocks should exhibit etching selectivity, as the remaining block following the etching will further function as an etch mask. Besides the orientation control, alignment control of microdomains is also required. Currently, two types of alignment method have been proposed, namely grapho-epitaxy, and chemical epitaxy, as schematically presented in Figure 1-10(a)[151] and (b)[152], respectively. If the alignment control is not achieved, the lamellar domains of block copolymer may merely exhibit a finger-printed pattern.

Currently, the block copolymer lithography is mainly developed using poly(styrene-*b*-methyl methacrylate) (PS-*b*-PMMA), based upon a number of fundamental studies. In these studies, PS-*b*-PMMA was shown to form an approximately 10 nm pattern. However, some major drawbacks, such as defect density issue, were revealed for the technique. Moreover, to enhance the resolution of the formed pattern, alternatives of higher $\chi$ parameter were developed.

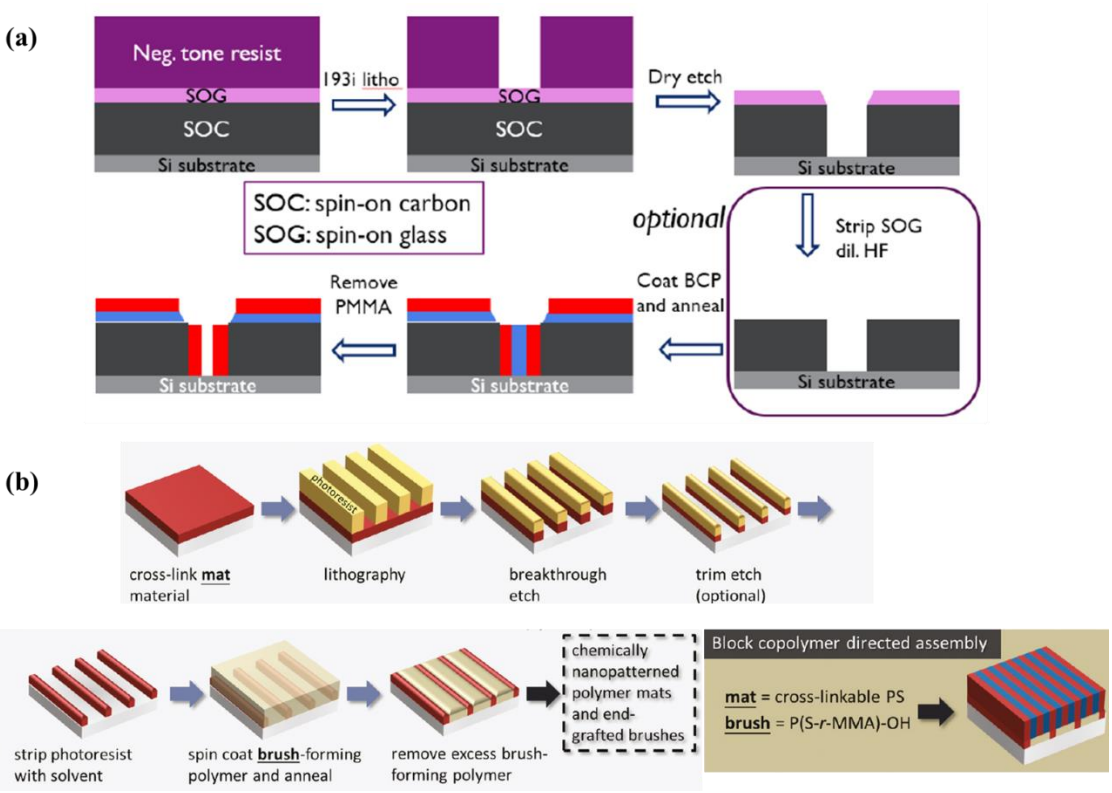


**Figure 1-10**. Schematic of (a) the grapho-epitaxy flow for hole patterning with cylindrical phase block copolymer (PS-*b*-PMMA) and (b) the chemical epitaxy flow for pattern formation process, followed by block copolymer (PS-*b*-PMMA) directed assembly.

## 1.10 Composition of this dissertation

As reviewed above, although there are reported studies on the self-assembly behaviors from diblock copolymers with fluorinated side chains, the minimization works on domain dimension are not even pushed to a physical limit, for instance sub-6 nm or even smaller feature. Besides, the hierarchical self-assembly with additional liquid crystalline side chain ordering had not been experimentally studied in depth. Moreover, as the lithographic applications are in demand of preparation of diverse high-quality patterns by using certain block copolymer, the development of facile and practical methodologies for thin film domain orientation control are attractive owing to the super-long ranged periodicity assisted by high-ordered liquid crystalline side chain self-assembly.

This dissertation is composed of 6 chapters, in which the self-assembly behaviors of high-$\chi$ parameter diblock copolymers with fluorinated side chains were studied for the advanced fabrication of sub-5 nm pattern using mass-production friendly process in next-generation semi-conducting manufacturing industry.

In Chapter 1, block copolymers (BCPs) self-assembly theory was firstly introduced. Owing to the advantage of high-$\chi$ parameter from BCPs with fluorinated side chains, the relevant works were further reviewed. The guideline for BCPs domain orientation control in thin film via tuning interface and the general BCP lithographic technology were also outlined.

In Chapter 2, the studies start with a novel type of diblock copolymers with semi-fluorinated liquid crystalline side chains, which are capable of forming 36.3-6.3 nm BCP domains coexisted with a fixed 3.6 nm liquid crystalline side chain ordering. The thin film orientation control for achieving long-ranged sub-5 nm half-pitch striation pattern was also successfully demonstrated.

Following Chapter 2, the hierarchy self-assembly morphology of one diblock copolymer capable of forming long-ranged sub-5 nm half-pitch striation pattern was deeply investigated in Chapter 3. In comparison, the effects of semi-fluorinated side chains lengths on the self-assembly morphology of BCPs were investigated.

Moving to Chapter 4, by using the same diblock copolymer discussed in Chapter 3, a convenient BCP thin film domain orientation control methodology via tuning bottom surface layer was successfully demonstrated. Owing to the asymmetry of hierarchy morphology, three distinctive patterns in response to three domain orientations could be fabricated with easy selectivity.

In Chapter 5 the same perfluoroalkylated side chain was extended to inorganic silicon backbone of BCPs for enhancing $\chi$ parameter and segments mobility. An orientation control methodology including development of top coat materials was utilized for this ultra-fasting annealing BCP material.

Additionally, Chapter 6 described a novel molecular design of incorporating quantitative 2,2,2-trifluoroethanethiol into the randomly polymerized glycidyl methacrylate along PMMA block of commonly studies PS-*b*-PMMA in BCP lithography field. The segregation between PS and PMMA segments was hence intensified and long-ranged sub-15 nm perpendicular domain was achieved in thin film upon fast thermal annealing.

In the end Chapter 7, these above research themes were concluded and the potential impact of the dissertation was described. Table 1-4 summarizes the contents from Chapter 2 to Chapter 6 and the correlation between each chapter is also indicated.

**Table 1-4.** The chemical structure of investigated BCPs with fluorinated side chains, the driving force for self-assembly under thermal annealing, the attained bulk/thin film morphologies and corresponding research target in Chapter 2-6.

| | BCPs with Fluorinated Side Chains | Driving Force for Self-assembly | Bulk Morphology | Thin Film Morphology | Research Target |
|---|---|---|---|---|---|
| Chapter 2 | 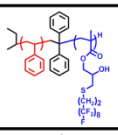 | Block segregation (variable)<br>Side chain LC ordering (constant) | $\chi N \downarrow$<br>LAM → HEX | 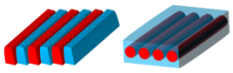 | Block segregation in hierarchical assembly |
| Chapter 3 | 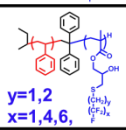 <br>y=1,2<br>x=1,4,6, 8 | Block segregation (constant)<br>Side chain LC ordering (variable) | Side chain length ↑<br>LAM →<br>Iso HEX →<br>Aniso HEX | Not included | Side chain ordering in hierarchical assembly |
| Chapter 4 | 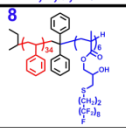 | Block segregation (constant)<br>Side chain LC ordering (constant) | Aniso HEX | 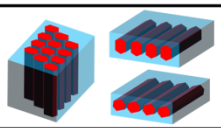 | Tailoring on pattern via tuning BSLs |
| Chapter 5 | 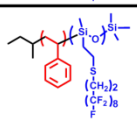 | Block segregation (variable) | $\chi N \downarrow$<br>LAM → HEX | 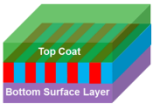 | Si-backbone for high etching contrast and fast-annealing |
| Chapter 6 | 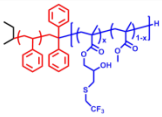 | Block segregation (variable) | LAM/HEX | 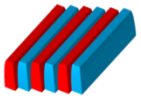 | Smaller vertical thin film domain of modified PS-*b*-PMMA |

**1-11. References**

1. Anastasiadis, S. H.; Russell, T. P.; Satija, S. K.; Majkrzak, C. F., The Morphology of Symmetric Diblock Copolymers as Revealed by Neutron Reflectivity. *J Chem Phys* 1990, *92* (9), 5677-5691.

2. Booth, C.; Attwood, D., Effects of block architecture and composition on the association properties of poly(oxyalkylene) copolymers in aqueous solution. *Macromol Rapid Comm* 2000, *21* (9), 501-527.

3. Choi, Y. R.; Bae, Y. H.; Kim, S. W., Star-shaped poly(ether-ester) block copolymers: Synthesis, characterization, and their physical properties. *Macromolecules* 1998, *31* (25), 8766-8774.

4. Tselikas, Y.; Iatrou, H.; Hadjichristidis, N.; Liang, K. S.; Mohanty, K.; Lohse, D. J., Morphology of miktoarm star block copolymers of styrene and isoprene. *J Chem Phys* 1996, *105* (6), 2456-2462.

5. Li, Z. B.; Kesselman, E.; Talmon, Y.; Hillmyer, M. A.; Lodge, T. P., Multicompartment micelles from ABC miktoarm stars in water. *Science* 2004, *306* (5693), 98-101.

6. Huckstadt, H.; Gopfert, A.; Abetz, V., Synthesis and morphology of ABC heteroarm star terpolymers of polystyrene, polybutadiene and poly(2-vinylpyridine). *Macromol Chem Physic* 2000, *201* (3), 296-307.

7. Li, Z. B.; Hillmyer, M. A.; Lodge, T. P., Morphologies of multicompartment micelles formed by ABC miktoarm star terpolymers. *Langmuir* 2006, *22* (22), 9409-9417.

8. Vanbeylen, M.; Bywater, S.; Smets, G.; Szwarc, M.; Worsfold, D. J., Developments in Anionic-Polymerization - a Critical-Review. *Adv Polym Sci* 1988, *86*, 87-143.

9. Muhlebach, A.; Gaynor, S. G.; Matyjaszewski, K., Synthesis of amphiphilic block copolymers by atom transfer radical polymerization (ATRP). *Macromolecules* 1998, *31* (18), 6046-6052.

10. Chong, Y. K.; Le, T. P. T.; Moad, G.; Rizzardo, E.; Thang, S. H., A more versatile route to block copolymers and other polymers of complex architecture by living radical polymerization: The RAFT process. *Macromolecules* 1999, *32* (6), 2071-2074.

11. Saunders, R. S.; Cohen, R. E.; Wong, S. J.; Schrock, R. R., Synthesis of Amphiphilic Star Block Copolymers Using Ring-Opening Metathesis Polymerization. *Macromolecules* 1992, *25* (7), 2055-2057.

12. Allen, R. D.; Long, T. E.; Mcgrath, J. E., Preparation of High-Purity, Anionic-Polymerization Grade Alkyl Methacrylate Monomers. *Polym Bull* 1986, *15* (2), 127-134.

13. Szwarc, M.; Levy, M.; Milkovich, R., Polymerization Initiated by Electron Transfer to Monomer - a New Method of Formation of Block Polymers. *J Am Chem Soc* 1956, *78* (11),

2656-2657.

14. Leibler, L., Theory of Microphase Separation in Block Co-Polymers. *Macromolecules* 1980, *13* (6), 1602-1617.

15. Likhtman, A. E.; Semenov, A. N., Theory of microphase separation in block copolymer/homopolymer mixtures. *Macromolecules* 1997, *30* (23), 7273-7278.

16. Matsen, M. W.; Schick, M., Stable and Unstable Phases of a Diblock Copolymer Melt. *Phys Rev Lett* 1994, *72* (16), 2660-2663.

17. Matsen, M. W.; Bates, F. S., Unifying weak- and strong-segregation block copolymer theories. *Macromolecules* 1996, *29* (4), 1091-1098.

18. Matsen, M. W.; Bates, F. S., Origins of complex self-assembly in block copolymers. *Macromolecules* 1996, *29* (23), 7641-7644.

19. Bates, F. S.; Fredrickson, G. H., Block copolymers - Designer soft materials. *Phys Today* 1999, *52* (2), 32-38.

20. Gido, S. P.; Schwark, D. W.; Thomas, E. L.; Goncalves, M. D., Observation of a Nonconstant Mean-Curvature Interface in an Abc Triblock Copolymer. *Macromolecules* 1993, *26* (10), 2636-2640.

21. Wu, N. L. Y.; Harris, K. D.; Buriak, J. M., Conversion of Bilayers of PS-b-PDMS Block Copolymer into Closely Packed, Aligned Silica Nanopatterns. *ACS Nano* 2013, *7* (6), 5595-5606.

22. Bita, I.; Yang, J. K. W.; Jung, Y. S.; Ross, C. A.; Thomas, E. L.; Berggren, K. K., Graphoepitaxy of self-assembled block copolymers on two-dimensional periodic patterned templates. *Science* 2008, *321* (5891), 939-943.

23. Inoue, H.; Matsumoto, A.; Matsukawa, K.; Ueda, A.; Nagai, S., Surface Characteristics of Polydimethylsiloxane-Poly(Methyl Methacrylate) Block Copolymers and Their Pmma Blends. *J Appl Polym Sci* 1990, *41* (7-8), 1815-1829.

24. Jeong, J. W.; Park, W. I.; Kim, M. J.; Ross, C. A.; Jung, Y. S., Highly Tunable Self-Assembled Nanostructures from a Poly(2-vinylpyridine-b-dimethylsiloxane) Block Copolymer. *Nano Lett* 2011, *11* (10), 4095-4101.

25. Rasappa, S.; Schulte, L.; Borah, D.; Morris, M. A.; Ndoni, S., Sub-15nm Silicon Lines Fabrication via PS-b-PDMS Block Copolymer Lithography. *J Nanomater* 2013.

26. Son, J. G.; Gotrik, K. W.; Ross, C. A., High-Aspect-Ratio Perpendicular Orientation of PS-b-PDMS Thin Films under Solvent Annealing. *ACS Macro Lett* 2012, *1* (11), 1279-1284.

27. Borah, D.; Shaw, M. T.; Holmes, J. D.; Morris, M. A., Sub-10 nm Feature Size PS-b-PDMS Block Copolymer Structures Fabricated by a Microwave-Assisted Solvothermal Process. *ACS Appl Mater Inter* 2013, *5* (6), 2004-2012.

28. Hobbs, R. G.; Farrell, R. A.; Bolger, C. T.; Kelly, R. A.; Morris, M. A.; Petkov, N.; Holmes,

J. D., Selective Sidewall Wetting of Polymer Blocks in Hydrogen Silsesquioxane Directed Self-Assembly of PS-b-PDMS. *ACS Appl Mater Inter* 2012, *4* (9), 4637-4642.

29. Park, S.; Kim, B.; Wang, J. Y.; Russell, T. P., Fabrication of highly ordered silicon oxide dots and stripes from block copolymer thin films. *Adv Mater* 2008, *20* (4), 681-685.

30. Son, J. G.; Hannon, A. F.; Gotrik, K. W.; Alexander-Katz, A.; Ross, C. A., Hierarchical Nanostructures by Sequential Self-Assembly of Styrene-Dimethylsiloxane Block Copolymers of Different Periods. *Adv Mater* 2011, *23* (5), 634-639.

31. Rasappa, S.; Caridad, J. M.; Schulte, L.; Cagliani, A.; Borah, D.; Morris, M. A.; Boggild, P.; Ndoni, S., High quality sub-10 nm graphene nanoribbons by on-chip PS-b-PDMS block copolymer lithography. *Rsc Adv* 2015, *5* (82), 66711-66717.

32. Bai, W. B.; Hannon, A. F.; Gotrik, K. W.; Choi, H. K.; Aissou, K.; Liontos, G.; Ntetsikas, K.; Alexander-Katz, A.; Avgeropoulos, A.; Ross, C. A., Thin Film Morphologies of Bulk-Gyroid Polystyrene-block-polydimethylsiloxane under Solvent Vapor Annealing. *Macromolecules* 2014, *47* (17), 6000-6008.

33. Yang, J. K. W.; Jung, Y. S.; Chang, J. B.; Mickiewicz, R. A.; Alexander-Katz, A.; Ross, C. A.; Berggren, K. K., Complex self-assembled patterns using sparse commensurate templates with locally varying motifs. *Nat Nanotechnol* 2010, *5* (4), 256-260.

34. Park, S. M.; Liang, X. G.; Harteneck, B. D.; Pick, T. E.; Hiroshiba, N.; Wu, Y.; Helms, B. A.; Olynick, D. L., Sub-10 nm Nanofabrication via Nanoimprint Directed Self-Assembly of Block Copolymers. *ACS Nano* 2011, *5* (11), 8523-8531.

35. Azuma, K.; Sung, J.; Choo, Y.; Rokhlenko, Y.; Dwyer, J. H.; Schweitzer, B.; Hayakawa, T.; Osuji, C. O.; Gopalan, P., Self-Assembly of an Ultrahigh-chi Block Copolymer with Versatile Etch Selectivity. *Macromolecules* 2018, *51* (16), 6460-6467.

36. Owen, M. J., Siloxane Surface-Activity. *Adv Chem Ser* 1990, (224), 705-739.

37. Hirai, T.; Leolukman, M.; Liu, C. C.; Han, E.; Kim, Y. J.; Ishida, Y.; Hayakawa, T.; Kakimoto, M.; Nealey, P. F.; Gopalan, P., One-Step Direct-Patterning Template Utilizing Self-Assembly of POSS-Containing Block Copolymers. *Adv Mater* 2009, *21* (43), 4334-4338.

38. Tada, Y.; Yoshida, H.; Ishida, Y.; Hirai, T.; Bosworth, J. K.; Dobisz, E.; Ruiz, R.; Takenaka, M.; Hayakawa, T.; Hasegawa, H., Directed Self-Assembly of POSS Containing Block Copolymer on Lithographically Defined Chemical Template with Morphology Control by Solvent Vapor. *Macromolecules* 2012, *45* (1), 292-304.

39. Nakatani, R.; Takano, H.; Chandra, A.; Yoshimura, Y.; Wang, L.; Suzuki, Y.; Tanaka, Y.; Maeda, R.; Kihara, N.; Minegishi, S.; Miyagi, K.; Kasahara, Y.; Sato, H.; Seino, Y.; Azuma, T.; Yokoyama, H.; Ober, C. K.; Hayakawa, T., Perpendicular Orientation Control without Interfacial Treatment of RAFT-Synthesized High-chi Block Copolymer Thin Films with Sub-10 nm Features Prepared via Thermal Annealing. *ACS Appl Mater Inter* 2017, *9* (37),

31266-31278.

40. Nakatani, R.; Takano, H.; Wang, L.; Chandra, A.; Tanaka, Y.; Maeda, R.; Kihara, N.; Minegishi, S.; Miyagi, K.; Kasahara, Y.; Sato, H.; Seino, Y.; Azuma, T.; Ober, C. K.; Hayakawa, T., Precise Synthesis of Fluorine-containing Block Copolymers via RAFT. *J Photopolym Sci Tec* 2016, *29* (5), 705-708.

41. Chandra, A.; Nakatani, R.; Uchiyama, T.; Seino, Y.; Sato, H.; Kasahara, Y.; Azuma, T.; Hayakawa, T., Direct In Situ Observation of the Early-Stage Disorder-Order Evolution of Perpendicular Lamellae in Thermally Annealed High-chi Block Copolymer Thin Films. *Adv Mater Interfaces* 2019, *6* (11).

42. Cushen, J. D.; Bates, C. M.; Rausch, E. L.; Dean, L. M.; Zhou, S. X.; Willson, C. G.; Ellison, C. J., Thin Film Self-Assembly of Poly(trimethylsilylstyrene-b-D,L-lactide) with Sub-10 nm Domains. *Macromolecules* 2012, *45* (21), 8722-8728.

43. Bates, C. M.; Seshimo, T.; Maher, M. J.; Durand, W. J.; Cushen, J. D.; Dean, L. M.; Blachut, G.; Ellison, C. J.; Willson, C. G., Polarity-Switching Top Coats Enable Orientation of Sub-10-nm Block Copolymer Domains. *Science* 2012, *338* (6108), 775-779.

44. Maher, M. J.; Bates, C. M.; Blachut, G.; Carlson, M. C.; Self, J. L.; Janes, D. W.; Durand, W. J.; Lane, A. P.; Ellison, C. J.; Willson, C. G., Photopatternable Interfaces for Block Copolymer Lithography. *ACS Macro Lett* 2014, *3* (8), 824-828.

45. Maher, M. J.; Bates, C. M.; Blachut, G.; Sirard, S.; Self, J. L.; Carlson, M. C.; Dean, L. M.; Cushen, J. D.; Durand, W. J.; Hayes, C. O.; Ellison, C. J.; Willson, C. G., Interfacial Design for Block Copolymer Thin Films. *Chem Mater* 2014, *26* (3), 1471-1479.

46. Durand, W. J.; Blachut, G.; Maher, M. J.; Sirard, S.; Tein, S.; Carlson, M. C.; Asano, Y.; Zhou, S. X.; Lane, A. P.; Bates, C. M.; Ellison, C. J.; Willson, C. G., Design of High-chi Block Copolymers for Lithography. *J Polym Sci Pol Chem* 2015, *53* (2), 344-352.

47. Maher, M. J.; Rettner, C. T.; Bates, C. M.; Blachut, G.; Carlson, M. C.; Durand, W. J.; Ellison, C. J.; Sanders, D. P.; Cheng, J. Y.; Willson, C. G., Directed Self-Assembly of Silicon-Containing Block Copolymer Thin Films. *ACS Appl Mater Inter* 2015, *7* (5), 3323-3328.

48. Cushen, J.; Wan, L.; Blachut, G.; Maher, M. J.; Albrecht, T. R.; Ellison, C. J.; Willson, C. G.; Ruiz, R., Double-Patterned Sidewall Directed Self-Assembly and Pattern Transfer of Sub-10 nm PTMSS-b-PMOST. *ACS Appl Mater Inter* 2015, *7* (24), 13476-13483.

49. Lane, A. P.; Yang, X. M.; Maher, M. J.; Blachut, G.; Asano, Y.; Soineya, Y.; Mallavarapu, A.; Sirard, S. M.; Ellison, C. J.; Willson, C. G., Directed Self-Assembly and Pattern Transfer of Five Nanometer Block Copolymer Lamellae. *ACS Nano* 2017, *11* (8), 7656-7665.

50. Maher, M. J.; Mori, K.; Sirard, S. M.; Dinhobl, A. M.; Bates, C. M.; Gurer, E.; Blachut, G.; Lane, A. P.; Durand, W. J.; Carlson, M. C.; Strahan, J. R.; Ellison, C. J.; Willson, C. G., Pattern

Transfer of Sub-10 nm Features via Tin-Containing Block Copolymers. *ACS Macro Lett* 2016, *5* (3), 391-395.

51. Rodwogin, M. D.; Spanjers, C. S.; Leighton, C.; Hillmyer, M. A., Polylactide - Poly(dimethylsiloxane) - Polylactide Triblock Copolymers as Multifunctional Materials for Nanolithographic Applications. *ACS Nano* 2010, *4* (2), 725-732.

52. Seshimo, T.; Bates, C. M.; Dean, L. M.; Cushen, J. D.; Durand, W. J.; Maher, M. J.; Ellison, C. J.; Willson, C. G., Block Copolymer Orientation Control Using a Top-Coat Surface Treatment. *J Photopolym Sci Tec* 2012, *25* (1), 125-129.

53. Nickmans, K.; Bogels, G. M.; Sanchez-Somolinos, C.; Murphy, J. N.; Leclere, P.; Voets, I. K.; Schenning, A., 3D Orientational Control in Self-Assembled Thin Films with Sub-5 nm Features by Light. *Small* 2017, *13* (33).

54. Seshimo, T.; Maeda, R.; Odashima, R.; Takenaka, Y.; Kawana, D.; Ohmori, K.; Hayakawa, T., Perpendicularly oriented sub-10-nm block copolymer lamellae by atmospheric thermal annealing for one minute. *Sci Rep-Uk* 2016, *6*.

55. Li, M. Q.; Ober, C. K., Block copolymer patterns and templates. *Mater Today* 2006, *9* (9), 30-39.

56. Park, S.; Wang, J. Y.; Kim, B.; Xu, J.; Russell, T. P., A simple route to highly oriented and ordered nanoporous block copolymer templates. *ACS Nano* 2008, *2* (4), 766-772.

57. Li, X.; Liu, Y. D.; Wan, L.; Li, Z. L.; Suh, H.; Ren, J. X.; Ocola, L. E.; Hu, W. B.; Ji, S. X.; Nealey, P. F., Effect of Stereochemistry on Directed Self-Assembly of Poly(styrene-b-lactide) Films on Chemical Patterns. *ACS Macro Lett* 2016, *5* (3), 396-401.

58. Kennemur, J. G.; Yao, L.; Bates, F. S.; Hillmyer, M. A., Sub-5 nm Domains in Ordered Poly(cyclohexylethylene)-block-poly(methyl methacrylate) Block Polymers for Lithography. *Macromolecules* 2014, *47* (4), 1411-1418.

59. Kwak, J.; Mishra, A. K.; Lee, J.; Lee, K. S.; Choi, C.; Maiti, S.; Kim, M.; Kim, J. K., Fabrication of Sub-3 nm Feature Size Based on Block Copolymer Self-Assembly for Next-Generation Nanolithography. *Macromolecules* 2017, *50* (17), 6813-6818.

60. Barreda, L.; Shen, Z. Y.; Chen, Q. L. P.; Lodge, T. P.; Siepmann, J. I.; Hillmyer, M. A., Synthesis, Simulation, and Self-Assembly of a Model Amphiphile To Push the Limits of Block Polymer Nanopatterning. *Nano Lett* 2019, *19* (7), 4458-4462.

61. Chen, Q. P.; Barreda, L.; Oquendo, L. E.; Hillmyer, M. A.; Lodge, T. P.; Siepmann, J. I., Computational Design of High-chi Block Oligomers for Accessing 1 nm Domains. *ACS Nano* 2018, *12* (5), 4351-4361.

62. Maeda, R.; Hayakawa, T.; Ober, C. K., Dual Mode Patterning of Fluorine-Containing Block Copolymers through Combined Top-down and Bottom-up Lithography. *Chem Mater* 2012, *24* (8), 1454-1461.

63. Isono, T.; Otsuka, I.; Suemasa, D.; Rochas, C.; Satoh, T.; Borsali, R.; Kakuchi, T., Synthesis, Self-Assembly, and Thermal Caramelization of Maltoheptaose-Conjugated Polycaprolactones Leading to Spherical, Cylindrical, and Lamellar Morphologies. *Macromolecules* 2013, *46* (22), 8932-8940.

64. Chang, S. W.; Chuang, V. P.; Boles, S. T.; Ross, C. A.; Thompson, C. V., Densely Packed Arrays of Ultra-High-Aspect-Ratio Silicon Nanowires Fabricated using Block-Copolymer Lithography and Metal-Assisted Etching. *Adv Funct Mater* 2009, *19* (15), 2495-2500.

65. Zhu, S.; Edmonds, W. F.; Hillmyer, M. A.; Lodge, T. P., Synthesis and self-assembly of highly incompatible polybutadiene–poly(hexafluoropropylene oxide) diblock copolymers. *Journal of Polymer Science Part B: Polymer Physics* 2005, *43* (24), 3685-3694.

66. Wang, J. G.; Mao, G. P.; Ober, C. K.; Kramer, E. J., Liquid crystalline, semifluorinated side group block copolymers with stable low energy surfaces: Synthesis, liquid crystalline structure, and critical surface tension. *Macromolecules* 1997, *30* (7), 1906-1914.

67. Xiang, M.; Li, X.; Ober, C. K.; Char, K.; Genzer, J.; Sivaniah, E.; Kramer, E. J.; Fischer, D. A., Surface Stability in Liquid-Crystalline Block Copolymers with Semifluorinated Monodendron Side Groups. *Macromolecules* 2000, *33* (16), 6106-6119.

68. Honda, K.; Morita, M.; Otsuka, H.; Takahara, A., Molecular Aggregation Structure and Surface Properties of Poly(fluoroalkyl acrylate) Thin Films. *Macromolecules* 2005, *38* (13), 5699-5705.

69. Busch, P.; Krishnan, S.; Paik, M.; Toombes, G. E. S.; Smilgies, D. M.; Gruner, S. M.; Ober, C. K., Surface induced tilt propagation in thin films of semifluorinated liquid crystalline side chain block copolymers. *Macromolecules* 2007, *40* (1), 81-89.

70. Al-Hussein, M.; Séréro, Y.; Konovalov, O.; Mourran, A.; Möller, M.; de Jeu, W. H., Nanoordering of Fluorinated Side-Chain Liquid Crystalline/Amorphous Diblock Copolymers. *Macromolecules* 2005, *38* (23), 9610-9616.

71. Iyengar, D. R.; Perutz, S. M.; Dai, C.-A.; Ober, C. K.; Kramer, E. J., Surface Segregation Studies of Fluorine-Containing Diblock Copolymers. *Macromolecules* 1996, *29* (4), 1229-1234.

72. Katano, Y.; Tomono, H.; Nakajima, T., Surface Property of Polymer Films with Fluoroalkyl Side Chains. *Macromolecules* 1994, *27* (8), 2342-2344.

73. Iyengar, D. R.; Perutz, S. M.; Dai, C. A.; Ober, C. K.; Kramer, E. J., Surface segregation studies of fluorine-containing diblock copolymers. *Macromolecules* 1996, *29* (4), 1229-1234.

74. Urushihara, Y.; Nishino, T., Effects of Film-Forming Conditions on Surface Properties and Structures of Diblock Copolymer with Perfluoroalkyl Side Chains. *Langmuir* 2005, *21* (6), 2614-2618.

75. Guo, W.; Tang, X.; Xu, J.; Wang, X.; Chen, Y.; Yu, F.; Pei, M., Synthesis, characterization,

and property of amphiphilic fluorinated abc-type triblock copolymers. *Journal of Polymer Science Part A: Polymer Chemistry* 2011, *49* (7), 1528-1534.

76. Martinelli, E.; Agostini, S.; Galli, G.; Chiellini, E.; Glisenti, A.; Pettitt, M. E.; Callow, M. E.; Callow, J. A.; Graf, K.; Bartels, F. W., Nanostructured Films of Amphiphilic Fluorinated Block Copolymers for Fouling Release Application. *Langmuir* 2008, *24* (22), 13138-13147.

77. Yang, S.; Wang, J.; Ogino, K.; Valiyaveettil, S.; Ober, C. K., Low-surface-energy fluoromethacrylate block copolymers with patternable elements. 2000.

78. Hayakawa, T.; Wang, J.; Sundararajan, N.; Xiang, M.; Li, X.; Glüsen, B.; Leung, G. C.; Ueda, M.; Ober, C. K., Switching surface polarity: synthesis and characterization of a fluorinated block copolymer with surface-active tert-butoxycarbonyl groups. *Journal of Physical Organic Chemistry* 2000, *13* (12), 787-795.

79. Sundararajan, N.; Yang, S.; Ogino, K.; Valiyaveettil, S.; Wang; Zhou, X.; Ober, C. K.; Obendorf, S. K.; Allen, R. D., Supercritical CO2 Processing for Submicron Imaging of Fluoropolymers. *Chem Mater* 2000, *12* (1), 41-48.

80. Sha, J.; Ober, C. K., Fluorine- and siloxane-containing polymers for supercritical carbon dioxide lithography. *Polymer International* 2009, *58* (3), 302-306.

81. Sanders, D. P.; Connor, E. F.; Grubbs, R. H.; Hung, R. J.; Osborn, B. P.; Chiba, T.; MacDonald, S. A.; Willson, C. G.; Conley, W., Metal-Catalyzed Addition Polymers for 157 nm Resist Applications. Synthesis and Polymerization of Partially Fluorinated, Ester-Functionalized Tricyclo[4.2.1.02,5]non-7-enes. *Macromolecules* 2003, *36* (5), 1534-1542.

82. Schmaljohann, D.; Young, C. B.; Dai, J.; Weibel, G. L.; Hamad, A. H.; Ober, C. K., Fundamental Studies of Fluoropolymer Photoresists for 157nm Lithography. *J Photopolym Sci Tec* 2000, *13* (3), 451-458.

83. Ober, C. K.; Douki, K.; Vohra, V. R.; Kwark, Y.-J.; Liu, X.-Q.; Conley, W.; Miller, D.; Zimmerman, P., New Strategies for High Resolution Photoresists. *J Photopolym Sci Tec* 2002, *15* (4), 603-611.

84. Schmaljohann, D.; Bae, Y. C.; Weibel, G. L.; Hamad, A. H.; Ober, C. K., *Design strategies for 157-nm single-layer photoresists: lithographic evaluation of a poly(A-trifluoromethyl vinyl alcohol) copolymer*. SPIE: 2000; Vol. 3999.

85. Martinelli, E.; Galli, G.; Krishnan, S.; Paik, M. Y.; Ober, C. K.; Fischer, D. A., New poly(dimethylsiloxane)/poly(perfluorooctylethyl acrylate) block copolymers: structure and order across multiple length scales in thin films. *Journal of Materials Chemistry* 2011, *21* (39), 15357-15368.

86. Genzer, J.; Sivaniah, E.; Kramer, E. J.; Wang, J. G.; Korner, H.; Xiang, M. L.; Char, K.; Ober, C. K.; DeKoven, B. M.; Bubeck, R. A.; Chaudhury, M. K.; Sambasivan, S.; Fischer, D. A.,

The orientation of semifluorinated alkanes attached to polymers at the surface of polymer films. *Macromolecules* 2000, *33* (5), 1882-1887.

87. Mielczarski, J. A.; Mielczarski, E.; Galli, G.; Morelli, A.; Martinelli, E.; Chiellini, E., The Surface-Segregated Nanostructure of Fluorinated Copolymer−Poly(dimethylsiloxane) Blend Films. *Langmuir* 2010, *26* (4), 2871-2876.

88. Genzer, J.; Sivaniah, E.; Kramer, E. J.; Wang, J. G.; Korner, H.; Char, K.; Ober, C. K.; DeKoven, B. M.; Bubeck, R. A.; Fischer, D. A.; Sambasivan, S., Temperature dependence of molecular orientation on the surfaces of semifluorinated polymer thin films. *Langmuir* 2000, *16* (4), 1993-1997.

89. Li, X.; Andruzzi, L.; Chiellini, E.; Galli, G.; Ober, C. K.; Hexemer, A.; Kramer, E. J.; Fischer, D. A., Semifluorinated Aromatic Side-Group Polystyrene-Based Block Copolymers: Bulk Structure and Surface Orientation Studies. *Macromolecules* 2002, *35* (21), 8078-8087.

90. Krishnan, S.; Kwark, Y. J.; Ober, C. K., Fluorinated polymers: Liquid crystalline properties and applications in lithography. *Chem Rec* 2004, *4* (5), 315-330.

91. He, J.; Ni, P.; Liu, C., Synthesis and characterization of amphiphilic fluorinated pentablock copolymers based on Pluronic F127. *Journal of Polymer Science Part A: Polymer Chemistry* 2008, *46* (9), 3029-3041.

92. Fang, B.; Walther, A.; Wolf, A.; Xu, Y.; Yuan, J.; Muller, A. H., Undulated multicompartment cylinders by the controlled and directed stacking of polymer micelles with a compartmentalized corona. *Angew Chem Int Ed Engl* 2009, *48* (16), 2877-80.

93. Qin, S.; Li, H.; Yuan, W.; Zhang, Y., Hierarchical self-assembly of fluorine-containing diblock copolymer:From onion-like nanospheres to superstructured microspheres. *Polymer* 2011, *52* (4), 1191-1196.

94. Nystrom, A. M.; Bartels, J. W.; Du, W.; Wooley, K. L., Perfluorocarbon-loaded Shell Crosslinked Knedel-like Nanoparticles: Lessons regarding polymer mobility and self assembly. *Journal of polymer science. Part A, Polymer chemistry* 2009, *47* (4), 1023-1037.

95. Thünemann, A. F.; Kubowicz, S.; von Berlepsch, H.; Möhwald, H., Two-Compartment Micellar Assemblies Obtained via Aqueous Self-Organization of Synthetic Polymer Building Blocks. *Langmuir* 2006, *22* (6), 2506-2510.

96. Triolo, F.; Triolo, A.; Triolo, R.; Londono, J. D.; Wignall, G. D.; McClain, J. B.; Betts, D. E.; Wells, S.; Samulski, E. T.; DeSimone, J. M., Critical Micelle Density for the Self-Assembly of Block Copolymer Surfactants in Supercritical Carbon Dioxide. *Langmuir* 2000, *16* (2), 416-421.

97. Mya, K. Y.; Lin, E. M. J.; Gudipati, C. S.; Gose, H. B. A. S.; He, C., Self-Assembly of Block Copolymer Micelles: Synthesis via Reversible Addition−Fragmentation Chain Transfer Polymerization and Aqueous Solution Properties. *The Journal of Physical Chemistry B* 2010,

*114* (28), 9128-9134.

98. Skrabania, K.; Laschewsky, A.; v Berlepsch, H.; Bottcher, C., Synthesis and micellar self-assembly of ternary hydrophilic-lipophilic-fluorophilic block copolymers with a linear PEO chain. *Langmuir* 2009, *25* (13), 7594-601.

99. Skrabania, K.; Berlepsch, H. v.; Böttcher, C.; Laschewsky, A., Synthesis of Ternary, Hydrophilic−Lipophilic−Fluorophilic Block Copolymers by Consecutive RAFT Polymerizations and Their Self-Assembly into Multicompartment Micelles. *Macromolecules* 2010, *43* (1), 271-281.

100. Cordella, D.; Ouhib, F.; Aqil, A.; Defize, T.; Jérôme, C.; Serghei, A.; Drockenmuller, E.; Aissou, K.; Taton, D.; Detrembleur, C., Fluorinated Poly(ionic liquid) Diblock Copolymers Obtained by Cobalt-Mediated Radical Polymerization-Induced Self-Assembly. *ACS Macro Lett* 2017, *6* (2), 121-126.

101. Hussain, H.; Busse, K.; Kressler, J., Poly(ethylene oxide)- and poly(perfluorohexylethyl methacrylate)-containing amphiphilic block copolymers: Association properties in aqueous solution. *Macromol Chem Physic* 2003, *204* (7), 936-946.

102. Kubowicz, S.; Baussard, J. F.; Lutz, J. F.; Thunemann, A. F.; von Berlepsch, H.; Laschewsky, A., Multicompartment micelles formed by self-assembly of linear ABC triblock copolymers in aqueous medium. *Angew Chem Int Ed Engl* 2005, *44* (33), 5262-5.

103. Shen, L.; Guo, H.; Zheng, J.; Wang, X.; Yang, Y.; An, Z., RAFT Polymerization-Induced Self-Assembly as a Strategy for Versatile Synthesis of Semifluorinated Liquid-Crystalline Block Copolymer Nanoobjects. *ACS Macro Lett* 2018, *7* (3), 287-292.

104. Hudson, Z. M.; Qian, J.; Boott, C. E.; Winnik, M. A.; Manners, I., Fluorous Cylindrical Micelles of Controlled Length by Crystallization-Driven Self-Assembly of Block Copolymers in Fluorinated Media. *ACS Macro Lett* 2015, *4* (2), 187-191.

105. Hillmyer, M. A.; Lodge, T. P., Synthesis and self-assembly of fluorinated block copolymers. *Journal of Polymer Science Part A: Polymer Chemistry* 2002, *40* (1), 1-8.

106. Kacar, G.; Atilgan, C.; Özen, A. S., Mapping and Reverse-Mapping of the Morphologies for a Molecular Understanding of the Self-Assembly of Fluorinated Block Copolymers. *The Journal of Physical Chemistry C* 2010, *114* (1), 370-382.

107. Durand, W. J.; Carlson, M. C.; Maher, M. J.; Blachut, G.; Santos, L. J.; Tein, S.; Ganesan, V.; Ellison, C. J.; Willson, C. G., Experimental and Modeling Study of Domain Orientation in Confined Block Copolymer Thin Films. *Macromolecules* 2016, *49* (1), 308-316.

108. Al-Hussein, M.; Serero, Y.; Konovalov, O.; Mourran, A.; Moller, M.; de Jeu, W. H., Nanoordering of fluorinated side-chain liquid crystalline/amorphous diblock copolymers. *Macromolecules* 2005, *38* (23), 9610-9616.

109. Hamley, I. W.; Castelletto, V.; Lu, Z. B.; Imrie, C. T.; Itoh, T.; Al-Hussein, M., Interplay

between smectic ordering and microphase separation in a series of side-group liquid-crystal block copolymers. *Macromolecules* 2004, *37* (13), 4798-4807.

110. Li, H.; Gu, W.; Li, L.; Zhang, Y.; Russell, T. P.; Coughlin, E. B., Synthesis of Semicrystalline/Fluorinated Side-Chain Crystalline Block Copolymers and Their Bulk and Thin Film Nanoordering. *Macromolecules* 2013, *46* (10), 3737-3745.

111. Riedel, M.; Stadermann, J.; Komber, H.; Simon, F.; Voit, B., Synthesis, post-modification and self-assembled thin films of pentafluorostyrene containing block copolymers. *Eur Polym J* 2011, *47* (4), 675-684.

112. Ishige, R.; Ohta, N.; Ogawa, H.; Tokita, M.; Takahara, A., Fully Liquid-Crystalline ABA Triblock Copolymer of Fluorinated Side-Chain Liquid-Crystalline A Block and Main-Chain Liquid-Crystalline B Block: Higher Order Structure in Bulk and Thin Film States. *Macromolecules* 2016, *49* (16), 6061-6074.

113. Mourran, A.; Tartsch, B.; Gallyamov, M.; Magonov, S.; Lambreva, D.; Ostrovskii, B. I.; Dolbnya, I. P.; de Jeu, W. H.; Moeller, M., Self-assembly of the perfluoroalkyl-alkane F14H20 in ultrathin films. *Langmuir* 2005, *21* (6), 2308-2316.

114. Verploegen, E.; Zhang, T.; Murlo, N.; Hammond, P. T., Influence of variations in liquid-crystalline content upon the self-assembly behavior of siloxane-based block copolymers. *Soft Matter* 2008, *4* (6), 1279.

115. Li, X. M.; Li, J.; Wang, C. X.; Liu, Y. Y.; Deng, H., Fast self-assembly of polystyrene-b-poly(fluoro methacrylate) into sub-5 nm microdomains for nanopatterning applications. *J Mater Chem C* 2019, *7* (9), 2535-2540.

116. Li, X. M.; Wang, C. X.; Zhou, J. N.; Yang, Z. Y.; Zhang, Y.; Deng, H., Ultra-Fast Block Copolymers for Sub-5 nm Lithographic Patterning. *J Photopolym Sci Tec* 2018, *31* (4), 483-486.

117. Wang, C. X.; Li, X. M.; Deng, H., Synthesis of a Fluoromethacrylate Hydroxystyrene Block Copolymer Capable of Rapidly Forming Sub-5 nm Domains at Low Temperatures. *ACS Macro Lett* 2019, *8* (4), 368-373.

118. Takano, H.; Wang, L.; Tanaka, Y.; Maeda, R.; Kihara, N.; Seino, Y.; Sato, H.; Kawamonzen, Y.; Miyagi, K.; Minegishi, S.; Azuma, T.; Ober, C. K.; Hayakawa, T., Vertical Oriented Lamellar Formation of Fluorine- and Silicon-containing Block Copolymers without Neutral Layers. *J Photopolym Sci Tec* 2015, *28* (5), 649-652.

119. Yoshimura, Y.; Chandra, A.; Nabae, Y.; Hayakawa, T., Chemically tailored high-chi block copolymers for perpendicular lamellae via thermal annealing. *Soft Matter* 2019, *15* (17), 3497-3506.

120. Cho, Y.; Kim, Y.; Choi, T.-L.; Lim, J.; Char, K., Swelling-induced pore generation in fluorinated polynorbornene block copolymer films. *Polym Chem-Uk* 2018, *9* (25), 3536-3542.

121. de León, A. S.; del Campo, A.; Fernández-García, M.; Rodríguez-Hernández, J.; Muñoz-Bonilla, A., Hierarchically Structured Multifunctional Porous Interfaces through Water Templated Self-Assembly of Ternary Systems. *Langmuir* 2012, *28* (25), 9778-9787.

122. Cho, S.; Yang, F.; Sun, G.; Eller, M. J.; Clark, C.; Schweikert, E. A.; Thackeray, J. W.; Trefonas, P.; Wooley, K. L., Directing self-assembly of nanoscopic cylindrical diblock brush terpolymers into films with desired spatial orientations: expansion of chemical composition scope. *Macromol Rapid Commun* 2014, *35* (4), 437-41.

123. Liu, J. Y.; Haynes, D.; Balliet, C.; Zhang, R.; Kowalewski, T.; McCullough, R. D., Self Encapsulated Poly(3-hexylthiophene)-poly(fluorinated alkyl methacrylate) Rod-Coil Block Copolymers with High Field Effect Mobilities on Bare SiO2. *Adv Funct Mater* 2012, *22* (5), 1024-1032.

124. Killops, K. L.; Gupta, N.; Dimitriou, M. D.; Lynd, N. A.; Jung, H.; Tran, H.; Bang, J.; Campos, L. M., Nanopatterning Biomolecules by Block Copolymer Self-Assembly. *ACS Macro Lett* 2012, *1* (6), 758-763.

125. Binder, W. H.; Kluger, C.; Straif, C. J.; Friedbacher, G., Directed Nanoparticle Binding onto Microphase-Separated Block Copolymer Thin Films. *Macromolecules* 2005, *38* (23), 9405-9410.

126. Nagano, S., Random Planar Orientation in Liquid-Crystalline Block Copolymers with Azobenzene Side Chains by Surface Segregation. *Langmuir* 2019, *35* (17), 5673-5683.

127. Liao, F.; Shi, L. Y.; Cheng, L. C.; Lee, S.; Ran, R.; Yager, K. G.; Ross, C. A., Self-assembly of a silicon-containing side-chain liquid crystalline block copolymer in bulk and in thin films: kinetic pathway of a cylinder to sphere transition. *Nanoscale* 2018, *11* (1), 285-293.

128. Yamashita, N.; Watanabe, S.; Nagai, K.; Komura, M.; Iyoda, T.; Aida, K.; Tada, Y.; Yoshida, H., Chemically directed self-assembly of perpendicularly aligned cylinders by a liquid crystalline block copolymer. *J Mater Chem C* 2015, *3* (12), 2837-2847.

129. Qu, T.; Guan, S.; Zhang, C.; Zheng, X. X.; Zhao, Y. B.; Chen, A. H., Liquid crystalline moiety-assisted perpendicular orientation of cylindrical domains within P4VP-b-PMA(Az) films with high aspect ratio. *Soft Matter* 2018, *14* (35), 7107-7112.

130. Jiang, X.-Q.; Zhao, R.-Y.; Chang, W.-Y.; Yin, D.-X.; Guo, Y.-C.; Wang, W.; Liang, D.-H.; Yang, S.; Shi, A.-C.; Chen, E.-Q., Highly Ordered Sub-10 nm Patterns Based on Multichain Columns of Side-Chain Liquid Crystalline Polymers. *Macromolecules* 2019.

131. Verploegen, E.; Zhang, T.; Jung, Y. S.; Ross, C.; Hammond, P. T., Controlling the Morphology of Side Chain Liquid Crystalline Block Copolymer Thin Films through Variations in Liquid Crystalline Content. *Nano Lett* 2008, *8* (10), 3434-3440.

132. Verploegen, E.; McAfee, L. C.; Tian, L.; Verploegen, D.; Hammond, P. T., Observation of

Transverse Cylinder Morphology in Side Chain Liquid Crystalline Block Copolymers. *Macromolecules* 2007, *40* (4), 777-780.

133.Ding, L. M.; Mao, H. M.; Xu, J.; He, J. B.; Ding, X.; Russell, T. P.; Robello, D. R.; Mis, M., Morphological study on an Azobenzene-containing liquid crystalline Diblock copolymer. *Macromolecules* 2008, *41* (6), 1897-1900.

134. Wang, T. J.; Li, X.; Dong, Z. J.; Huang, S.; Yu, H. F., Vertical Orientation of Nanocylinders in Liquid-Crystalline Block Copolymers Directed by Light. *ACS Appl Mater Inter* 2017, *9* (29), 24864-24872.

135. Jo, S.; Jeon, S.; Jun, T.; Park, C.; Ryu, D. Y., Fluorine-Containing Styrenic Block Copolymers toward High χ and Perpendicular Lamellae in Thin Films. *Macromolecules* 2018, *51* (18), 7152-7159.

136. Islam, M. T.; Islam, M. R.; Lim, K. T., A paradigm shift in morphological architecture of PEO-b-PFOMA semi-fluorinated block copolymer thin films upon facile solvent annealing. *Polymer* 2011, *52* (22), 5212-5220.

137. Muthukumar, M.; Ober, C. K.; Thomas, E. L., Competing interactions and levels of ordering in self-organizing polymeric materials. *Science* 1997, *277* (5330), 1225-1232.

138. Matsen, M. W.; Barrett, C., Liquid-crystalline behavior of rod-coil diblock copolymers. *J Chem Phys* 1998, *109* (10), 4108-4118.

139.Netz, P. R.; Schick, M., Liquid-crystalline phases of semiflexible diblock copolymer melts. *Phys Rev Lett* 1996, *77* (2), 302-305.

140. Matsen, M. W., Melts of semiflexible diblock copolymer. *J Chem Phys* 1996, *104* (19), 7758-7764.

141. Kumar, N. A.; Ganesan, V., Communication: Self-assembly of semiflexible-flexible block copolymers. *J Chem Phys* 2012, *136* (10).

142. Shah, M.; Pryarnitsyn, V.; Ganesan, V., A model for self-assembly in side chain liquid crystalline block copolymers. *Macromolecules* 2008, *41* (1), 218-229.

143. Li, X. K.; Huang, F.; Jiang, T.; He, X. H.; Lin, S. L.; Lin, J. P., Phase behaviors of side chain liquid crystalline block copolymers. *Rsc Adv* 2015, *5* (2), 1514-1521.

144. Lv, Y. S.; Wang, L. Q.; Wu, F. S.; Gong, S. T.; Wei, J.; Lin, S. L., Self-assembly and stimuli-responsive behaviours of side-chain liquid crystalline copolymers: a dissipative particle dynamics simulation approach. *Phys Chem Chem Phys* 2019, *21* (14), 7645-7653.

145. Gong, M. Q.; Yu, Q. Y.; Ma, S. Y.; Luo, F.; Wang, R.; Chen, D. Z., Self-Assembly Behavior of Triphenylene-Based Side-Chain Discotic Liquid Crystalline Polymers. *Macromolecules* 2017, *50* (14), 5556-5564.

146. Qiang, X. W.; Wang, X. H.; Ji, Y. Y.; Li, S. B.; He, L. L., Liquid-crystal self-assembly of lipid membranes on solutions: A dissipative particle dynamic simulation study. *Polymer* 2017,

*115*, 1-11.

147. Chiang, W. S.; Lin, C. H.; Yeh, C. L.; Nandan, B.; Hsu, P. N.; Lin, C. W.; Chen, H. L.; Chen, W. C., Tetragonally Packed Cylinder Structure of Comb-Coil Block Copolymer Bearing Heteroarm Star Architecture. *Macromolecules* 2009, *42* (6), 2304-2308.

148. Polovnikov, K. E.; Potemkin, I. I., Effect of Architecture on Micelle Formation and Liquid-Crystalline Ordering in Solutions of Block Copolymers Comprising Flexible and Rigid Blocks: Rod-Coil vs Y-Shaped vs Comblike Copolymers. *J Phys Chem B* 2017, *121* (43), 10180-10189.

149. Wu, D. D.; Huang, Y. J.; Xu, F. G.; Mai, Y. Y.; Yan, D. Y., Recent Advances in the Solution Self-Assembly of Amphiphilic "Rod-Coil" Copolymers. *J Polym Sci Pol Chem* 2017, *55* (9), 1459-1477.

150. Xiang, W. J.; Zhu, Z. J.; Wang, K.; Zhou, L. S., Mesoscopic simulation study on the structural transition of comb-shaped block copolymer lamellae on chemically patterned substrates: from vertical to lateral. *Phys Chem Chem Phys* 2019, *21* (2), 641-649.

151. Gronheid, R.; Bekaert, J.; Kuppuswamy, V. K. M.; Vandenbroeck, N.; Doise, J.; Cao, Y.; Lin, G. Y.; Sayan, S.; Parnell, D.; Somervell, M., Process Optimization of Templated Dsa Flows. *Proc Spie* 2014, *9051*.

152. Liu, C. C.; Han, E.; Onses, M. S.; Thode, C. J.; Ji, S. X.; Gopalan, P.; Nealey, P. F., Fabrication of Lithographically Defined Chemically Patterned Polymer Brushes and Mats. *Macromolecules* 2011, *44* (7), 1876-1885.

# Chapter 2

# The Role of Liquid Crystalline Side Chains for Long-range Ordering in the Block Copolymer Thin Films

## 2-1. Introduction

The ability to self-assemble into 1-100 nm scale regular patterns gives block copolymers (BCPs) great potential in various industrial applications. Especially, perpendicularly-oriented lamellae with sub-10 nm feature sizes can be applied to next-generation lithography for semiconductor manufacturing. However, numerous issues including increasing the strength of segregation ($\chi_{eff}$), lowering the defectivity of the nanostructures, and inducing perpendicular orientation on thin films, need to be addressed simultaneously before any practical applications[1 2]. Although previous studies have achieved the formation of sub-10 nm lamellae on thin films, additional processing such as the use of solvent vapor annealing[3 4 5 6 7] or a top-coat[8 9 10 11 12 13 14] can complicate and add to the cost of manufacturing.

By designing a novel BCP with advanced functionalities, a BCP can be tailored to fulfill the requirements of such lithographic applications with relative ease[15 16]. Previously, Hayakawa and co-workers introduced a trifluoroethyl-containing functionality to the glycidyl moieties of a polystyrene-*block*-poly(glycidyl methacrylate) (PS-*b*-PGMA) precursor polymer to obtain polystyrene-block-poly[2-hydroxy-3-(2,2,2-trifluoroethylsulfanyl)propyl methacrylate] (PS-*b*-PHFMA)[17]. Since the trifluoroethyl functionality is incompatible with the polar (PGMA) and non-polar (PS) segments, PS-*b*-PHFMA exhibited a high $\chi_{eff}$ value of 0.191 at 25 ˚C and was capable of forming sub-5 nm lamellae in the bulk. Additionally, the relatively hydrophobic trifluoroethyl moieties counteracted the hydrophilic PGMA moieties, balancing the surface free energies (SFE) of the two segments in PS-*b*-PHFMA and facilitating the formation of perpendicular lamellae on thin films. However, as confinement can heavily influence the self-assembly of BCPs, sub-5 nm structures could not form on the PS-*b*-PHFMA thin films.

Besides controlling the SFE of a BCP segment, side chain liquid crystalline (SCLC) functionalities have also been shown to be capable of controlling the orientation of the BCP domains[18 19 20 21 22]. In thermal annealing process, the formation of the self-assembled periodic nano-structures will be synergistically influenced by the interplay of liquid crystal (LC) ordering and segregation between blocks. Verploegen and coworkers[23] systematically controlled the percent covalent attachment of a smectic LC side chain onto the vinyl functionalities of polystyrene-*block*-poly(methylvinyl siloxane) (PS-*b*-PMVS). Due to the drastically different SFEs of PS and PMVS, PS-*b*-PMVS typically forms parallel structures on thin films, and with low LC content, the LC mesophase does not affect domain orientation.

However, at high LC content, perpendicular structures could be achieved despite the disparate SFEs. This was attributed to the tendency for homogenous or parallel alignment of the LC moieties, which possessed less conformational freedoms compared to the polymeric backbone, driving the hierarchical BCP nanostructures to orient normal to the substrate. Therefore, the introduction of LC functionalities onto the side chains of BCPs is a promising method for developing a novel BCP that can simultaneously fulfill the requirements for next-generation BCP lithography applications.

In this study, the formation of perpendicularly-oriented lamellar/parallel-oriented cylindrical thin films with minimized 6 nm feature sizes and long range ordering was successfully demonstrated by introducing 1H,1H,2H,2H-perfluorodecanethiol onto a PS-*b*-PGMA precursor polymer to obtain a novel BCP with a $C_8F_{17}$-containing LC side chain (PS-*b*-P8FMA). Small (SAXS) and wide angle X-ray scattering (WAXS) analyses of the bulk films revealed the formation of hierarchical structures in which lamellae/clyinder with domain spacings ($d_{spacing}$) of 6.3 to 36.3 nm and smectic structures with 3.6 nm periodicities have co-assembled. Atomic force microscopy (AFM) of the thin films also revealed the formation of fingerprint patterns with increased long-range ordering when the $d_{spacing}$ of the BCP is closer to the periodicity of the smectic structures. The schematic illustration for the correlation between molecular design and orientation/ordering control on domain of PS-*b*-P8FMA is depicted in Scheme 2-1.

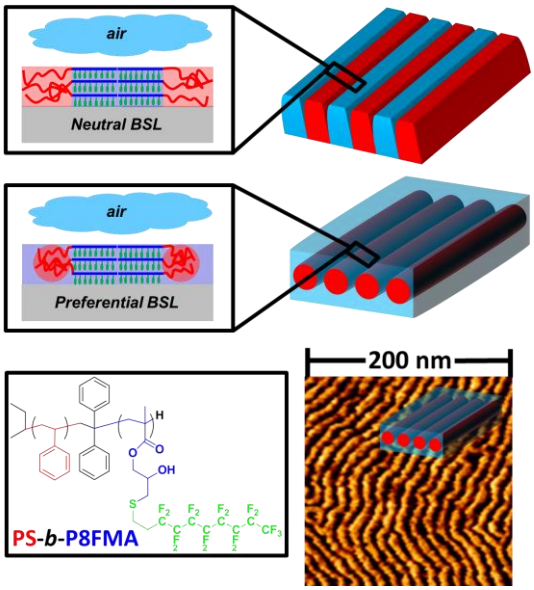


**Scheme 2-1.** Schematic illustrations for the correlation between molecular design and orientation control on thin film domain of PS-*b*-P8FMAs.

## 2-2. Experimental Section

### 2-2-1. Materials

Lithium chloride (LiCl) was obtained from Kanto Chemical Co. Inc. and baked under a reduced pressure at 200 °C overnight before use. Styrene was washed by 0.1M sodium hydroxide (NaOH) aqueous solution three times and dried by magnesium sulfate ($MgSO_4$); afterwards, calcium hydride ($CaH_2$) was added and stirred overnight before distillation. After the distillation, *di-n-buty*lmagnesium ($MgBu_2$) was added under Ar protection to remove the residual water in styrene. Second distillation over *di-n-buty*lmagnesium was further carried out. Similarly, glycidyl methacrylate (GMA) was distilled over $CaH_2$ and subsequently degassed under Ar. Diphenylethene (DPE) was distilled over *n-butyl* lithium and subsequently degassed under Ar. All other materials were reagent grade, purchased from Kanto Chemical Co. Inc., Tokyo Chemical Industry, FUJIFILM Wako Pure Chemical Corporation, and Sigma-Aldrich, and used as received.

### 2-2-2. Methods

$^1$H NMR spectra were recorded with a JEOL JNM-ECS400 (400 MHz) instrument using chloroform-*d* as the solvent. Size exclusion chromatography (SEC) analysis was performed on a Shodex GPC-101 instrument, which was equipped with Shodex LF804 columns. The number average molecular weights ($M_n$) and molecular weight distributions ($M_w/M_n$) were determined by SEC with polymer/tetrahydrofuran solution at a flow rate of 1.0 ml/min at 40 °C and calibrated with polystyrene. Thermal behavior of polymers was characterized with a Seiko DSC 7020 differential scanning calorimeter (DSC) at a heating or cooling rate of 10 °C/min under a nitrogen flow. The transition temperature values were determined from the second heating and cooling scan. The scanning temperature range was set from 25 ℃ to 250 ℃. Microscopic observation of thermal events was also conducted using an Olympus BH-2 polarized optical microscope (POM) equipped with a Mettler FP82HT hot-stage system. Small angle X-ray scattering (SAXS) measurements were carried out using synchrotron radiation facility at BL40B2 Spring-8 with a sample-to-detector of 2.0 meters and Bruker SAXS NanoSTAR (Output:50kV, 50mA) instrument. After monochromatic processing by a Göbel mirror, a concentrated CuKα radiation (wavelength:1.5416Å) was applied to the sample with a 1.0 m distance to the detector. Wide-angle X-ray scattering (WAXS) spectra were measured by a Bruker Discover D8 at a distance of 88 mm from the sample using CuKα radiation (wavelength:1.5416Å). Bright-field transmission electron microscope (TEM) images of the sample structure were also obtained using a Hitachi H7650 Zero A under a 100 kV accelerating voltage. Bulk samples were prepared for TEM analysis by first embedding in epoxy resin for handling then microtomed (Leica EM UC7) by to a preset thickness of 70 nm.

The sections produced were then placed onto TEM grids and stained by ruthenium oxide for observation. Contact angle measurements were performed using a Kyowa DM-501YH, with water and diiodomethane. $O_2$ plasma etching was performed by etching instrument (SATO VAC, Inc.). The oxygen flow rate was set to 40 sccm and the applied power used was 20 W. The thin film samples were prepared using a MIKASA spin coater IH-D7, and the film thicknesses were measured by a FILMETRICS F20-EXR. AFM (NanoWizard Ultra Speed A, JPK) was used to observe the surface architectures of the BCP thin films at room temperature.

### 2-2-3. Synthesis of homopolymer

**Synthesis of homo-PGMA by living anionic polymerization**

All anionic polymerization procedures were performed under Ar protection. Here, 30 mL of THF and LiCl (21.2 mg, 0.500 mmol) were transferred to a 50 mL Schlenk flask and then cooled to -78 °C. *sec-Butyllithium* (*sec*-BuLi) (in 1.05 M hexane/cyclohexane solution) was added until the color changed to yellow. The Schlenk flask was removed from the cooling bath and kept under room temperature till the solution became colorless. The Schlenk flask was again cooled to -78 °C, and sec-BuLi solution in cyclohexane and n-hexane (0.48 mL, 0.500 mmol) was added as initiator. DPE (0.26 mL, 1.5 mmol) was added, changing the color to deep red color. After 30 min of stirring, GMA (0.93 mL, 7.04 mmol) was added and stirred for 30 min at -40 °C. The solution became colorless. Finally, 1 mL of methanol (MeOH) (excess amount) purged with Ar and added to the Schlenk flask to yield proton-terminated PGMA. The polymer was precipitated into hexane and filtered, and then the product was dried under a reduced pressure at 40 °C overnight to yield PS-*b*-PGMA as a white powder (1.80 g, 90% yield). The $M_n$ and $Đ$ of the product tested by SEC were 1700 g mol$^{-1}$ and 1.18, respectively. The extremely low $M_n$ of synthesized homo-PGMA was due to the poor solubility of product following post-functionalization. $^1$H NMR (400 MHz, chloroform-*d*, δ, ppm): 0.87 (s, α-$CH_3$), 1.08 (s, α-$CH_3$), 1.89 (br, backbone, -$CH_2$-C($CH_3$)-), 2.63 (s, -$CH_2$-CH($CH_2$)-O-), 2.83 (s, -$CH_2$-CH($CH_2$)-O-), 3.21 (s, -$CH_2$-CH($CH_2$)-O-), 3.80 (s, -(C=O)O-$CH_2$-), 4.28 (s, -(C=O)O-$CH_2$-). 7.15-7.20 (m, aromatic, DPE).

**Synthesis of homo-P8FMA through the post-functionalization of PGMA**

A 10 ml glass tube was charged with homo-PGMA and THF (20 mole equiv. to PGMA repeating units) and immersed in an ice-water bath. 1 wt% lithium hydroxide (LiOH) aqueous solution (LiOH 0.05 mole equiv. to PGMA repeating units) and 1H,1H,2H,2H-perfluorodecanethiol (1.2 mole equiv. to PGMA repeating units) were added to the tube. After stirring for 20 min at room temperature, the tube was transferred to a thermal reactor set to 30 °C and stirred for 3 h. The crude solution was precipitated from methanol for 3

times to remove the residual reagents. The product was dried under a reduced pressure at room temperature overnight to yield a white powder (59% yield).

Characterization of homo-P8FMA. The $M_n$ and $Đ$ of the product measured by SEC were 7 700 g $mol^{-1}$ and 1.03, respectively. $^1$H NMR (400 MHz, homo-P8FMA, δ, ppm): 0.87 (s, α-$CH_3$, P8FMA), 1.25 (s, α-$CH_3$, P8FMA), 1.56 (br, backbone, -$CH_2$-C($CH_3$)-, P8FMA).

### 2-2-4. Estimating the surface free energies of the homopolymers

The surface free energies (SFEs) of the homopolymers were calculated by measuring the water and diiodomethane contact angles (C.A.) of the homopolymer thin films. The thin films were prepared by spin-coating a 1-2 wt.% THF or toluene solution on bare silicon wafers at 3000 rpm for 30 s to obtain thin films with thicknesses of 40-50 nm. These thin films were annealed at 120 °C for 10 min before the C.A. measurements.

### 2-2-5. Synthesis of PS-*b*-PGMA

An example of the anionic polymerization of styrene and GMA is as follows. All anionic polymerization procedures were performed under Ar. Here, 30 mL of THF and LiCl (21.2 mg, 0.500 mmol) were transferred to a 50 mL Schlenk flask and then cooled to -78 °C. *Sec-buty*llithium (*sec*-BuLi) (1.05 M hexane/cyclohexane solution) was added until the color changed to yellow. The Schlenk flask was removed from the cooling bath and warmed to room temperature until the solution became colorless. The Schlenk flask was again cooled to -78 °C and *sec*-BuLi (0.099 mL, 0.100 mmol) was added as initiator. Styrene (1.65 mL, 14.42 mmol) was added and stirred for 30 min, resulting in bright orange color of the solution. DPE (0.088 mL, 0.47 mmol) was added, changing the color to deep red color. After 30 min of stirring, GMA (0.47 mL, 3.52 mmol) was added, causing the color to disappear, and stirred for 30 min. Finally, 3 mL of degassed methanol (MeOH) was added to the Schlenk flask to yield proton-terminated PS-*b*-PGMA. The polymer was precipitated into MeOH and filtered.The product was dried under reduced pressure at 40 °C overnight to yield PS-*b*-PGMA as a white powder (1.80 g, 90% yield).

### Characterization of PS-*b*-PGMA

The $M_n$ and dispersity ($Đ = M_w/M_n$) of the product determined by SEC were 27200 g $mol^{-1}$ and 1.15, respectively.

$^1$H NMR (400 MHz, $CDCl_3$, δ, ppm): 0.98 (s, α-$CH_3$, PGMA), 1.14 (s, α-$CH_3$, PGMA), 1.29-1.80 (br, backbone, -$CH_2$-CH-, PS), 1.84-2.30 (br, backbone, -$CH_2$-CH-, PS, br, backbone, -$CH_2$-C($CH_3$)-, PGMA), 2.70 (s, -$CH_2$-CH($CH_2$)-O-, PGMA), 2.82 (s, -$CH_2$CH($CH_2$)-O-, PGMA), 3.28 (s, -$CH_2$-CH($CH_2$)-O-, PGMA), 3.84 (s, -(C=O)O-$CH_2$-, PGMA), 4.37 (s,

-(C=O)O-$CH_2$-, PGMA), 6.39-6.85 (m, o-aromatic, PS) 6.91-7.42 (m, m-, p-aromatic, PS).

### 2-2-6. Synthesis of PS-*b*-P8FMA through the post-functionalization of PS-*b*-PGMA with 1H,1H,2H,2H-Perfluorodecanethiol

A general procedure for the functionalization of the precursor PS-*b*-PGMA is given here. A 10 ml glass tube was charged with PS-*b*-PGMA and THF (20 mole equiv. perGMA unit) and immersed in an ice-water bath. 1 wt% lithium hydroxide (LiOH) aqueous solution (LiOH 0.05 mole equiv. per GMA unit) and 1H,1H,2H,2H-perfluorodecanethiol (1.5 mole equiv. per GMA unit) were added to the tube. After stirring for 20 min at room temperature, the reactor was set to 30 ℃ and stirred for 3 h. The crude solution was precipitated from hexane and then filtered. After filtration, the solid was again dissolved in THF and precipitated from hexane, and then filtered 2 or 3 more times to remove the residual reagents. Finally, precipitation from methanol was used to remove residual lithium hydroxide. The product was dried under a reduced pressure at room temperature overnight to yield a white powder (0.78g, 65% yield). The $^1$H NMR spectra of all synthesized BCPs is presented (Figure 2-1).

**Characterization of PS-*b*-P8FMA**

$^1$H NMR (400 MHz, $CDCl_3$, δ, ppm): 0.98 (s, α-$CH_3$, P8FMA), 1.12 (s, α-$CH_3$, P8FMA), 1.26-1.74 (br, backbone, -$CH_2$-CH-, PS), 1.82-2.30 (br, backbone, -$CH_2$-CH-, PS, br, backbone, -$CH_2$-C($CH_3$)-, P8FMA), 2.30-2.45 (t, -$CH_2$-$CF_2$-, P8FMA), 2.60-2.76 (t, -S-$CH_2$-$CH_2$-$CF_2$-, P8FMA), 2.76-2.87 (d, -CH(OH)-$CH_2$-S-, P8FMA), 3.82-4.17 (d, -(C=O)O-$CH_2$-, P8FMA) (m, -CH(OH)-, P8FMA), 6.39-6.82 (m, o-aromatic, PS), 6.92-7.32 (m, m-, p-aromatic, PS).

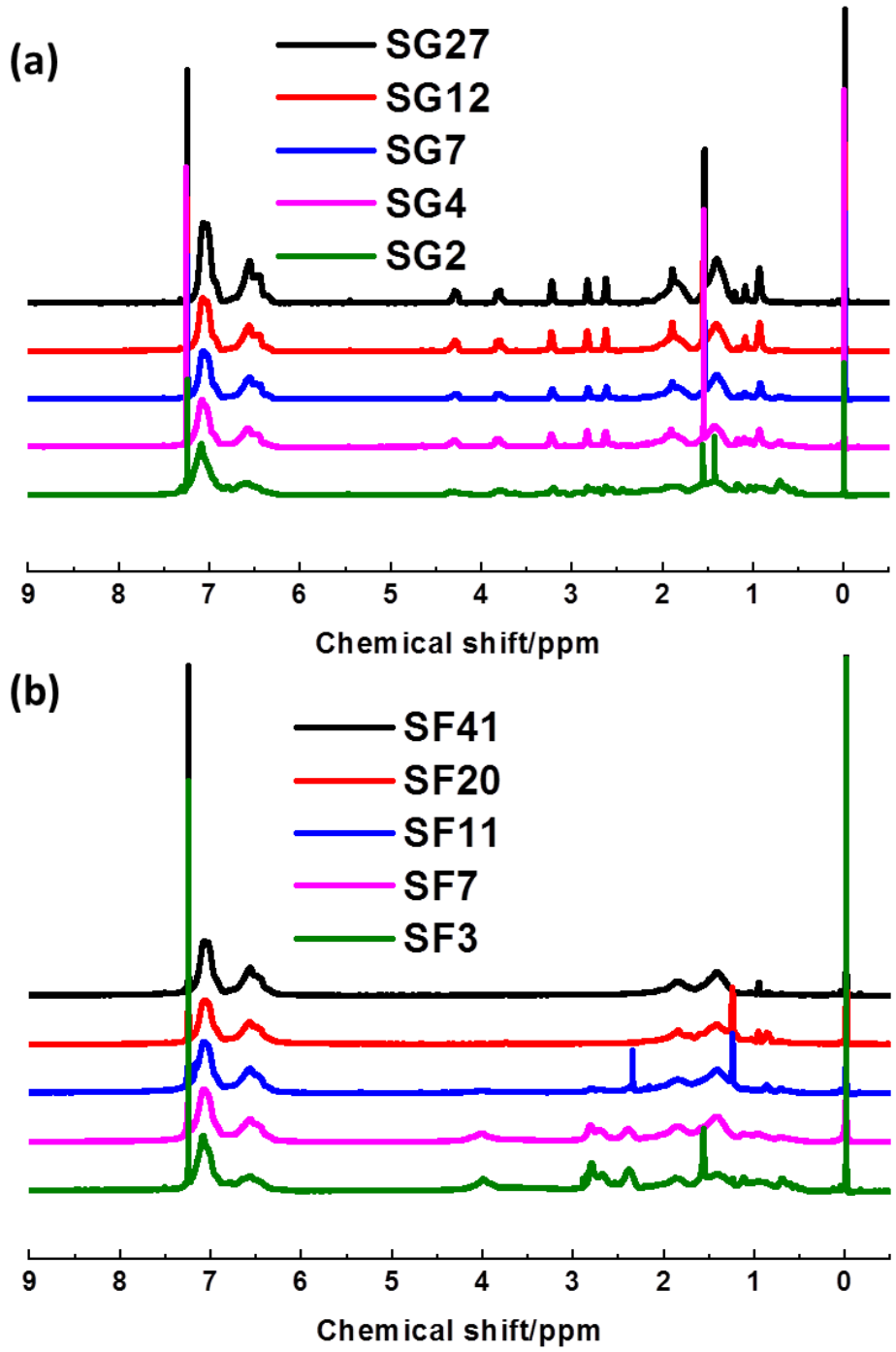


**Figure 2-1**. $^{1}$H NMR spectra of synthesized PS-*b*-PGMAs (SG) and post-functionalized PS-*b*-P8FMAs (SF) in $CDCl_3$ solvent. The suffix number to the right refers to the number-average molecular weight ($M_n$) of the polymer in thousand Dalton units.

**2-2-7. Detailed information about the estimation of $\chi_{eff}$**

Molten BCP samples were placed in 0.01 mm thick glass tubes and the SAXS profiles were collected at each temperature in 10 °C decrement in cooling cycles, at which the temperature was maintained for 30 min prior to the measurements to reach a thermally equilibrated state. The scattering function $I(q)$ from the disordered melt of the BCPs with a dispersity in the molecular weight and asymmetry in the segmental volume was summarized below, where $A_0$ is a fitting constant, $S(q)$ and $W(q)$ together are correlation functions of the BCP, $g(q)$ is a modified Debye function and $y(q)$ is a dimensionless wave vector, $r_c$ is the molar volume normalized over the degree of polymerization of the BCP, $f_X$ is volume fraction of $X$ calculated using the bulk densities for each block (1.05 g cm$^{-3}$ for PS and 1.73 g cm$^{-3}$ for P8FMA), $v_X$ is the molar volume of $X$. $N_X$ is the degree of polymerization normalized over a common reference volume ($v_0$ = 118 Å$^3$) for $X$, $FW$ is the formula weight of $X$, $N_A$ is Avogadro's constant, and $b_X$ is the segmental length of $X$. Here the dispersities for each homopolymer segment ($D_X$) are assumed equal and were estimated from the $M_w/M_n$ of the BCP and weight fraction of $X$ ($w_X$). Four parameters, including $b_X$ for both polymers, $A_0$ and $\chi_{eff}$, were optimized in a least-squares fit to the SAXS profiles at a certain temperature. The calculated parameters for each sample were summarized in Table 2-5 and Table 2-6. Discontinuous changes attributed to the transition from mean-field to non-mean-field type disordered states were observed at 160-170 °C for SF3 in the $I_{max}^{-1}$–$T^{-1}$ plots. (Figure 2-15). Therefore, the estimation of $\chi_{eff}$ for each sample was done at temperatures higher than the transition.

$$I(q) = \frac{A_0}{\frac{S(q)}{W(q)} - 2\chi}$$

$$S(q) = \langle S_{PS,PS} \rangle + 2\langle S_{PS,Y} \rangle + \langle S_{Y,Y} \rangle$$

$$W(q) = \langle S_{PS,PS} \rangle \cdot \langle S_{Y,Y} \rangle - \langle S_{PS,Y} \rangle^2$$

$$\langle S_{X,X}(q) \rangle = r_c {f_X}^2 {g^{(2)}}_X(q) \quad \langle S_{PS,Y}(q) \rangle = r_c f_{PS} f_Y {g^{(1)}}_{PS}(q) {g^{(1)}}_Y(q)$$

$$r_c = \frac{(v_{PS}N_{PS} + v_Y N_Y)}{(v_{PS} \cdot v_Y)^{1/2}} \quad v_X = \frac{FW_X}{\rho_X N_A} \quad N_X = \frac{v_X M_{n,X}}{v_0 FW_X}$$

$${g^{(1)}}_X(q) = \frac{1}{y_X(q)} \cdot \left\{1 - [y_X(q) \cdot (D_X - 1) + 1]^{-(D_X - 1)^{-1}}\right\}$$

$${g^{(2)}}_X(q) = \frac{2}{{y_X(q)}^2} \cdot \left\{-1 + y_X(q) + [y_X(q) \cdot (D_X - 1) + 1]^{-(D_X - 1)^{-1}}\right\}$$

$$y_X(q) = \frac{N_X {b_X}^2}{6} q^2 \quad D \equiv D_{PS} = D_Y = \frac{M_w/M_n - 1}{{w_{PS}}^2 + {w_Y}^2} + 1$$

$X$ = PS or $Y$ ($Y$ = P8FMA)

**2-2-8. Synthesis of PTFEMA-*r*-PMMA-*r*-PMAAs**

The following procedure was used for PTFEMA-*r*-PMMA-*r*-PMAA 54-43-3, but is representative of all neutral bottom surface layer materials syntheses. The suffix numeric label denotes the weigh fraction of each block (Figure 2-2 and Table 2-1).

2,2,2-Trifluoroethyl methacrylate (TFEMA), methyl methacrylate (MMA) and methacrylic acid (MAA) were distilled to yield clear and colorless liquid prior to use. Azobisisobutyronitrile (AIBN) was recrystallized prior to use. 2,2,2-Trifluoroethyl methacrylate (1.08g, 6.4 mmol, 0.41 eq), methyl methacrylate (0.86 g, 8.6 mmol, 0.55 eq), methacrylic acid (0.06 g, 0.7 mmol, 0.04 eq), and AIBN (0.007 g, 0.004 mmol, 0.00025 eq) were added to a 50 mL 3-neck round bottom flask equipped with a stir bar and rubber septa. The reagents were dissolved in THF (7.5 mL) and the solution was deoxygenated by vigorously bubbling nitrogen through the solution for 30 minutes. The reaction vessel, under positive nitrogen pressure, was immersed in an oil bath at 70 ˚C. The reaction was heated and stirred for 24 h and quenched at 0 ˚C. The viscous liquid was precipitated into methanol (300 mL) and filtered. The resulting polymer was dissolved in THF and reprecipitated into methanol for two additional times. The polymer was dried in vacuo overnight at 40 ˚C and the white powder product (93% yield) was obtained.

$^1$H NMR (400 MHz, chloroform-*d*, δ, ppm): 0.84-0.89, 1.01-1.11, 1.21-1.26, 1.40-1.48, 1.76-2.08, 3.49-3.70, 4.20-4.45.

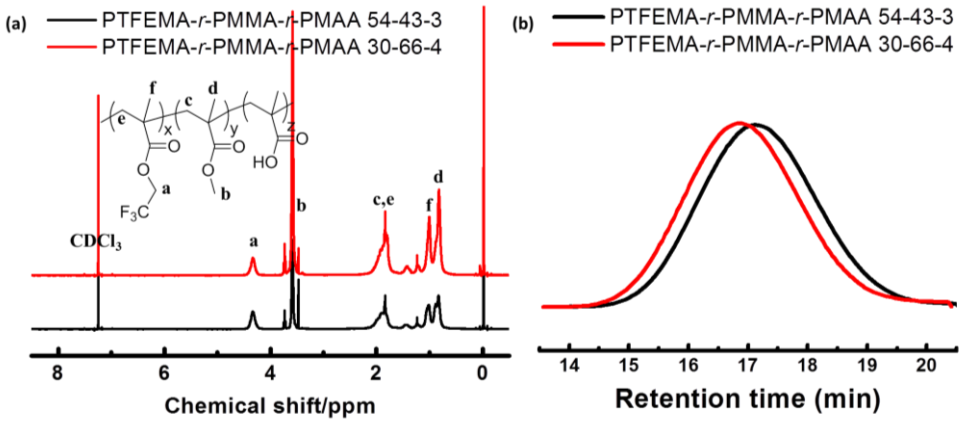


**Figure 2-2**. $^1$H NMR spectra (a) and GPC chromatograms (b) the synthesized random copolymers PTFEMA-*r*-PMMA-*r*-PMAAs. The labeled number indicates the weight fraction of each component in percentage. In this study, PTFEMA-*r*-PMMA-*r*-PMAA 54-43-3 was used as non-preferential bottom surface layer for all BCPs and PTFEMA-*r*-PMMA-*r*-PMAA 30-66-3 was used as PS-preferential one for cylinder-forming SF7.

**Table 2-1.** Characterisitics of the synthesized PTFEMA-*r*-PMMA-*r*-PMAAs.

| Random Copolymer | Weight Composition[a] | | | $M_n$ | $Đ$ |
|---|---|---|---|---|---|
| | TFEMA | MMA | MAA | | |
| PTFEMA-*r*-PMMA-*r*-PMAA | 54 | 43 | 3 | 31900 | 1.81 |
| | 30 | 66 | 4 | 26800 | 1.77 |

[a] TFEMA, MMA compositions were determined by $^1$H NMR and MAA composition was estimated from monomer feeding ratio.

### 2-2-9. Bulk sample preparation

The bulk samples used to investigate the bulk morphologies and domain spacings (*d*-spacing) of the microphase-separated structures were prepared by slowly evaporating a dilute BCP THF solution filtered through a 0.25 μm pore size PTFE membrane syringe filter at 30 °C. The as-prepared samples were dried under a reduced pressure before annealing at 150 °C for 24 h.

### 2-2-10. Thin film preparation

Bare silicon wafers cut into 1 $cm^2$ pieces were sonicated in toluene for 3 min, and dried in a stream of nitrogen. The substrates were treated with a mixture of $H_2O_2$ (30%) and $H_2SO_4$ (70%) (v/v) (piranha solution) at 80 °C for 40 min. The wafers were rinsed with water repeatedly and dried in a stream of nitrogen. Bottom surface layers (BSL) were prepared by spin coating a 1.0 wt% poly(2, 2, 2-trifluoroethyl methacrylate)-*random*-poly(methyl methacrylate)-*random*-poly(methacrylic acid) (PTFEMA-*r*-PMMA-*r*-PMAA) solution in propylene glycol monomethyl ether acetate (PGMEA) solution at 3000 rpm and 30 s onto the cleaned silicon wafers, followed by crosslinking at 200 °C for 5 min. The substrates were sonicated in toluene to remove any random copolymers that were not attached to the substrate and rinsed with fresh toluene. Furthermore, approximately 1.0 wt % solutions of the BCPs in toluene were spin-coated at 3000 rpm for 30 s onto the surface-modified silicon substrates to obtain thin films with ca. 1.4 $L_0$ thicknesses (1.0 $L_0$ denotes one periodic length of self-assembled nanostructure). The film thickness was tuned by changing BCP solution concentration. The thin films were annealed at 150 °C for 24 h under ambient conditions. An $O_2$-RIE treatment was conducted for a certain time (40 sccm, 20 W, 20 Pa) to selectively remove the methacrylate-based block.

### 2-2-11. Etch contrast in $O_2$-RIE

The etch resistances against $O_2$-RIE treatment for PS and P8FMA were obtained using thin

films of the homopolymers. The thin films were prepared by spin-coating toluene or THF solutions onto bare silicon wafers to produce approximately 50 nm thickness films. The P8FMA block was removed at approximately 1.9 times rate of PS segments.

## 2-3. Results and Discussion

### 2-3-1. Synthesis and characterization of the homopolymers

Prior to the study on BCPs, the homopolymer P8FMA was synthesized and corresponding surface characteristics were conducted. The precursor homopolymer PGMA was prepared via living anionic polymerization of GMA monomer using *sec*-BuLi as initiator in THF at -40 ℃. Subsequently, fluorinated homopolymers of P8FMA were synthesized via the thiol-epoxy reaction. PGMA was mixed with excessive 1H,1H,2H,2H-perfluorodecanethiol in THF solution with catalytic amount of LiOH at 30 ℃. LiOH is the best catalyst as quantitative conversions are obtained at a catalyst loading over a few hours reaction time.[24] The ring-opening nature of epoxy groups in PGMA was used to introduce functionality of thiol reagent. It's worthy to note that hydrophilic hydroxyl moieties were also introduced onto each repeating unit of PGMA along with the thiol reagent as the ring-opening reaction results. The synthesized homopolymer was then characterized by NMR, SEC and DSC (Figure 2-3) and summarized (Table 2-2). The glass transition temperature ($T_g$) of the fluorinated homopolymer determined from the base-line shifts in the DSC was measured to be 116.8 ℃. Compared to the measured $T_g$ of 68 ℃ for homopolymer PGMA[17], the high $T_g$ of P8FMA was likely due to the bulky and rigid long fluorinated side chain. Additionally, the transition related to LC ordering was detected at 78 ℃, and POM results (Figure 2-3(c)) further suggested a transition from ordered to isotropic phase under the same temperature.

**Table 2-2**. Characteristics of the synthesized homopolymers.

| Homopolymer | $M_n$ (kg mol$^{-1}$) | $Đ$ | $T_g$ (℃) | $T_{iso}$ (℃) |
|---|---|---|---|---|
| homo PGMA | 1700 | 1.18 | 71.7 | - |
| homo P8FMA | 7700 | 1.03 | 116.8 | 78.2 |

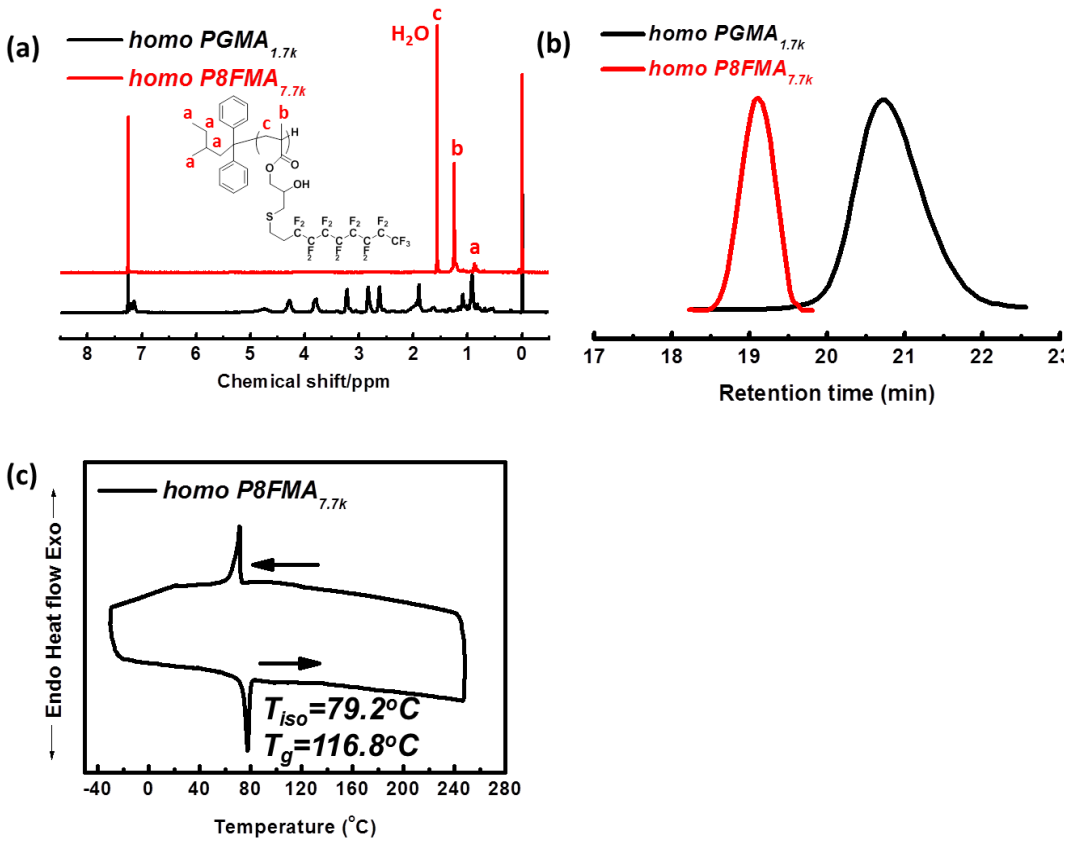


**Figure 2-3**. $^{1}$H NMR spectra (a) SEC chromatograms (b) and DSC curves at a heating rate of 10 °C /min under nitrogen atmosphere (c) of the investigated homopolymer prior to and after thiol-epoxy reaction.

The surface free energie (SFE) of P8FMA, estimated via the water and diiodomethane contact angle measurements based on the Owens-Wendt method was 21.6 mJ m$^{-2}$ (Table 2-3). The SFE of PS was measured to be 40.7 mJ m$^{-2}$ [25]. Comparatively, the SFEs of poly(2,2,2-trifluoroethyl methacrylate) (PTFEMA) and analogous mono-fluorinated poly[2-hydroxy-3-(2,2,2-trifluoroethylsulfanyl)propyl methacrylate] (PHFMA) in which carbonyl groups were replaced by hydroxyl groups, were measured to be 25.1 and 33.3 mJ m$^{-2}$ using the same method[17]. When only mono-fluorine unit was present in each repeating unit, compared to carbonyl group, hydroxyl group more significantly contributes to the hydrophilicity of homopolymer in response to a higher SFE. Thus, a balance between SFEs of PS and mono-fluorinated PHFMA block was achieved[17]. In contrast, the introduction of long-fluorinated group drove the surface characteristics towards increased hydrophobicity despite the presence of the hydroxyl group, as the introduced super-hydrophobic bulky fluorinated side chain will dominate the properties of fluorinated-blocks as major components.

Therefore, the SFEs of PS and P8FMA are far from being balanced.

**Table 2-3**. Contact angles and surface free energies (SFEs) of homopolymers.

| Homopolymer | C.A.($H_2O$)[a] ($^o$) | C.A.($CH_2I_2$)[a] ($^o$) | SFE[b] (mJ $m^{-2}$) |
|---|---|---|---|
| P8FMA | 89.0±1.1 | 80.5±1.5 | 21.6 |
| PS[c] | 90.5±0.8 | -[d] | -[d] |

[a] Average values of measurements taken at 5 positions. [b] Calculated by the Owens-Wendt method. [c] The C.A. measurement for PS used a homopolymer with $M_n$=34.6 kg $mol^{-1}$ and Đ=1.09, prepared through anionic polymerization. [d] The SFE of PS could not be obtained as PS was partially soluble in diiodomethane.

### 2-3-2. Synthesis and characterization of the BCPs

The synthetic routine to targeted diblock copolymer was classified into two steps, the synthesis of precursor main chain polymer PS-*b*-PGMA via sequential anionic living polymerization and the subsequent post-functionalization for introduction of fluorine-rich side chain. A series of PS-*b*-PGMA precursor polymers (Table 2-4) were successfully synthesized via the sequential anionic polymerization of styrene and GMA using *sec*-BuLi, excess LiCl, and DPE in THF at -78 $^{\circ}$C under an Ar atmosphere (Scheme 2-2). Based on $^1$H NMR and SEC

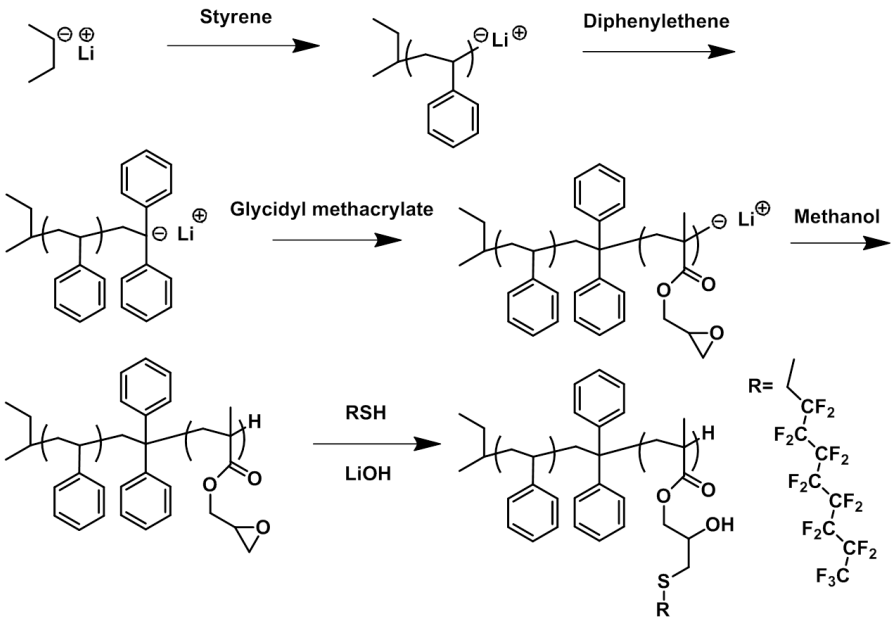


**Scheme 2-2.** Synthetic scheme of PS-*b*-PGMA precursor via sequential living anionic polymerization of styrene and glycidyl methacrylate and post-functionalization with thiols.

**Table 2-4 .** Characterization data of the synthesized BCPs.

| BCP | Label[a] | $M_n$[b](kg mol$^{-1}$) | $Đ$ | $w_{PS}$[c] | $f_{PS}$[d] |
|---|---|---|---|---|---|
| PS-*b*-PGMA | SG27 | 27.2 | 1.18 | 0.78 | 0.73 |
| | SG12 | 12.0 | 1.19 | 0.76 | 0.71 |
| | SG7 | 6.9 | 1.19 | 0.77 | 0.72 |
| | SG4 | 3.9 | 1.23 | 0.73 | 0.67 |
| | SG2 | 2.0 | 1.40 | 0.79 | 0.74 |

| BCP | Label[a] | $M_n$[b] (kg mol$^{-1}$) | $Đ$ | $w_{PS}$[c] | $f_{PS}$[d] | $d_{spacing}$[e](nm) | Morphology[f] | $\chi N$ (150$^o$C) |
|---|---|---|---|---|---|---|---|---|
| PS-*b*-P8FMA | SF41 | 40.8 | 1.21 | 0.45 | 0.57 | 36.3 | Lamella | 98.7 |
| | SF20 | 19.9 | 1.12 | 0.43 | 0.55 | 21.6 | Mixed | 46.7 |
| | SF11 | 11.1 | 1.16 | 0.45 | 0.57 | 13.7 | Cylinder | 26.4 |
| | SF7 | 7.5 | 1.15 | 0.38 | 0.50 | 11.5 | Cylinder | 16.7 |
| | SF3 | 3.2 | 1.18 | 0.47 | 0.59 | 6.3 (8.0) | Cylinder | 7.7 |

[a] The labels SG and SF refer to PS-*b*-PGMA and PS-*b*-P8FMA, respectively, while the number to the right refers to the number-average molecular weight ($M_n$) of the polymer. [b] $M_n$ and dispersities ($Đ$) were obtained by SEC using THF as the eluent based on PS standards. [c] PS weight fractions ($w_{PS}$) of PS-*b*-PGMA were calculated via $^1$H NMR and PS weight fractions ($w_{PS}$) of PS-*b*-P8FMA were further estimated from SEC based on constant $M_n$ of PS block. [d] The PS volume fractions ($f_{PS}$) were calculated via $^1$H NMR based on the densities of 1.05 g cm$^{-3}$ for PS, 0.805 g cm$^{-3}$ for PGMA and 1.73 g cm$^{-3}$ for P8FMA. [e] The domain spacings ($d_{spacing}$) were estimated from the position of first-order scattering peak in the SAXS profile upon thermal annealing at 150$^o$C for 24h. [f] The morphologies in the bulk were determined by SAXS and TEM.

analyses, the synthesized BCPs were found to have number-average molecular weights ranging from 27 to 2 kg mol$^{-1}$ and narrow dispersities.

The precursor PS-*b*-PGMAs were then functionalized with 1H,1H,2H,2H-perfluorodecanethiol in THF with LiOH as the catalyst at 30 ˚C for 3 h to yield the targeted PS-*b*-P8FMAs (Scheme 2-2). Following the post-functionalization reaction, the $M_n$ of the BCPs increased while dispersities remained low (Table 2-4 and Figure 2-5). Additionally, as the characteristic $^1$H NMR signals corresponding to the glycidyl moieties in PS-*b*-PGMA (a, a', b, c, and c' at 2.70, 2.82, 3.28, 3.84, and 4.37 ppm, respectively) (Figure 2-4(a)) had disappeared in the $^1$H NMR spectra of the PS-*b*-P8FMAs, only to be replaced with signals at 4.03, 2.82, 2.72, and 2.39 ppm (Figure 2-4(b)), the post-functionalization of the PS-*b*-PGMAs had proceeded to completion to successfully yield a series of PS-*b*-P8FMAs with well-defined primary structures and a wide range of molecular weights. However, the intensity of proton signals attributed to fluorinated side chain in spectra were significantly reduced with the increment of molecular weight, because the extremely bulky fluorinated side chain is poorly

soluble in chloroform (Figure 2-1). The density of the functionalized PGMA block was estimated using the method of Fedors[26] and calculated to be approximately 1.70 g/cm$^3$. All the functionalized PS-*b*-P8FMAs are of approximately symmetric block volume fractions.

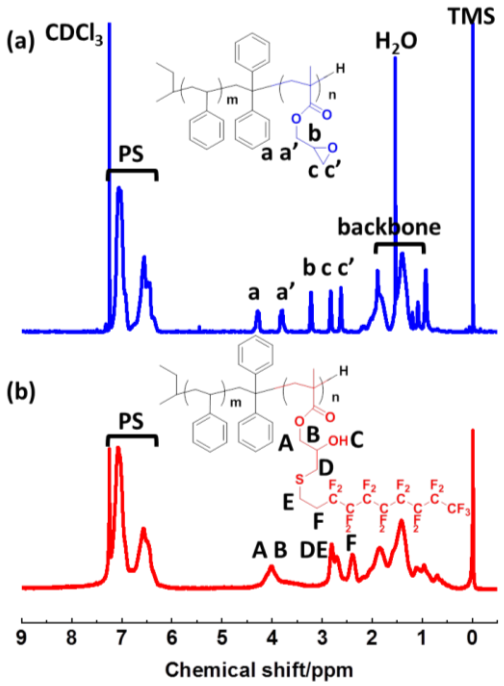


**Figure 2-4.** $^1$H NMR spectra of (A) PS-*b*-PGMA (SG7) and (B) chemically modified PS-*b*-P8FMA (SF11).

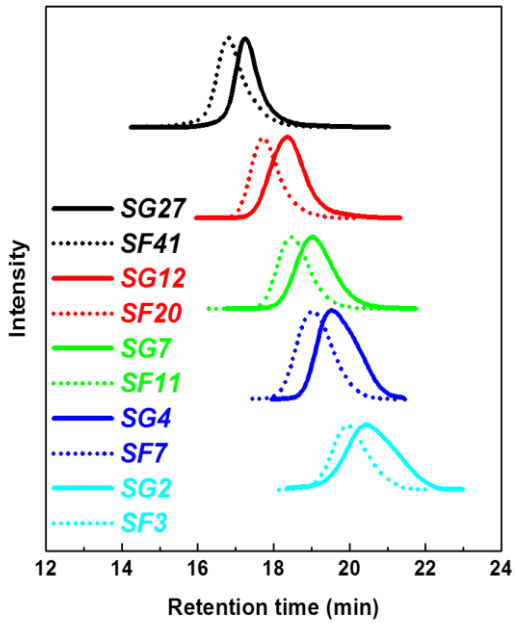


**Figure 2-5.** SEC chromatography of precursor PS-*b*-PGMA (SG) and corresponding PS-*b*-P8FMA (SF) after post functionalization.

**2-3-3. Morphologies in the bulk**

The bulk morphologies of the synthesized PS-*b*-P8FMAs were then analyzed by SAXS using synchroton radiation and TEM. The bulk samples were prepared through the slow evaporation of a dilute BCP solution in THF and characterized after thermal annealing under reduced pressure at 150 ˚C for 24 h, a temperature significantly higher than the $T_g$ of PS-*b*-P8FMA (Figure 2-7). Thermal analysis based on DSC measurements between 25 and 250 ˚C also suggested that all investigated PS-*b*-P8FMAs of varied $M_n$ exhibited LC phase transition, which is consistent with the representative POM results of SF7. The detected $T_{iso}$ was proportional to $M_n$ of P8FMA blocks. As the LC transition in kinetics was dependent on the number of LC side chain within one polymer chain, the transition from ordered to isotropic phase could be achieved under a reduced temperature. The $T_{iso}$ of all PS-*b*-P8FMAs, except SF3 which had only three LC side chains, are well-above 150 ˚C annealing temperatures. Herein, the LC ordering of side chain will be co-existed with block segregation in thermal annealing process. Additionally, the coupling and competition between side chain LC ordering and microphase separation[27] caused a significantly higher $T_{iso}$ than that of P8FMA homopolymer because of the confinement from segregated PS segments in nanometer scales. The measured $T_g$ from DSC was attributed to PS segments and became higher by the increased $M_n$. The two-dimensional SAXS profiles were azimuthally integrated to generate one-dimensional scattering profiles and analyzed using the equation, $q = 4\pi \sin(\theta/2)/\lambda$, where $\theta$ and $\lambda$ are the scattering angle and wavelength, respectively. The domain spacings were subsequently determined using the equation, $d = 2\pi/q^*$, where $q^*$ is the position of the first-order scattering peak.

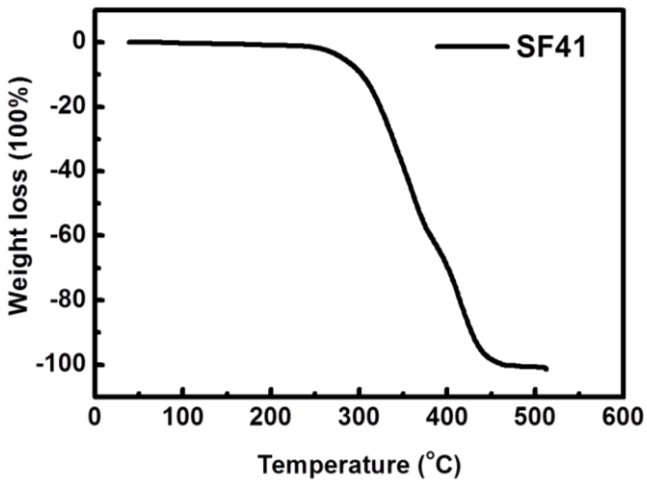


**Figure 2-6.** TGA curves of one representative PS-*b*-P8FMA at a heating rate of 10 ˚C /min under nitrogen atmosphere. The 2 wt% decomposition temperature was above 250 ˚C and the thermal treatment under 250 ˚C is secured.

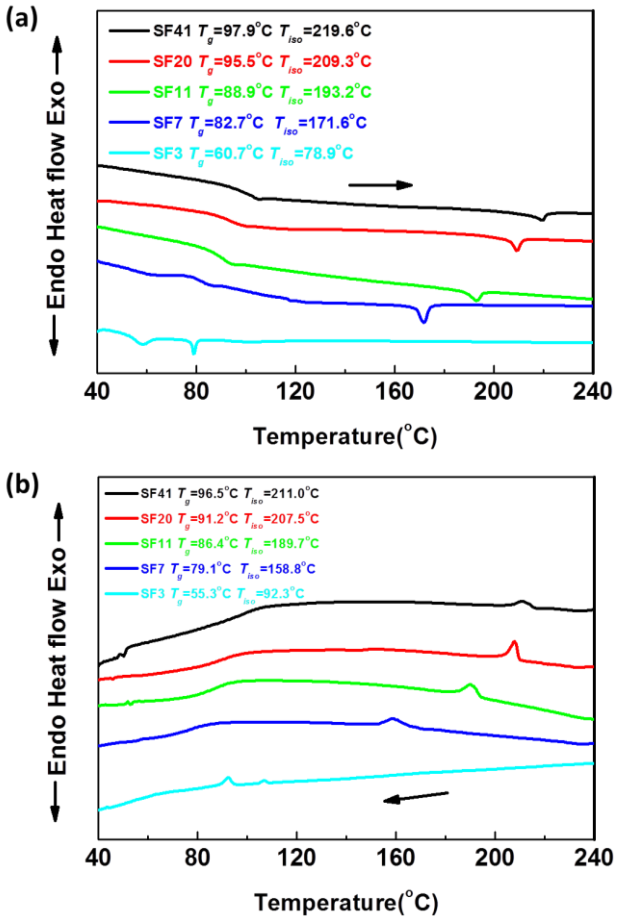


**Figure 2-7**. DSC curves of the studied PS-*b*-P8FMAs at (a) a heating and (b) a cooling rate of 10 ℃ /min under nitrogen atmosphere, respectively.

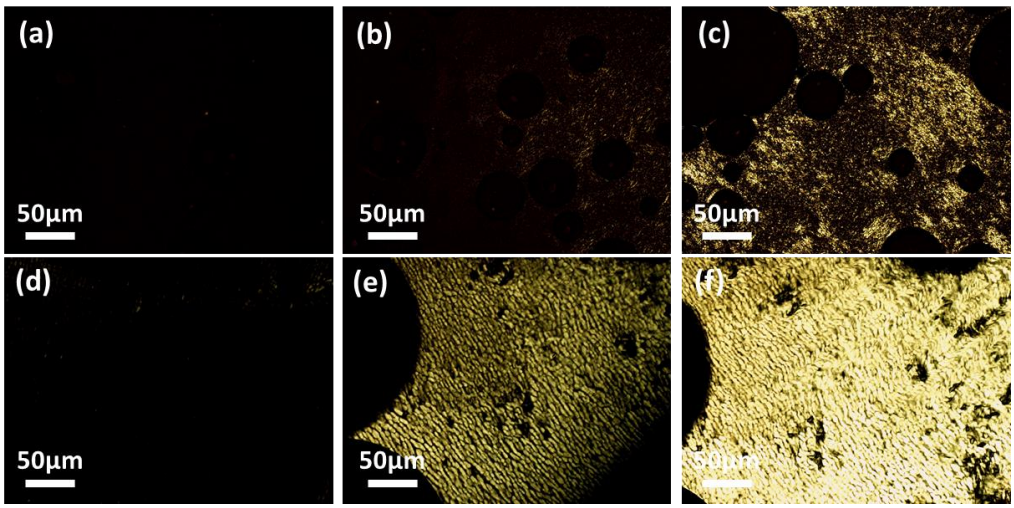


**Figure 2-8.** POM images of Homopolymer P8FMA (a)-(c) and BCP SF7 (d)-(f). (a) 150 ℃ on the cooling scan. (b) 110 ℃ on the cooling scan. (c) 80 ℃ on the cooling scan. (d) 250 ℃ on the cooling scan. (e) 190 ℃ on the cooling scan. (f) 140 ℃ on the cooling scan.

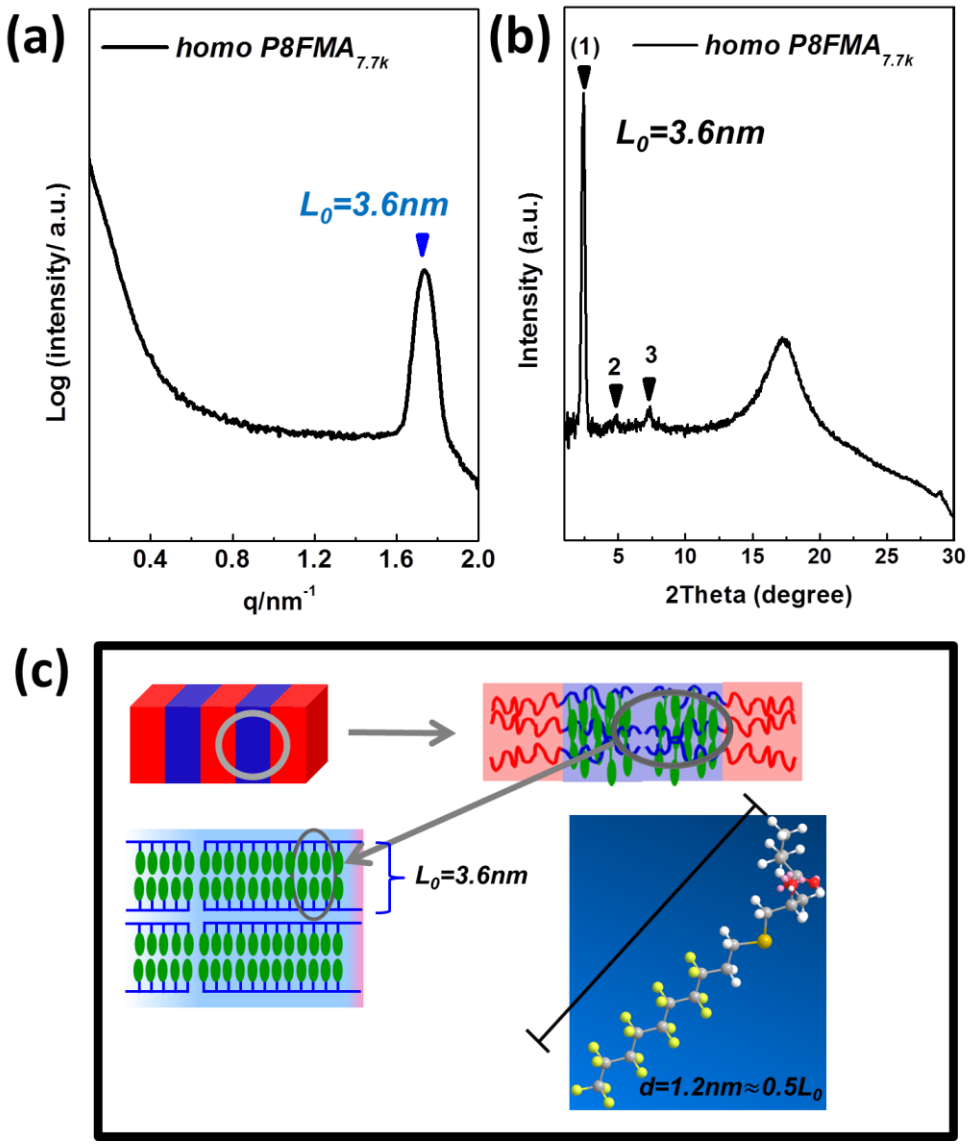


**Figure 2-9**. (a) SAXS and (b) WAXD profiles of P8FMA bulk samples following thermal annealing (c) molecular packing model of LC side chain in lamellar domains.

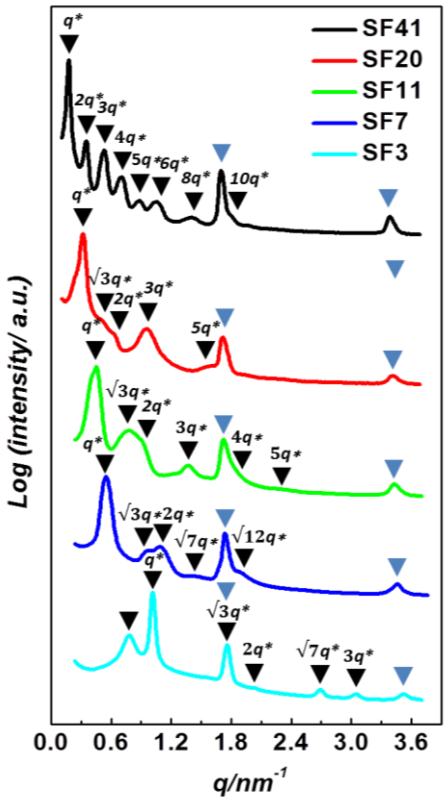


**Figure 2-10.** SAXS (synchrotron radiation) profiles of the PS-*b*-P8FMA bulk samples following thermal annealing.

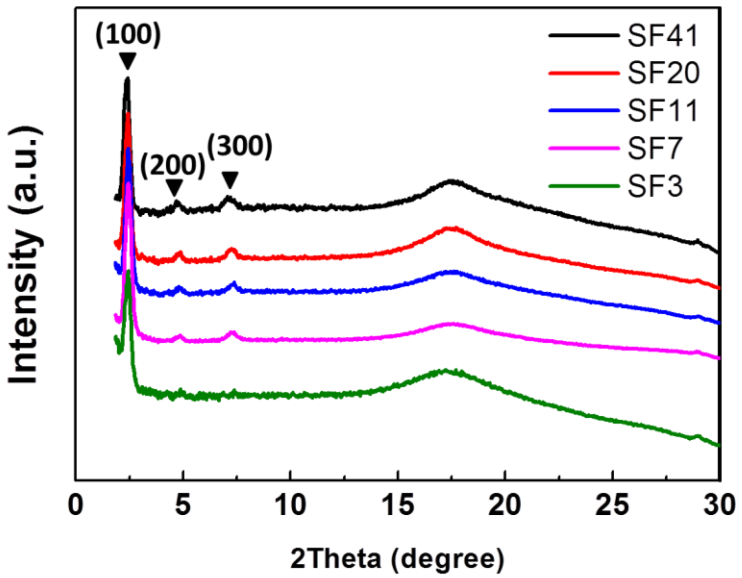


**Figure 2-11.** Normalized WAXD profiles of the studied PS-*b*-P8FMAs following thermal annealing.

As for SF41 of the highest $M_n$, the scattering peak resulting from micro-phase separation was labeled with upside-down black triangles at the integer ratios to the first-order peaks, suggesting the formation of well-ordered lamellar architecture. In contrast, a mixed morphology consisted of lamellar and cylindrical domains in SF20 sample was revealed by the insignificant scattering peak at $\sqrt{3}\,q^*$, which is the characteristic evidence of minor hexagonally packed cylindrical morphology. As $M_n$ of the studied PS-*b*-P8FMAs was further scaled down, more obvious cylindrical morphologies were revealed by the featured $\sqrt{3}q^*$, $\sqrt{7}q^*$ and even $\sqrt{12}q^*$ scatting peak. The broad peak in respose to disordered morphology with 8.0 nm $d_{spacing}$ next to the primary scattering peaks in SF3 was merely caused by the driving force from block segregation, as indicated by the SAXS profiles collected above the isotropic transition of LC side chain. (Figure 2-14) As the temperature is further cooled down into side chain LC phase regime, a morphology transition to hexgonally packed cylinder of 6.1 nm $d_{spacing}$ was suggested by the appearance of characteristic scattering peaks in higher $q$ region. (Figure 2-10)

Based on TEM characterization results (Figure 2-13), hexagonally packed cylindrical domains of long-range ordering were observed for SF7 and SF3 of lowest $M_n$. In contrast, minor cylindrical domains ($d_{spacing}$=27.3 nm) mixed with major lamellar domains ($d_{spacing}$=17.0 nm) were typically observed in SF20 of higher $M_n$, which is highly consistent with the SAXS analysis. Furthermore, SF41 of the highest $M_n$ reveals a typical lamellar morphology. According to the flexible coil-coil model in Leibler's theory, amorphous symmetric BCPs were predicted to form lamellar structure. However, the studied side chain liquid crystalline (SCLC) block copolymers were recently predicted to exhibit cylindrical morphology[28 29] even under symmetric block volume fraction, which are consistent with the discoveries in this study.

Remarkably, the peaks labeled with upside-down blue triangles were attributed to the featured periodicity from LC side chain, which were further verified by the SAXS and WAXS of bulk sample prepared from homopolymer P8FMA under the same annealing condition with those of BCPs (Figure 2-9(a)-(b)). The possible LC side chain conformation was also depicted based on the estimation on monomer molecular size using MM2 energy-minimization based on Chem 3D 16.0 (Figure 2-9(c)). The estimated side chain length (1.8 nm) was equal to half of LC periodic length (3.6 nm). Therefore, a single LC periodic length was composed of a pair of mesogens with end-to-end stereo-regularity.

In theory, the *d*-spacing of BCP domain is scaled by $\chi_{eff}^{1/6}N^{\alpha}$ [30 31 32], where $N$ is the degree of polymerization normalized over the volume, and $\alpha$= 2/3 or 1/2 in the strong or weak segregation regimes. As shown in Figure 2-12, logarithmic molecular weight values plotted as a function of logarithmic *d*-spacing values from SAXS gives a linear relationship ($r^2$ = 0.998),

and $\alpha$=0.68 extracted from that fit was consistent with the micro-phase behaviors in strong segregation regime[30 31 32 33]. The $M_n$ boundaries between strong and weak segregation are further estimated between 7.5 k and 3.4 kg $mol^{-1}$, however, the contributor from side chain LC ordering in self-assembly morphology of SF3 may also cause the shift from the theoretic fitting. The periodic length of cylinderical structure made of fluorinated BCPs was characterized to be as narrow as 6.3 nm, indicating the nature of high $\chi$ parameter.

To verify the LC ordering of side chain in BCPs, WAXS was used to characterize the investigated annealed BCPs bulk samples (Figure 2-11). All investigated BCPs of varied $M_n$ reveal three reflections at 2θ = 2.44, 4.86 and 7.31 ° with respective *d-spacing* values as 36.2, 18.2 and 12.1 Å in the small-angle region. The ratio of the *d-spacing* values of 3:2:1 was indexed as the (001), (002) and (003) reflections of a lamellar structure[34 35]. The secondary scattering peak in SF3 is not significant because of the extremely short polymer chain composed of averaged three mesogens. The board scattering peak centered at 5.06 Å (2θ = 17.5 °) in the wide-angle region is indicative of the distance among -$CF_3$ side chain end group. According to the previous studies on LC behaviors of long fluorinated side chain, the width of the peak at 5.06 Å indicates the type of LC phase. A scematic A phase was further assigned as no transition from higher-ordered scematic B to A phase was revealed in thermal analysis, which was additionally consistent with the literatures[36 37]. The observed LC lamellar structure in WAXS analysis is also in good agreement with the revealed LC properties of P8FMA homopolymer or PS-*b*-P8FMA in DSC and POM characterization results.

These morphological studies in the bulk suggest that the fluorination of PGMA led to BCPs capable of forming nano-structure of sub-5 nm *d-spacing*. Two distinctive periodicities from micro-phase separation (36.3 nm to 6.3 nm, dependent on $M_n$) and constant LC ordering (3.6 nm) were identified in bulk samples. Conclusively the molecular design for next-generation sub-5 nm (half pitch) BCP lithography was firstly successfully achieved in bulk sample.

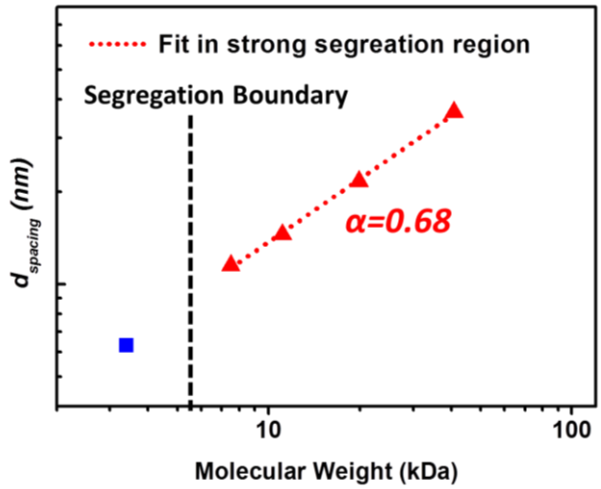


**Figure 2-12.** The linear fitting on the relationship between *molecular weight* and $d_{\text{-}spacing}$ of PS-*b*-P8FMA in log scales.

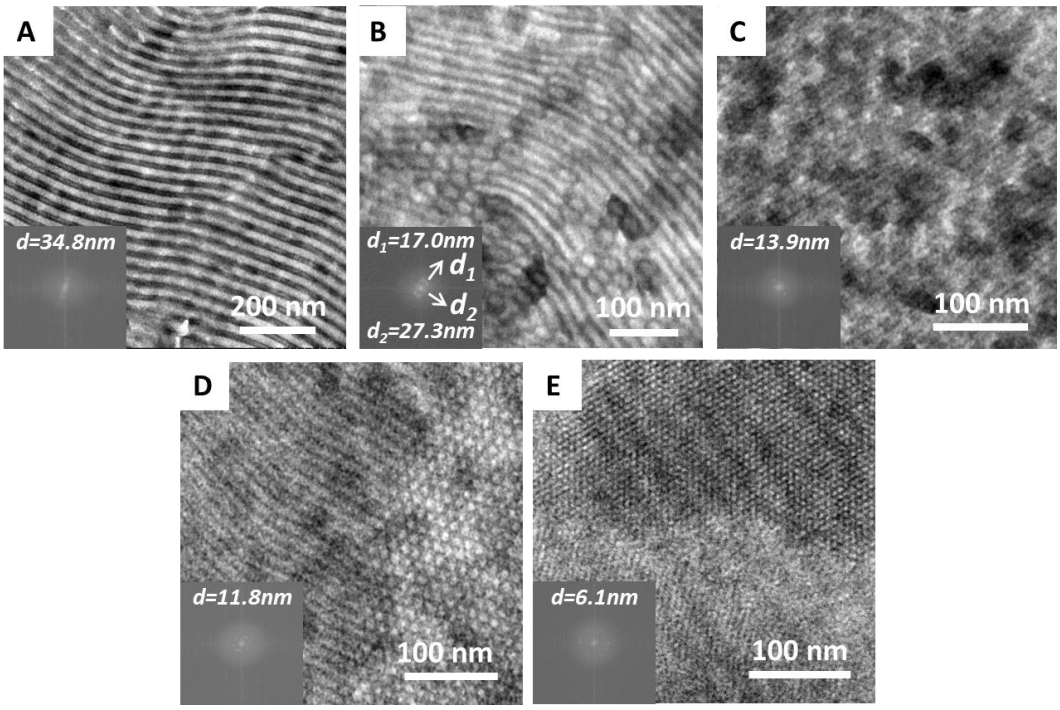


**Figure 2-13.** TEM images of PS-*b*-P8FMA (A: SF41, B: SF20, C: SF11, D: SF7, E: SF3). The dark regions correspond to the P8FMA block owing to heavy $RuO_4$ staining on hydroxyl groups. The bottom left inset displays the Fourier-transform pattern of the real-space image and the periodic length was also indicated based on the pattern. The estimated $d_{spacing}$ from TEM is highly consistent with $d_{spacing}$ extracted from SAXS.

### 2-3-4. Estimation of $\chi_{eff}$

To quantify the degree of the segregation of P8FMA against PS, random-phase approximation (RPA) method[17] in terms of the effective Flory-Huggins interaction parameter, expressed by $\chi_{eff} = AT^{-1} + B$, where $AT^{-1}$ is the enthalpic contribution, and $B$ is the entropic contribution. Firstly, temperature-dependent SAXS analyses were conducted on SF3 starting from 250 ˚C and in 10 ˚C decrements (Figure 2-14). The SAXS profiles of SF3 showed a discontinuous change in the $I_{max}^{-1}$-$T^{1}$ plot between 160-170 ˚C, as typically observed in BCP ODTs[16] (Figure 2-15). As the observed ODT is also well-above the LC isotropic transition temperature, no modification from side chain LC ordering is considered for the RPA method based on coil-coil BCP model. Therefore, the SAXS profiles in the mean-field disordered state were then analyzed based on Leibler's mean-field theory modified to include the effects from the molecular weight dispersity and asymmetry in the segmental volume. Since $\chi_{eff}$ is dependent on the reference volume used to calculate $N$, a common reference volume ($v_0$ = 118 Å$^3$) was utilized to compare the $\chi_{eff}$ values with other reported values. $\chi_{eff}$ of SF3 was expressed by $\chi_{eff\ PS/P8FMA} = 21.5/T + 0.172$ (Table 2-6, Table 2-7 and Figure 2-17) with $\chi_{eff\ PS/P8FMA}$=0.244 at 25 ˚C. In contrast, $\chi_{eff}$ value for PS-*b*-PMMA at 25 ˚C was measured to be 0.04[38], which was barely 1/6 of $\chi_{eff}$ of PS-*b*-P8FMA. Additionally, a $\chi_{eff}$ value of 0.191 at 25 ˚C for trifluoroethyl side chain in the same PS-*b*-PGMA backbone was reported by our group[17]. The perfluorinated LC side chain exhibited a higher $\chi_{eff}$ attributed to both higher enthalpic and entropic contributions. The

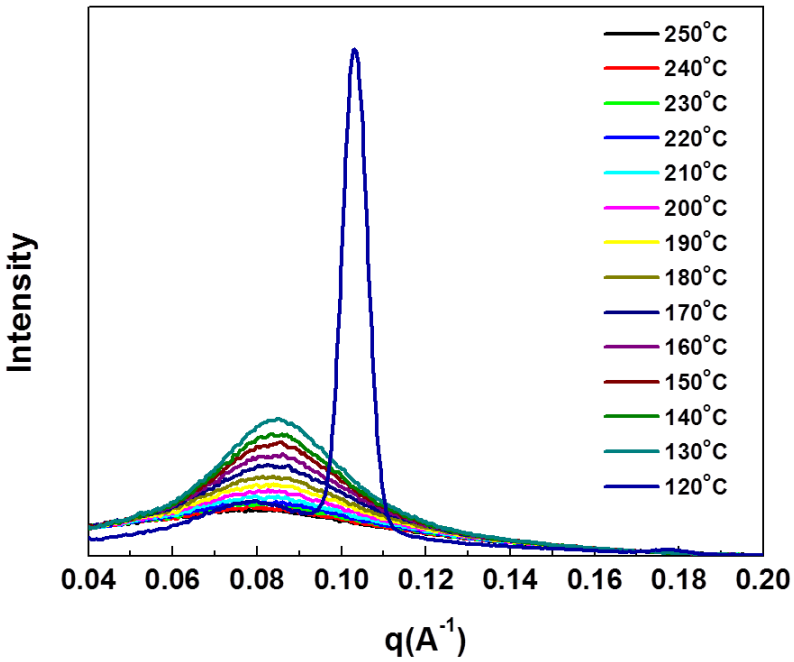


**Figure 2-14.** The scattering profiles measured by SAXS at different temperatures for PS-*b*-P8FMA (SF3).

measured higher $\chi_{eff}$ is also in good agreement with the significantly unbalanced SFEss of counter-blocks without any additional sacrifice of segregation strength in BCPs of balanced SFEs, as unbalanced SFEs of counter-blocks of usually indicate a high interfacial tension between blocks[39] and the intensive incompatibility between blocks is quantified by a high $\chi_{eff}$.

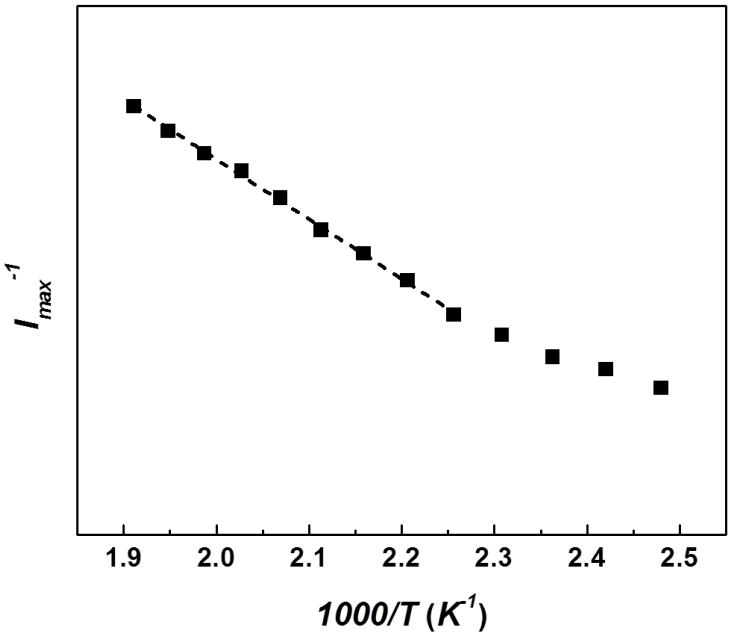


**Figure 2-15.** The $I_{max}$-$T^{-1}$ plots for for PS-*b*-P8FMA (SF3).

**Table 2-5.** The fixed parameters used to estimate $\chi_{eff}$ for PS-*b*-P8FMA (SF3).

| BCP | $r_c$ | $M_n$ (kg mol$^{-1}$) | $M_w$ (kg mol$^{-1}$) | $M_{n,PS}$[a] (kg mol$^{-1}$) | $f_{PS}$ | $w_{PS}$ |
|---|---|---|---|---|---|---|
| PS-*b*-P8FMA(SF3) | 39 | 3.2 | 3.9 | 1.6 | 0.61 | 0.50 |

[a] The molecular weight of sec-butyl from the initiator and DPE were counted as PS chain.

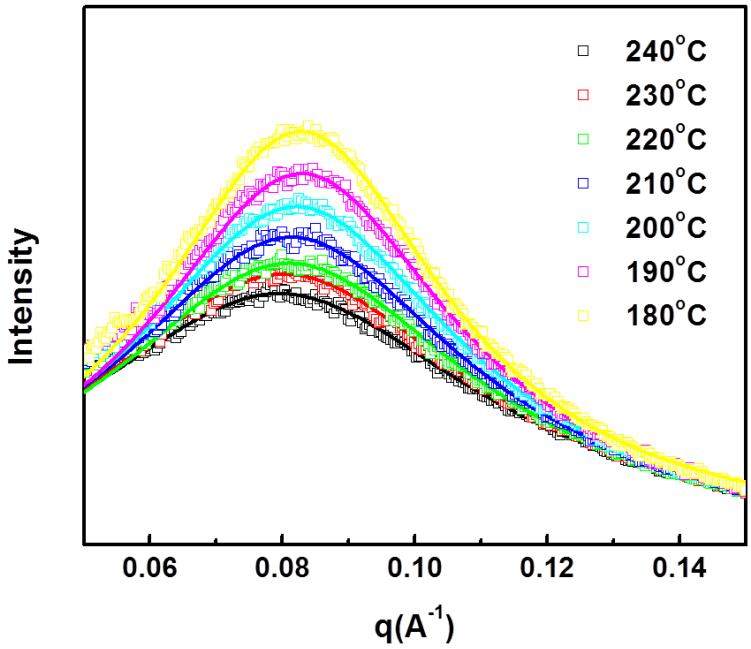


**Figure 2-16.** The scattering profiles (square scatters) measured by SAXS and the fitting profiles (smooth lines) at different temperatures for PS-*b*-P8FMA (SF3).

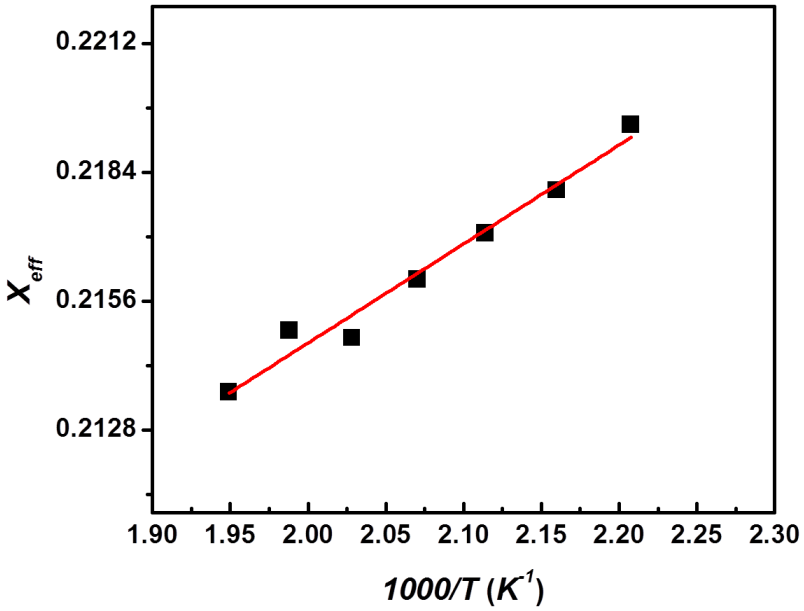


**Figure 2-17.** Temperature dependences of the effective Flory-Huggins interaction parameter for PS-*b*-P8FMA (SF3) using a reference volume of 118 $Å^3$.

**Table 2-6.** The fixed parameters used to estimate $\chi_{eff}$ for PS-*b*-P8FMA (SF3).

| $T$ (°C) | Estimated $\chi_{eff}$ PS-*b*-P8FMA (SF3) |
|---|---|
| 180 | 0.21943 |
| 190 | 0.21801 |
| 200 | 0.21708 |
| 210 | 0.21607 |
| 220 | 0.21480 |
| 230 | 0.21496 |
| 240 | 0.21362 |

**Table 2-7.** Estimated enthalpic and entropic contributions for PS-*b*-P8FMA (SF3) and PS-*b*-PMMA.

| BCP | Label | $A/T$ | $B$ |
|---|---|---|---|
| PS-*b*-P8FMA | SF3 | 21.5/$T$ | 0.172 |
| PS-*b*-PMMA[a] | - | 3.4/$T$ | 0.034 |

[a] Estimated in Chapter 6.

**2-3-5. Nanostructure and domain orientation in thin films**

Besides the capability of forming sub-5 nm nanostructure, another goal of introducing LC side chain into backbone of BCPs is to realize control on domain orientation. In previous study, BCPs of extremely unbalanced SFEs are predicted to form parallel oriented domains, as the segments of lower SFE is highly preferential towards the air interface during thermal annealing process leading to a featureless flat surface, or appearance of holes/island structure with 1.0 or 0.5 $L_0$ height differences. The specific situation is dependent on the preference of bottom substrate interface and BCP thickness[9]. Therefore, BCPs of balanced SFEs or neutralized top air interface are in demand for perpendicular orientation in thin film. In this study, two synthesized random copolymers PTFEMA-*r*-PMMA-*r*-PMAA (Figure 2-2 and Table 2-2) were spin coated onto bare silicon substrate and cross-linked to neutralize any preferential affinity of segments to the bottom substrate. The volume fraction of fluorine-containing PTFEMA was designed near to that of fluorinated P8FMA in lamellae-forming BCPs. In contrast, a PS-preferential random copolymer was used to induce the desired parallel orientation of cylinder-forming SF7. The BCPs was then spin coated from varied concentration of toluene solutions and annealed at 150 ˚C for 24 h under ambient conditions. According to the free energy equations depicting parallel or perpendicular domain orientation in thin film[14 40], BCP film thickness is one of the decisive factors in orientation control. Hence, the film thickness was first optimized by using SF41. The AFM image (Figure 2-18) of SF41 thin film exhibited perpendicularly oriented finger-printed pattern or a hybrid morphology with disordered short lines and dots, depending on the specific BCP thickness. The disordered short lines combined with dots were probably caused by the cylindrical domains in partially parallel orientation[41]. As

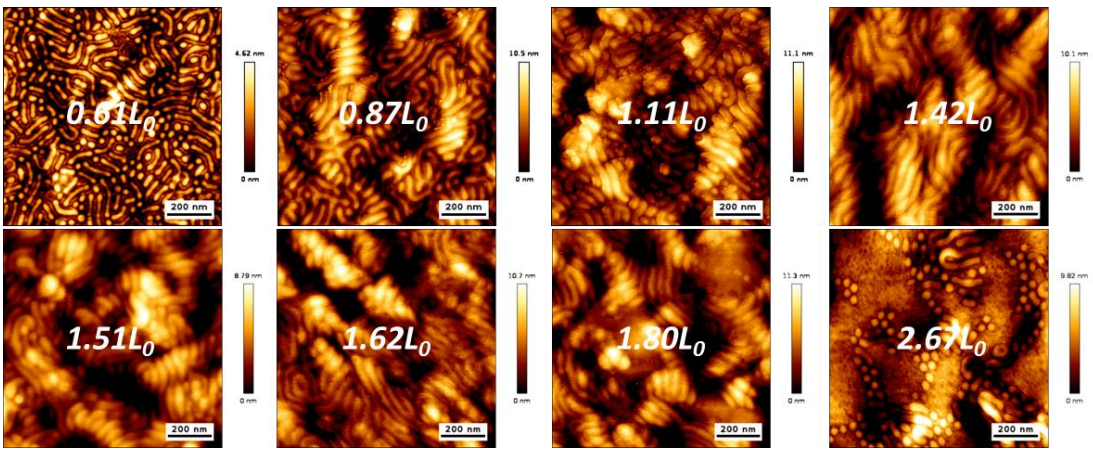


**Figure 2-18.** AFM height images of SF41 thin films with varied thickness on chemically-modified Si wafers following thermal annealing at 150 ˚C for 24h.

thickness varied 0.6 $L_0$ to 1.4 $L_0$, a gradual transition from parallel to perpendicular orientation

was revealed. When BCP thickness is between 1.4 and 1.5 $L_0$, the most uniform and ordered finger-printed pattern was attained. The previous simulation study[40] predicts that non-preferential interaction at both top and bottom interfaces are required for perpendicular orientation of domains. However, as the requirement is based on the approximation of flexible BCP in coil-coil model, the additional entropy contributor from SCLC is not included in the enthalpy-driven equation. Therefore, SCLC BCPs of unbalanced SFEs or preferential top interface may still reveal perpendicular domain orientation in thin film under optimized conditions.

As the optimized BCP thickness was determined, BCPs of varied molecular weights was spin coated onto neutral bottom surface layer. In the AFM images (Figure 2-22) for SF41, SF20, SF11 and SF7, striped patterns were clearly observed for all samples after thermal annealing. No discernible pattern was observed for SF3 (Figure 2-20), because the detected $T_{iso}$ of LC side chain is near to $T_g$ of PS segments. Therefore, no side chain LC ordering could be existed under the annealing temperature of 130 ˚C, although which is still below the measured ODT in $\chi$ parameter estimation. The fact also supports the key role of LC ordering in the formation of thin film pattern.

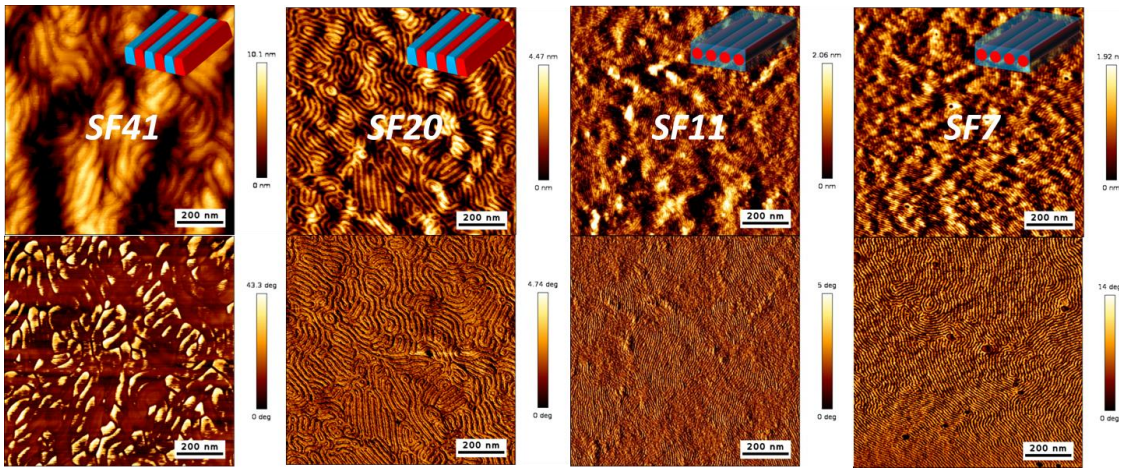


**Figure 2-19.** AFM height (upper row) and phase (bottom row) images of the thin films prepared from SF41, SF20, SF11, and SF7 on chemically-modified Si wafers after thermal annealing at 150 ˚C for 24h. The upper right inset schemes in height images indicate the BCP morphology in thin film, in which red and navy color represented PS and P8FMA domain, respectively.

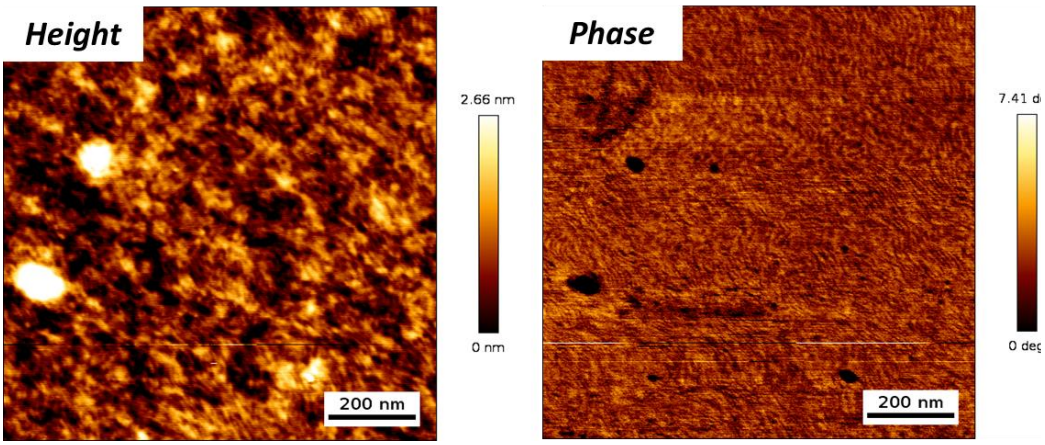


**Figure 2-20.** AFM images of the thin film prepared from SF3 after thermal annealing at 130 ℃ for 24hr.

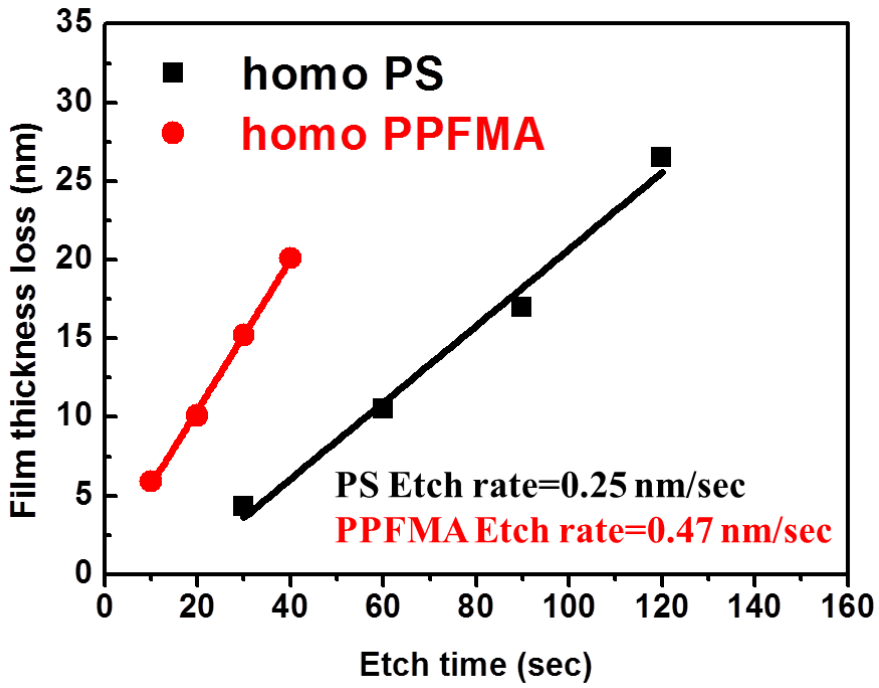


**Figure 2-21.** Oxygen plasma etching rate of homopolymers.

To obtain further information regarding the internal structure of the investigated thin film, an $O_2$-RIE treatment was further conducted to selectively remove the P8FMA domain and again characterized using AFM (the etch contrast between PS and P8FMA is described in the Figure 2-21). In AFM images (Figure 2-22), clear fingerprinted patterns with removal of P8FMA domain were observed. The periodic length of formed pattern was highly correlated with that characterized in bulk samples. The high correlation between the pattern dimension of bulk and thin film was reasonably thought caused by the LC side chain in P8FMA, which may suppress the interfacial effects in thin film states. In contrast, the observed sub-20 nm domain of BCPs with amorphous mono-fluorine side chain[17] in bulk could not be reproduced in thin film states. As entropy plays a more important role on the thin film self-assembly confined between two interfaces compared to the isotropic surrounding in bulk, the intrinsic LC ordering from long fluorine-containing side chains were thought to confine the entropy change of polymer chain[42] and thus minimize the interface effects. Therefore, the molecular design enables the formation of the pattern dimension analogous to that characterized in thin film. As $M_n$ of BCP was reduced to 11k, cylinder-forming SF11 began to exhibit a pattern of relatively long-ranged orders with an averaged dimension of 16-17 nm in thin film, which is response to the

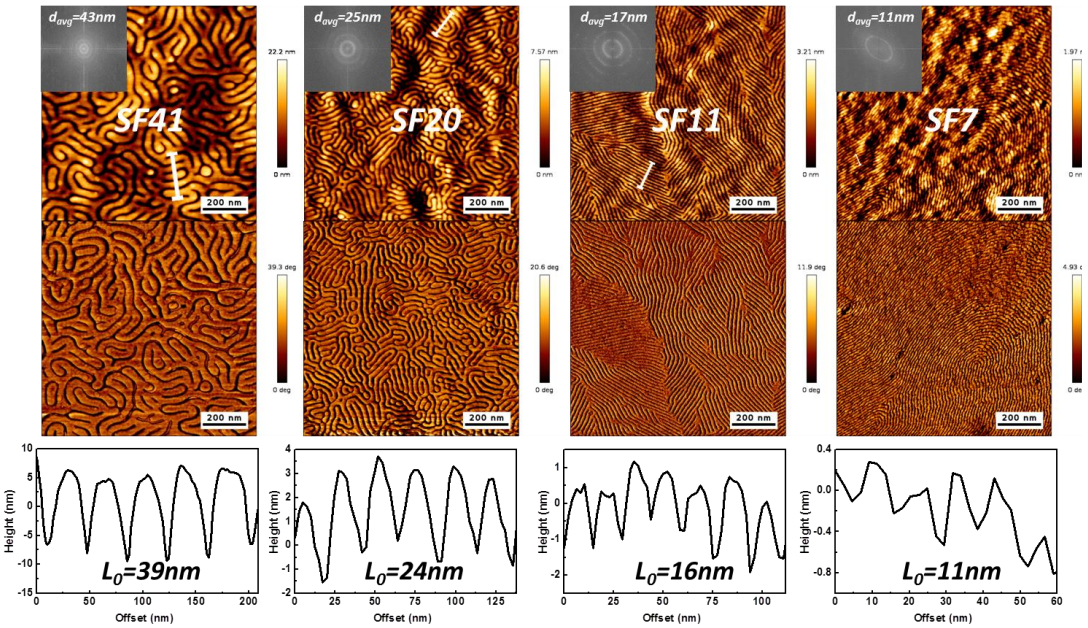


**Figure 2-22.** AFM height (upper row), phase images (middle row) and phase cross-section profiles (bottom row) of the thin films prepared from SF41, SF20, SF11, and SF7 after $O_2$-RIE treatment. The upper left inset displays the Fourier-transform pattern of the real-space image and the averaged periodic length was indicated.

characterized distance ($d$= $2/\sqrt{3}$ $d_{spacing}$=15.8 nm) between adjacent PS cylinder domains in bulk. Compared to the morphologies of BCPs with higher molecular weights, SF11 revealed a pattern consisted of significantly elongated stripes in smaller width. As the micro-phase separation and LC ordering occur simultaneously under thermal annealing, the competition between the two driving forces plays a decisive role on the formed nano-structure. When the molecular weight is scaled down with a reduced value of $\chi N$, the driving force of micro-phase separation is also minimized. Meanwhile, the driving force for LC ordering is not significantly changed by reduced $M_n$[43], as evidenced by the similar characteristic peaks indicating LC smectic phase in WAXS measurements. In fact, as the temperature is below $T_{iso}$, the LC ordering may be even kinetically accelerated at reduced $M_n$ because of the increased mobility of BCP backbone segments. Therefore, the LC ordering from side chain begins to dominate the formation of nano-structure, and the LC ordering was capable of forming regularly elongated stripe and nearly defect-free morphology[22]. Moreover, another PTFEMA-*r*-PMMA-*r*-PMAA of different composition was used as bottom surface layer for SF7, in accordance with the desired parallel domain orientation of cylinder-forming SF7. Following thermal annealing, SF7

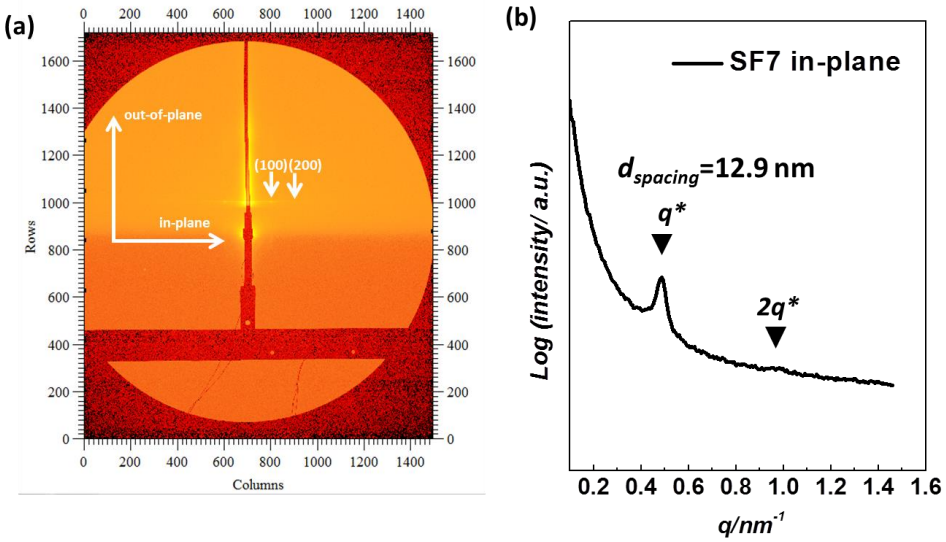


**Figure 2-23**. (a) Grazing-incidence small-angle scattering (GISAXS) results of the thin film prepared from SF7. In-plane and out-of-plane directions were indicated and reflection peak from (100) (200) were observed along in-plane direction, meanwhile no significant scattering peak was observed along out-of-plane direction due to the overlapping with beamline. (b) The integration along in-plane direction in GISAXS profiles and a periodicity of $d_{spacing}$=12.9 nm perpendicular to Si substrate was suggested.

thin film revealed a finger-printed pattern of averaged 12 nm width. The fast Fourier transform (FFT) inset in Figure 2-22 gives information on the averaged domain size and periodicity. Apparently, the periodicity of pattern was improved by the reduced $M_n$ of BCPs. The asymmetric FFT ring in SF7 sample is caused by the mixed featured dimensions from two distinctive planes in asymmetric array of SF7. Besides, the periodicity of SF7 is underestimated because of the limit on AFM image resolution in fixed pixel number scale. In Figure 2-24 of a larger scanning area covering multiple grains, a relatively more symmetric FFT ring is obtained, because one specific orientation of paralleled domain becomes dominating across several grains area. The synchrotron GISAXS measurement (Figure 2-23) is also highly consistent with the AFM observation results. A periodic lamellae of $d_{spacing}$=13 nm perpendicular to bottom substrate was revealed by scattering profile because of the 1.5 $L_0$ BCP thickness near to monolayer.

The above results suggested that the molecular design for perpendicular orientation control on lamellae-forming SF41 and SF20 and parallel orientation control on cylinder-forming SF11 and SF7, were successfully achieved in all thin film samples. Additionally, the ordered finger-printed pattern of 5.5 nm half pitch was prepared in thin film, which is extremely near to sub-5 nm patterning regime. A paralleled PS cylinder domain was formed because of the bottom surface layer preferential to PS. The cross-sectional SEM observation (Figure 2-25) on thin film also reveals the PS cylinder domain in parallel orientation. In contrast, a non-preferential bottom surface layer led to perpendicularly orientated cylindrical PS domains in hexagonally packed array, as supported by the AFM measurements results in Chapter 3. The high correlation between periodic length characterized in bulk and thin film was obviously due to the interplay between the ordering of LC side chain and self-assembly of BCP. The LC side chain ordering was believed to minimize the interfacial effects in thin film.

For SF7 of minimized pattern dimension, the clear grain boundary of micro-phase separated structure was observed over an expanded scanning area (Figure 2-24). As the competition between LC ordering and micro-phase separation undergoes under thermal annealing, the significantly increased grain size of observed structure is reasonably attributed to the dominating LC ordering owing to the reduced driving force of block segregation (indicated by the value of $\chi N$ ) in SF7. The interplay of LC side chain ordering and self-assembly process contributed to the extremely long-ranged alignment of domains with reduced defects density. The edge roughness of pattern following plasma etching was observed increased in AFM, because dry etching is considered incompatible with extremely minimized pattern caused by organic BCP self-assembly[44]. The etching results suggested that the alignments of BCP domains were extended down from the thin film surface.

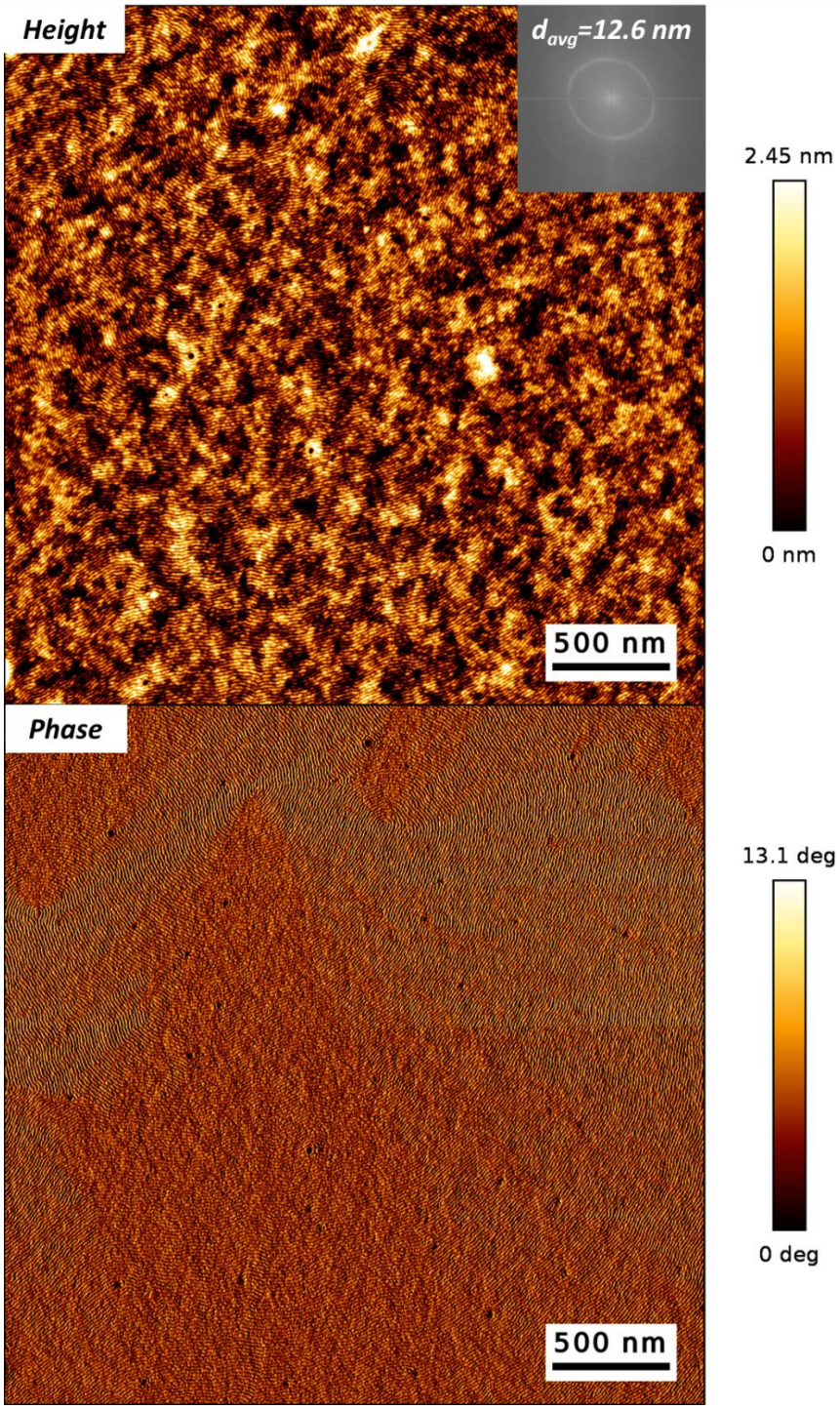


**Figure 2-24.** AFM images of the thin film prepared from SF7 after $O_2$-RIE treatment over a 3μm × 3μm scanning area. The inset presents the FFT of the height image and the number-averaged periodic length of domain is estimated from FFT.

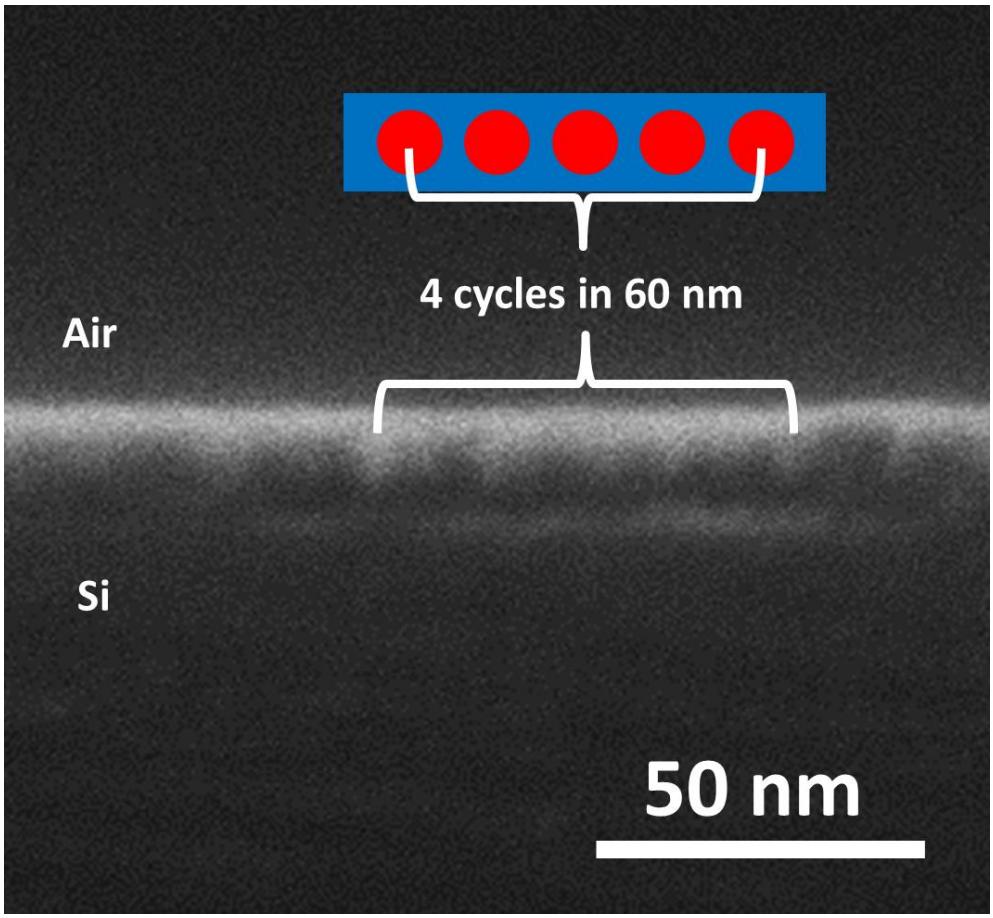


**Figure 2-25.** Cross-sectional SEM images of the thin film prepared from SF7 following thermal annealing. The inset indicates the observed four continuous periodic PS (red) cylinders parallel to the substrate at air-silicon substrate interface.

**2-3-6. Quantitative analysis on thin film patterns**

To better investigate the role of LC side chain on the formed thin film pattern, a quantitative analysis based on Matlab R2018a[45] is applied to the AFM phase images prepared from SF41, SF20, SF11, and SF7 after $O_2$ plasma treatment. In this quantitative analysis, three key parameters including correlation length ( $\xi$ ), line width roughness (LWR) and line edge roughness (LER) were estimated from the line patterns shown in AFM phase images (Figure 2-26), as listed in Table 2-8.

Firstly the color mapping results (Figure 2-27) indicate the varied BCP domain orientation in distinctive grains. As $M_n$ of BCP is reduced, the grain size was significantly enlarged possibly because of the enhanced LC side chain ordering in the hierarchical self-assembly driving forces. Therefore, the correlation length of line pattern (Figure 2-28) was significantly increased despite the reduced line width. Especially in SF7 sample of lowest $M_n$, an extremely elongated correlation length of 11.1 times of periodic length was estimated, in comparison to the commonly reported correlation length of a maximum 5~6 times of periodic length for other high $\chi$ parameter BCPs[45] or widely studied PS-*b*-PMMA[46]. The observations are consistent with the reported super long-ranged ordering and defect-free nature of hierarchical self-assembled domains assisted by arrangements of liquid crystal side chains [22 47 48].

Besides, LWR and LER (Figure 2-29 and Figure 2-30) were found proportional to the averaged line width. The ratio of LWR to LER in each sample is always much greater than $\sqrt{2}$ and near to 2, indicating anti-correlated profiles of adjacent two edges[49]. A minimal LWR of 1.55 nm and LER of 0.6 nm in SF7 sample were estimated. The estimated minimal roughness values of line pattern are within the requirements in lithographic process[50]. The fact indicates the application potential of the studied materials in next-generation sub-5 nm lithographic industry.

**Table 2-8**. Estimated parameters from of quantitative analysis on AFM images.

| Sample | Periodic length $L_0$ (nm) | $\xi$ (nm) | $\xi/L_0$ | Average line width (nm) | LWR (nm) | Line edge (nm) | LER (nm) | LWR/$L_0$ | LER/$L_0$ |
|---|---|---|---|---|---|---|---|---|---|
| SF41 | 41.7 | 29.2 | 0.7 | 19.0 | 5.8 | 9.5 | 2.3 | 0.139 | 0.055 |
| SF20 | 27.8 | 52.3 | 1.9 | 12.0 | 3.6 | 6.0 | 1.5 | 0.129 | 0.054 |
| SF11 | 17.5 | 111.1 | 6.3 | 6.1 | 2.0 | 3.0 | 1.1 | 0.114 | 0.063 |
| SF7 | 12.7 | 141.1 | 11.1 | 4.2 | 1.5 | 2.1 | 0.6 | 0.117 | 0.047 |

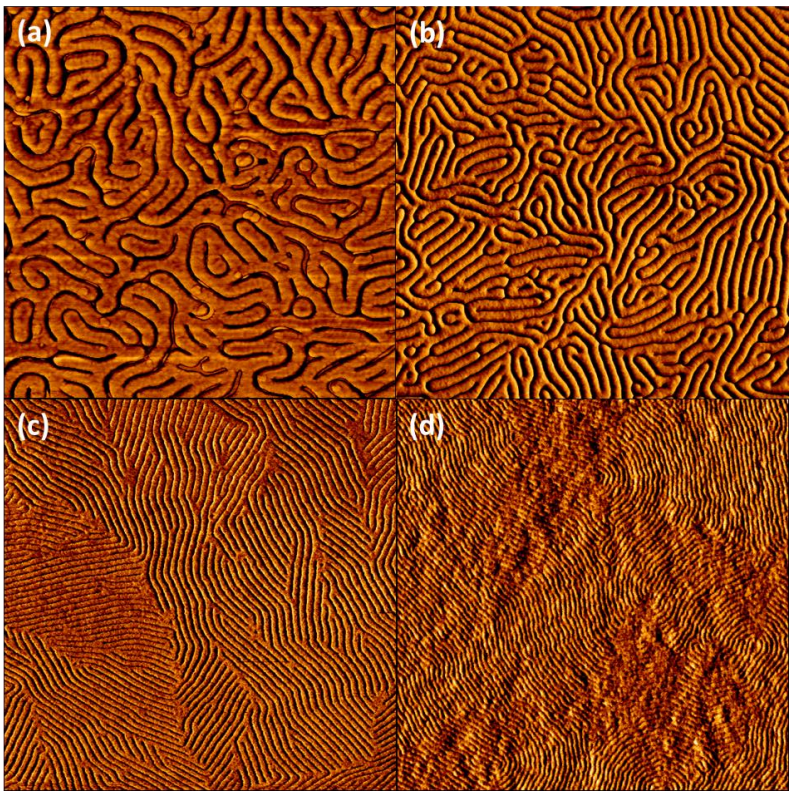


**Figure 2-26.** AFM phase images of the thin films prepared from (a) SF41, (b) SF20, (c) SF11, and (d) SF7 in 1.0 μm × 1.0 μm scale after oxygen plasma etching used for quantitative analysis.

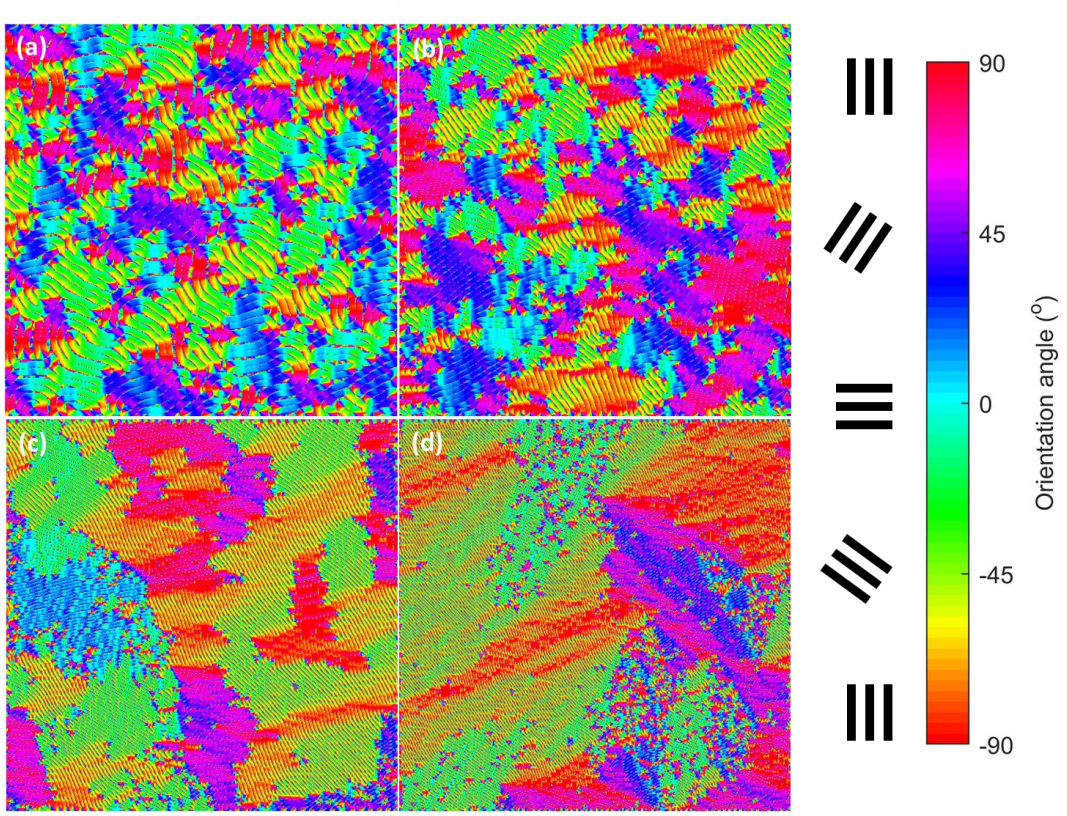


**Figure 2-27.** The corresponding orientation color map of (a) SF41, (b) SF20, (c) SF11, and (d) SF7 in 1.0 μm × 1.0 μm scale respectively. The distinctive color denotes the orientation angle of domain as shown in the right bar.

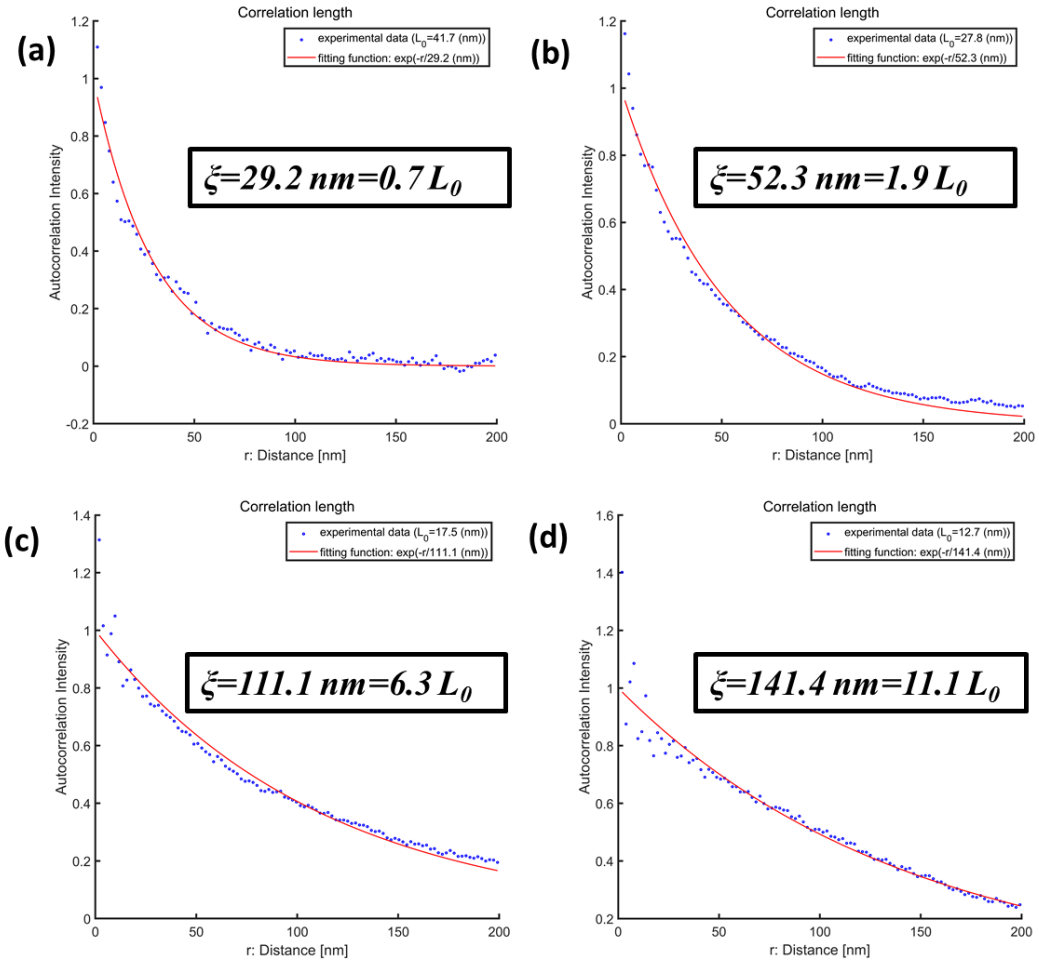


**Figure 2-28.** The autocorrelation intensity plot and fitting for correlation length of (a) SF41, (b) SF20, (c) SF11, and (d) SF7, respectively.

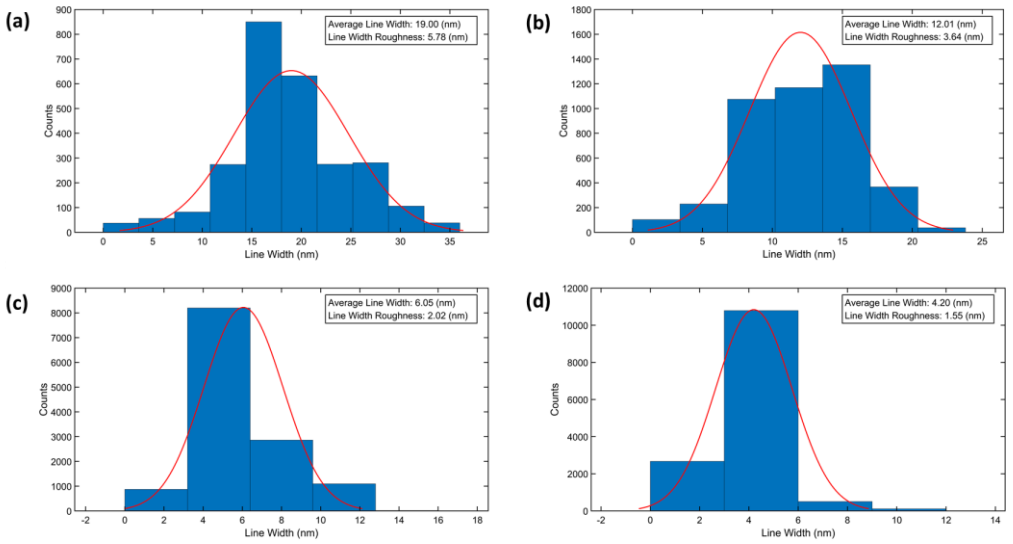


**Figure 2-29.** The histograms of line width of (a) SF41, (b) SF20, (c) SF11, and (d) SF7, respectively. The red curve indicates the fitting in Gaussian distribution and average line width is obtained. The line width roughness (LWR) is further estimated from the standard deviation of line width.

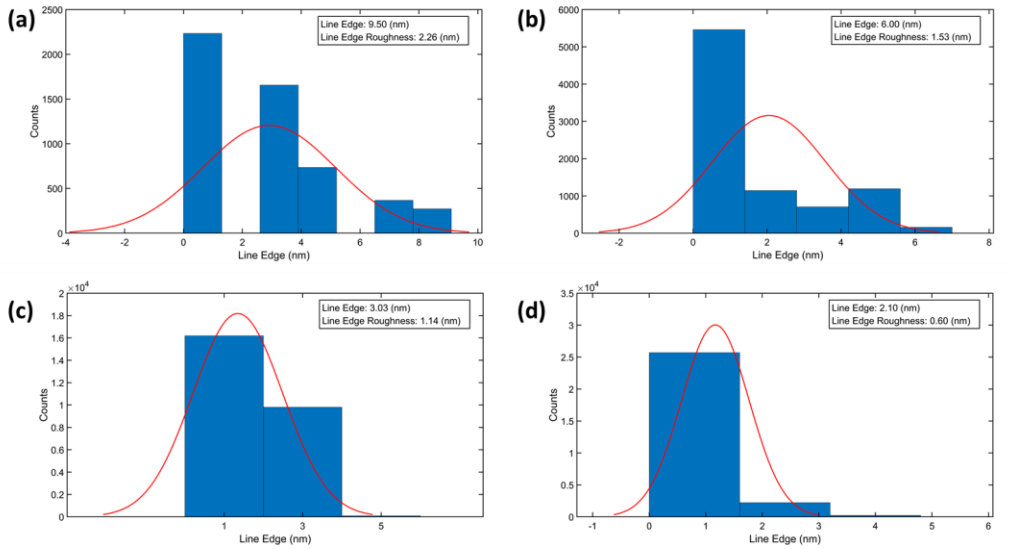


**Figure 2-30.** The histograms of line edge of (a) SF41, (b) SF20, (c) SF11, and (d) SF7, respectively. The red curve indicates the fitting in Gaussian distribution and average line edge is obtained. The line edge roughness (LER) is further estimated from the standard deviation of line edge.

## 2-4. Conclusion

In this study, a BCP molecular design capable of forming striation pattern in thin films under thermal annealing via facile introduction of LC side chain was demonstrated. A precursor BCP, PS-*b*-PGMA, was first synthesized via the sequential living anionic polymerization of styrene and glycidyl methacrylate. Due to the potential reactive glycidyl moieties in backbone of polymer, the following introduction of long fluorinated LC side chain into polymer was conducted easily in a mild and efficient way. The super-hydrophobic long fluorinated functionalities dominated the surface tension properties of block despite the existence of minor hydroxyl group in side chain, which was verified by surface free energy measurements. The SAXS and TEM analyses of the PS-*b*-P8FMA revealed a gradual morphology transition from ordered lamellae to hexagonally packed cylinder with a minimum $d_{spacing}$ of 6.3 nm in bulk. The LC ordering of side chain in bulk was also studied by using WAXS, DSC and POM. In thin film studies, the formation of perpendicular lamellae or parallel cylinder on surface-modified silicon wafers was demonstrated using thermal annealing. The periodic length of the formed finger-printed pattern was successfully minimized to 12 nm with high-orders, in accordance with 6 nm half-pitch. The results suggested that by introduction of LC fluorinated side chain, diblock copolymer of extremely unbalanced SFEs reveals a high $\chi$ parameter and is capable of forming line patterns in thin film following thermal annealing without any modification at top air interface. The mechanism is in correlation with the interplay between entropy-driven LC side chain ordering and enthalpy-driven block segregation in annealing process. As the mainly entropy-driven LC side ordering is less affected by the interfacial enthalpy change at interfaces, the side chain LC ordering in thin film could assist in suppressing interfacial effects in thermally induced self-assembly process. Therefore, the self-assembly behaviors of investigated BCPs exhibited a high correlation in domain scale of bulk and thin film states. Moreover, as the segregation between blocks become weak at lower $M_n$ of BCPs, the enhanced role from LC ordering of side chain significantly contribute to the long-ranged ordered pattern of significantly reduced defects, which are further supported by the estimated increased correlation length for BCPs of lower $M_n$. And LWR/LER is proportional to the average line width with a minimal 0.6 nm LER for the smallest line pitch. Based on the thin film results, PS-*b*-P8FMA has proven to be a highly competitive candidate for sub-5 nm next-generation BCP lithography resist. More importantly, the SCLC molecular design could be extended to other BCP system for the development of materials for sub-5 nm next-generation lithographic application.

**2.5 References**

1. Bates, C. M.; Maher, M. J.; Janes, D. W.; Ellison, C. J.; Willson, C. G., Block Copolymer Lithography. *Macromolecules* **2014,** *47* (1), 2-12.

2. Hawker, C. J.; Russell, T. P., Block copolymer lithography: Merging "bottom-up" with "top-down" processes. *Mrs Bull* **2005,** *30* (12), 952-966.

3. Jung, Y. S.; Ross, C. A., Orientation-controlled self-assembled nanolithography using a polystyrene-polydimethylsiloxane block copolymer. *Nano Lett* **2007,** *7* (7), 2046-2050.

4. Son, J. G.; Gotrik, K. W.; Ross, C. A., High-Aspect-Ratio Perpendicular Orientation of PS-b-PDMS Thin Films under Solvent Annealing. *ACS Macro Lett* **2012,** *1* (11), 1279-1284.

5. Son, J. G.; Chang, J. B.; Berggren, K. K.; Ross, C. A., Assembly of Sub-10-nm Block Copolymer Patterns with Mixed Morphology and Period Using Electron Irradiation and Solvent Annealing. *Nano Lett* **2011,** *11* (11), 5079-5084.

6. Bai, W. B.; Gadelrab, K.; Alexander-Katz, A.; Ross, C. A., Perpendicular Block Copolymer Microdomains in High Aspect Ratio Templates. *Nano Lett* **2015,** *15* (10), 6901-6908.

7. Jeong, J. W.; Park, W. I.; Kim, M. J.; Ross, C. A.; Jung, Y. S., Highly Tunable Self-Assembled Nanostructures from a Poly(2-vinylpyridine-b-dimethylsiloxane) Block Copolymer. *Nano Lett* **2011,** *11* (10), 4095-4101.

8. Seshimo, T.; Bates, C. M.; Dean, L. M.; Cushen, J. D.; Durand, W. J.; Maher, M. J.; Ellison, C. J.; Willson, C. G., Block Copolymer Orientation Control Using a Top-Coat Surface Treatment. *J Photopolym Sci Tec* **2012,** *25* (1), 125-129.

9. Maher, M. J.; Bates, C. M.; Blachut, G.; Sirard, S.; Self, J. L.; Carlson, M. C.; Dean, L. M.; Cushen, J. D.; Durand, W. J.; Hayes, C. O.; Ellison, C. J.; Willson, C. G., Interfacial Design for Block Copolymer Thin Films. *Chem Mater* **2014,** *26* (3), 1471-1479.

10. Cushen, J.; Wan, L.; Blachut, G.; Maher, M. J.; Albrecht, T. R.; Ellison, C. J.; Willson, C. G.; Ruiz, R., Double-Patterned Sidewall Directed Self-Assembly and Pattern Transfer of Sub-10 nm PTMSS-b-PMOST. *ACS Appl Mater Inter* **2015,** *7* (24), 13476-13483.

11. Maher, M. J.; Rettner, C. T.; Bates, C. M.; Blachut, G.; Carlson, M. C.; Durand, W. J.; Ellison, C. J.; Sanders, D. P.; Cheng, J. Y.; Willson, C. G., Directed Self-Assembly of Silicon-Containing Block Copolymer Thin Films. *ACS Appl Mater Inter* **2015,** *7* (5), 3323-3328.

12. Lane, A. P.; Yang, X. M.; Maher, M. J.; Blachut, G.; Asano, Y.; Soineya, Y.; Mallavarapu, A.; Sirard, S. M.; Ellison, C. J.; Willson, C. G., Directed Self-Assembly and Pattern Transfer of Five Nanometer Block Copolymer Lamellae. *ACS Nano* **2017,** *11* (8), 7656-7665.

13. Maher, M. J.; Mori, K.; Sirard, S. M.; Dinhobl, A. M.; Bates, C. M.; Gurer, E.; Blachut, G.; Lane, A. P.; Durand, W. J.; Carlson, M. C.; Strahan, J. R.; Ellison, C. J.; Willson, C. G., Pattern

Transfer of Sub-10 nm Features via Tin-Containing Block Copolymers. *ACS Macro Lett* **2016,** *5* (3), 391-395.

14. Bates, C. M.; Seshimo, T.; Maher, M. J.; Durand, W. J.; Cushen, J. D.; Dean, L. M.; Blachut, G.; Ellison, C. J.; Willson, C. G., Polarity-Switching Top Coats Enable Orientation of Sub-10-nm Block Copolymer Domains. *Science* **2012,** *338* (6108), 775-779.

15. Seshimo, T.; Maeda, R.; Odashima, R.; Takenaka, Y.; Kawana, D.; Ohmori, K.; Hayakawa, T., Perpendicularly oriented sub-10-nm block copolymer lamellae by atmospheric thermal annealing for one minute. *Sci Rep-Uk* **2016,** *6*.

16. Nakatani, R.; Takano, H.; Chandra, A.; Yoshimura, Y.; Wang, L.; Suzuki, Y.; Tanaka, Y.; Maeda, R.; Kihara, N.; Minegishi, S.; Miyagi, K.; Kasahara, Y.; Sato, H.; Seino, Y.; Azuma, T.; Yokoyama, H.; Ober, C. K.; Hayakawa, T., Perpendicular Orientation Control without Interfacial Treatment of RAFT-Synthesized High-chi Block Copolymer Thin Films with Sub-10 nm Features Prepared via Thermal Annealing. *ACS Appl Mater Inter* **2017,** *9* (37), 31266-31278.

17. Yoshimura, Y.; Chandra, A.; Nabae, Y.; Hayakawa, T., Chemically tailored high-chi block copolymers for perpendicular lamellae via thermal annealing. *Soft Matter* **2019,** *15* (17), 3497-3506.

18. Wei, W.; Xiong, H. M., Orientation and Morphology Control of the Liquid Crystalline Block Copolymer Thin Film by Liquid Crystalline Solvent. *Langmuir* **2018,** *34* (50), 15455-15461.

19. Beppu, K.; Nagashima, Y.; Hara, M.; Nagano, S.; Seki, T., Photoalignment of Vertically Oriented Microphase Separated Lamellae in LC-LC Diblock Copolymer Thin Film. *Macromol Rapid Comm* **2017,** *38* (13).

20. Komura, M.; Yoshitake, A.; Komiyama, H.; Iyoda, T., Control of Air-Interface-Induced Perpendicular Nanocylinder Orientation in Liquid Crystal Block Copolymer Films by a Surface-Covering Method. *Macromolecules* **2015,** *48* (3), 672-678.

21. Zhao, Y.; Qi, B.; Tong, X.; Zhao, Y., Synthesis of double side-chain liquid crystalline block copolymers using RAFT polymerization and the orientational cooperative effect. *Macromolecules* **2008,** *41* (11), 3823-3831.

22. Ding, L. M.; Mao, H. M.; Xu, J.; He, J. B.; Ding, X.; Russell, T. P.; Robello, D. R.; Mis, M., Morphological study on an Azobenzene-containing liquid crystalline Diblock copolymer. *Macromolecules* **2008,** *41* (6), 1897-1900.

23. Verploegen, E.; Zhang, T.; Jung, Y. S.; Ross, C.; Hammond, P. T., Controlling the Morphology of Side Chain Liquid Crystalline Block Copolymer Thin Films through Variations in Liquid Crystalline Content. *Nano Lett* **2008,** *8* (10), 3434-3440.

24. Gadwal, I.; Stuparu, M. C.; Khan, A., Homopolymer bifunctionalization through

sequential thiol-epoxy and esterification reactions: an optimization, quantification, and structural elucidation study. *Polym Chem-Uk* **2015,** *6* (8), 1393-1404.

25. Harris, M.; Appel, G.; Ade, H., Surface morphology of annealed polystyrene and poly(methyl methacrylate) thin film blends and bilayers. *Macromolecules* **2003,** *36* (9), 3307-3314.

26. Fedors, R. F., A method for estimating both the solubility parameters and molar volumes of liquids. *Polymer Engineering & Science* **1974,** *14* (2), 147-154.

27. Li, L. B.; Meng, F. H.; Zhong, Z. Y.; Byelov, D.; de Jeu, W. H.; Feijen, J., Morphology of a highly asymmetric double crystallizable poly(epsilon-caprolactone-b-ethylene oxide) block copolymer. *J Chem Phys* **2007,** *126* (2).

28. Shah, M.; Pryarnitsyn, V.; Ganesan, V., A model for self-assembly in side chain liquid crystalline block copolymers. *Macromolecules* **2008,** *41* (1), 218-229.

29. Li, X. K.; Huang, F.; Jiang, T.; He, X. H.; Lin, S. L.; Lin, J. P., Phase behaviors of side chain liquid crystalline block copolymers. *Rsc Adv* **2015,** *5* (2), 1514-1521.

30. Bates, F. S.; Fredrickson, G. H., Block Copolymer Thermodynamics - Theory and Experiment. *Annu Rev Phys Chem* **1990,** *41*, 525-557.

31. Matsen, M. W.; Bates, F. S., Unifying weak- and strong-segregation block copolymer theories. *Macromolecules* **1996,** *29* (4), 1091-1098.

32. Bates, F. S., Polymer-Polymer Phase-Behavior. *Science* **1991,** *251* (4996), 898-905.

33. Kennemur, J. G.; Yao, L.; Bates, F. S.; Hillmyer, M. A., Sub-5 nm Domains in Ordered Poly(cyclohexylethylene)-block-poly(methyl methacrylate) Block Polymers for Lithography. *Macromolecules* **2014,** *47* (4), 1411-1418.

34. Karim, M. R.; Takehira, H.; Rahman, M. M.; Asiri, A. M.; Amin, M. K.; Ohtani, R.; Hayami, S., Magnetic and liquid crystalline property of long-alkyl chain appended iron (II) imidazole complexes. *J Organomet Chem* **2016,** *808*, 42-47.

35. Wang, L.; Ishida, Y.; Maeda, R.; Tokita, M.; Horiuchi, S.; Hayakawa, T., Alkylated Cage Silsesquioxane Forming a Long-Range Straight Ordered Hierarchical Lamellar Nanostructure. *Langmuir* **2014,** *30* (32), 9797-9803.

36. Wang, J. G.; Mao, G. P.; Ober, C. K.; Kramer, E. J., Liquid crystalline, semifluorinated side group block copolymers with stable low energy surfaces: Synthesis, liquid crystalline structure, and critical surface tension. *Macromolecules* **1997,** *30* (7), 1906-1914.

37. Al-Hussein, M.; Serero, Y.; Konovalov, O.; Mourran, A.; Moller, M.; de Jeu, W. H., Nanoordering of fluorinated side-chain liquid crystalline/amorphous diblock copolymers. *Macromolecules* **2005,** *38* (23), 9610-9616.

38. Russell, T. P.; Hjelm, R. P.; Seeger, P. A., Temperature-Dependence of the Interaction Parameter of Polystyrene and Poly(Methyl Methacrylate). *Macromolecules* **1990,** *23* (3),

890-893.

39. Owens, D. K.; Wendt, R., Estimation of the surface free energy of polymers. *J Appl Polym Sci* **1969,** *13* (8), 1741-1747.

40. Durand, W. J.; Carlson, M. C.; Maher, M. J.; Blachut, G.; Santos, L. J.; Tein, S.; Ganesan, V.; Ellison, C. J.; Willson, C. G., Experimental and Modeling Study of Domain Orientation in Confined Block Copolymer Thin Films. *Macromolecules* **2016,** *49* (1), 308-316.

41. Majewski, P. W.; Yager, K. G., Reordering transitions during annealing of block copolymer cylinder phases. *Soft Matter* **2016,** *12* (1), 281-294.

42. Lo, T. Y.; Dehghan, A.; Georgopanos, P.; Avgeropoulos, A.; Shi, A. C.; Ho, R. M., Orienting Block Copolymer Thin Films via Entropy. *Macromolecules* **2016,** *49* (2), 624-633.

43. Jiang, X.-Q.; Zhao, R.-Y.; Chang, W.-Y.; Yin, D.-X.; Guo, Y.-C.; Wang, W.; Liang, D.-H.; Yang, S.; Shi, A.-C.; Chen, E.-Q., Highly Ordered Sub-10 nm Patterns Based on Multichain Columns of Side-Chain Liquid Crystalline Polymers. *Macromolecules* **2019**.

44. Belete, Z.; Baer, E.; Erdmann, A., Modeling of block copolymer dry etching for directed self-assembly lithography. *Advanced Etch Technology for Nanopatterning Vii* **2018,** *10589*.

45. Nakatani, R.; Chandra, A.; Uchiyama, T.; Nabae, Y.; Hayakawa, T., Dynamic Ordering in High-chi Block Copolymer Lamellae Based on Cross-Sectional Orientational Alignment. *ACS Macro Lett* **2019,** *8* (9), 1122-1127.

46. Perego, M.; Ferrarese Lupi, F.; Ceresoli, M.; Giammaria, T. J.; Seguini, G.; Enrico, E.; Boarino, L.; Antonioli, D.; Gianotti, V.; Sparnacci, K.; Laus, M., Ordering dynamics in symmetric PS-b-PMMA diblock copolymer thin films during rapid thermal processing. *J Mater Chem C* **2014,** *2* (32), 6655-6664.

47. Jiang, X.-Q.; Zhao, R.-Y.; Chang, W.-Y.; Yin, D.-X.; Guo, Y.-C.; Wang, W.; Liang, D.-H.; Yang, S.; Shi, A.-C.; Chen, E.-Q., Highly Ordered Sub-10 nm Patterns Based on Multichain Columns of Side-Chain Liquid Crystalline Polymers. *Macromolecules* **2019,** *52* (13), 5033-5041.

48. Shi, L.-Y.; Lee, S.; Cheng, L.-C.; Huang, H.; Liao, F.; Ran, R.; Yager, K. G.; Ross, C. A., Thin Film Self-Assembly of a Silicon-Containing Rod–Coil Liquid Crystalline Block Copolymer. *Macromolecules* **2019,** *52* (2), 679-689.

49. Constantoudis, V.; Kuppuswamy, V.-K.; Gogolides, E.; Pret, A.; Pathangi, H.; Gronheid, R., *Challenges in LER/CDU metrology in DSA: placement error and cross-line correlations*. SPIE: 2016; Vol. 9778.

50. Ruiz, R.; Wan, L.; Lopez, R.; Albrecht, T. R., Line Roughness in Lamellae-Forming Block Copolymer Films. *Macromolecules* **2017,** *50* (3), 1037-1046.

# Chapter 3

# Study on Effects of Semifluorinated Side Chains with Varied Lengths on Self-assembly Morphology of Diblock Copolymer

## 3-1. Introduction

Block copolymers (BCPs) are widely studied due to the capability of self-assembling into a variety of long-ranged structure. The commonly observed morphologies in coil-coil flexible diblock copolymer include sphere, cylinder and lamellae, dependent on the specific volume fraction of blocks[1 3 4]. This unique feature resulting from self-assembly behaviors reveals potential application on perspective nanofabrication in semi-conductor industry[5].

In Chapter 2, a novel class of high $\chi$ parameter diblock copolymers, with liquid crystalline semifluorinated side chains, had been shown potential applications in nano-fabrication of extremely narrow sub-5 nm periodic patterns. However, the detailed self-assembly morphology is not clear because of the hierarchy self-assembly in side chain liquid crystalline (SCLC) block copolymer. In SCLC BCPs self-assembly process, their microstructure will be influenced by two driving forces, side-chain crystalline LC ordering and mirco-phase separation from block segregation, which is different from other BCPs as merely mirco-phase separation was involved. Therefore, two periodicities of distinctive scales from side chain LC ordering and microphase separation of the counter-blocks will be co-existed in the hierarchy system. Accordingly, modified models based on SCFT approach[6] or dissipative particle dynamics (DPD) simulations[7 8] were developed to characterize the self-assembly behavior in SCLC BCP. Based on the experimental and theoretic studies, the hierarchical self-assembly system exhibits morphologies significantly different from those derived from conventional amorphous BCPs in coil model. As the self-assembly morphologies from PS-*b*-P8FMAs of varied $M_n$ but similar block fractions were studied in Chapter 2, the role of block segregation in this hierarchy self-assembly system became unveiled.

However, another self-assembly driving force from side-chain crystalline LC ordering is not systematically studied. Especially, the confinement effects from liquid crystalline ordering on the block segregation-induced periodic nanostructure is of paramount importance to the understanding on the hierarchy self-assembly. In specific, the previous morphology study in Chapter 2 reveals anisotropic characteristics of SF7 sample with low $M_n$ following thermal annealing, which is possibly caused by the confinement effects from liquid crystalline side chain ordering. The confinement effects are considered becoming amplified as the scales of the two types of periodicity become comparable. In previous studies, the cylinder of SF7

sample in unique packing, which is different from commonly seen isotropic hexagonally packing array, is usually associated with BCP domain interface of non-constant mean-curvature. For instance, the observation of rectangular-shaped cylinder in rectangular array[9] and similar morphology by using self-consistent field theory (SCFT)[10] were reported. The anisotropic packing of cylinder with stability in thermodynamics was more predicted in rod-coil[11] or semiflexible-flexible[12] [13] BCPs by using SCFT model. Remarkably, in diblock copolymer melt model, an elliptical domain in distorted hexagonally packing array is found more energy-favored stable than circular domain in thin film. Besides, the ellipse's eccentricity is dependent on the minority block fraction.

Therefore, to better investigate the observed asymmetric array reasonably attributed to LC side chain ordering, the effects of the fluorinated side chain length on the self-assembly bulky morphologies were studied by using the same model precursor PS-*b*-PGMAs attached by varied CF3, C4F9, C6F13 and C8F17-containing side chains, as the side chain liquid crystal properties are highly dependent on the lengths of side chain.

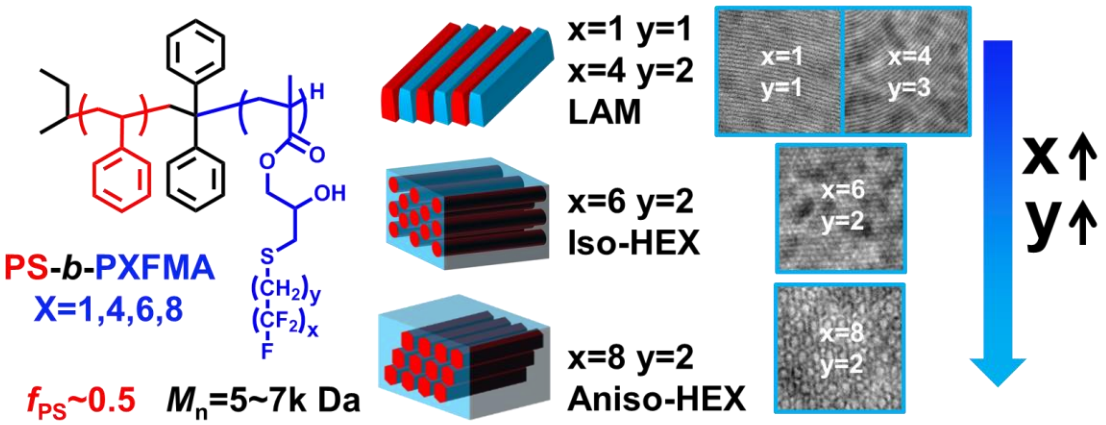


**Scheme 3-1.** Schematic of nearly symmetric diblock copolymers self-assembly morphologies with semi-fluorinated side chains of varied lengths.

## 3-2. Experimental Section

### 3-2-1. Materials

Lithium chloride (LiCl) was obtained from Kanto Chemical Co. Inc. and baked under a reduced pressure at 200 °C overnight before use. Styrene was washed by 0.1M sodium hydroxide (NaOH) aqueous solution for three times and dried by magnesium sulfide ($MgSO_4$), afterwards, calcium hydride ($CaH_2$) was added and stirred overnight before distillation. After the distillation, *di-n-butyl*magnesium ($MgBu_2$) was added under Ar protection to remove the residual water in styrene. Trap to trap process was further carried out to degas using liquid nitrogen as the freezing source. Similarly, glycidyl methacrylate (GMA) was distilled, dehydrated by $CaH_2$ and subsequently degassed under Ar. Diphenylethene (DPE) was distilled, dehydrated by *n-butyl* lithium and subsequently degassed under Ar. 3,3,4,4,5,5,6,6,6-Nonafluoro-1-hexanethiol was synthesized from 1,1,1,2,2,3,3,4,4-nonafluoro-6-iodohexane, which was purchased from Sigma-Aldrich. The synthetic approach was carried out following the previous literature[14]. The $^1$H NMR spectra of the prepared 3,3,4,4,5,5,6,6,6-nonafluoro-1-hexanethiol was presented in the following sections.

All other materials were reagent grade, purchased from Kanto Chemical Co. Inc., Tokyo Chemical Industry, FUJIFILM Wako Pure Chemical Corporation, and Sigma-Aldrich, and used as received. The detailed synthetic procedures of the homopolymers and the random copolymers are described in the later parts.

### 3-2-2. Methods

$^1$H NMR spectra were recorded with a JEOL JNM-ECS400 (400 MHz) instrument using chloroform-d as the solvent. SEC (size exclusion chromatography) analysis was performed on a Shodex GPC-101 instrument, which was equipped with columns of Shodex LF804. The number average molecular weights ($M_n$) and molecular weight distributions ($M_w/M_n$) were determined by SEC at a flow rate of 1.0 ml/min at 40 °C and calibrated with polystyrene. Thermal behaviors of polymer were estimated from a Seiko DSC 7020 differential scanning calorimeter (DSC) at a heating rate of 10 °C /min under a nitrogen flow. The transition temperature values were determined from the second heating and cooling scan. The scanning temperature range was set from 25 °C to 250 °C, and the second scanning curve was used for analysis. Microscopic observation of thermal events was also conducted using an Olympus BH-2 polarized optical microscope equipped with a Mettler FP82HT hot-stage system. Small angle X-ray scattering (SAXS) measurements were carried out using synchrotron radiation facility at BL40B2 Spring-8 with a sample-to-detector of 2.0 meters and Bruker SAXS NanoSTAR (Output:50kV, 50mA) instrument. After monochromatic processing by a Göbel

mirror, a concentrated CuKα radiation (wavelength:1.5416Å) was applied to the sample. The scatted X-ray was collected by a 2D-PSPC detector to determine the morphologies in bulk sample. Wide-angle X-ray scattering (WAXS) patterns were measured by a Bruker NanoSTAR-U instrument equipped with imaging plate (IP) at a distance of 210 mm from the sample using CuKα radiation (wavelength:1.5416Å). The WAXS pattern recorded on the IP was read and analyzed by a Rigaku automatic X-ray imaging system (R-AXIS) DS3C. Bright-field transmission electron microscope (TEM) images of the sample structure were also obtained using a Hitachi H7650 Zero A under a 100 kV accelerating voltage. Bulk samples were prepared for TEM analysis by first being pasted onto epoxy resin for handling and then microtomed (Reichert-Jung Ultracut E) by a DiATOME diamond knife at room temperature to a preset thickness of 70 nm. The sections produced were then placed onto TEM grids and stained by ruthenium oxide for observation. Contact angle measurements were performed using a Kyowa DM-501YH, water, and diiodomethane.

### 3-2-3. Synthesis of ,3,4,4,5,5,6,6,6-nonafluoro-1-hexanethiol

A mixture of 1.87 g. (5.0 mmol) of 1,1,1,2,2,3,3,4,4-nonafluoro-6-iodohexane, 0.41 g. (5.5 mmol) of thiourea, and 3 ml ethanol are vigorously stirred and refluxed for 3 hours. Then ethanol is fully evaporated and white solid is obtained. A solution of 0.20 g (5.0 mmol) of sodium hydroxide in 2 ml of water is added, and the mixture is refluxed for another 2 hours under Ar protection. During this period the prepared thiols are continuously separated from

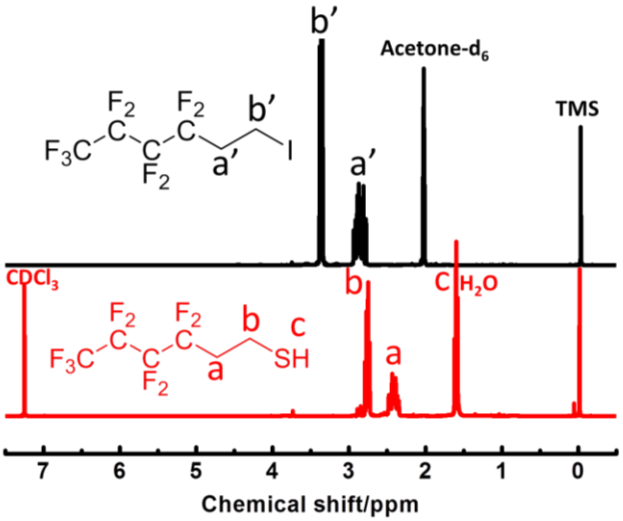


**Figure 3-1**. 1H NMR spectra of 1,1,1,2,2,3,3,4,4-nonafluoro-6-iodohexane (black) in acetone-$d_6$ and the synthesized 3,3,4,4,5,5,6,6,6-nonafluoro-1-hexanethiol (red) in chloroform-*d*.

aqueous solution and precipitated at the bottom of flask. And the aqueous layer is neutralized

with dilute sulfuric acid and then extracted with 5 ml of ethyl ether for twice. The extract is dried over anhydrous sodium sulfate and the residual oil was distilled to yield a colorless liquid (80% yield).

$^1$H NMR (400 MHz, chloroform-*d*, δ, ppm): 1.60 (t, -SH), 2.41 (m, -$CF_2$-$CH_2$-), 2.76 (q, SH-$CH_2$-).

### 3-2-4. Synthesis of homopolymer

**Synthesis of homo-PGMA by living anionic polymerization**

The synthesis of PGMA was performed under the same condition for the synthesis of PS-*b*-PGMA, except a higher polymerization temperature at -40 ℃. The $M_n$ and $Đ$ of the product tested by SEC were 1700 g mol$^{-1}$ and 1.18, respectively.

$^1$H NMR (400 MHz, chloroform-*d*, δ, ppm): 0.87 (s, α-$CH_3$), 1.08 (s, α-$CH_3$), 1.89 (br, backbone, -$CH_2$-$C(CH_3)$-), 2.63 (s, -$CH_2$-$CH(CH_2)$-O-), 2.83 (s, -$CH_2$-$CH(CH_2)$-O-), 3.21 (s, -$CH_2$-$CH(CH_2)$-O-), 3.80 (s, -(C=O)O-$CH_2$-), 4.28 (s, -(C=O)O-$CH_2$-), 7.15-7.20 (m, aromatic, DPE).

**Synthesis of homo-PXFMA through the post-functionalization of PGMA**

The post-functionalizations of PGMA were also performed under the same condition for the synthesis of PS-*b*-PXFMA. Lower loading of thiols (1.2~1.3 mole equiv. to PGMA repeating units) were added because of the difficulty on purification of excessive thiols in precipitation process. Homo-P8FMA and homo-P6FMA were precipitated in methanol for three times, while homo-P4FMA was precipitated in mixture of methanol and water (*v:v*=1:2) for three times. The product was dried under a reduced pressure at room temperature overnight to yield a white powder (59~33% yield). Homo-P8FMA only reveals the proton signals from the backbone of polymer because of the poor solubility of bulky semi-fluorinated side chain in common organic solvent. The properties of homo-P1FMA were previously reported by our group[2].

**Characterization of homo-P4FMA.** The $M_n$ and $Đ$ of the product measured by SEC were 4600 g mol$^{-1}$ and 1.08, respectively. $^1$H NMR (400 MHz, homo-P4FMA, δ, ppm): 0.96 (s, α-$CH_3$, P4FMA), 1.09 (s, α-$CH_3$, P4FMA), 1.86 (br, backbone, -$CH_2$-$C(CH_3)$-), 2.30-2.50 (t, -$CH_2$-$CF_2$-, P4FMA), 2.60-2.76 (t, -S-$CH_2$-$CH_2$-$CF_2$-, P4FMA), 2.76-2.87 (d, -CH(OH)-$CH_2$-S-, P4FMA), 3.82-4.17 (d, -(C=O)O-$CH_2$-, P4FMA) (m, -CH(OH)-, P4FMA),7.06-7.30 (m, aromatic, DPE).

**Characterization of homo-P6FMA.** The $M_n$ and $Đ$ of the product measured by SEC were 5800 g mol$^{-1}$ and 1.12, respectively. $^1$H NMR (400 MHz, homo-P6FMA, δ, ppm): 0.96 (s,

α-$CH_3$, P6FMA), 1.09 (s, α-$CH_3$, P6FMA), 1.86 (br, backbone, -$CH_2$-C($CH_3$)-), 2.30-2.50 (t, -$CH_2$-$CF_2$-, P6FMA), 2.60-2.76 (t, -S-$CH_2$-$CH_2$-$CF_2$-, P6FMA), 2.76-2.87 (d, -CH(OH)-$CH_2$-S-, P6FMA), 3.82-4.17 (d, -(C=O)O-$CH_2$-, P6FMA) (m, -CH(OH)-, P6FMA),7.06-7.30 (m, aromatic, DPE).

**Characterization of homo-P8FMA.** The $M_n$ and $Đ$ of the product measured by SEC were 7 700 g $mol^{-1}$ and 1.03, respectively. $^1$H NMR (400 MHz, homo-P8FMA, δ, ppm): 0.87 (s, α-$CH_3$, P8FMA), 1.25 (s, α-$CH_3$, P8FMA), 1.56 (br, backbone, -$CH_2$-C($CH_3$)-, P8FMA), 7.06-7.27 (m, aromatic, DPE).

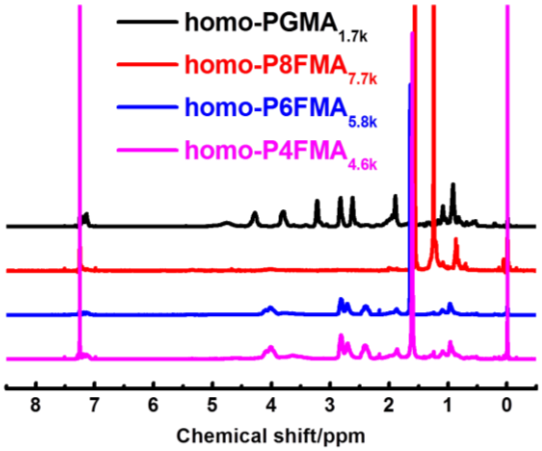


**Figure 3-2**. $^1$H NMR spectra of synthesized homo-PGMA and post-functionalized homo-PXFMA (X=4, 6 and 8) in $CDCl_3$ solvent. The below right number indicates the molecular weight of each homo-polymer.

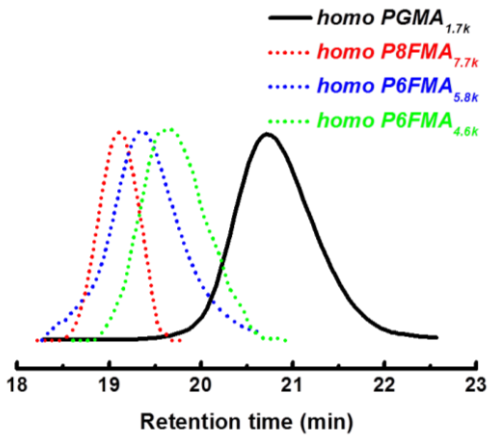


**Figure 3-3**. SEC chromatograms of the precursor homo-PGMA and post-functionalized homo-PXFMA (X=4, 6 and 8) in THF eluent. The below right number indicates the molecular weight of each homo-polymer.

**Table 3-1**. Characteristics of the synthesized homopolymers.

| Homopolymer | $M_n$ [a] (kg mol$^{-1}$) | Estimated $M_n$ [b] (kg mol$^{-1}$) | $Đ$ [a] | $T_g$ (°C) [c] | $T_{iso}$ (°C) [c] |
|---|---|---|---|---|---|
| homo PGMA | 1700 | - | 1.18 | 68.0[d] | - |
| homo P1FMA[d] | 27700[d] | - | 1.19[d] | 37.0[d] | - |
| homo P4FMA | 4600 | 4700 | 1.08 | 60.5 | - |
| homo P6FMA | 5800 | 5700 | 1.12 | 62.7 | 145.8 |
| homo P8FMA | 7700 | 6800 | 1.03 | 116.8 | 78.2 |

[a] Determined by SEC. [b] Estimated from $M_n$ of homo-PGMA and assumption of 100% conversion in thiol-epoxy reaction. [c] Determined by DSC. [d] Referred from our previous paper[2].

### 3-2-5. Synthesis of PS-*b*-PGMA

The synthetic routine to targeted diblock copolymer was classified into two steps, the synthesis of precursor main chain polymer PS-*b*-PGMA via sequential anionic living polymerization and the subsequent post-functionalization for introduction of fluorine-rich side chain.

An example of the anionic polymerization of styrene and GMA is as follows. All anionic polymerization procedures were performed under Ar protection. Here, 30 mL of THF and LiCl (29.7 mg, 0.700 mmol) were transferred to a 50 mL Schlenk flask and then cooled to -78 °C. *Sec-Butyl*lithium (*sec*-BuLi) (in 1.05 M hexane/cyclohexane solution) was added until the color changed to yellow. The Schlenk flask was removed from the cooling bath and kept under room temperature till the solution became colorless. The Schlenk flask was again cooled to -78 °C, and *sec*-BuLi solution in cyclohexane and n-hexane (0.69 mL, 0.700 mmol) was added as initiator. Styrene (1.65 mL, 14.42 mmol) was further added and stirred for 30 min, resulting in bright orange color of solution. DPE (0.39 mL, 2.1 mmol) was added, changing the color to deep red color. After 30 min of stirring, GMA (0.47 mL, 3.52 mmol) was added and stirred for 30 min. The solution became colorless. Finally, 3 mL of methanol (MeOH) (excess amount) purged with Ar and added to the Schlenk flask to yield proton-terminated PS-*b*-PGMA. The polymer was precipitated into MeOH and filtered, and then the product was dried under a reduced pressure at 40 °C overnight to yield PS-*b*-PGMA as a white powder (1.80 g, 90% yield). The $M_n$ and dispersity ($Đ = M_w/M_n$) of the product determined by SEC were 3900 g mol$^{-1}$ and 1.38, respectively.

$^1$H NMR (400 MHz, $CDCl_3$, δ, ppm): 0.98 (s, α-$CH_3$, PGMA), 1.14 (s, α-$CH_3$, PGMA), 1.29-1.80 (br, backbone, -$CH_2$-CH-, PS), 1.84-2.30 (br, backbone, -$CH_2$-CH-, PS, br, backbone, -$CH_2$-C($CH_3$)-, PGMA), 2.70 (s, -$CH_2$-CH($CH_2$)-O-, PGMA), 2.82 (s, -$CH_2$CH($CH_2$)-O-, PGMA), 3.28 (s, -$CH_2$-CH($CH_2$)-O-, PGMA), 3.84 (s, -(C=O)O-$CH_2$-, PGMA), 4.37 (s, -(C=O)O-$CH_2$-, PGMA), 6.39-6.85 (m, o-aromatic, PS) 6.91-7.42 (m, m-, p-aromatic, PS).

**3-2-6. Synthesis of PS-*b*-PXFMA (X=1 or 4 or 6 or 8) through the post-functionalization of PS-*b*-PGMA with 2,2,2-Trifluoroethanethiol or 3,3,4,4,5,5,6,6,6-Nonafluoro-1-hexanethiol or 3,3,4,4,5,5,6,6,7,7,8,8,8-Tridecafluoro-1-octanethiol or 1H,1H,2H,2H-Perfluorodecanethiol**

Thiol-epoxy click reaction was utilized to introduce the semi-fluorinated side chains to the backbone of precursor copolymers PS-*b*-PGMA. The general procedure is as follows regardless of the type of thiols: A 10 ml glass tube was charged with PS-*b*-PGMA and THF (20 mole equiv. to PGMA repeating units) and immersed in an ice-water bath. 1 wt% lithium hydroxide (LiOH) aqueous solution (LiOH 0.05 mole equiv. to PGMA repeating units) and thiol (1.3~1.5 mole equiv. to PGMA repeating units) were added to the tube. After stirring for 20 min at room temperature, the tube was transferred to a thermal reactor set to 30 ℃ and stirred for 3 h. The crude solution was precipitated from hexane or methanol or mixture of water and methanol, depending on the $M_n$ of BCP and type of thiol. After filtration, the solid was again dissolved in THF and precipitated and then filtered two more times to remove any residual reagents. The product was dried under a reduced pressure at room temperature overnight to yield a white powder (41% yield).

**Characterization of PS-*b*-P1FMA**

$^1$H NMR (400 MHz, $CDCl_3$, δ, ppm): 0.95 (s, α-$CH_3$, P1FMA), 1.07 (s, α-$CH_3$, P1FMA), 1.22-1.70 (br, backbone, -$CH_2$-CH-, PS), 1.72-2.23 (br, backbone, -$CH_2$-CH-, PS, br, backbone, -$CH_2$-C($CH_3$)-, P1FMA), 2.72-2.90 (m, -CH(OH)-$CH_2$-S-, P1FMA), 3.11-3.31 (q, -S-$CH_2$-$CF_3$, P1FMA), 3.88-4.18 (m, -(C=O)O-$CH_2$-CH(OH)- P1FMA), 6.28-6.73 (m, o-aromatic, PS), 6.86-7.32 (m, m-, p-aromatic, PS).

**Characterization of PS-*b*-P4FMA**

$^1$H NMR (400 MHz, $CDCl_3$, δ, ppm): 0.96 (s, α-$CH_3$, P4FMA), 1.12 (s, α-$CH_3$, P4FMA), 1.20-1.68 (br, backbone, -$CH_2$-CH-, PS), 1.70-2.28 (br, backbone, -$CH_2$-CH-, PS, br, backbone, -$CH_2$-C($CH_3$)-, P4FMA), 2.30-2.50 (t, -$CH_2$-$CF_2$-, P4FMA), 2.60-2.76 (t,

-S-$CH_2$-$CH_2$-$CF_2$-, P4FMA), 2.76-2.87 (d, -CH(OH)-$CH_2$-S-, P4FMA), 3.82-4.17 (d, -(C=O)O-$CH_2$-, P4FMA) (m, -CH(OH)-, P4FMA), 6.28-6.85 (m, o-aromatic, PS), 6.86-7.32 (m, m-, p-aromatic, PS).

**Characterization of PS-*b*-P6FMA**

$^1$H NMR (400 MHz, $CDCl_3$, δ, ppm): 0.98 (s, α-$CH_3$, P6FMA), 1.12 (s, α-$CH_3$, P6FMA), 1.21-1.70 (br, backbone, -$CH_2$-CH-, PS), 1.72-2.25 (br, backbone, -$CH_2$-CH-, PS, br, backbone, -$CH_2$-C($CH_3$)-, P6FMA), 2.29-2.50 (t, -$CH_2$-$CF_2$-, P6FMA), 2.60-2.76 (t, -S-$CH_2$-$CH_2$-$CF_2$-, P6FMA), 2.76-2.87 (d, -CH(OH)-$CH_2$-S-, P6FMA), 3.82-4.17 (d, -(C=O)O-$CH_2$-, P6FMA) (m, -CH(OH)-, P6FMA), 6.28-6.85 (m, o-aromatic, PS), 6.86-7.32 (m, m-, p-aromatic, PS).

**Characterization of PS-*b*-P8FMA**

$^1$H NMR (400 MHz, $CDCl_3$, δ, ppm): 0.98 (s, α-$CH_3$, P8FMA), 1.12 (s, α-$CH_3$, P8FMA), 1.21-1.70 (br, backbone, -$CH_2$-CH-, PS), 1.72-2.25 (br, backbone, -$CH_2$-CH-, PS, br, backbone, -$CH_2$-C($CH_3$)-, P8FMA), 2.29-2.50 (t, -$CH_2$-$CF_2$-, P8FMA), 2.60-2.76 (t, -S-$CH_2$-$CH_2$-$CF_2$-, P8FMA), 2.76-2.87 (d, -CH(OH)-$CH_2$-S-, P8FMA), 3.82-4.17 (d, -(C=O)O-$CH_2$-, P8FMA) (m, -CH(OH)-, P8FMA), 6.28-6.85 (m, o-aromatic, PS), 6.86-7.32 (m, m-, p-aromatic, PS).

### 3-2-7. Estimating the surface free energies of the homopolymers

The surface free energies (SFEs) of the homopolymers were calculated by measuring the water and diiodomethane contact angles (C.A.) of the homopolymer thin films. The thin films were prepared by spin-coating a 1-2 wt % THF or toluene solution on bare silicon wafers at 3000 rpm for 30 s to obtain thin films with thicknesses of 40-50 nm. These thin films were annealed at 120 °C for 10 min before the C.A. measurements.

### 3-2-8. Detailed information about the estimation of $\chi_{eff}$

Molten BCP samples were placed in 0.01 mm thick glass tubes and the SAXS profiles were collected at each temperature in 5 or 10 °C decrement in cooling cycles, at which the temperature was maintained for 30 min prior to the measurements to reach a thermally equilibrated state. The scattering function $I(q)$ from the disordered melt of the BCPs with a dispersity in the molecular weight and asymmetry in the segmental volume was summarized below, where $A_0$ is a fitting constant, $S(q)$ and $W(q)$ together are correlation functions of the BCP, $g(q)$ is a modified Debye function and $y(q)$ is a dimensionless wave vector, $r_c$ is the molar volume normalized over the degree of polymerization of the BCP, $f_X$ is volume fraction

of $X$ calculated using the bulk densities for each block (1.05 g cm$^{-3}$ for PS, 1.45 g cm$^{-3}$ for P4FMA, 1.66 g cm$^{-3}$ for P6FMA and 1.73 g cm$^{-3}$ for P8FMA, estimated from a knowledge of the structural formula of the material[15]), $v_X$ is the molar volume of $X$. $N_X$ is the degree of polymerization normalized over a common reference volume ($v_0$ = 118 Å$^3$) for $X$, $FW$ is the formula weight of $X$, $N_A$ is Avogadro's constant, and $b_X$ is the segmental length of $X$. Here the dispersities for each homopolymer segment ($D_X$) are assumed equal and were estimated from the $M_w/M_n$ of the BCP and weight fraction of $X$ ($w_X$). Four parameters, including $b_X$ for both polymers, $A_0$ and $\chi_{eff}$, were optimized in a least-squares fit to the SAXS profiles at a certain temperature. The calculated parameters for each sample were summarized in Table 3-4. The estimation of $\chi_{eff}$ for each sample was done at temperatures higher than the order-to-disorder transition ($T_{ODT}$).

$$I(q) = \frac{A_0}{\frac{S(q)}{W(q)} - 2\chi}$$

$$S(q) = \langle S_{PS,PS} \rangle + 2\langle S_{PS,Y} \rangle + \langle S_{Y,Y} \rangle$$

$$W(q) = \langle S_{PS,PS} \rangle \cdot \langle S_{Y,Y} \rangle - \langle S_{PS,Y} \rangle^2$$

$$\langle S_{X,X}(q) \rangle = r_c {f_X}^2 {g^{(2)}}_X(q) \quad \langle S_{PS,Y}(q) \rangle = r_c f_{PS} f_Y {g^{(1)}}_{PS}(q) {g^{(1)}}_Y(q)$$

$$r_c = \frac{(v_{PS}N_{PS} + v_Y N_Y)}{(v_{PS} \cdot v_Y)^{1/2}} \quad v_X = \frac{FW_X}{\rho_X N_A} \quad N_X = \frac{v_X M_{n,X}}{v_0 FW_X}$$

$${g^{(1)}}_X(q) = \frac{1}{y_X(q)} \cdot \left\{1 - [y_X(q) \cdot (D_X - 1) + 1]^{-(D_X - 1)^{-1}}\right\}$$

$${g^{(2)}}_X(q) = \frac{2}{y_X(q)^2} \cdot \left\{-1 + y_X(q) + [y_X(q) \cdot (D_X - 1) + 1]^{-(D_X - 1)^{-1}}\right\}$$

$$y_X(q) = \frac{N_X {b_X}^2}{6} q^2 \quad D \equiv D_{PS} = D_Y = \frac{M_w/M_n - 1}{{w_{PS}}^2 + {w_Y}^2} + 1$$

$X$ = PS or $Y$ ($Y$ = PXFMA X=4, 6 and 8)

### 3-2-9. Bulk sample preparation

The bulk samples used to investigate the bulk morphologies and domain spacings ($d$-spacing) of the microphase-separated structures were prepared by slowly evaporating a dilute BCP

THF solution filtered through a 0.25 μm pore size PTFE membrane syringe filter at 30 ℃. The as-prepared samples were dried under a reduced pressure before annealing at 150 ℃ for 24 h.

### 3-3. Results and Discussion

#### 3-3-1. Synthesis and characterization of the homopolymers

The homo-polymers with fluorinated side chains of various length were firstly synthesized using the same precursor homo-polymer PGMA and corresponding characteristics were investigated. The precursor homo-polymer PGMA was prepared via living anionic polymerization of GMA monomer using *sec*-BuLi as initiator in THF under -40 ℃. The $M_n$ of the synthesized PGMA was intentionally kept low because of the poor solubility of the post-functionalized homo-polymers especially with the relatively long side chains. In the thiol-epoxy reaction, PGMA was mixed with approximately 1.5 times of excessive thiols in THF solution loaded with catalytic amount of LiOH at 30 ℃. LiOH is considered as the optimized catalyst as quantitative conversions are obtained at a catalyst loading over a few

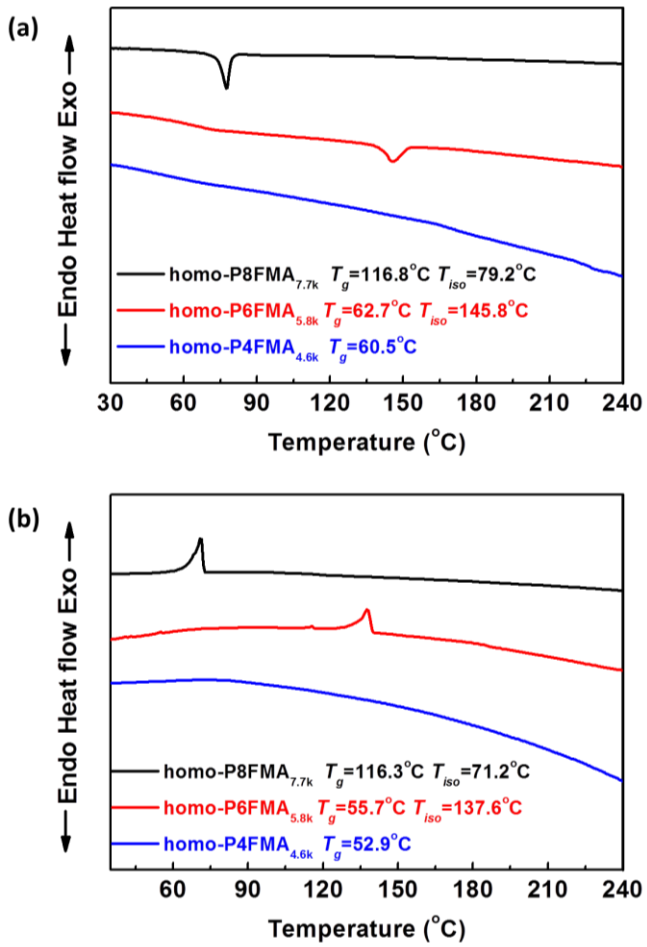


**Figure 3-4**. DSC curves of the synthesized homo-PXFMA (X=4, 6 and 8) at (a) a heating and a cooling rate of 10 ℃/min under nitrogen atmosphere, respectively.

hours reaction time under mild reaction temperatures. The synthesized homo-polymers, including homo-P4FMA, homo-P6FMA and homo-P8FMA were characterized by NMR, SEC, DSC and WAXD (Figure 3-2 to Figure 3-5) and summarized (Table 3-1). The properties of homo-P1FMA were listed in our previously published paper[2]. In NMR spectra, homo-P8FMA only reveals the characteristic proton signals from polymer backbone because of the bulky C8F17 side chain of high rigidity. The solubility of homopolymer in THF or chloroform was significantly improved as the length of introduced side chain was reduced. Except C8F17-containing homo-polymer, other homo-polymers reveal the characteristic proton signals from various side chains and the epoxy unit in precursor PGMA becomes disappeared, indicating the nearly 100% introduction rate of side chain. In SEC results, a significant shift to higher $M_n$ was observed after thiol-epoxy reaction and the measured $M_n$ of homo-polymers were in good agreement with the $M_n$ estimated from precursor PGMA, indicating the complete conversion in chemical modification. Additionally, the thermal analysis reveals an increased $T_g$ of homo-polymer with elongated side chain, which is highly correlated with the reduced mobility of elongated semi-fluorinated side chain. More importantly, significant transitions from LC to isotropic phase were detected in C6F13 and C8F17-containing homo-polymers. In contrast, CF3 and C4F9-containing homo-polymers merely reveal a glass transition within the scanning temperature range.

The liquid crystalline (LC) structures of C6F13 and C8F17-containing homo-polymers in bulk were further characterized by X-ray. The LC lamellar structure of 3.2 nm and 3.6 nm periodicity was observed in C6F13 and C8F17-containing homo-polymers, respectively. C8F17-containing homo-polymer reveals a higher periodicity evidenced by more refined diffraction peaks. According to the previous study on the relationship between LC phase and number of fluorocarbon in side chain[16], smectic A and higher-ordered smectic B LC phase was assigned to C6F13 and C8F17-containing homo-polymer, respectively. The *S-cis* conformation of semi-fluorinated side chain was also reconstructed using MM2 energy-minimization based on Chem 3D 16.0 (Figure 3-6). The estimated distance in model compound from backbone carbon atom to end carbon atom of -CF3 is 1.5 nm (C6F13-containing side chain) and 1.8 nm (C8F17-containing side chain), respectively, which are in good agreements with the half LC periodic length estimated from WAXD. Based on the molecular simulation results, a single LC periodic length is composed of a pair of mesogens with end-to-end stereo-regularity.

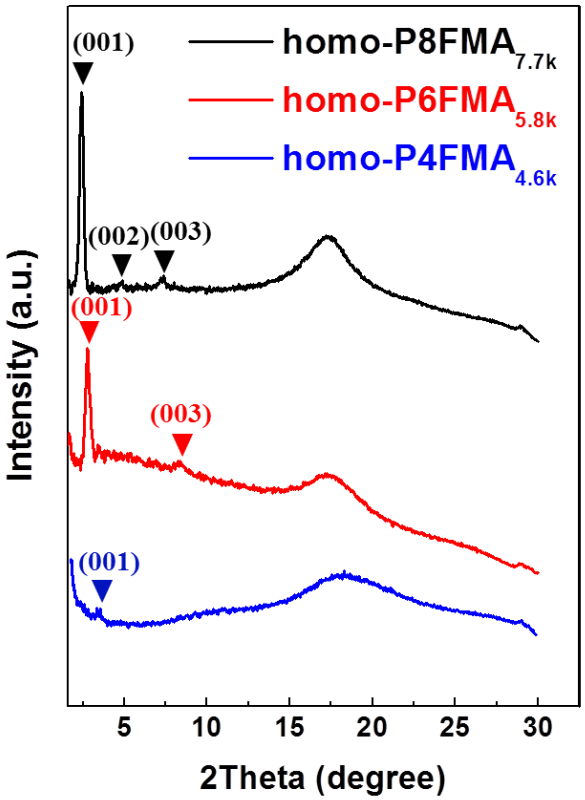


**Figure 3-5**. WAXD profiles of the homo-PXFMA (X=4, 6 or 8) following thermal annealing.

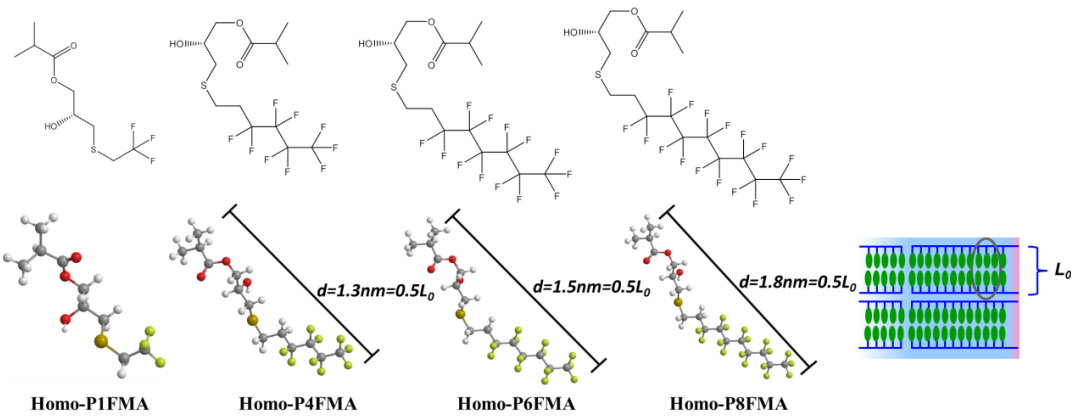


**Figure 3-6**. The optimized conformations of model compounds with various side chains using MM2 energy-minimization based on Chem 3D 16.0. The below right scheme represents the LC lamellar structure consisted of a pair of mesogens with end-to-end stereo-regularity.

The surface free energies (SFEs) of PXFMA with various semi-fluorinated side chain length, estimated via the water and diiodomethane contact angle measurements based on the Owens-Wendt method was 33.3[2], 25.7, 23.1 and 21.6 mJ $m^{-2}$, respectively (Table 3-2). SFE of PS was measured to be 40.7 mJ $m^{-2}$ [17]. Comparatively, the SFE of poly(2,2,2-trifluoroethyl methacrylate) (PTFEMA) was measured to be 25.1 mJ $m^{-2}$ using the same method. For CF3-containing side chain, the hydrophobicity of CF3 and the hydrophilicity of hydroxyl group will be cancelled off with each other. Therefore, a balance between SFEs of PS and CF3-containing P1FMA block was achieved for perpendicular orientation on BCP domain in thin film. However, the introduction of the elongated semi-fluorinated side chain contributed more to the hydrophobicity of PXFMA block and a gradually decreasing SFE value was accompanied.

**Table 3-2**. Contact angles and surface free energies (SFEs) of homopolymers.

| Homopolymer | C.A.($H_2O$)[a] ($^o$) | C.A.($CH_2I_2$)[a] ($^o$) | SFE[b] (mJ $m^{-2}$) |
|---|---|---|---|
| P4FMA | 82.1±1.5 | 75.5±1.6 | 25.7 |
| P6FMA | 86.3±1.3 | 77.8±1.9 | 23.1 |
| P8FMA | 89.0±1.1 | 80.5±1.5 | 21.6 |
| PS[c] | 90.5±0.8 | -[d] | -[d] |

[a] Average values of measurements taken at 5 positions. [b] Calculated by the Owens-Wendt method. [c] The C.A. measurement for PS used a homopolymer with $M_n$=34.6 kg $mol^{-1}$ and $Đ$=1.09, prepared through anionic polymerization. [d] The SFE of PS could not be obtained as PS was partially soluble in diiodomethane.

### 3-3-2. Synthesis and characterization of the BCPs

PS-*b*-PGMA precursor polymer (SG4) was successfully synthesized via the sequential anionic polymerization (Scheme 3-2). Based on NMR and SEC analyses, the synthesized BCPs revealed a molecular weight of 3.9 kg $mol^{-1}$ and a narrow dispersity of 1.38.

Semi-fluorinated thiols of various F numbers were then introduced to the precursor PS-*b*-PGMA in THF solution with LiOH as the catalyst at 30 °C for 3 h reaction. The $M_n$ of the BCPs were increased in accordance with the molecular weight of introduced thiol, while dispersities remained low (Table 3-3 and Figure 3-8) Besides, the characteristic $^1$H NMR signals corresponding to the glycidyl moieties in PS-*b*-PGMA (a, a', b, c, and c' at 2.70, 2.82, 3.28, 3.84, and 4.37 ppm, respectively) (Figure 3-7(a) ) had disappeared and the signals

attributed to the introduced side chains were observed, indicating the complete conversion of side chain functionalities in all chemical modifications. (Figure 3-7(b) )

In thermal analysis (Figure 3-9), only S6F and S8F with sufficient long semi-fluorinated side chain reveal a transition from LC ordered phase to isotropic phase. Besides, the $T_g$ mainly attributed to PS segments almost remained constant because of the same PS-*b*-PGMA precursor polymer used in the study. The observation results of BCPs are in good agreement with those revealed in homo-polymer studies.

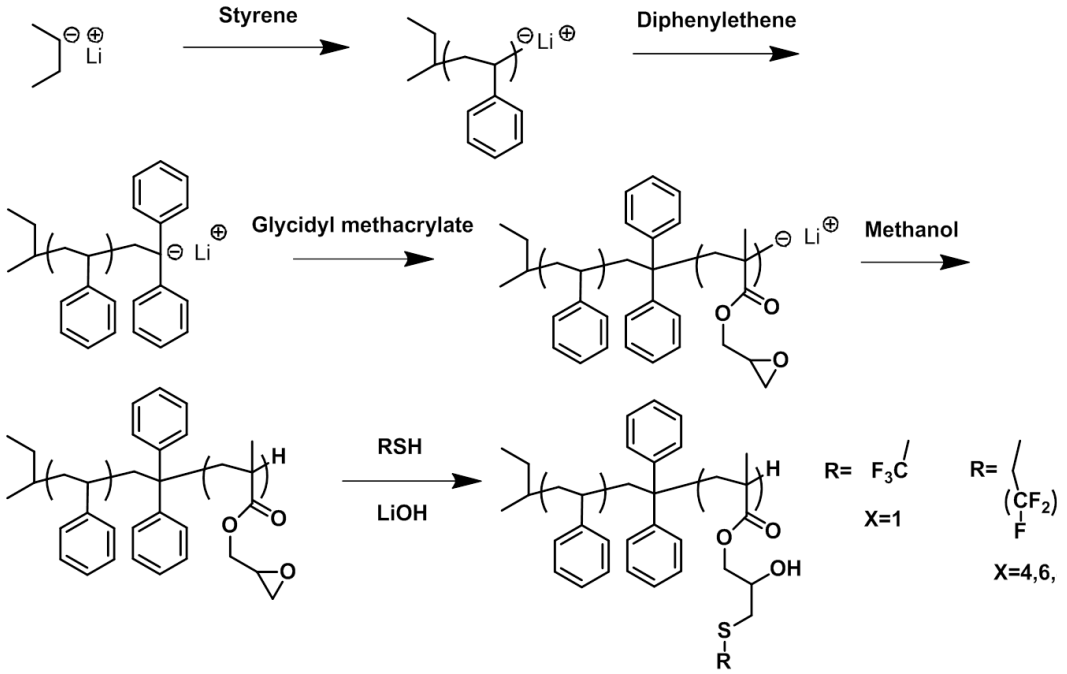


**Scheme 3-2.** Synthetic scheme of PS-*b*-PGMA precursor via sequential living anionic polymerization of styrene and glycidyl methacrylate and post-functionalization with a variety of semi-fluorinated thiols.

**Table 3-3**. Characterization data of the synthesized BCPs.

| BCP | Label[a] | $M_n$[b] (kg mol$^{-1}$) | $Đ$ | $w_{PS}$[c] | $f_{PS}$[c] | $d_{spacing}$[d] (nm) | LC periodicity[e] (nm) | Morphology[f] |
|---|---|---|---|---|---|---|---|---|
| PS-*b*-PGMA | SG4 | 3.9 | 1.38 | 0.73 | 0.68 | 8.9 | - | Disorder |
| PS-*b*-P1FMA | S1F | 5.2 | 1.25 | 0.60 | 0.67 | 9.6 | - | LAM |
| PS-*b*-P4FMA | S4F | 6.4 | 1.21 | 0.48 | 0.56 | 12.1 | (2.6) | LAM |
| PS-*b*-P6FMA | S6F | 6.6 | 1.19 | 0.42 | 0.54 | 11.6 | 3.2 | Iso HCP |
| PS-*b*-P8FMA | S8F | 7.5 | 1.18 | 0.38 | 0.50 | 11.5 | 3.6 | Aniso HCP |

[a] The labels SG and S(X)F refer to PS-*b*-PGMA and PS-*b*-PXFMA, respectively, while the number to the right refers to the number-average molecular weight ($M_n$) of the polymer. [b] $M_n$ and dispersities ($Đ$) were obtained by SEC using THF as the eluent based on PS standards. [c] PS weight fractions ($w_{PS}$) of PS-*b*-PGMA were calculated via $^1$H NMR and PS weight ($w_{PS}$) and volume fractions ($f_{PS}$) of PS-*b*-PXFMA were further estimated based on 100% introduction rate of side chain using bulk densities for each block (1.05 g cm$^{-3}$ for PS, 0.805 g cm$^{-3}$ for PGMA, 1.43 g cm$^{-3}$ for P1FMA, 1.45 g cm$^{-3}$ for P4FMA, 1.66 g cm$^{-3}$ for P6FMA and 1.73 g cm$^{-3}$ for P8FMA) [d] The domain spacings (d-spacing) were estimated from the position of first-order scattering peak in the SAXS profile upon thermal annealing at 150 °C for 24h. [e] The periodicity of LC side chain was determined by the position of first-order scattering peak in the WAXD profile of homo-polymer upon thermal annealing at 150 °C for 24h. [f] The morphologies in the bulk were determined by SAXS and TEM.

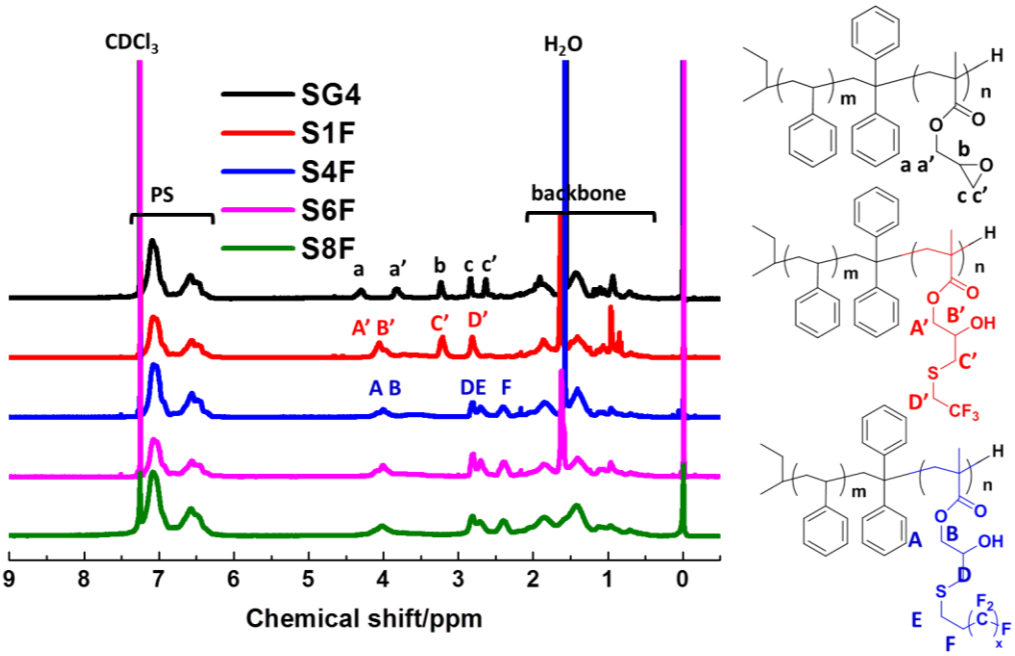


**Figure 3-7**. $^{1}$H NMR spectra of PS-*b*-PGMA (SG4) and chemically modified PS-*b*-PXFMA(S1F, S4F, S6F and S8F).

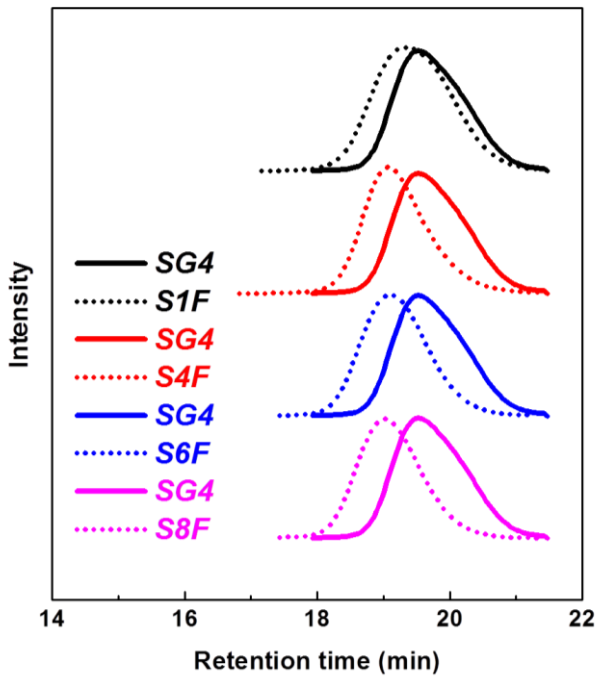


**Figure 3-8.** SEC chromatography of precursor PS-*b*-PGMA (SG4) and corresponding PS-*b*-PXFMA (SXF, X=1,4,6 and 8) after post functionalization.

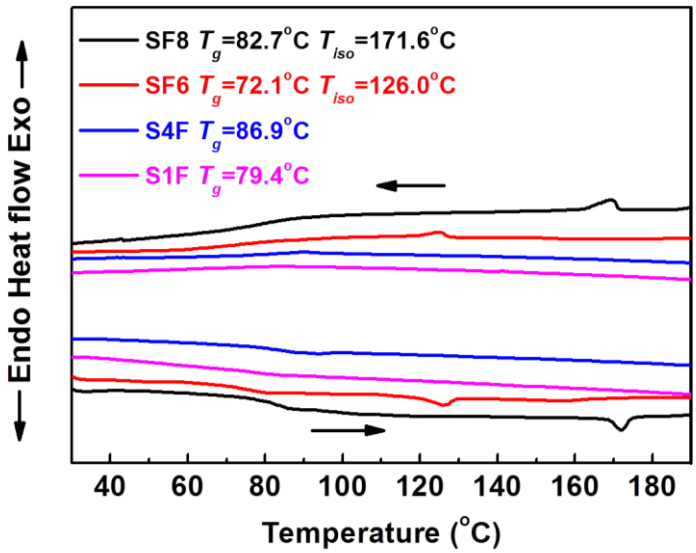


**Figure 3-9**. DSC curves of the studied PS-*b*-PXFMA (SXF, X=1,4,6 and 8) at a heating rate of 10 ℃/min under nitrogen atmosphere in heating and cooling cycles. The noted transition temperatures are estimated from the heating cycles.

### 3-3-3. Morphologies in the bulk

The bulk morphologies of the synthesized PS-*b*-PXFMAs were then analyzed via SAXS (synchrotron radiation) (Figure 3-10). and TEM characterizations (Figure 3-11 and Figure 3-12).

The precursor PS-*b*-PGMA (SG4) exhbits a disordered morphology because of the relatively low χ parameter[2]. However, following the chemical modifcation of semi-fluorinated side chain, all PS-*b*-PXFMAs reveal significant self-assembly morphologies, indicating enhanced χ parameters. The $d_{spacing}$ estimated from the position of primary scattering peak in SAXS is narrowly distributed among 9.6-12.1 nm, which are reasonably attributed to the similar $M_n$ and estimated $\chi_{eff}$ of PS-*b*-PXFMAs. However, the observed morpology of PS-*b*-PXFMAs exhibits a transition from lamellar to hexagonally packed cylinderical type as the incorporated side chain becomes longer. The SAXS profiles of amorphous PS-*b*-P1FMA and PS-*b*-P4FMA both suggest *q* ratios of integers, which are representative indicators of formation of lamellar morphology. A lamellar morpholgy of PS-*b*-P1FMA with similar $M_n$ and more symmetric volume fraction ($f_{ps}$=0.62) was also observed in the reported experimentals[2]. Besides, an insignfcant 2.6 nm periodic length was detected by SAXS, which is related to the extremly weak ordering from C4F9 side chain. Accordingly, no signifcant LC phase transition was observed in DSC analysis.

The thresohold of side chain length for exhibiting LC phase is C6F13. Owing to the

formation of side chain LC structure, a hierarchical self-assembly strucuture containing segments segregation and LC ordering begins to emerge. A lamellar structure of 3.2 nm periodic length was indicated by the X-ray analysis on PS-*b*-P6FMA and corresponding homopolymer. DSC results also suggested a transition from the assigned semetic A to isotripic phase at 126 ℃, which is below the annealing temperature of 150 ℃. Therefore, the contribution from side chain LC ordering is partially suppressed during the thermal annealing process. The SAXS characterizaiton revealed characteristic *q* ratios of *1:*√3*:2* in response to symmetric hexagonally packed cylinderical morphology. The significant peak with *q* ratio of √3 indicates the high symmetry of hexagonal array. Besides, the high symmetry of hexagonal array was evidenced by the TEM observation results (Figure 3-11). The observed self-assembly cylinderical morphology based on symmetic volume fraction of diblock copolymer with LC side was also predicted by SCFT theory[6].

As the length of side chain was further increased to C8F17, LC lamellar strucutre of higher periodicity and larger periodic legnth is expected based on the prevous study[16]. The interpaly between the segments segregation and enhanced LC ordering creates a unique asymmetric morphology, which is different from any known morphology reuslting from amorphous BCP. Firstly, SAXS and synchrotron radiation reveal a significant primary scattering peak of high-intenisty in response to 3.6 nm $d_{spacing}$ and its sceondary scattering peak could be even detected using synchrotron radiation. The observation based on BCPs were highly consisent with the lamellar stucutre chararterized in correpoding homopolymer. Combined with the sharper phase-transition peaks of both BCP and homopolymer in DSC compared to those of PS-*b*-P6FMA, semetic B phase with higher periodicity compared to semetic A phase could be assgined to LC ordering of PS-*b*-P8FMA. The higher periodicity of LC structure could also be inferred from the sharper scattering peak attributed to 0.53 nm spacing, which corresponds to the distance between adjacent CF3-end of semi-fluorinated side chain[16 18].

Addtionally the SAXS profiles of amorphous PS-*b*-P1FMA, PS-*b*-P4FMA and liquid crystalline PS-*b*-P6FMA were analyzed using Scatter (Version 2.5, 03/2011) (Figure 3-13). The predicted periodic nano-strucutres estimated from the fitting profiles are highly consistent with the TEM observations (Figure 3-11). PS-*b*-P4FMA reveals a more assymetric lamellar structure in compasion with that of PS-*b*-P1FMA, which is possibly related to the weak ordering of fluorinated side chain. The minor domain of 4.1 nm width is possibly consisted of an adjacent pair of C4F9 side chain with a predicted 2.6 nm length. For PS-*b*-P6FMA with significant LC side chain ordering, hexagonally packed cylinders with 5.4 nm radius are predicted. The volume fraction of cylinder is estimated being 0.56, which is close to the estimated PS volume fraction ($f_{PS}$=0.54) in synthesis characterizaiton. Beisdes, the minmial

spacing between adjacent cylinders is esimtated being 3.0 nm, which is close to the spacing of a pair of C6F13 side chain in head-to-head regularity. Therefore, the self-assembly morpholgy transition is likely caused by the spacing confinments from the enhanced side chain ordering.

As the length of side chain was further increased to C8F17, LC lamellar strucutre of higher periodicity and larger periodic legnth is expected based on the previous study[16]. The interpaly between the segments segregation and enhanced LC ordering creates a unique asymmetric morphology, which is different from any known morphology reuslting from amorphous BCP. Firstly, SAXS reveal a significant primary scattering peak of high-intenisty in response to 3.6 nm $d_{spacing}$ and its sceondary scattering peak at 2$q$ position could be even detected, indicating a well-defined lamellar structutre. This observation on BCPs were also highly consistent with the lamellar stucutre chararterized in correpoding homopolymer. Combined with the observed narrower transition peaks in DSC of both BCP and homopolymer compared to those of PS-*b*-P6FMA, a semetic phase with higher periodicity than that of PS-*b*-P6FMA could be assgined to LC ordering of PS-*b*-P8FMA. The higher periodicity of LC structure could also be inferred from the sharper scattering peak attributed to 0.53 nm spacing, which corresponds to the distance between adjacent CF3-end of semi-fluorinated side chain[16 18].

Besides, the self-assembly structure resulting from block segregation was also revealed by X-ray analysis in combination with TEM. In SAXS characterizations, characteristic $q$ ratios of $1{:}\sqrt{3}{:}2{:}\sqrt{7}{:}\sqrt{12}$ were observed and hexagonall packed cylinderical morhology was thereby assigned. However, in TEM characteization three distinctive phases could be observed: two striation phase with characterisitc 10.9 and 12.7 nm $d_{spacing}$, respectively, and a hexgonally packed array consisted of these two distinctive $d_{spacing}$ (Figure 3-12). In addition, the grain boundaries between those distinctive phases were clearly revealed in TEM images. The inset of TEM image clearly reveals the hexgonally packed array of significant anisotropy in which the elliptical PS domains are surrounded by a lamellar fringe of 3.6 nm periodicity length. The observed 3.6 nm lamellar strucuture in TEM was likely attributed to the semetic strucutre of LC side chain. The fast Fourier transform of this anisotropic array was further given by Image-J (Figure 3-14(a)). Two distinctive $d_{spacing}$ with a $125^{o}$ intersection angle and their secondary singals at $\sqrt{3}{:}2{:}\sqrt{7}$ $q$ positions were successfully assgined. These sginals were further intergrated along the radius to the center and a 1-D integration profile was obtained (Figure 3-14(c)). The peak posititons in the integrated profile could be correlated with those in SAXS profile. And the overlapped signals from two distinctive $d_{spacing}$ possibly lead to the broader scattering peaks of PS-*b*-P8FMA compared to other studied BCPs. A schematic illustration on the hierarchical structure of PS-*b*-P8FMA is further proposed based on the characterization results. The volume fraction of PS domain based on this self-assembly

model ($f_{PS}$=0.46) is highly consistent with the estimated value ($f_{PS}$=0.50) in Table 3-3.

As the length of lamellar fringe is fixed because of side chain LC ordering, the surrounded PS domain has to take the asymmetric shape in accordance with the symmetric volume fraction of block. Therefore, the periodic array of various characteristic lengths is caused by the confined spacing of LC ordering, which is incompatible with the given volume fraction of block.

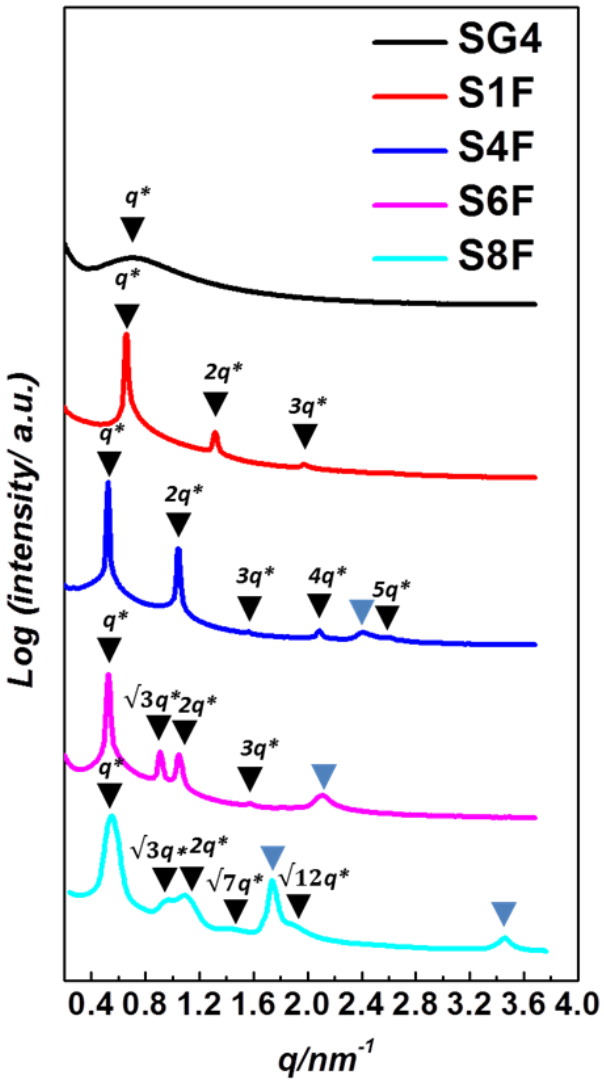


**Figure 3-10.** SAXS profiles of the precursor PS-*b*-PGMA and PS-*b*-PXFMAs (X=1, 4, 6 and 8) bulk samples following thermal annealing. The blue triangle indicates the peak from LC phase of side chain.

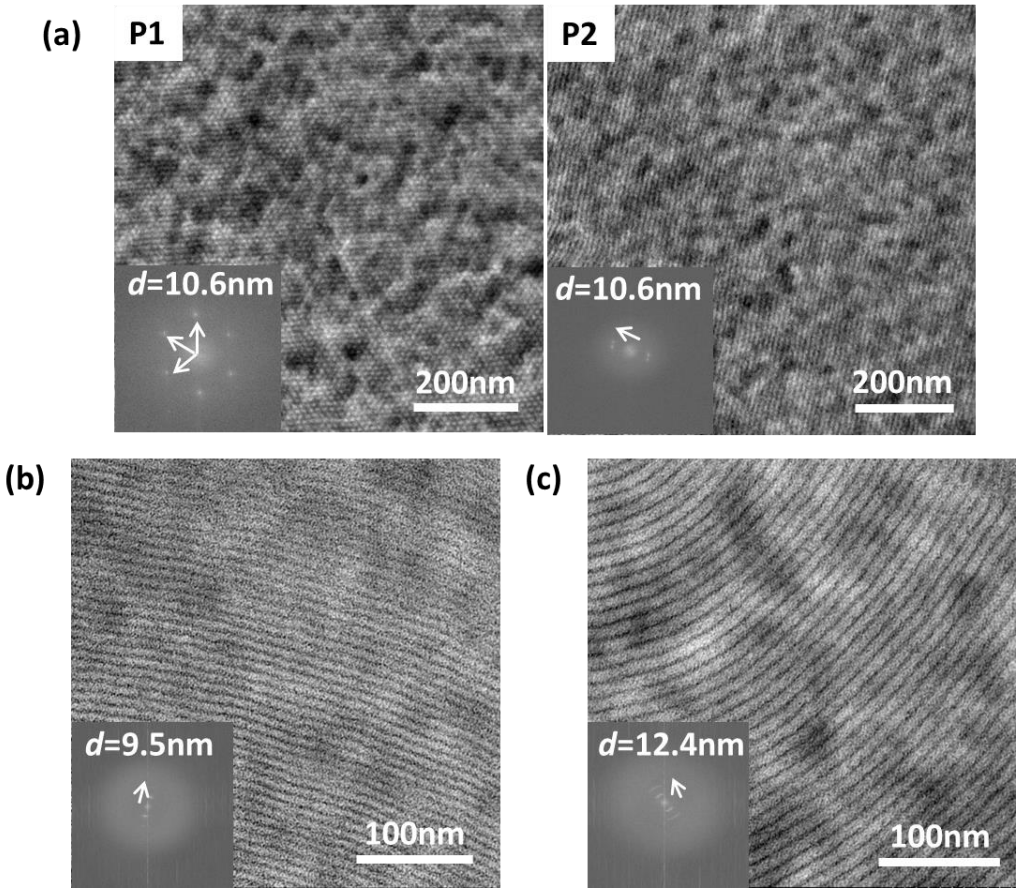


**Figure 3-11.** (a) TEM micrographs showing the regular symmetric hexagonally packed cylindrical morphology of annealed PS-*b*-P6FMA bulk sample. Two phases noted as P1 and P2 are from top and side view of the cylinder structure, respectively. The bottom left inset in TEM images displays the Fourier-transform pattern of the real-space image and in P1 six periodic lengths of 10.6 nm with an averaged $60^{o}$ intersection angle indicating symmetric hexagonal packed array are clearly revealed. (b) TEM micrographs showing the averaged 9.5 nm width lamellar morphology of annealed PS-*b*-P1FMA bulk sample. (c) TEM micrographs showing the averaged 12.4 nm width lamellar morphology of annealed PS-*b*-P4FMA bulk sample. The bright and dark region corresponds to PS and heavily ruthenium tetroxide-stained hydroxyl groups in fluorinated segments, respectively.

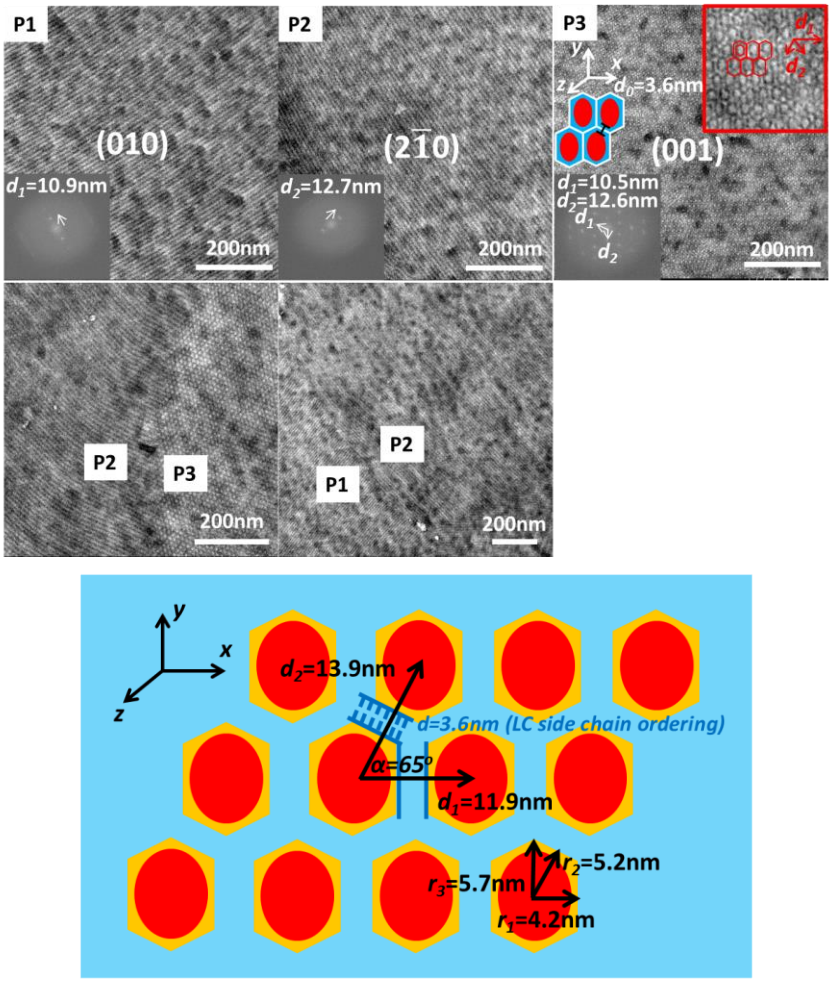


**Figure 3-12.** TEM micrographs showing the asymmetric hexagonally packed ellipsoids with 3.6 nm-wide lamellar fringe of annealed PS-*b*-P8FMA bulk sample. Three phases noted as P1, P2 and P3 are in response to the striations of two distinctive dimensions from (010) and (2$\bar{1}$0) directions in side view and the asymmetrical hexagonally packed array in top view. In TEM images the bright elliptical domain and surrounding lamellar network region corresponds to PS and smectic phase of liquid crystalline side chain block, respectively. The middle dark interface was caused by intensive ruthenium oxide staining on hydroxyl groups in P8FMA backbone, which is consistent with the proposed end-to-end configuration in side chain ordering. The bottom left inset in TEM images displays the Fourier-transform pattern of the real-space image. The array of anisotropic hexagonally packed cylinder was further proposed based on TEM results and the characteristic dimensions were noted as shown in the below scheme. Here the core elliptical PS (red) and adjunct P8FMA backbone (orange) domains are approximated as an integrated PS hexagon because of minor volume fraction of P8FMA backbone. The simplified PS volume fraction calculated from the model ($f_{PS}$=0.46) is consistent with that ($f_{PS}$=0.50) estimated from $M_n$ of block.

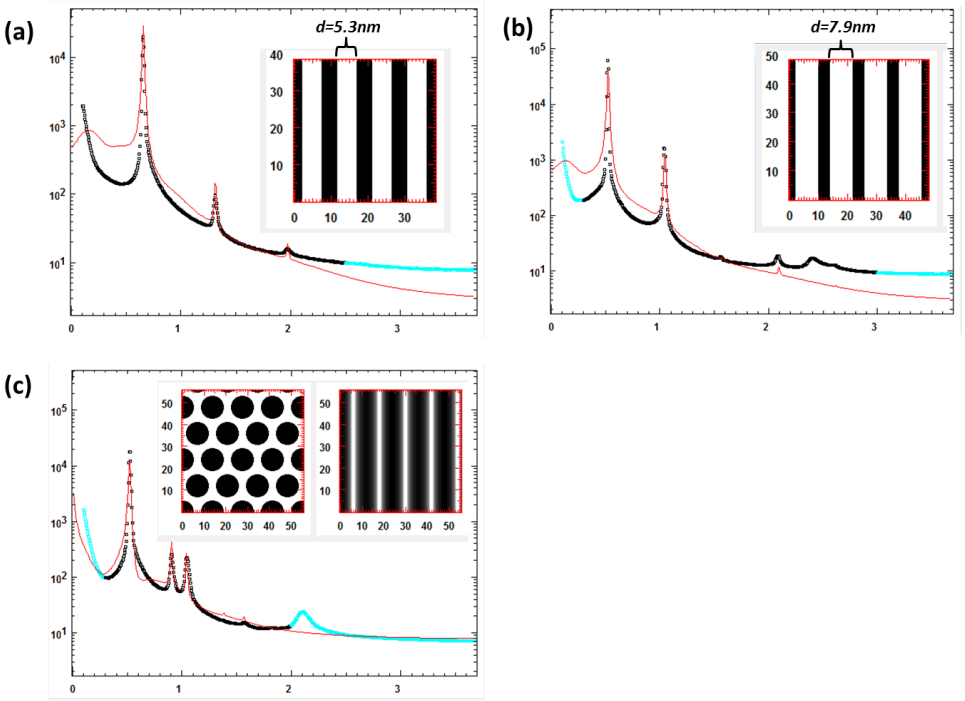


**Figure 3-13.** The experimental SAXS profile (black scatters) and the fitted SAXS profiles (red line) based on the model shown in the insets of (a) PS-*b*-P1FMA, (b) PS-*b*-P4FMA and (c) PS-*b*-P6FMA using Scatter (Version 2.5, 03/2011) 1D (scatter curve). The insert figure in (c) shows the hexagonally packed cylinder in top (left) and side (right) views and the red scales in nanometer units are also given in each inset.

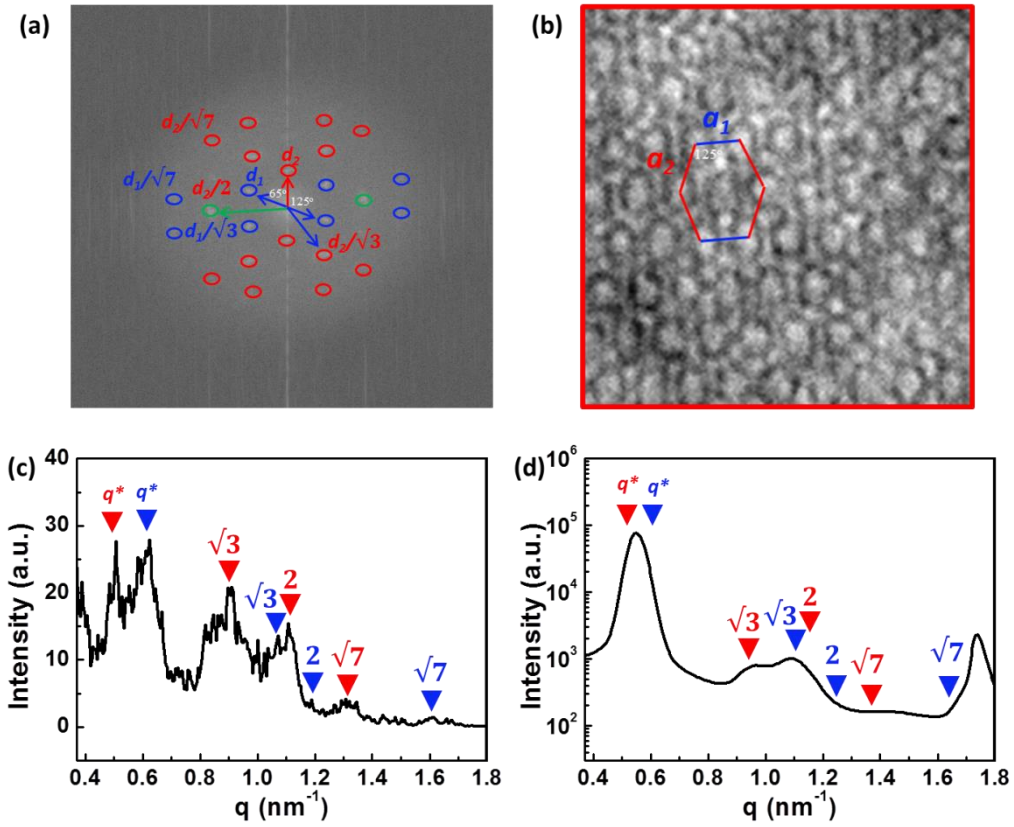


**Figure 3-14**. (a) The fast Fourier transform of P3 phase and the signals in response to $d_1$ and $d_2$, as labeled in blue and red circle, respectively. The green circle indicates the overlapping signals from $\sqrt{3}q$ of $d_1$ and $2q$ of $d_2$. (b) The TEM images showing the dimension $a_1$ and $a_2$ in response to $d_1$ and $d_2$, respectively, in anisotropic hexagonal packing array. (c) The 1-D integration profile of (a) along the radius to the center of image and the signals from two spacings were labeled. (d) The experimental SAXS 1-D integration profile in comparison with (c).

To further investigate the interpaly between block segregation between LC ordering, SAXS was taken at temperatures higher than the observed $T_{iso}$ of PS-*b*-P8FMA (Figure 3-15). As the annealing temperature is cooling from 250 °C to 190 °C, the characteristic secondary peaks at $\sqrt{3}:2:\sqrt{7}$ $q$ positions indicating the hexagonal packing arrray became increased, suggesting an ehanced hexgonally packing ordering. As the temperature was further cooled to 170 °C, the scattering peak attributed to LC side chain ordering at high $q$ region began to appear, which is in good agreement with detected $T_{iso}$ at 171.6 °C in DSC analysis. The ordering of LC side chain was increased with elongated spacing with lowering temperature. Accordingly the domain spacing determined by the position of primary scattering peak became smaller, which is against the change of χ parameter, as the domain spacing is scaled by the higher χ parameter at lower temperature. Besides, at lower temperature the relatively intensities of secondary peaks at $\sqrt{3}:2:\sqrt{7}$ $q$ positions to the primary peak became basically constant, indicating a thermally stable morphology from block segregation under $T_{iso}$. Therefore, a morphology transition from isotropic to anisotropic hexagonal packing array caused by the appearance of LC side chain ordering could be inferred.

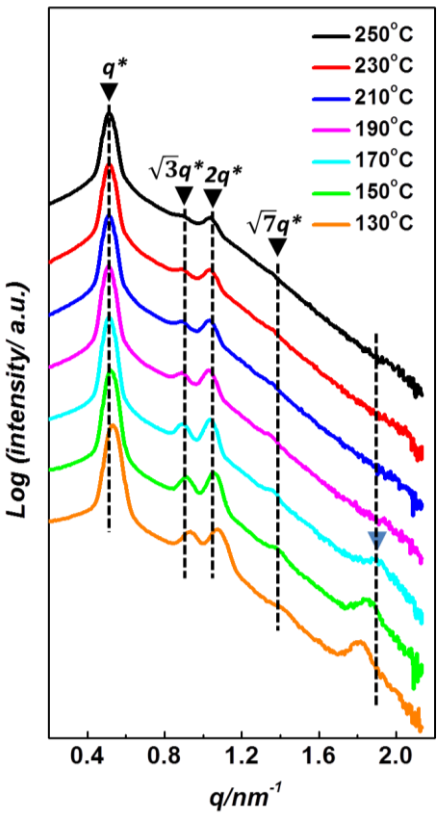


**Figure 3-15**. SAXS profiles of PS-*b*-P8FMA bulk sample taken at varied temperatures in a cooling process. The blue triangle marker indicates the scattering peak from LC side chain ordering.

### 3-3-4. Estimation of $\chi_{eff}$

To quantify the strength of the segregation of PXFMA against PS, random-phase approximation (RPA) method[2] in terms of the effective Flory-Huggins interaction parameter, expressed by $\chi_{eff} = A/T + B$, where $A/T$ is the enthalpic contribution, and $B$ is the entropic contribution. Firstly, temperature-dependent SAXS analyses were conducted on PS-*b*-PXFMA (X=4, 6 or 8), starting in 10 °C decrements (Figure 3-16), which are all above ODTs of BCPs (Figure 3-17). As all measuring temperatures are well-above the LC isotropic transition temperature of C6F13 or C8F17-based side chains, no modification from side chain LC ordering is included into the existed RPA method based on coil-coil BCP model. Herein, the SAXS profiles in the mean-field disordered state were then analyzed based on Leibler's mean-field theory modified to include the effects from the molecular weight dispersity and asymmetry in the segmental volume. Remarkably, as $\chi_{eff}$ is dependent on the reference volume used to calculate $N$, a common reference volume ($v_0$ = 118 Å$^3$) was utilized to compare the $\chi_{eff}$ values with other reported values.

$\chi_{eff}$ of S4F, S6F and S8F was expressed by $\chi_{eff\ PS/P4FMA} = 7.1/T + 0.139$, $\chi_{eff\ PS/P6FMA} = 8.2/T + 0.142$ and $\chi_{eff\ PS/P8FMA} = 21.5/T + 0.172$ (Table 3-5, Table 3-6 and Figure 3-18). $\chi_{eff}$ of S1F was previously reported by our group with an expression of $\chi_{eff\ PS/P1FMA} = 19.4/T + 0.126$ [2]. The difference in the enthalpic contributors may come from the distinctive $M_n$ and dispersities of BCPs of varied chain end effects. Considering the estimated $\chi_{eff}$ of BCPs with varied side chain lengths at 150 °C annealing temperature ($\chi_{eff\ PS/P1FMA}$=0.172, $\chi_{eff\ PS/P4FMA}$=0.155, $\chi_{eff\ PS/P6FMA}$=0.161 and $\chi_{eff\ PS/P8FMA}$=0.223), the driving forces of block segregation are further quantified based on the known $M_n$ of BCPs ($\chi_{eff\ PS/P1FMA}N$=10.5, $\chi_{eff\ PS/P4FMA}N$=11.3, $\chi_{eff\ PS/P6FMA}N$=11.2 and $\chi_{eff\ PS/P8FMA}N$=16.9) The estimated driving forces are of the similar magnitudes, however, in bulk study a morphology transition of BCPs with increased side chain lengths was clearly observed. Therefore, the significant differences on morphologies are reasonably correlated to the LC ordering of introduced side chain.

Besides, all estimated $\chi_{eff}$ of BCPs with semi-fluorinated side chains are several times higher than that of commonly used poly(styrene-*b*-methyl methacrylate) (PS-*b*-PMMA). For instance, $\chi_{eff}$ value of PS-*b*-PMMA at 25 °C was measured being 0.04[19], which was barely 1/6 of $\chi_{eff\ PS/P8FMA}$=0.244 at 25 °C. The measured higher $\chi_{eff}$ is also indicated by the significantly unbalanced SFEs of counter-blocks in contact-angle characterization.

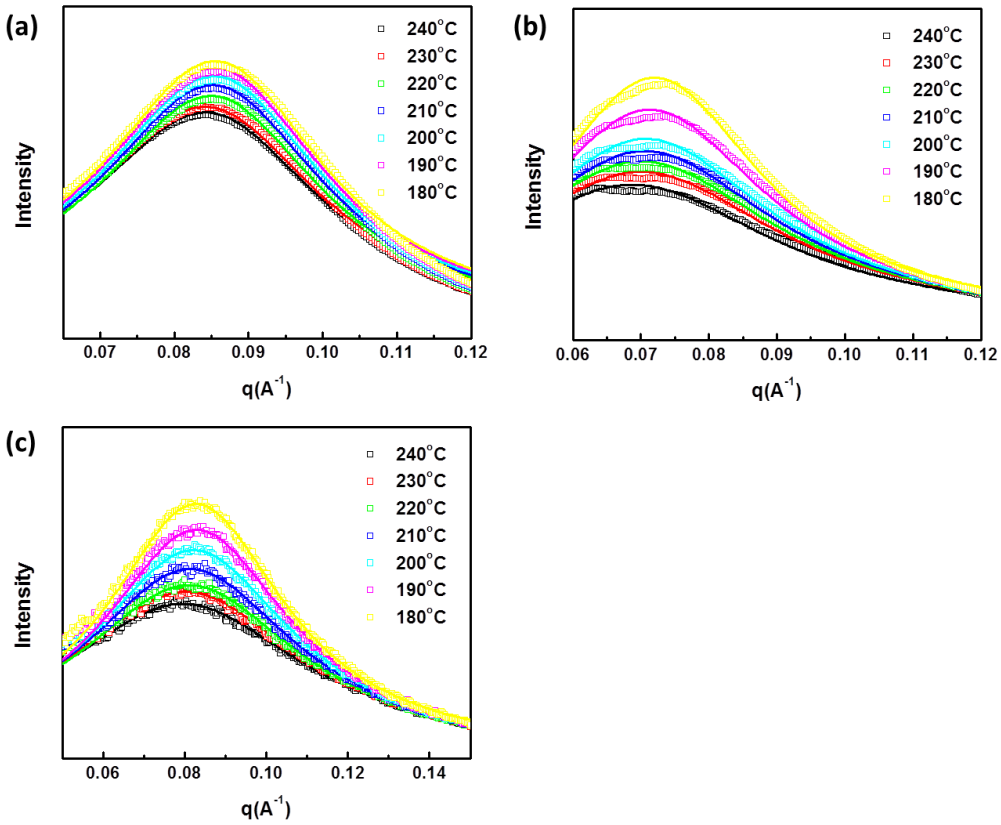


**Figure 3-16.** The scattering profiles (dotted lines) measured by SAXS and the fitting profiles (smooth lines) at different temperatures for (a) PS-*b*-P4FMA (S4F), (b) PS-*b*-P6FMA (S6F) and (c) PS-*b*-P8FMA (S8F).

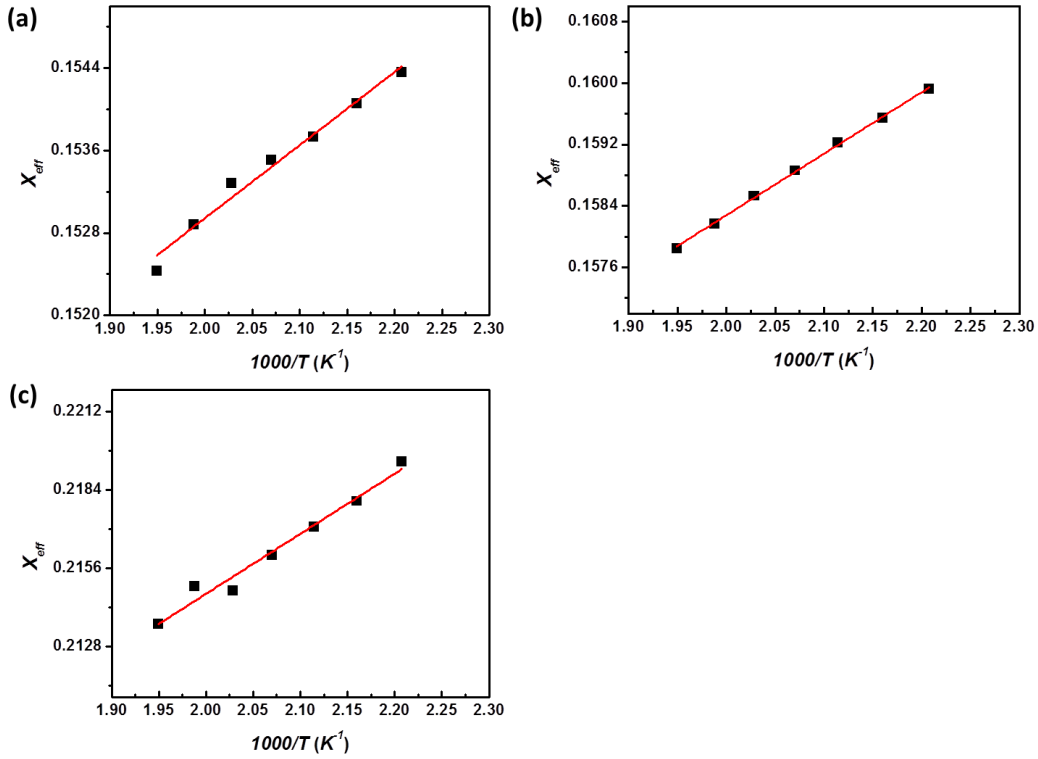


**Figure 3-17.** Temperature dependences of the effective Flory-Huggins interaction parameter for (a) PS-*b*-P4FMA (S4F), (b) PS-*b*-P6FMA (S6F) and (c) PS-*b*-P8FMA (S8F) using a reference volume of 118 Å$^3$.

**Table 3-4.** The fixed parameters used to estimate $\chi_{eff}$ for PS-*b*-PXFMA. (X=4,6 or 8)

| BCP | $r_c$ | $M_n$ (kg mol$^{-1}$) | $M_w$ (kg mol$^{-1}$) | $M_{n,PS}$[a] (kg mol$^{-1}$) | $f_{PS}$ | $w_{PS}$ | $Đ$ |
|---|---|---|---|---|---|---|---|
| PS-*b*-P4FMA(S4F) | 32 | 2.7 | 3.8 | 1.4 | 0.60 | 0.52 | 1.39 |
| PS-*b*-P6FMA(S6F) | 43 | 3.4 | 4.4 | 1.2 | 0.47 | 0.36 | 1.27 |
| PS-*b*-P8FMA(S8F) | 39 | 3.2 | 3.9 | 1.6 | 0.62 | 0.50 | 1.18 |

[a] The molecular weight of *sec-butyl* from the initiator and DPE were counted as PS chain.

**Table 3-5.** The fixed parameters used to estimate $\chi_{eff}$ for PS-*b*-PXFMA. (X=4,6 or 8)

| | Estimated $\chi_{eff}$ | | |
|---|---|---|---|
| $T$ (°C) | PS-*b*-P4FMA (S4F) | PS-*b*-P6FMA (S6F) | PS-*b*-P8FMA (S8F) |
| 180 | 0.15436 | 0.15992 | 0.21943 |
| 190 | 0.15406 | 0.15954 | 0.21801 |
| 200 | 0.15373 | 0.15922 | 0.21708 |
| 210 | 0.15351 | 0.15886 | 0.21607 |
| 220 | 0.15328 | 0.15853 | 0.21480 |
| 230 | 0.15288 | 0.15817 | 0.21496 |
| 240 | 0.15243 | 0.15785 | 0.21362 |

**Table 3-6.** Estimated enthalpic ($A/T$ ) and entropic ($B$ ) contributions for PS-*b*-PXFMA (X=4,6 or 8) and PS-*b*-PMMA.

| BCP | Label | $A/T$ | $B$ |
|---|---|---|---|
| PS-*b*-P1FMA[a] | S1F | 19.4/$T$ | 0.126 |
| PS-*b*-P4FMA | S4F | 7.1/$T$ | 0.138 |
| PS-*b*-P6FMA | S6F | 8.2$T$ | 0.142 |
| PS-*b*-P8FMA | S8F | 21.5/$T$ | 0.172 |
| PS-*b*-PMMA[b] | - | 3.4/$T$ | 0.034 |

[a] Referred from our previously published paper [2].

[b] Estimated in Chapter 6.

**3-4. Conclusion**

In this study, semi-fluorinated C8F17-containing liquid crystal (LC) side chain was introduced to the backbone of precursor BCP PS-*b*-PGMA for enhanced segregation, which enables the formation of approximately 11.5 nm cylindrical domain in bulk, which presents an averaged 13.3 nm distance between adjacent cylinders. The observed hexagonally packed cylindrical morphology of PS-*b*-P8FMA exhibits asymmetric characteristics, which is reasonably caused by the interplay between block segregation and side chain LC ordering. Based on previous related studies, the LC ordering with a 3.6 nm lamellar structure is assigned as smectic phase according to DSC and WAXD results. Furthermore, a hierarchical self-assembly structure model including both block segregation and LC ordering characteristic spacing is proposed, which is highly consistent with the known volume fraction of BCP. Furthermore, semi-fluorinated side chains with various CF2 lengths are introduced to the same precursor BCP for unveiling the role of LC ordering in this system. As the length of side chain is gradually reduced to C6F13, C4F9 and CF3, a transition from LC smectic to amorphous phase is observed. The asymmetry of hexagonally packed array is significantly reduced in PS-*b*-P6FMA with LC side chain structure of lower periodicity and shorter spacing. Besides, without any significant side chain LC ordering, PS-*b*-P4FMA of symmetric volume fraction begins to transform from cylindrical into lamellar morphology. Although the estimated $\chi$ parameter from PS-*b*-PXFMA was slightly increased with the elongated semi-fluorinated side chain, the magnitude of block segregation intensity indicator ($\chi N$) responsible for micro-phase separation remains similar. Therefore, the differences on self-assembled morphologies are originated from the effects of introduced side chains. The comparative results from various side chain lengths indicate the essential role of LC side chain for anisotropy in the hierarchy self-assembly system, as only PS-*b*-P8FMA reveals a cylindrical morphology with significant anisotropic packing feature. The unique anisotropic hexagonal packing array gives BCPs the potential for tailoring on pattern size in next-generation lithographic application.

**3-5. Reference**

1. Leibler, L., Theory of Microphase Separation in Block Co-Polymers. *Macromolecules* **1980,** *13* (6), 1602-1617.

2. Yoshimura, Y.; Chandra, A.; Nabae, Y.; Hayakawa, T., Chemically tailored high-chi block copolymers for perpendicular lamellae via thermal annealing. *Soft Matter* **2019,** *15* (17), 3497-3506.

3. Bates, F. S.; Fredrickson, G. H., Block Copolymer Thermodynamics - Theory and Experiment. *Annu Rev Phys Chem* **1990,** *41*, 525-557.

4. Bates, F. S.; Fredrickson, G. H., Block copolymers - Designer soft materials. *Phys Today* **1999,** *52* (2), 32-38.

5. Hawker, C. J.; Russell, T. P., Block copolymer lithography: Merging "bottom-up" with "top-down" processes. *Mrs Bull* **2005,** *30* (12), 952-966.

6. Shah, M.; Pryarnitsyn, V.; Ganesan, V., A model for self-assembly in side chain liquid crystalline block copolymers. *Macromolecules* **2008,** *41* (1), 218-229.

7. Li, X. K.; Huang, F.; Jiang, T.; He, X. H.; Lin, S. L.; Lin, J. P., Phase behaviors of side chain liquid crystalline block copolymers. *Rsc Adv* **2015,** *5* (2), 1514-1521.

8. Lv, Y. S.; Wang, L. Q.; Wu, F. S.; Gong, S. T.; Wei, J.; Lin, S. L., Self-assembly and stimuli-responsive behaviours of side-chain liquid crystalline copolymers: a dissipative particle dynamics simulation approach. *Phys Chem Chem Phys* **2019,** *21* (14), 7645-7653.

9. Asai, Y.; Yamada, K.; Yamada, M.; Takano, A.; Matsushita, Y., Formation of Tetragonally-Packed Rectangular Cylinders from ABC Block Terpolymer Blends. *ACS Macro Lett* **2014,** *3* (2), 166-169.

10. Yu, J. Y.; Liu, F. Q.; Tang, P.; Qiu, F.; Zhang, H. D.; Yang, Y. L., Effect of Geometrical Asymmetry on the Phase Behavior of Rod-Coil Diblock Copolymers. *Polymers-Basel* **2016,** *8* (5).

11. Pryamitsyn, V.; Ganesan, V., Self-assembly of rod–coil block copolymers. *The Journal of Chemical Physics* **2004,** *120* (12), 5824-5838.

12. Gao, J.; Tang, P.; Yang, Y. L., Non-lamellae structures of coil-semiflexible diblock copolymers. *Soft Matter* **2013,** *9* (1), 69-81.

13. Kumar, N. A.; Ganesan, V., Communication: Self-assembly of semiflexible-flexible block copolymers. *J Chem Phys* **2012,** *136* (10).

14. Dieng, S. Y.; Bertaina, B.; Cambon, A., Synthesis and Application of New Sulfurs with Perfluorated Chain. *J Fluorine Chem* **1985,** *28* (3), 341-355.

15. Fedors, R. F., A method for estimating both the solubility parameters and molar volumes of liquids. *Polymer Engineering & Science* **1974,** *14* (2), 147-154.

16. Wang, J. G.; Mao, G. P.; Ober, C. K.; Kramer, E. J., Liquid crystalline, semifluorinated

side group block copolymers with stable low energy surfaces: Synthesis, liquid crystalline structure, and critical surface tension. *Macromolecules* **1997,** *30* (7), 1906-1914.

17. Harris, M.; Appel, G.; Ade, H., Surface morphology of annealed polystyrene and poly(methyl methacrylate) thin film blends and bilayers. *Macromolecules* **2003,** *36* (9), 3307-3314.

18. Al-Hussein, M.; Sérézo, Y.; Konovalov, O.; Mourran, A.; Möller, M.; de Jeu, W. H., Nanoordering of Fluorinated Side-Chain Liquid Crystalline/Amorphous Diblock Copolymers. *Macromolecules* **2005,** *38* (23), 9610-9616.

19. Russell, T. P.; Hjelm, R. P.; Seeger, P. A., Temperature-Dependence of the Interaction Parameter of Polystyrene and Poly(Methyl Methacrylate). *Macromolecules* **1990,** *23* (3), 890-893.

# Chapter 4

# Adjusting Thin Film Domain Spacings of Side-Chain Liquid Crystalline Semi-fluorinated Block Copolymers with Elliptical Cylinders with Anisotropic Hexagonal Packing

## 4-1. Introduction

Block copolymers (BCPs) are widely studied due to the capability of self-assembling into a variety of long-ranged structure. The commonly observed morphologies in coil-coil flexible diblock copolymer include sphere, cylinder and lamellae, dependent on the specific volume fraction of blocks[2 4 6]. This unique feature resulting from self-assembly behaviors reveals potential application on perspective nanofabrication in semi-conductor industry[7]. However, compared to the conventional photolithographic technology, lithographic application based on block copolymer self-assembly is confronted with the limitation on pattern size and type in thin film. Therefore, BCPs of tunable thin film periodicities and thin film pattern type is in high demand.

The thin film pattern size could be tailored by BCPs of specific chain architectures with crosslinking technique[8] or using cyclic analogues instead of linear one[9]. Another effective approach to tunable thin film periodicities is utilization on asymmetric self-assembly morphology, as the asymmetric feature can provide distinctive domain dimensions by precisely tuning the thin film domain orientation. In comparison with asymmetric lamellae, the cylinder in anisotropic packing array is more appealing to lithographic application, as top and side views of cylindrical domain even indicate two accessible pattern types in thin film. In previous studies, the cylinder in unique packing, which is different from commonly seen isotropic hexagonally packing array, is usually associated with BCP domain interface of non-constant mean-curvature. For instance, the observation of rectangular-shaped cylinder in rectangular array[10] and similar morphology by using self-consistent field theory (SCFT)[11] were reported. The anisotropic packing of cylinder with stability in thermodynamics was more predicted in rod-coil[12] or semiflexible-flexible[13 14] BCPs by using SCFT model. Remarkably, in diblock copolymer melt model, an elliptical domain in distorted hexagonally packing array is found more energy-favored stable than circular domain in thin film. Besides, the ellipse's eccentricity is dependent on the minority block fraction.

Similar to the previously mentioned rod-coil or semiflexible-flexible BCPs, a special class of BCPs, called side chain liquid crystalline (SCLC) block copolymer has been shown various potential applications in the field of nanotechnology. For example, SCLC BCP is reported capable of controlling the orientation of the BCP domains in thin film[15 16 17 18]. In

SCLC BCPs self-assembly process, their microstructure will be influenced by two driving forces, side-chain crystalline LC ordering and mirco-phase separation, which is different from other BCPs as only mirco-phase separation was involved. Two periodicities of distinctive scales from side chain LC ordering and microphase separation of the counter-blocks will be co-existed and hence material properties (for instance, the BCP domain orientation in thin film) could be tailored by the hierarchical system. Accordingly, modified models based on SCFT approach[19] or dissipative particle dynamics (DPD) simulations[20 21] were developed to characterize the self-assembly behavior in SCLC BCP. Based on the experimental and theoretic studies, the hierarchical self-assembly system exhibits morphologies significantly different from those derived from conventional amorphous BCPs in coil model.

In previous studies, orientation tunings on BCP domain by introducing liquid crystal ordering or other entropy-confined architecture were widely reported for tailoring thin film pattern types. Hammond[22] manipulated the morphology of side-chain liquid crystalline block copolymers through variations in the liquid crystalline content. Nealey[23] achieved the orientation control of BCP cylindrical domains by varying the substitution on the tail of the side chain azobenzene mesogen. Without chemical change in BCPs, Iyoda[24] and Takahiro[25] developed a surface covering method to switch the parallel cylinder formation of BCP with liquid crystalline side chain to perpendicular cylinder formation or inversely. Yu[26] developed a light-directed regulation of nanostructures in thin films of liquid-crystalline diblock copolymers containing photoresponsive mesogen. Besides SCLC BCPs, Ho[27] demonstrated that for star-block copolymers with symmetric volume fraction, perpendicularly oriented BCP nanostructures could be induced instead of enthalpy-driven parallel orientation via an entropic effect regulated by the number of arms. Satoh[28] utilized thermal annealing for inducing a drastic change in the domain orientation of a biomass-based A-B-A triblock copolymer from horizontal to vertical. However, these methodologies all involve the massive synthesis works or time-consuming process, and the accessible pattern is limited to parallel and perpendicular domain of a fixed dimension. Additionally, the improvement on the periodicity of prepared patterns in thin film was in demand.

In this study, the precise orientation control on thin film BCP domain is readily realized by tuning the composition of bottom surface layer copolymers. Two thin film pattern types including striations and hexagonally packed dots were thereby prepared. Besides, the dimensions of long-ranged ordered striation patterns could be easily tailored because of the asymmetry in cylinder domain packing array.

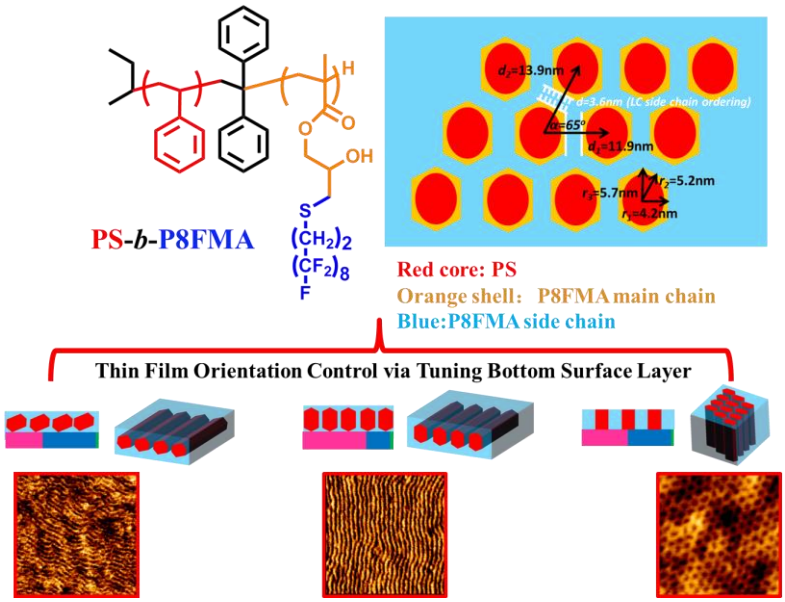


**Scheme 4-1.** Schematic of thin film orientation control concept by tuning compositions of bottom random copolymer layers.

## 4-2. Experimental Section

### 4-2-1. Materials

Lithium chloride (LiCl) was obtained from Kanto Chemical Co. Inc. and baked under a reduced pressure at 200 °C overnight before use. Styrene was washed by 0.1M sodium hydroxide (NaOH) aqueous solution for three times and dried by magnesium sulfide ($MgSO_4$), afterwards, calcium hydride ($CaH_2$) was added and stirred overnight before distillation. After the distillation, *di-n-butyl*magnesium ($MgBu_2$) was added under Ar protection to remove the residual water in styrene. Trap to trap process was further carried out to degas using liquid nitrogen as the freezing source. Similarly, glycidyl methacrylate (GMA) was distilled, dehydrated by $CaH_2$ and subsequently degassed under Ar. Diphenylethene (DPE) was distilled, dehydrated by *n-butyl* lithium and subsequently degassed under Ar. All other materials were reagent grade, purchased from Kanto Chemical Co. Inc., Tokyo Chemical Industry, FUJIFILM Wako Pure Chemical Corporation, and Sigma-Aldrich, and used as received.

### 4-2-2. Methods

$^1$H NMR spectra were recorded with a JEOL JNM-ECS400 (400 MHz) instrument using chloroform-d as the solvent. SEC (size exclusion chromatography) analysis was performed on a Shodex GPC-101 instrument, which was equipped with columns of Shodex LF804. The number average molecular weights ($M_n$) and molecular weight distributions ($M_w/M_n$) were determined by SEC at a flow rate of 1.0 ml/min at 40 °C and calibrated with polystyrene.

$O_2$-RIE treatments were performed by etching instrument (SATO VAC, Inc.). The oxygen flow rate was set to 40 sccm and the applied power used was 20 W. The thin film samples were prepared using a MIKASA spin coater IH-D7, and the film thicknesses were measured by a FILMETRICS F20-EXR. AFM (NanoWizard Ultra Speed A, JPK) was used to observe the surface architectures of the BCP thin films at room temperature.

### 4-2-3. Synthesis of PS-*b*-PGMA

The synthetic routine to targeted diblock copolymer was classified into two steps, the synthesis of precursor main chain polymer PS-*b*-PGMA via sequential anionic living polymerization and the subsequent post-functionalization for introduction of fluorine-rich side chain.

An example of the anionic polymerization of styrene and GMA is as follows. All anionic polymerization procedures were performed under Ar protection. Here, 30 mL of THF and LiCl (29.7 mg, 0.700 mmol) were transferred to a 50 mL Schlenk flask and then cooled to -78 °C. *Sec-Butyl* lithium (*sec*-BuLi) (in 1.05 M hexane/cyclohexane solution) was added until the color changed to yellow. The Schlenk flask was removed from the cooling bath and kept under room temperature till the solution became colorless. The Schlenk flask was again cooled to -78 °C, and *sec*-BuLi solution in cyclohexane and *n*-hexane (0.69 mL, 0.700 mmol) was added as initiator. Styrene (1.65 mL, 14.42 mmol) was further added and stirred for 30 min, resulting in bright orange color of solution. DPE (0.39 mL, 2.1 mmol) was added, changing the color to deep red color. After 30 min of stirring, GMA (0.47 mL, 3.52 mmol) was added and stirred for 30 min. The solution became colorless. Finally, 3 mL of methanol (MeOH) (excess amount) purged with Ar and added to the Schlenk flask to yield proton-terminated PS-*b*-PGMA. The polymer was precipitated into MeOH and filtered, and then the product was dried under a reduced pressure at 40 °C overnight to yield PS-*b*-PGMA as a white powder (1.80 g, 90% yield). The $M_n$ and dispersity ($Đ = M_w/M_n$) of the product determined by SEC were 3900 g mol$^{-1}$ and 1.38, respectively.

$^1$H NMR (400 MHz, $CDCl_3$, δ, ppm): 0.98 (s, α-$CH_3$, PGMA), 1.14 (s, α-$CH_3$, PGMA), 1.29-1.80 (br, backbone, -$CH_2$-CH-, PS), 1.84-2.30 (br, backbone, -$CH_2$-CH-, PS, br, backbone, -$CH_2$-C($CH_3$)-, PGMA), 2.70 (s, -$CH_2$-CH($CH_2$)-O-, PGMA), 2.82 (s, -$CH_2$CH($CH_2$)-O-, PGMA), 3.28 (s, -$CH_2$-CH($CH_2$)-O-, PGMA), 3.84 (s, -(C=O)O-$CH_2$-, PGMA), 4.37 (s, -(C=O)O-$CH_2$-, PGMA), 6.39-6.85 (m, o-aromatic, PS) 6.91-7.42 (m, m-, p-aromatic, PS).

### 4-2-4. Synthesis of PS-*b*-P8FMA through the post-functionalization of PS-*b*-PGMA with 1H,1H,2H,2H-Perfluorodecanethiol

Thiol-epoxy click reaction was utilized to introduce the semi-fluorinated side chains to the backbone of precursor copolymers PS-*b*-PGMA. The general procedure is as follows regardless of the type of thiols: A 10 ml glass tube was charged with PS-*b*-PGMA and THF (20 mole equiv. to PGMA repeating units) and immersed in an ice-water bath. 1 wt% lithium hydroxide (LiOH) aqueous solution (LiOH 0.05 mole equiv. to PGMA repeating units) and thiol (1.3~1.5 mole equiv. to PGMA repeating units) were added to the tube. After stirring for 20 min at room temperature, the tube was transferred to a thermal reactor set to 30 ℃ and stirred for 3 h. The crude solution was precipitated from methanol. After filtration, the solid was again dissolved in THF and precipitated and then filtered two more times to remove any residual reagents. The product was dried under a reduced pressure at room temperature overnight to yield a white powder (41% yield).

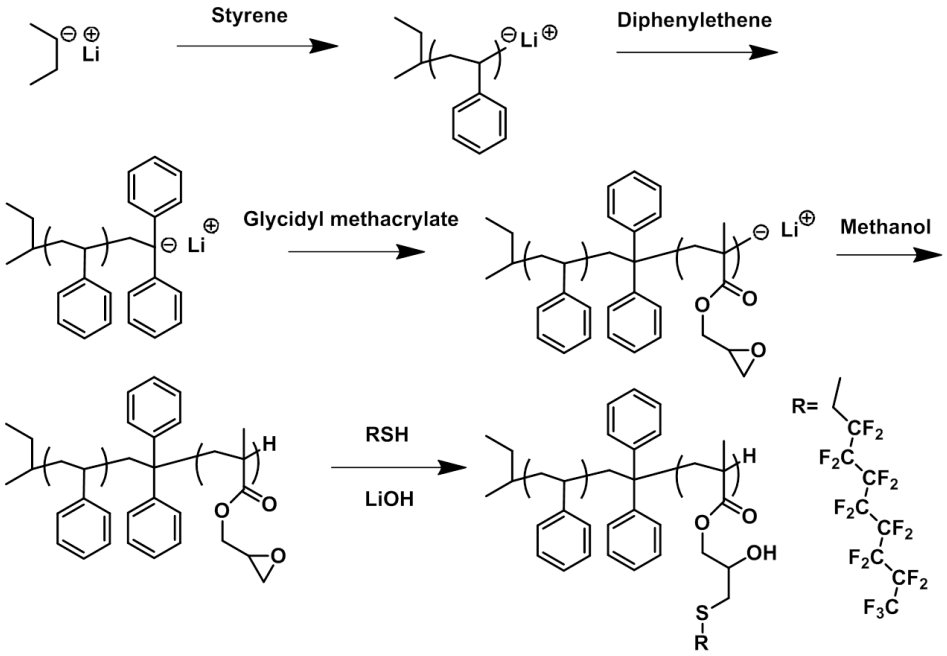


**Scheme 4-2.** Synthetic scheme of PS-*b*-PGMA precursor via sequential living anionic polymerization of styrene and glycidyl methacrylate and post-functionalization with 1H,1H,2H,2H-Perfluorodecanethiol.

$^1$H NMR (400 MHz, $CDCl_3$, δ, ppm): 0.98 (s, α-$CH_3$, P8FMA), 1.12 (s, α-$CH_3$, P8FMA), 1.21-1.70 (br, backbone, -$CH_2$-CH-, PS), 1.72-2.25 (br, backbone, -$CH_2$-CH-, PS, br, backbone, -$CH_2$-C($CH_3$)-, P8FMA), 2.29-2.50 (t, -$CH_2$-$CF_2$-, P8FMA), 2.60-2.76 (t, -S-$CH_2$-$CH_2$-$CF_2$-, P8FMA), 2.76-2.87 (d, -CH(OH)-$CH_2$-S-, P8FMA), 3.82-4.17 (d, -(C=O)O-$CH_2$-, P8FMA) (m, -CH(OH)-, P8FMA), 6.28-6.85 (m, o-aromatic, PS), 6.86-7.32 (m, m-, p-aromatic, PS).

**4-2-5. Synthesis of PMMA-*r*-PTFEMA-*r*-PMAAs**

The following procedure was used for PMMA-*r*-PTFEMA-*r*-PMAA 43-54-3, but is representative of all bottom surface layer materials syntheses. The numeric label denotes the weigh fraction of each block.

2,2,2-Trifluoroethyl methacrylate (TFEMA), methyl methacrylate (MMA) and methacrylic acid (MAA) were distilled to yield clear and colorless liquid prior to use. Azobisisobutyronitrile (AIBN) was recrystallized prior to use. 2,2,2-Trifluoroethyl methacrylate (1.08g, 6.4 mmol, 0.41 eq), methyl methacrylate (0.86 g, 8.6 mmol, 0.55 eq), methacrylic acid (0.06 g, 0.7 mmol, 0.04 eq), and AIBN (0.007 g, 0.004 mmol, 0.00025 eq) were added to a 50 mL 3-neck round bottom flask equipped with a stir bar and rubber septa. The reagents were dissolved in THF (7.5 mL) and the solution was deoxygenated by vigorously bubbling nitrogen through the solution for 30 minutes. The reaction vessel, under positive nitrogen pressure, was immersed in an oil bath at 70 ˚C. The reaction was heated and stirred for 24 h and quenched at 0 ˚C. The viscous liquid was precipitated into methanol (300 mL) and filtered. The resulting polymer was dissolved in THF and reprecipitated into methanol for two additional times. The polymer was dried in vacuo overnight at 40 ˚C and the white powder product (93% yield) was obtained.

$^1$H NMR (400 MHz, chloroform-*d*, δ, ppm): 0.84-0.89, 1.01-1.11, 1.21-1.26, 1.40-1.48, 1.76-2.08, 3.49-3.70, 4.20-4.45.

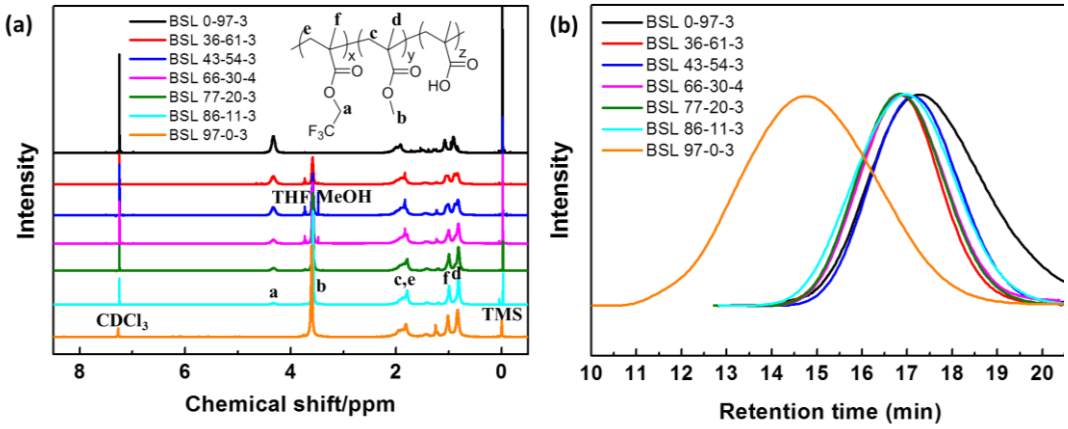


**Figure 4-1**. (a) $^1$H NMR spectra and (b) GPC chromatograms of the synthesized random copolymers PMMA-*r*-PTFEMA-*r*-PMAAs. The labeled number in XX-YY-ZZ form indicates the weight fraction of each component in percentage.

**Table 4-1.** Characteristics of the synthesized BSL copolymers.

| Random Copolymer | Weight Composition[a] | | | Volume Composition[b] | | | $M_n$ | $Đ$ |
|---|---|---|---|---|---|---|---|---|
| | TFEMA | MMA | MAA | TFEMA | MMA | MAA | | |
| PMMA-*r*-PTFEMA-*r*-PMAA | 11 | 86 | 3 | 9 | 88 | 3 | 28800 | 2.04 |
| | 20 | 77 | 3 | 16 | 81 | 3 | 32700 | 1.77 |
| | 30 | 66 | 4 | 26 | 70 | 4 | 26800 | 1.77 |
| | 54 | 43 | 3 | 50 | 47 | 3 | 31900 | 1.81 |
| | 61 | 36 | 3 | 57 | 40 | 3 | 34500 | 1.74 |
| PTFEMA-*r*-PMAA | 97 | - | 3 | 96 | - | 4 | 16700 | 2.43 |
| PMMA-*r*-PMAA | - | 97 | 3 | - | 97 | 3 | 76600 | 2.28 |

[a] MMA and TFEMA compositions were determined by $^1$H NMR and MAA composition was estimated from monomer feeding ratio. [b] Volume Composition was determined using bulk densities for each unit (1.47 g cm$^{-3}$ for PTFEMA[1], 1.18 g cm$^{-3}$ for PMMA[3], 1.29 g cm$^{-3}$ for PMAA[5]).

### 4-2-6. Thin film preparation

Bare silicon wafers cut into 1 $cm^2$ pieces were sonicated in toluene for 3 min, and dried in a stream of nitrogen. The substrates were treated with a mixture of $H_2O_2$ (30%) and $H_2SO_4$ (70%) (v/v) at 80 ˚C for 40 min. The wafers were rinsed with water repeatedly and dried in a stream of nitrogen. Bottom surface layer (BSL) were generated by spin coating a 1.0 wt% poly(methyl methacrylate)-*random*-poly(2, 2, 2-trifluoroethyl methacrylate)-*random*-poly(methacrylic acid) (PMMA-*r*-PTFEMA-*r*-PMAA) solution in propylene glycol monomethyl ether acetate (PGMEA) solution at 3000 rpm and 30 s onto the cleaned silicon wafers, followed by crosslinking at 200 ˚C for 5 min. The substrates were sonicated in toluene to remove any random copolymers that were not attached to the substrate and rinsed with fresh toluene. Furthermore, approximately 1.0 wt % solutions of the BCPs in toluene were spin-coated at 3000 rpm for 30 s onto the surface-modified silicon substrates to obtain thin films with ca. 1.5 $L_0$ thicknesses (1.0 $L_0$ denotes one periodic length of self-assembled nanostructure). The film thickness was tuned by changing BCP solution concentration. The thin films were annealed at 150 ˚C for 24 hr or 120 ˚C for 10 min (PS-*b*-P1FMA) under ambient conditions. An $O_2$-RIE treatment was conducted for a certain time (40 sccm, 20 W, 20 Pa) to selectively remove the methacrylate-based segments.

## 4-3. Results and Discussion

### 4-3-1. Synthesis and characterization of the BCPs

The synthesis of PS-*b*-PGMA precursor polymer (SG4) and post-functionalized PS-*b*-P8FMA (SF7) with liquid crystalline semi-fluorinated side chains were successful as discussed in previous chapter 3. The characterizations of the investigated BCPs are summarized in Table 4-2.

**Table 4-2.** Characterization data of the synthesized BCPs.

| BCP | Label[a] | $M_n$[b] (kg mol$^{-1}$) | $Đ$ | $w_{PS}$[c] | $f_{PS}$[c] | $d_{\text{-spacing}}$[d] (nm) | LC periodicity[e] (nm) | Morphology[f] |
|---|---|---|---|---|---|---|---|---|
| PS-*b*-PGMA | SG4 | 3.9 | 1.38 | 0.73 | 0.68 | 8.9 | - | Disorder |
| PS-*b*-P8FMA | S8F | 7.5 | 1.18 | 0.38 | 0.50 | 11.5 | 3.6 | Asym HEX |

[a] The labels SG and S8F refer to PS-*b*-PGMA and PS-*b*-P8FMA, respectively, while the number to the right refers to the number-average molecular weight ($M_n$) of the polymer. [b] $M_n$ and dispersities ($Đ$) were obtained by SEC using THF as the eluent based on PS standards. [c] PS weight fractions ($w_{PS}$) of PS-*b*-PGMA were calculated via $^1$H NMR and PS weight ($w_{PS}$) and volume fractions ($f_{PS}$) of PS-*b*-P8FMA were further estimated based on 100% introduction rate of side chain using bulk densities for each block (1.05 g cm$^{-3}$ for PS, 0.805 g cm$^{-3}$ for PGMA, and 1.73 g cm$^{-3}$ for P8FMA) [d] The domain spacings (d-spacing) were estimated from the position of first-order scattering peak in the SAXS profile upon thermal annealing at 150 ˚C for 24h. [e] The periodicity of LC side chain was determined by the position of first-order scattering peak in the WAXD profile of homo-polymer upon thermal annealing at 150 ˚C for 24h. [f] The morphologies in the bulk were determined by SAXS and TEM.

### 4-3-2. Domain orientation control in thin film

Owing to the potential for creating a variety of morphologies in thin film, PS-*b*-P8FMA was spin coated onto bottom surface layers (BSLs) of distinctive SFEs. In this study, five synthesized random (precisely should be called statistical) copolymers poly-(methyl methacrylate-*random*-2,2,2-trifluoroethyl methacrylate-*random*-methacrylic acid) (PMMA-*r*-PTFEMA-*r*-PMAA) (Figure 4-1 and Table 4-1) of various compositions, poly-(methyl methacrylate-*random*-methacrylic acid) (PMMA-*r*-PMAA) and poly-(2,2,2-trifluoroethyl methacrylate-*random*-methacrylic acid) (PTFEMA-*r*-PMAA) were spin coated onto bare silicon substrate and cross-linked to induce the desired orientation of BCP ontop bottom substrate. In all used BSL copolymers, approximately 3% molar methyl acid was added as cross-linking functionalities. PTFEMA and PMMA units were selected for tuning SFE of BSL, because the SFE of PTFEMA and PMMA is near to the estimated SFE of P8FMA and PS block, respectively, as listed in experimental section of Chapter 3. The periodic length of thin film pattern obtained from AFM characterizations was extracted from fast Fourier transform (FFT) and 1-D integration results of 2D FFT signals was also presented (Figure 4-3).

The AFM phase images (Figure 4-2) reveal the morphologies of PS-*b*-P8FMA on BSLs of distinctive SFEs. A typical hole topology of 0.5 $L_0$ depth was observed for PS-*b*-P8FMA on PMMA-based BSL and the BCP thickness was measured to be 1.79 $L_0$. According to the hole-island theory for optimization on neutral BSL[27], PS blocks seems to wet the most

hydrophilic PMMA-based BSL at bottom interface while PS and P8FMA blocks equally wet the top air interface. The block wetting model was also indicated in inset of AFM image. However, PS and P8FMA exhibit significantly imbalanced SFEs (estimated in Chapter 3) and P8FMA is expected more preferential to the air interface. The incompatibility with the hole-island theory is caused by the assumption of flexible coil-coil BCP model[27] and the additional entropy contributor from SCLC is not even concluded in the hole-island methodology.

When the composition of PTFEMA was gradually increased from BSL (86-11-3) to BSL (77-20-3), the ontop PS-*b*-P8FMA begins to exhibit a morphology transition from featureless flat surface to long-ranged striation patterns of 12.0 nm domain spacing. With the further increment of PTFEMA composition in BSL, hybrid striation patterns with 12.3 nm or 14.3 nm domain spacing were observed for the PS-*b*-P8FMA ontop BSL (66-30-4). The observed two domain spacings were highly consistent the two distinctive distances between adjacent PS cylinders in anisotropic hexagonal packing array in bulk morphology. Therefore, the striation pattern was thought in response to the parallel oriented cylinder domain with titled angle to the substrate.

As the PTFEMA composition in BSL was continuously tuned, a neutral BSL (43-54-3) without any preferential interaction to the either block was obtained. Therefore, the BCP domains perpendicular to the substrate was achieved. As shown in the inset image, a hexagonally packed array perpendicular to the substrate was observed. Two distinctive $d_{\text{-spacing}}$ of 11.9 nm and 13.4 nm obtained from fast Fourier transform characterized in thin film was highly consistent with that observed in bulk. Remarkably, following the selective etching of surrounding P8FMA segments, a clearer hexagonally packing array of PS cylinders with significant anisotropy was suggested by AFM characterization (Figure 4-4).

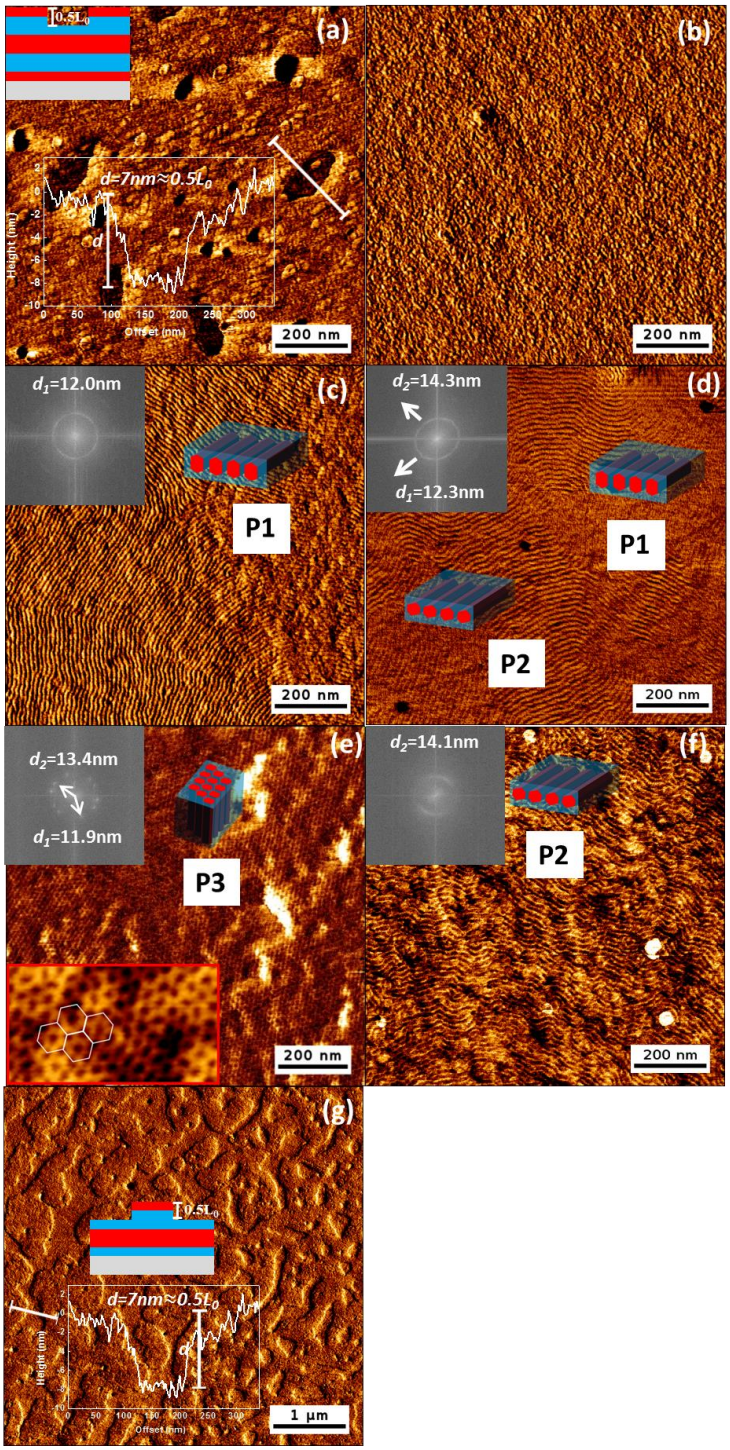


**Figure 4-2**. AFM phase images of the thin films prepared from PS-*b*-P8FMA on various BSLs: (a) PMMA (97-0-3), (b) (86-11-3), (c) (77-20-3) , (d) (66-30-4) , (e) (43-54-3), (f) (36-61-3) and (g) PTFEMA (0-97-3). The BCP thickness is controlled within 1.5-2.0 $L_0$. The upper left inset displays the Fourier-transform pattern of the real-space image and the periodic length of domain is estimated from FFT. The insets in (a)/(g) indicate the wetting model of block and height profile of the cross-section, respectively. The inset in (e) clearly shows the hexagonally packing array in magnified scanning area.

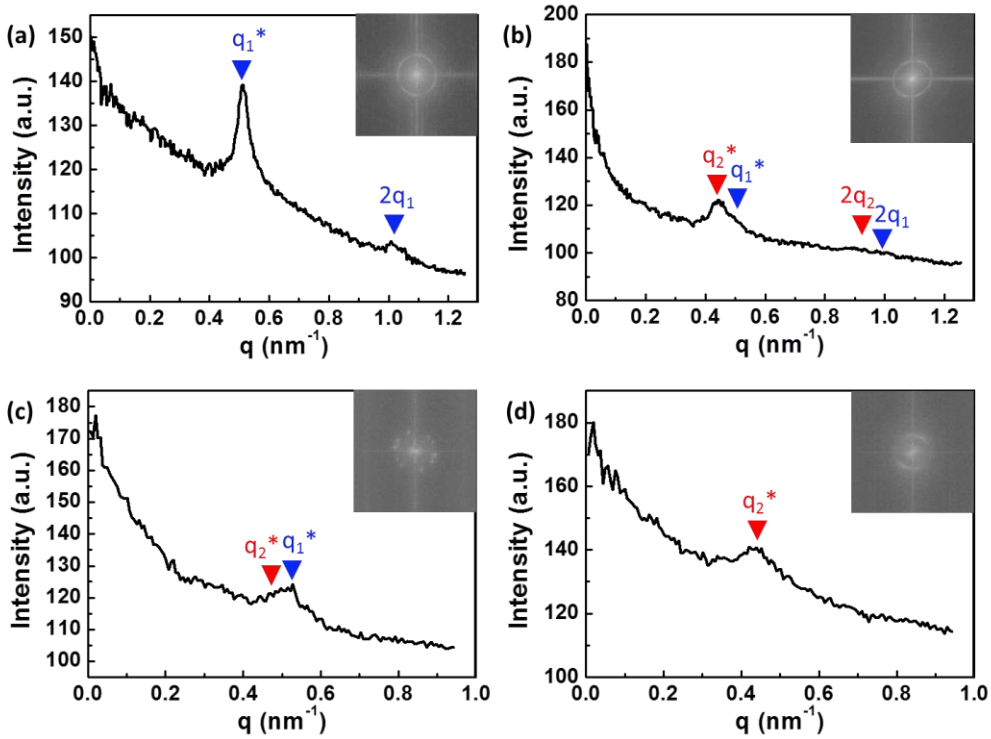


**Figure 4-3.** The 1-D integration profile of 2D FFT signals along the radius to the center of FFT inset image extracted from AFM phase images of the thin films prepared from PS-*b*-P8FMA on various BSLs: (a) (77-20-3), (b) (66-30-4), (c) (43-54-3) and (d) (36-61-3). The signals from two distinctive spacings $d_1$ and $d_2$ were marked in blue and red color, respectively.

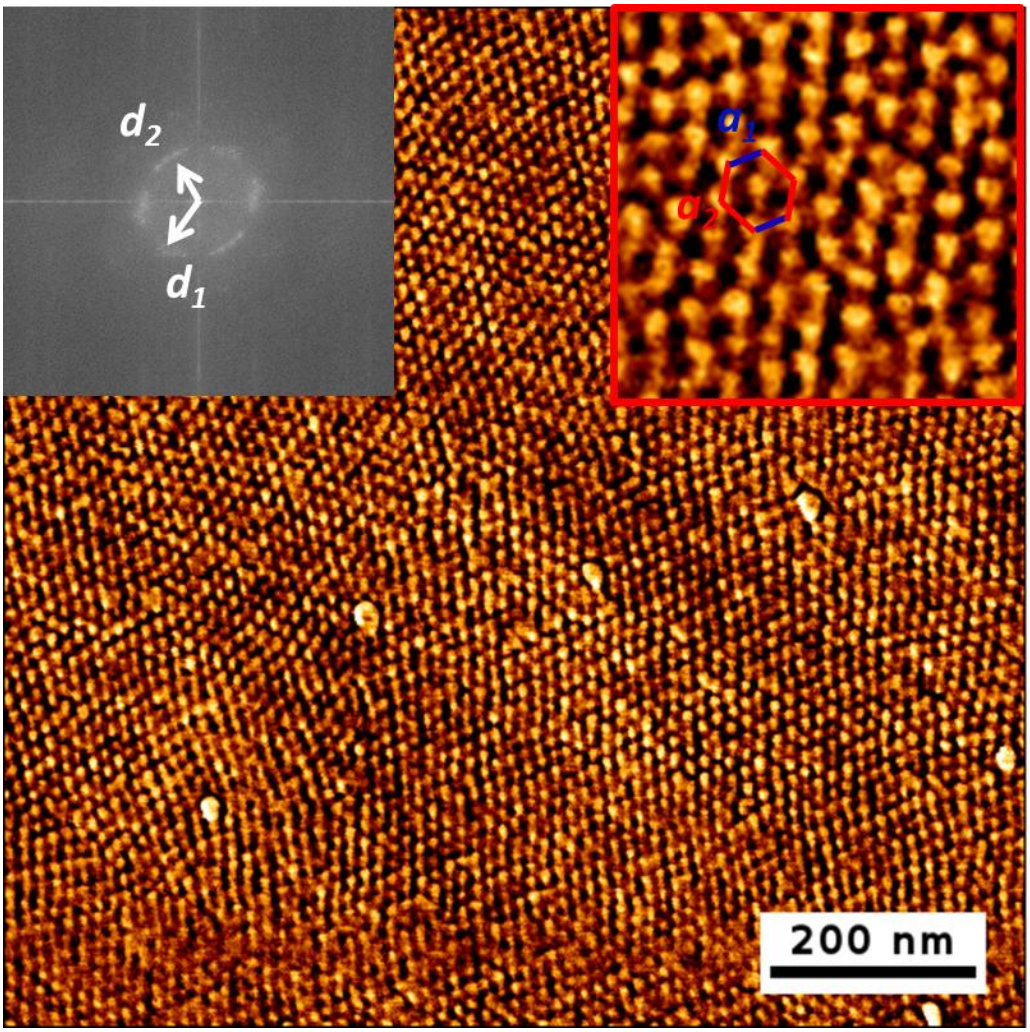


**Figure 4-4.** The AFM phase image of the thin film prepared from PS-*b*-P8FMA on BSL (43-54-3) following oxygen plasma etching. The inset reveals the fast Fourier transform of the image and the signals in response to $d_1$ and $d_2$ are marked. The inset magnified AFM images shows the dimension $a_1$ (blue marker) and $a_2$ (red marker) in response to $d_1$ and $d_2$, respectively, in anisotropic hexagonal packing array.

As the composition of PTFEMA in BSL was further slightly increased, which is drifted away from the neutral condition, parallel orientation of BCP domain with monopolized 14.1 nm spacing was achieved on BSL (36-61-3) again. Besides, the most hydrophobic PTFEMA-based BSL reveals the island topology with 0.5 $L_0$ height at 1.40 $L_0$ BCP film thickness. The wetting model based on the observed topology suggests the preferential wetting of P8FMA segments in bottom interface, meanwhile the equal wetting of two blocks in top air interface.

Different from the commonly observed hexagonally packed cylinder of symmetry, PS-*b*-P8FMA reveal asymmetric hexagonally packed array in bulk study because of the interplay between side chain LC ordering and segments segregation. Therefore, two characteristic dimensions of 10.9 nm and 12.7 nm were observed in side view of cylindrical morphology, depending on the specific direction in side view. Surprisingly, the unique feature containing two distinctive dimensions observed in bulk is inherited to thin film morphology despite the interfacial effects. When BSL (66-30-4) slightly preferential to PS block was used, a hierarchical lined pattern was observed in AFM characterization. The long-ranged patterns with 12.3 nm and 14.5 nm characteristic dimensions are revealed and the stripes with the same dimension are concentrated within the same grain boundary. Two phase indicator P1 and P2 was assigned to the region with the 12 nm and the wider 14 nm periodic length, respectively. P1 phase with smaller periodic length took a major fraction in a broader scanning region, as evidenced by the AFM scanning over a 4 μm × 4 μm area consisted of multiplied grains. (Figure 4-5) In contrast, BSL (36-61-3) slightly preferential to P8FMA block and BSL (77-20-3) slightly preferential to PS block exhibits a monopolized striation pattern of 12 nm and 14 nm periodic width, respectively. Accordingly the entire region of thin film morphology was labeled as P1 and P2, respectively. The difference on line pattern dimension using various BSL systems is originated from the titled angle of cylinder domain in parallel orientation to the substrate. As presented in Scheme 4-3, PS domain is inclined to wet the slightly PS-preferential BSL while slightly P8FMA-preferential BSL is resistant to the wetting of PS domain. The resistance to PS domain wetting enables the titled angle of parallel cylinder to the substrate, thus another characteristic spacing is revealed in the thin film surface. Besides the BSL with intermediate compositions (66-30-4) leads to mixed domain wetting conditions across the bottom surface and hybrid striation patterns could be observed. Conclusively, the precise adjustments on aligned angle of PS domain enable the tailoring on pattern dimensions.

Interestingly, the effective working distance of BSL seems to be limited by the thickness of ontop BCP. When BCP thickness is increased to more than 3.0 $L_0$, mixed morphologies containing both perpendicular and parallel orientations of domains were observed in AFM

characterization (Figure 4-6). As the reported study revealed that the perpendicular alignment of BCP domains occurs from the bottom and extends to the top interface[29], the fully developed domain orientation in upper layer of thick film may need extended annealing time.

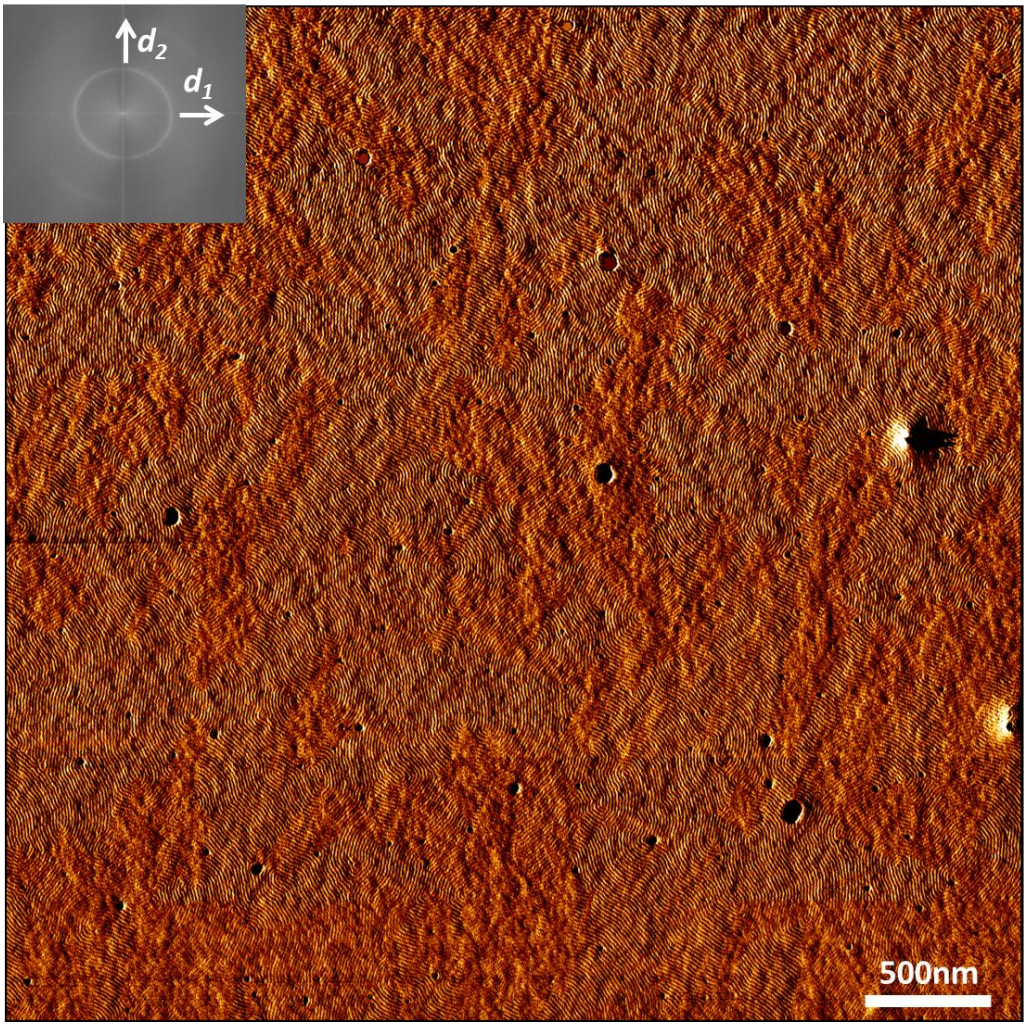


**Figure 4-5.** AFM phase images of the thin films prepared from PS-*b*-P8FMA on BSL (30-66-4) over a 4 μm × 4 μm area. The upper left inset displays the Fourier-transform pattern of the real-space image and the two distinctive periodic lengths $d_1$ and $d_2$ indicate the two different tilted angles of parallel BCP domains on surface.

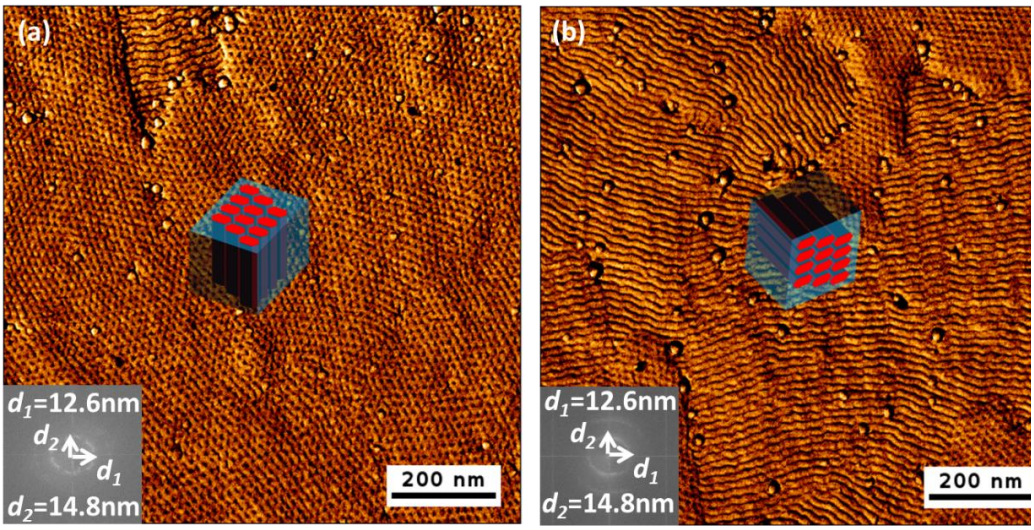


**Figure 4-6.** AFM phase images of the thin films prepared from PS-*b*-P8FMA on BSL (66-30-4). The BCP thickness is controlled to be $3.1L_0$. The below left inset displays the Fourier-transform pattern of the real-space image and the averaged periodic length of domain is estimated from FFT. The middle 3-D schemes depict the specific orientation of domain in the region. Perpendicular (a) and parallel orientation (b) of domain was mainly revealed in different region, respectively.

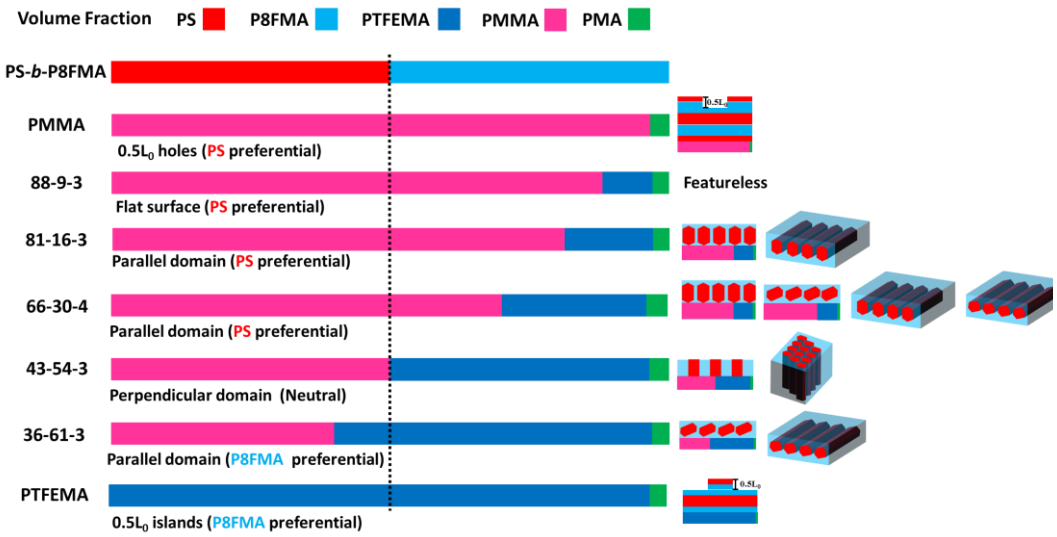


**Scheme 4-3.** The different colored blocks represent corresponding monomer unit and the length of block is scaled by the block volume fraction. The right cross-sectional and 3-D schemes depict the specific orientation of domain on varied BSLs.

**4-3-3. Effects of side chain length on thin film morphology**

To better investigate the role of semi-fluorinated side chain in thin film self-assembly, PS-*b*-PXFMAs (X=4 and 6) with various side chain lengths were spin-coated onto BSL (43-54-3), which is neutral to PS-*b*-P8FMA.

As shown in Figure 4-7., annealed PS-*b*-P6FMA on BSL exhibits a striation pattern of an averaged 13.0 nm periodic length, which is similar to the observed parallel orientated PS-*b*-P6FMA domain. However, the observed surface of as-prepared thin film contains some disordered regions, which may be caused by the coverage of P6FMA segments. Even following oxygen plasma etching, the height or phase contrast of the observed pattern remains insignificant. The difference is obviously attributed to the less ordered smectic phase of side chain. Compared to the highly ordered smectic phase of C8F17-containing side chain, the LC structure consisted of shorter fluorinated side becomes thermally unstable at 150 °C of annealing temperature. Therefore, the fluorinated segments with lower SFE are strongly inclined to occupy the top interface of thin film and PS cylindrical domains are covered underneath.

Besides, the lamella-forming PS-*b*-P4FMA with similar symmetric volume fraction exhibits a typical hole structure of 1.0 $L_0$ depth on BSL, despite the estimated SFE close to that of PS-*b*-PXFMA (X=6 or 8). The results suggested the existence of both preferential top and bottom interfaces[30]. Based on the estimated BCP thickness, an asymmetric wetting model is proposed in which P4FMA block fully occupies the top air interface and PS block wets bottom interface of BSL. The above results suggested the importance of side chain LC ordering for creating transferable periodic patterns in thin film.

Furthermore, the lamella-forming PS-*b*-P1FMA was spin coated on PS-*r*-PMMA ($f_{PS}$=0.73), which is verified as neutral BSL in previous study[31]. However, instead of the desired perpendicularly orientated lamellar domain, only a flat surface was observed in as-prepared thin film. Following oxygen plasma etching, a morphology composed of randomly packed dots was revealed, which may be related to the relatively insufficient segregation driving force ($\chi_{eff}N$=10.5) around segregation limit.

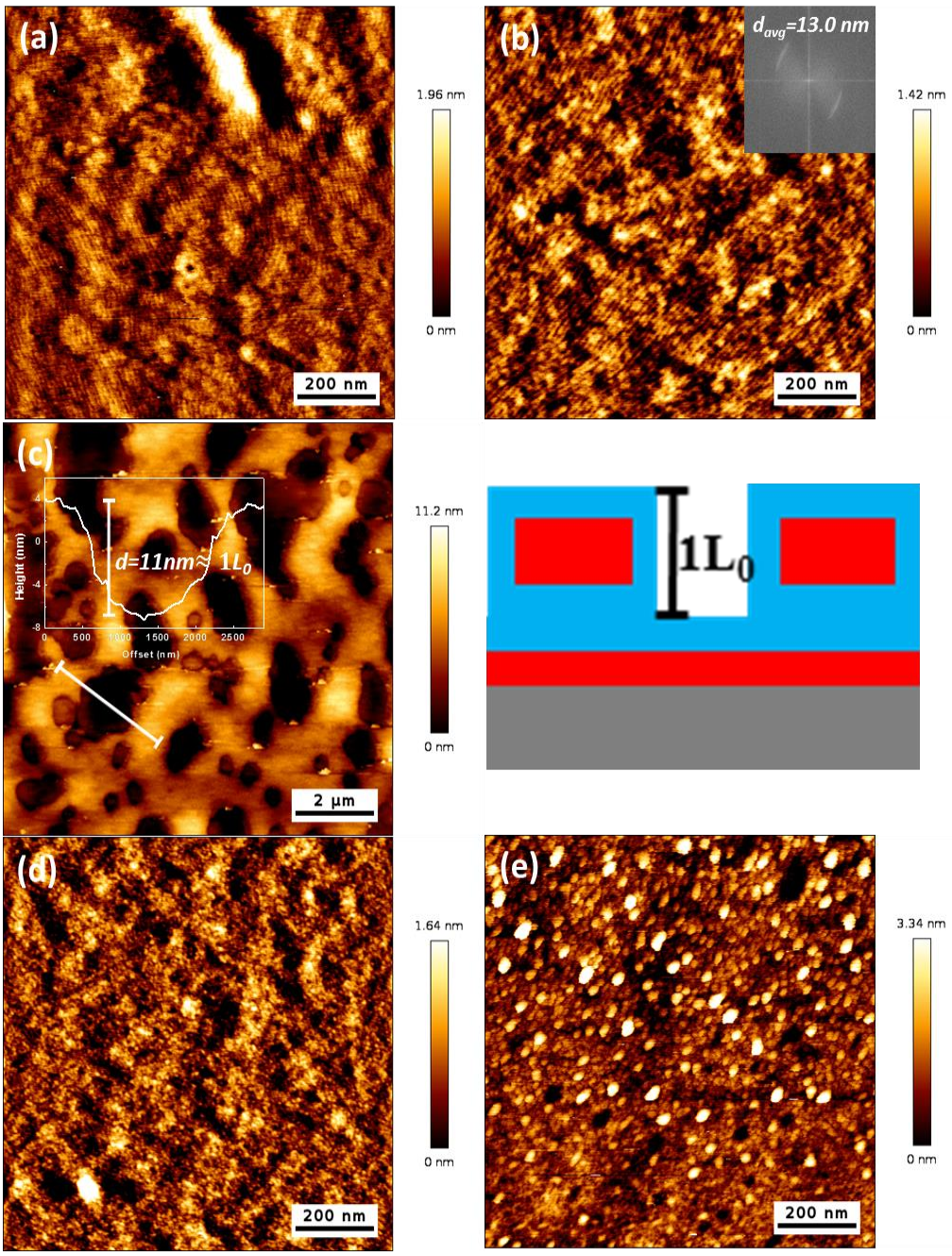


**Figure 4-7.** AFM height images of the thin films prepared from PS-*b*-PXFMA (X=1,4 or 6) on various BSLs: (a) As prepared and (b) $O_2$-RIE etched PS-*b*-P6FMA on BSL (43-54-3); (c) As prepared PS-*b*-P4FMA on BSL (43-54-3) . The inset and right scheme represents the cross-sectional height profile and corresponding block wetting model, respectively, in which red and blue denotes PS and P4FMA block, respectively; (d) As prepared and (e) $O_2$-RIE etched PS-*b*-P1FMA on neutral BSL of PS-*r*-PMMA ($f_{PS}$=0.73). The BCP thickness is controlled being 1.5-2.0 $L_0$.

## 4-4. Conclusion

In this study, semi-fluorinated C8F17-containing liquid crystal (LC) side chain was introduced to the backbone of precursor BCP PS-*b*-PGMA for enhanced segregation and orientation control, which enables the tailoring on pattern type or dimension in thin film. The domain orientation of PS-*b*-P8FMA in thin film is readily adjusted by varying the composition of copolymers as bottom surface layers (BSL). In accordance with the discovered morphologies in bulk, two types of striations with distinctive periodic lengths and anisotropic hexagonally packed cylinder, in response to non-titled or titled parallel and vertical domain orientation respectively, are prepared by merely tuning on the composition of BSLs. This simple but with high efficiency approach to tailoring on both BCP pattern type and size using one certain BCP enables the easy fabrication of various sub-10 nm patterns in lithographic application. The comparative thin film results from various side chain lengths indicate the essential role of LC side chain with high periodicity and appropriate spacing for preparation of long-ranged ordered domain with potential tailoring on thin film pattern type and pattern size.

## 4-5. Reference

1. Akpinar, B.; Fielding, L. A.; Cunningham, V. J.; Ning, Y.; Mykhaylyk, O. O.; Fowler, P. W.; Armes, S. P., Determining the Effective Density and Stabilizer Layer Thickness of Sterically Stabilized Nanoparticles. *Macromolecules* **2016,** *49* (14), 5160-5171.

2. Leibler, L., Theory of Microphase Separation in Block Co-Polymers. *Macromolecules* **1980,** *13* (6), 1602-1617.

3. Aouachria, K.; Belhaneche-Bensemra, N., Miscibility of PVC/PMMA blends by vicat softening temperature, viscometry, DSC and FTIR analysis. *Polym Test* **2006,** *25* (8), 1101-1108.

4. Bates, F. S.; Fredrickson, G. H., Block Copolymer Thermodynamics - Theory and Experiment. *Annu Rev Phys Chem* **1990,** *41*, 525-557.

5. Ho, B. C.; Chin, W. K.; Lee, Y. D., Solubility Parameters of Polymethacrylonitrile, Poly(Methacrylic Acid) and Methacrylonitrile Methacrylic-Acid Copolymer. *J Appl Polym Sci* **1991,** *42* (1), 99-106.

6. Bates, F. S.; Fredrickson, G. H., Block copolymers - Designer soft materials. *Phys Today* **1999,** *52* (2), 32-38.

7. Hawker, C. J.; Russell, T. P., Block copolymer lithography: Merging "bottom-up" with "top-down" processes. *Mrs Bull* **2005,** *30* (12), 952-966.

8. Watanabe, K.; Katsuhara, S.; Mamiya, H.; Yamamoto, T.; Tajima, K.; Isono, T.; Satoh, T., Downsizing feature of microphase-separated structures via intramolecular crosslinking of

block copolymers. *Chemical Science* **2019,** *10* (11), 3330-3339.

9. Poelma, J. E.; Ono, K.; Miyajima, D.; Aida, T.; Satoh, K.; Hawker, C. J., Cyclic Block Copolymers for Controlling Feature Sizes in Block Copolymer Lithography. *ACS Nano* **2012,** *6* (12), 10845-10854.

10. Asai, Y.; Yamada, K.; Yamada, M.; Takano, A.; Matsushita, Y., Formation of Tetragonally-Packed Rectangular Cylinders from ABC Block Terpolymer Blends. *ACS Macro Lett* **2014,** *3* (2), 166-169.

11. Yu, J. Y.; Liu, F. Q.; Tang, P.; Qiu, F.; Zhang, H. D.; Yang, Y. L., Effect of Geometrical Asymmetry on the Phase Behavior of Rod-Coil Diblock Copolymers. *Polymers-Basel* **2016,** *8* (5).

12. Pryamitsyn, V.; Ganesan, V., Self-assembly of rod–coil block copolymers. *The Journal of Chemical Physics* **2004,** *120* (12), 5824-5838.

13. Gao, J.; Tang, P.; Yang, Y. L., Non-lamellae structures of coil-semiflexible diblock copolymers. *Soft Matter* **2013,** *9* (1), 69-81.

14. Kumar, N. A.; Ganesan, V., Communication: Self-assembly of semiflexible-flexible block copolymers. *J Chem Phys* **2012,** *136* (10).

15. Zhao, Y.; Qi, B.; Tong, X.; Zhao, Y., Synthesis of double side-chain liquid crystalline block copolymers using RAFT polymerization and the orientational cooperative effect. *Macromolecules* **2008,** *41* (11), 3823-3831.

16. Nagano, S., Random Planar Orientation in Liquid-Crystalline Block Copolymers with Azobenzene Side Chains by Surface Segregation. *Langmuir* **2019,** *35* (17), 5673-5683.

17. Jiang, X.-Q.; Zhao, R.-Y.; Chang, W.-Y.; Yin, D.-X.; Guo, Y.-C.; Wang, W.; Liang, D.-H.; Yang, S.; Shi, A.-C.; Chen, E.-Q., Highly Ordered Sub-10 nm Patterns Based on Multichain Columns of Side-Chain Liquid Crystalline Polymers. *Macromolecules* **2019,** *52* (13), 5033-5041.

18. Verploegen, E.; Zhang, T.; Murlo, N.; Hammond, P. T., Influence of variations in liquid-crystalline content upon the self-assembly behavior of siloxane-based block copolymers. *Soft Matter* **2008,** *4* (6), 1279.

19. Shah, M.; Pryarnitsyn, V.; Ganesan, V., A model for self-assembly in side chain liquid crystalline block copolymers. *Macromolecules* **2008,** *41* (1), 218-229.

20. Li, X. K.; Huang, F.; Jiang, T.; He, X. H.; Lin, S. L.; Lin, J. P., Phase behaviors of side chain liquid crystalline block copolymers. *Rsc Adv* **2015,** *5* (2), 1514-1521.

21. Lv, Y. S.; Wang, L. Q.; Wu, F. S.; Gong, S. T.; Wei, J.; Lin, S. L., Self-assembly and stimuli-responsive behaviours of side-chain liquid crystalline copolymers: a dissipative particle dynamics simulation approach. *Phys Chem Chem Phys* **2019,** *21* (14), 7645-7653.

22. Verploegen, E.; Zhang, T.; Jung, Y. S.; Ross, C.; Hammond, P. T., Controlling the

Morphology of Side Chain Liquid Crystalline Block Copolymer Thin Films through Variations in Liquid Crystalline Content. *Nano Lett* **2008,** *8* (10), 3434-3440.

23. Xie, H. L.; Li, X.; Ren, J.; Bishop, C.; Arges, C. G.; Nealey, P. F., Controlling domain orientation of liquid crystalline block copolymer in thin films through tuning mesogenic chemical structures. *Journal of Polymer Science Part B: Polymer Physics* **2017,** *55* (6), 532-541.

24. Komura, M.; Yoshitake, A.; Komiyama, H.; Iyoda, T., Control of Air-Interface-Induced Perpendicular Nanocylinder Orientation in Liquid Crystal Block Copolymer Films by a Surface-Covering Method. *Macromolecules* **2015,** *48* (3), 672-678.

25. Fukuhara, K.; Fujii, Y.; Nagashima, Y.; Hara, M.; Nagano, S.; Seki, T., Liquid‐Crystalline Polymer and Block Copolymer Domain Alignment Controlled by Free‐Surface Segregation. *Angewandte Chemie International Edition* **2013,** *52* (23), 5988-5991.

26. Wang, T. J.; Li, X.; Dong, Z. J.; Huang, S.; Yu, H. F., Vertical Orientation of Nanocylinders in Liquid-Crystalline Block Copolymers Directed by Light. *ACS Appl Mater Inter* **2017,** *9* (29), 24864-24872.

27. Lo, T. Y.; Dehghan, A.; Georgopanos, P.; Avgeropoulos, A.; Shi, A. C.; Ho, R. M., Orienting Block Copolymer Thin Films via Entropy. *Macromolecules* **2016,** *49* (2), 624-633.

28. Isono, T.; Ree, B. J.; Tajima, K.; Borsali, R.; Satoh, T., Highly Ordered Cylinder Morphologies with 10 nm Scale Periodicity in Biomass-Based Block Copolymers. *Macromolecules* **2018,** *51* (2), 428-437.

29. Nakatani, R.; Takano, H.; Chandra, A.; Yoshimura, Y.; Wang, L.; Suzuki, Y.; Tanaka, Y.; Maeda, R.; Kihara, N.; Minegishi, S.; Miyagi, K.; Kasahara, Y.; Sato, H.; Seino, Y.; Azuma, T.; Yokoyama, H.; Ober, C. K.; Hayakawa, T., Perpendicular Orientation Control without Interfacial Treatment of RAFT-Synthesized High-chi Block Copolymer Thin Films with Sub-10 nm Features Prepared via Thermal Annealing. *ACS Appl Mater Inter* **2017,** *9* (37), 31266-31278.

30. Maher, M. J.; Bates, C. M.; Blachut, G.; Sirard, S.; Self, J. L.; Carlson, M. C.; Dean, L. M.; Cushen, J. D.; Durand, W. J.; Hayes, C. O.; Ellison, C. J.; Willson, C. G., Interfacial Design for Block Copolymer Thin Films. *Chem Mater* **2014,** *26* (3), 1471-1479.

31. Yoshimura, Y.; Chandra, A.; Nabae, Y.; Hayakawa, T., Chemically tailored high-chi block copolymers for perpendicular lamellae via thermal annealing. *Soft Matter* **2019,** *15* (17), 3497-3506.

# Chapter 5

# A High-χ Silicon-backbone in Combination with Fluorinated Side Chains Block Copolymer of Ultra-fast Thermal Annealing for Forming Perpendicular Pattern

## 5-1. Introduction

The self-assembly of block copolymers (BCPs) could form pattern in 1-100 nm scale, holding promise for the next-generation lithography applications. In general, lithography demands BCPs with a high χ parameter, high etching contrast, and orientation control. Among all reported BCP materials, silicon-based BCPs exhibited advantages of the high χ parameter and etching contrast. The high χ parameter enables the minimization of both self-assembled periodic nanostructure and interfacial roughness[1 2 3 4]. For example, one widely studied silicon-based BCP is poly(styrene-*b*-dimethylsiloxane) (PS-*b*-PDMS), which has a χ parameter of PS-*b*-PDMS (χ~0.2) five times that of poly(styrene-*b*-methyl methacrylate) PS-*b*-PMMA (χ~0.04).[5] As a result, the reported minimum feature size of PS-*b*-PDMS (~8 nm[6 5]) was much smaller than that achieved in PS-*b*-PMMA (~24 nm[7]). Additionally, the Si-containing block within the self-assembled BCP can be directly transformed into siloxane into silicon oxide via oxygen plasma etching.

One limitation for common silicon-based BCPs, such as poly(dimethylsiloxane-*b*-methyl methacrylate) (PDMS-*b*-PMMA)[8], polyhedral oligomeric silsesquioxane (POSS) containing BCP[9], poly(trimethylsilylstyrene-*b*-D,L-lactide)[10], poly(lactide-*b*-dimethylsiloxane-*b*-lactide)[10] and poly(3-hydroxystyrene)-*b*-poly(dimethylsiloxane)[11], is that the imbalanced surface free energy (SFE) of counter-blocks poses difficulty on orientation control of the self-assembled patterns in thin films. In fact, the desired perpendicular orientation of domains requires long-time solvent annealing, which is incompatible with current process in semi-conductor manufacturing. To address the problem, our group introduced the hydroxyl-end groups to the siloxane-based backbone of BCP[12 13], as to balance SFE of PS and siloxane-based blocks. Methyl vinyl siloxane was selected as the precursor because it can be introduced to functional side chain via a thiol-ene reaction or hydrosilylation. The thiol-ene click reaction is particularly attractive because of the usage of metal-free catalyst[14]. However, the attempt to balance SFE via chemical tailoring on BCP diminishes the segregation strength between blocks and limits the minimization of feature domain size.

Alternatively, Bates [15]invented the neutralization control on interfaces for perpendicular orientation of BCP domain. However， neutralization of the both top and bottom interfaces in

thin film became challenging, as the designed BCPs of imbalanced SFEs easily exhibit strongly preferential interaction with a broad accessible temperature range[15]. To facilitate the perpendicular orientation of BCP domain, development of neutral materials for both interfaces were desired. Optimization of top neutralized interface was more difficult, because the similar polarity of BCP and top neutral materials in organic solvent leads to the problem on processability based on direct spin coating in steps. Bates and Wilson et al. [15 16 17 18 19 20 21] recently invented the spin-coatable polarity switching top coats and demonstrated the orientation control using Si-containing BCPs by thermal annealing in ambient conditions. The core polarity-switching mechanism relies on the maleic anhydride moiety, which undergoes ring opening and closing reactions that modulate the polarity of the top coat between the as-cast and annealed states. A convenient methodology based on topography analysis ("hole" or "island") was also established to guide the estimation on optimized neutral conditions at top and bottom interfaces.

Conclusively, a silicon-containing BCP of higher $\chi$ parameter without any preferential interaction to thin film interfaces is in demand. On the other hand, the long fluorinated side chain exhibited an extremely low SFE (SFE~10 mN/m, dependent on type of crystal or liquid crystal phase[22 23]), which is even lower than that of siloxane (SFE~20 mN/m)[24]. Thus, the introduction of fluorinated side chain into backbone of siloxane could effectively enhance the hydrophobicity of block[25] and create a higher $\chi$ parameter with PS (SFE~43 mN/m)[24] segments. Additionally, the low friction property of fluorinated side chain[26 27 28] in combination with highly mobile siloxane backbone promotes the self-assembly in kinetics during thermal annealing process, which is decisive for rapid annealing requirements. The high etch resistance of the siloxane block should be expected despite the introduction of side chain. The hole and island test was used in this study for development of neutral surface materials. The combination of neutral top and bottom interfaces resulted in a perpendicular orientation of lamellae within optimized BP film thickness scope when annealed at 180 ℃ for 5 minutes or less.

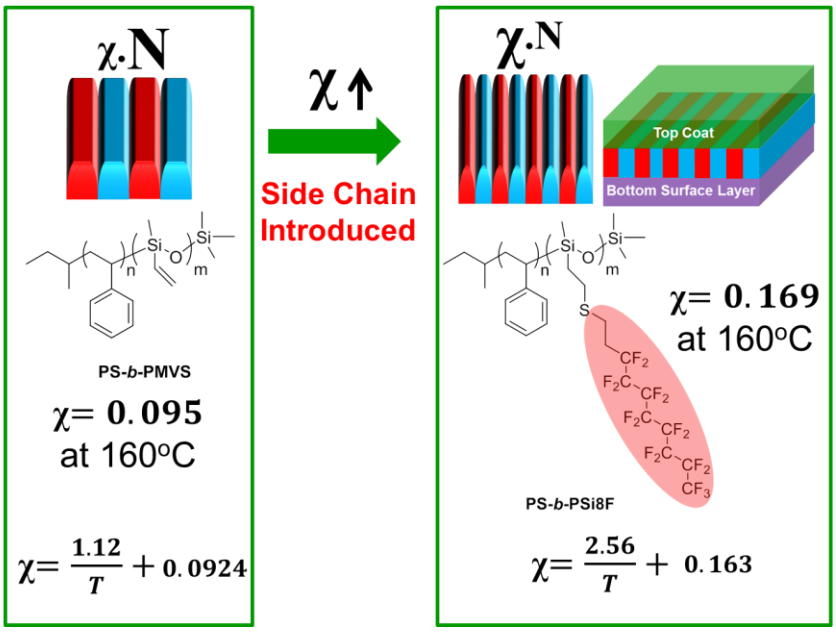


**Scheme 5-1.** Schematic illustration of the molecular design on block copolymer.

## 5-2. Experimental Section

### 5-2-1. Materials

Styrene was washed by 0.1M sodium hydroxide (NaOH) aqueous solution for three times and dried by magnesium sulfide ($MgSO_4$), afterwards, calcium hydride ($CaH_2$) was added and stirred overnight before distillation. After the distillation, *di-n-butyl*magnesium ($MgBu_2$) was added under Ar protection to remove any residual water in styrene. Trap to trap process was further carried out to degas using liquid nitrogen as the freezing source. Similarly, 1,3,5-trimethyl-1,3,5-trivinylcyclotrisiloxane (D3v) was distilled over $CaH_2$ and subsequently degassed under Ar. Chlorotrimethylsilane (TMSiCl) was degassed under Ar. All other materials were reagent grade, purchased from Kanto Chemical Co. Inc., Tokyo Chemical Industry, FUJIFILM Wako Pure Chemical Corporation, and Sigma-Aldrich, and used as received. The detailed synthetic procedures of the homopolymers, top coat and bottom random copolymers are described in the following sections.

### 5-2-2. Methods

$^1$H NMR spectra were recorded with a JEOL JNM-ECS400 (400 MHz) instrument using chloroform-d as the solvent. GPC (gel permeation chromatography) analysis was performed on a Shodex GPC-101 instrument, which was equipped with columns of Shodex LF804. The number average molecular weights ($M_n$) and molecular weight distributions ($M_w/M_n$) were determined by GPC (Showa-Denko GPC-101) with polymer/tetrahydrofuran solution at a flow rate of 1.0 ml/min at 40 °C and calibrated with polystyrene. Thermal behaviors of polymer were estimated from a Seiko DSC 7020 differential scanning calorimeter (DSC) at a heating rate of 10 °C /min under a nitrogen flow. The transition temperature values were determined from the second heating and cooling scan. The scanning temperature range was set from -30 °C to 200 °C, and the second scanning curve was used for analysis. Small angle X-ray scattering (SAXS) measurements were carried out using Bruker SAXS NanoSTAR (Output:50kV, 50mA) instrument. After monochromatic processing by a Göbel mirror, a concentrated CuKα radiation (wavelength:1.5416Å) was applied to the sample. The scatted X-ray was collected by a 2D-PSPC detector to determine the morphologies in bulk sample. Bright-field transmission electron microscope (TEM) images of the sample structure were also obtained using a Hitachi H7650 Zero A under a 100 kV accelerating voltage. Bulk samples were prepared for TEM analysis by first being pasted onto epoxy resin for handling and then microtomed (Reichert-Jung Ultracut E) by a DiATOME diamond knife at room temperature to a preset thickness of 70 nm. The sections produced were then placed onto TEM grids and stained by ruthenium oxide for observation. $O_2$-RIE treatments were performed by etching instrument (SATO VAC, Inc.). The oxygen flow rate was set to 40

sccm and the applied power used was 20 W. The thin film samples were prepared using a MIKASA spin coater IH-D7, and the film thicknesses were measured by a FILMETRICS F20-EXR. AFM (NanoWizard Ultra Speed A, JPK) was used to observe the surface architectures of the BCP thin films at room temperature. Using the method allowing the estimation of δ from a knowledge of the structural formula of the material[29], the density of fluorinated block is estimated and the volume fraction of the fluorinated block is further calculated.

**5-2-3. Synthesis of homopolymer homo-PMVS**

In a 30 mL Schlenk flask 15 mL dehydrated tetrahydrofuran (THF) without stabilizer was added under Ar protection. To remove the moisture and oxygen dissolved in THF, after being cooled down to -78 ℃, roughly 0.2 ml *sec*-BuLi (in 1.04 M hexane/cyclohexane solution) was added with THF solution color changing from transparent to yellow. Afterwards, Schlenk flask was kept under room temperature till the previous yellow color vanished, indicating that *sec*-BuLi in solution became inactive. Again, Schlenk flask was cooled down to -78 ℃, 0.200 mL *sec*-BuLi (0.003 g, 0.208 mmol in 1.04 M cyclohexane solution) was added as the initiator of the anionic polymerization. Subsequently, a calculated amount of 1,3,5-trimethyl-1,3,5-trivinylcyclotrisiloxane (D3v) monomers (2.0 g, 7.75 mmol) was added into the reactor. After 10 min, the reaction temperature was increased to -20 ℃. Excessive TMSiCl was added into the reactor after 24 hr and the resulting polymer was precipitated in methanol. A transparent viscous liquid was obtained.

$^1$H NMR($CDCl_3$, 400MHz) δ(ppm): 0.14 (s, 3H, $CH_3$), 5.76-6.04 (br, 3H, $CH=CH_2$).

**5-2-4. Synthesis of homopolymer homo-PSi8F**

In a 10 mL recovery flask, 0.10 g synthesized homo-PMVS (1.16 mmol MVS units), 1.67 g 1H,1H,2H,2H-perfluorodecanethiol (3.0 mole equiv. to MVS repeating units) and 28.6 mg Azobisisobutyronitrile (AIBN) (0.15 mole equiv. to MVS repeating units) were added to degased 2.0 mL THF. The solution was stirred at 65 ℃ for 5 hr under Ar atmosphere. Afterwards, the flask was soaked in liquid $N_2$ for termination of reaction. A chunk of white solid was precipitated after the reaction. The insoluble solid was repeatedly washed with THF and dried in vacuo under 40 ℃ overnight to yield the product.

**Table 5-1.** Characteristics of the synthesized homopolymers.

| Homopolymer | $M_n$ (kg mol$^{-1}$) | $Đ$ | $T_g$ (°C) | $T_{iso}$(°C) |
|---|---|---|---|---|
| Homo-PMVS | 9900 | 1.54 | - | - |
| Homo-PSi8F | insoluble | insoluble | - | 53.5 |

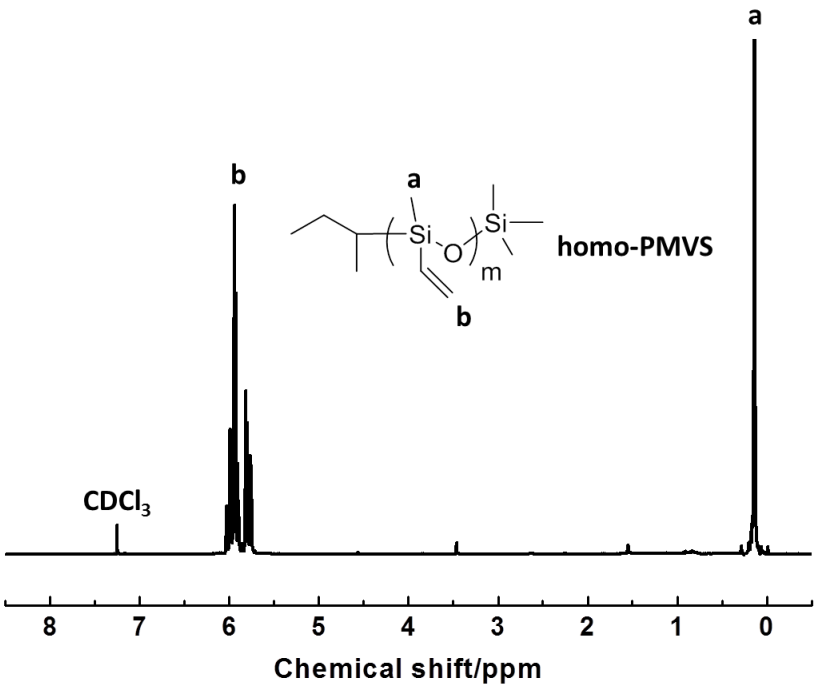


**Figure 5-1**. $^1$H NMR spectra of synthesized homo-PMVS in $CDCl_3$ solvent.

**5-2-5. Synthesis of poly(styrene-*b*-methyl vinyl siloxane) (PS-*b*-PMVS)**

The synthesis of the targeted diblock copolymer could be divided into two steps, the synthesis of precursor main chain polymer PS-*b*-PMVS via sequential anionic living polymerization and the subsequent post-functionalization for introduction of side chains.

Here, SV13.6 ($PS_{11.3k}$-*b*-$PMVS_{2.3k}$ the subscripts indicate the molecular weight of block) was used to illustrate the synthetic routine. In a 50 mL Schlenk flask 30 mL dehydrated tetrahydrofuran (THF) without stabilizer was added under Ar protection. To remove the moisture and oxygen dissolved in THF, after being cooled down to -78 °C, roughly 0.3 ml *sec*-BuLi (in 1.04 M hexane/cyclohexane solution) was added with THF solution color changing from transparent to yellow. Afterwards, Schlenk flask was kept under room temperature till the previous yellow color vanished, indicating that *sec*-BuLi in solution became inactive. Again, Schlenk flask was cooled down to -78 °C, 0.014 mL *sec*-BuLi

(0.0009 g, 0.015 mmol in 1.04 M cyclohexane solution) was added as the initiator of the anionic polymerization. Subsequently, a calculated amount of styrene (1.50 g, 14.42 mmol) was added into the tetrahydrofuran (THF) with initiators and stirred at -78 ℃ for 30 min under Ar atmosphere, with solution color changed to orange. Afterwards, a calculated amount of 1,3,5-trimethyl-1,3,5-trivinylcyclotrisiloxane (D3v) monomers (0.50 g, 1.94 mmol) was added into the reactor. After 10 min, the reaction temperature was increased to -20 ℃. Excessive TMSiCl was added into the reactor after 24 hr and the resulting polymer was precipitated in methanol.

$^1$H NMR($CDCl_3$, 400MHz) δ(ppm): 0.14 (s, 3H, $CH_3$), 1.42 (br, 2H, $CH_2$), 1.84 (br, 1H, CH), 5.76-6.04 (br, 3H, $CH=CH_2$), 6.31-6.72 (br, 2H, Ar), 6.89-7.22 (br, 3H, Ar).

### 5-2-6. Synthesis of side chain modified PS-*b*-PSi8F

Thiol-ene reaction was utilized to introduce the functional side chains to the backbone of precursor BCP. In a 10 mL recovery flask, 0.20 g SV13.6 (0.40 mmol MVS units), 0.57 g 1H,1H,2H,2H-perfluorodecanethiol (3.0 mole equiv. to MVS repeating units) and 9.8 mg Azobisisobutyronitrile (AIBN) (0.15 mole equiv. to MVS repeating units) were added to degased 2.0 mL THF. The solution was stirred at 65 ℃ for 5 hr under Ar atmosphere. Afterwards, the flask was soaked in liquid $N_2$ for termination of reaction. The solution was then precipitated in hexane (or mixed hexane and methanol *v:v*=1:3, dependent on $M_n$ of BCP) and repeated for twice. The white powder was dried in vacuo under 40 ℃ overnight to yield the desired product.

$^1$H NMR($CDCl_3$, 400MHz) δ(ppm): 0.15(s, 3H, $CH_3$ PSi8F), 0.90(br, 2H, Si-$CH_2$), 1.41(br, 2H, $CH_2$ PS), 1.82(br, 1H, CH PS), 2.29(t, 2H, Si-$CH_2$-S-$CH_2$ PSi8F), 2.59(t, 2H, $CF_2$-$CH_2$ PSi8F), 2.69(t, 2H, $CF_2$-$CH_2$ -$CH_2$ PSi8F), 6.31-6.72 (br, 2H, Ar), 6.89-7.22 (br, 3H, Ar).

### 5-2-7. Estimating the surface free energies of the homopolymer Homo-PSi8F

The surface free energies (SFEs) of the homopolymers were calculated by measuring the water and diiodomethane contact angles (C.A.) of the homopolymer thin films. The thin films were prepared by spin-coating 1.0 w.t. % propylene glycol methyl ether acetate (PGMEA) (PTFEMA-*r*-PMMA-*r*-PMAA) or methanol (TC) solution on bare silicon wafers at 3000 rpm for 30 s to obtain thin films with thicknesses of 40-50 nm. These thin films were annealed at 200 ℃ for 10 min for polarity switch or cross-linking before the C.A. measurements. Because of the poor solubility of Homo-PSi8F in common organic solvents, the thin films were prepared by uniformly placing approximately 20 mg homopolymer powders on 1cm × 1cm bare silicon wafer, and melted at 180 ℃ for 24 hours under vacuum to obtain the thin film sample for the C.A. measurements.

**Table 5-2(a)**. Contact angles and surface free energies (SFEs) of homopolymers.

| Homopolymer | C.A.($H_2O$)[a] ($^o$) | C.A.($CH_2I_2$)[a] ($^o$) | Dispersive (mJ $m^{-2}$) | Polar (mJ $m^{-2}$) | SFE[b] (mJ $m^{-2}$) |
|---|---|---|---|---|---|
| PSi8F | 125.6±1.1 | 108.6±1.3 | 5.6 | 0.3 | 5.9 |
| TC | 91.8±1.1 | 52.8±1.3 | 31.2 | 1.7 | 32.9 |
| PTFEMA-*r*-PMMA -*r*-PMAA | 92.9±0.7 | 67.2±0.6 | 22.3 | 3.1 | 25.4 |
| PS[c] | - | - | 34.5 | 6.1 | 40.7 |

[a] Average values of measurements taken at 5 positions. [b] Calculated by the Owens-Wendt method. [c] The SFE of PS was obtained from the reference[39] as PS was partially soluble in diiodomethane.

**Table 5-2(b)**. Interfacial tensions estimated from Owens-Wendt model.

| Block-interface | $\gamma_{PS\text{-}Top}$ | $\gamma_{PSi8F\text{-}Top}$ | $\gamma_{PS\text{-}Btm}$ | $\gamma_{PSi8F\text{-}Btm}$ | $\gamma_{PS\text{-}PSi8F}$ |
|---|---|---|---|---|---|
| Interfacial tension $\gamma^a$ (mJ $m^{-2}$) | 1.44 | 10.93 | 1.83 | 7.02 | 15.99 |

[a] Estimated from the equation 6a in the reference[24].

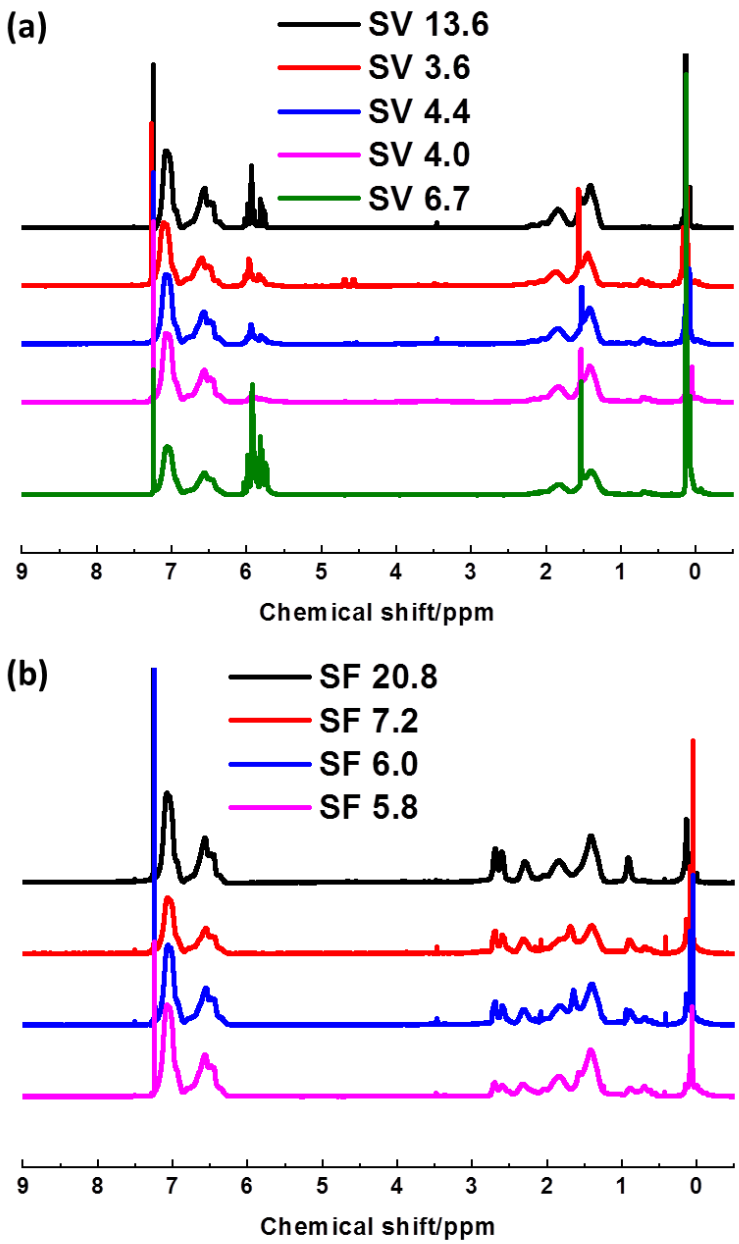


**Figure 5-2.** $^{1}$H NMR spectras of synthesized (a) PS-*b*-PMVSs and (b) PS-*b*-PSi8Fs in $CDCl_3$ solvent.

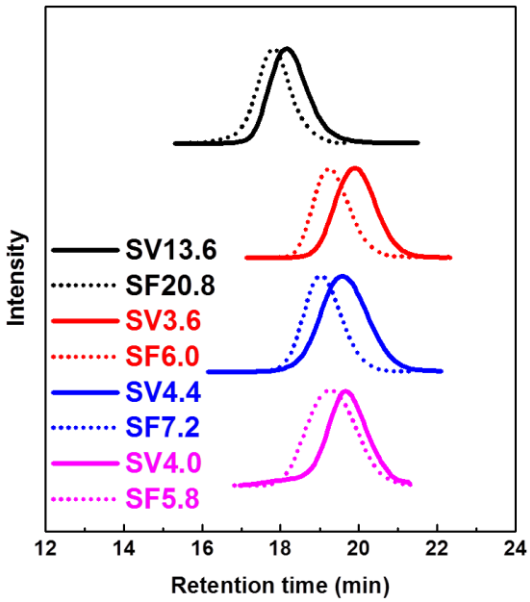


**Figure 5-3.** SEC chromatography of precursor PS-*b*-PMVS (SV) and corresponding PS-*b*-PSi8F (SF) after post-functionalization.

### 5-2-8. Detailed information about the estimation of $\chi_{eff}$

Molten BCP samples were placed in 0.01 mm thick glass tubes and the SAXS profiles were collected at each temperature in 10 ˚C decrement in cooling cycles, at which the temperature was maintained for 30 min prior to the measurements to reach a thermally equilibrated state. The scattering function $I(q)$ from the disordered melt of the BCPs with a dispersity in the molecular weight and asymmetry in the segmental volume was summarized below, where $A_0$ is a fitting constant, $S(q)$ and $W(q)$ together are correlation functions of the BCP, $g(q)$ is a modified Debye function and $y(q)$ is a dimensionless wave vector, $r_c$ is the molar volume normalized over the degree of polymerization of the BCP, $f_X$ is volume fraction of $X$ calculated using the bulk densities for each block (1.05 g cm$^{-3}$ for PS, 1.01 g cm$^{-3}$ for PMVS and 1.65 g cm$^{-3}$ for PSi8F, $v_X$ is the molar volume of $X$. $N_X$ is the degree of polymerization normalized over a common reference volume ($v_0$ = 118 Å$^3$) for $X$, $FW$ is the formula weight of $X$, $N_A$ is Avogadro's constant, and $b_X$ is the segmental length of $X$. Here the dispersities for each homopolymer segment ($D_X$) are assumed equal and were estimated from the $M_w/M_n$ of the BCP and weight fraction of $X$ ($w_X$). Four parameters, including $b_X$ for both polymers, $A_0$ and $\chi_{eff}$, were optimized in a least-squares fit to the SAXS profiles at a certain temperature. The calculated parameters for each sample at varied temperatures were summarized in Table 5-6.

$$I(q) = \frac{A_0}{\frac{S(q)}{W(q)} - 2\chi}$$

$$S(q) = \langle S_{PS,PS} \rangle + 2\langle S_{PS,Y} \rangle + \langle S_{Y,Y} \rangle$$

$$W(q) = \langle S_{PS,PS} \rangle \cdot \langle S_{Y,Y} \rangle - \langle S_{PS,Y} \rangle^2$$

$$\langle S_{X,X}(q) \rangle = r_c {f_X}^2 {g^{(2)}}_X(q) \quad \langle S_{PS,Y}(q) \rangle = r_c f_{PS} f_Y {g^{(1)}}_{PS}(q) {g^{(1)}}_Y(q)$$

$$r_c = \frac{(v_{PS} N_{PS} + v_Y N_Y)}{(v_{PS} \cdot v_Y)^{1/2}} \quad v_X = \frac{FW_X}{\rho_X N_A} \quad N_X = \frac{v_X M_{\mathrm{n},X}}{v_0 FW_X}$$

$${g^{(1)}}_X(q) = \frac{1}{y_X(q)} \cdot \left\{1 - [y_X(q) \cdot (\mathrm{D}_X - 1) + 1]^{-(\mathrm{D}_X - 1)^{-1}}\right\}$$

$${g^{(2)}}_X(q) = \frac{2}{y_X(q)^2} \cdot \left\{-1 + y_X(q) + [y_X(q) \cdot (\mathrm{D}_X - 1) + 1]^{-(\mathrm{D}_X - 1)^{-1}}\right\}$$

$$y_X(q) = \frac{N_X {b_X}^2}{6} q^2 \quad \mathrm{D} \equiv \mathrm{D}_{PS} = \mathrm{D}_Y = \frac{M_\mathrm{w}/M_\mathrm{n} - 1}{{w_{PS}}^2 + {w_Y}^2} + 1$$

$X$ = PS or $Y$ ($Y$ = PMVS or PSi8F)

**Table 5-3.** The fixed parameters used to estimate $\chi_{\mathrm{eff}}$ for PS-*b*-PMVS (SF6.7) and PS-*b*-PSi8F (SF5.8).

| BCP | $r_c$ | $M_\mathrm{n}$ (kg mol$^{-1}$) | $M_\mathrm{w}$ (kg mol$^{-1}$) | $M_{\mathrm{n,PS}}$ (kg mol$^{-1}$) | $f_{\mathrm{PS}}$ | $w_{\mathrm{PS}}$ |
|---|---|---|---|---|---|---|
| PS-*b*-PMVS (SV6.7) | 92 | 6.7 | 7.6 | 3.7 | 0.55 | 0.56 |
| PS-*b*-PSi8F (SF5.8) | 61 | 5.8 | 7.4 | 3.6 | 0.72 | 0.62 |

### 5-2-9. Bulk sample preparation

The bulk samples used to investigate the bulk morphologies and domain spacings ($d_{\mathrm{spacing}}$) of the microphase-separated structures were prepared by slowly evaporating a dilute BCP THF solution filtered through a 0.25 μm pore size PTFE membrane syringe filter at 30 ˚C. The as-prepared samples were dried under a reduced pressure before annealing at 160 ˚C for 24 hr.

### 5-2-10. Synthesis of PTFEMA-*r*-PMMA-*r*-PMAAs

The following procedure was used for PTFEMA-*r*-PMMA-*r*-PMAA 61-36-3, but is representative of all neutral bottom surface layer materials syntheses. The numeric label denotes the weight composition. Cross-linkable PMAA was fixed to 5% molar percentage in all syntheses.

2,2,2-Trifluoroethyl methacrylate (TFEMA), methyl methacrylate (MMA) and methacrylic acid (MAA) were distilled to yield clear and colorless liquid prior to use. Azobisisobutyronitrile (AIBN) was recrystallized prior to use. 2,2,2-Trifluoroethyl methacrylate (1.22 g, 7.2 mmol, 0.48 eq), methyl methacrylate (0.72 g, 7.2 mmol, 0.48 eq), methacrylic acid (0.06 g, 0.7 mmol, 0.04 eq), and AIBN (0.007 g, 0.004 mmol, 0.00025 eq) were added to a 50 mL 3-neck round bottom flask equipped with a stir bar and rubber septa. The reagents were dissolved in THF (7.5 mL) and the solution was deoxygenated by vigorously bubbling nitrogen through the solution for 30 minutes. The reaction vessel, under positive nitrogen pressure, was immersed in an oil bath at 70 °C. The reaction was heated and stirred for 24 h and quenched at 0 °C. The viscous liquid was precipitated into methanol (300 mL) and filtered. The resulting polymer was dissolved in THF and reprecipitated into methanol for two additional times. The polymer was dried in vacuo overnight at 40 °C and the white powder product (93% yield) was obtained.

$^1$H NMR (400 MHz, chloroform-*d*, δ, ppm): 0.84-0.89, 1.01-1.11, 1.21-1.26, 1.40-1.48, 1.76-2.08, 3.49-3.70, 4.20-4.45.

**5-2-11. Synthesis of top coat TC**

The following procedure was used for TC syntheses. Maleic anhydride (0.52 g, 5.3 mmol, 0.50 eq), 4-*tert*-butylstyrene (0.86 g, 5.3 mmol, 0.50 eq), and AIBN (0.009 g, 0.053 mmol, 0.005 eq) were added to 50 mL three-neck round bottom flask equipped with stir bar and rubber septa. The contents of the flask were dissolved in 10 mL of uninhibited THF. Nitrogen was vigorously bubbled through the stirring solution for 30 minutes. The vessel was kept under positive nitrogen pressure and was immersed into an oil bath at 65 ˚C for 16 hours. The reaction was quenched at 0 ˚C, and the solvent was reduced in vacuo to yield a viscous liquid. The viscous liquid was precipitated into either 200 mL of 3:1 (by volume) hexanes:dichloromethane and filtered. The resulting polymer was dissolved in 10 mL of THF and reprecipitated into 3:1 (by volume) hexanes:dichloromethane two more times. The white solid was dried at 100 ˚C in *vacuo* overnight.

**Table 5-4.** Characteristics of the synthesized BSLs and TC.

| Random Copolymer | $M_n$ (kg mol$^{-1}$) | $Đ$ |
|---|---|---|
| PTFEMA-*r*-PMMA-*r*-PMAA | 34500 | 1.74 |
| PS-*r*-PMAA | 11700 | 1.66 |
| PMMA-*r*-PMAA | 76600 | 2.28 |
| TC | 10300 | 3.77 |

**Preparation of TC salt**

In a 10 mL scintillation vial, 0.5 g of polymer was added to circa 10 mL of 50% aqueous trimethylamine (TMA). The vial was sealed and stirred until the polymer was completely dissolved. Isolation of the salt was achieved via precipitation into THF solution. The solution of polymer in aqueous TMA was slowly added to the precipitation solution. The precipitate was filtered and dried in vacuo at room temperature.

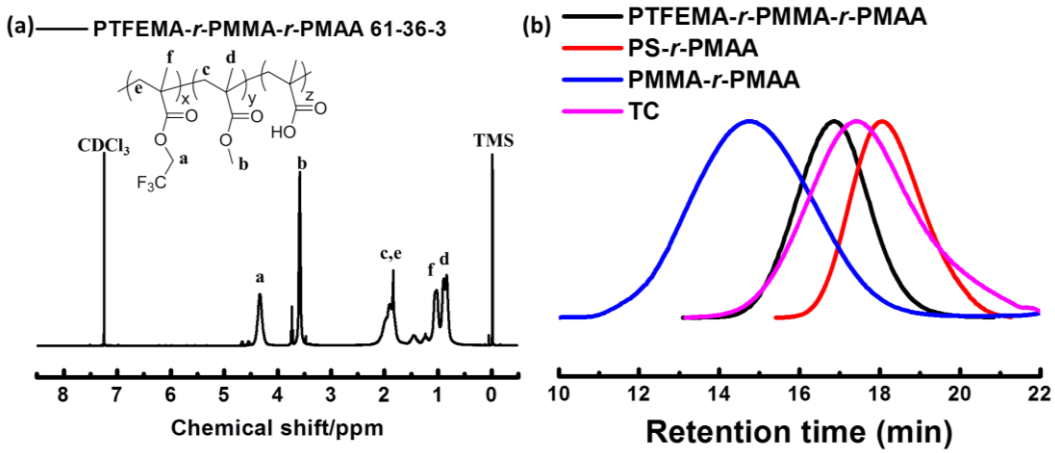


**Figure 5-4**. $^1$H NMR spectra of the synthesized PTFEMA-*r*-PMMA-*r*-PMAA and (b) GPC chromatograms of the used random copolymers in thin film study.

**5-2-12. Thin film preparation**

Bare silicon wafers cut into 1 cm$^2$ pieces were sonicated in toluene for 3 min, and dried in a stream of nitrogen. The substrates were treated with a mixture of $H_2O_2$ (30%) and $H_2SO_4$ (70%) (*v/v*) at 80 ˚C for 40 min. The wafers were rinsed with water repeatedly and dried in a stream of nitrogen. Bottom surface layer (BSL) were generated by spin coating a 1.0 wt% poly(2, 2, 2-trifluoroethyl methacrylate)-*random*-poly(methyl

methacrylate)-*random*-poly(methacrylic acid) (PTFEMA-*r*-PMMA-*r*-PMAA) solution in propylene glycol monomethyl ether acetate (PGMEA) solution at 3000 rpm and 30 s onto the cleaned silicon wafers, followed by crosslinking at 200 ˚C for 5 min. The substrates were sonicated in toluene to remove any random copolymers that were not attached to the substrate and rinsed with fresh toluene. Furthermore, approximately 1.0 wt % solutions of the BCPs in toluene were spin-coated at 5000 rpm for 30 s onto the surface-modified silicon substrates to obtain thin films with ca. 1.0 $L_0$ thicknesses. The film thickness was tuned by changing BCP solution concentration. A 0.5 wt% top coat (TC) methanol solution were filtered and spin coated onto the BCP film at 7500 rpm for 30 s. The thin films were then annealed at 180 ˚C for 5min under ambient conditions for polarity switch of TC. An $O_2$-RIE treatment was conducted for a certain time (40 sccm, 20 W, 30 Pa) to selectively remove the top coat and any organic compound in BCP.

## 5-3. Results and Discussion

### 5-3-1. Synthesis of PS-*b*-PMVS

The synthesis routine for the targeted BCP was illustrated in Scheme 5-2. All precursor BCPs PS-*b*-PMVS with distinctive molecular weights were synthesized via sequential anionic polymerization of styrene and 1,3,5-trimethyl-1,3,5-trivinyl cyclotrisiloxane. As shown in the Figure 5-5(a), the appearance of characteristic proton signals from two blocks indicated the

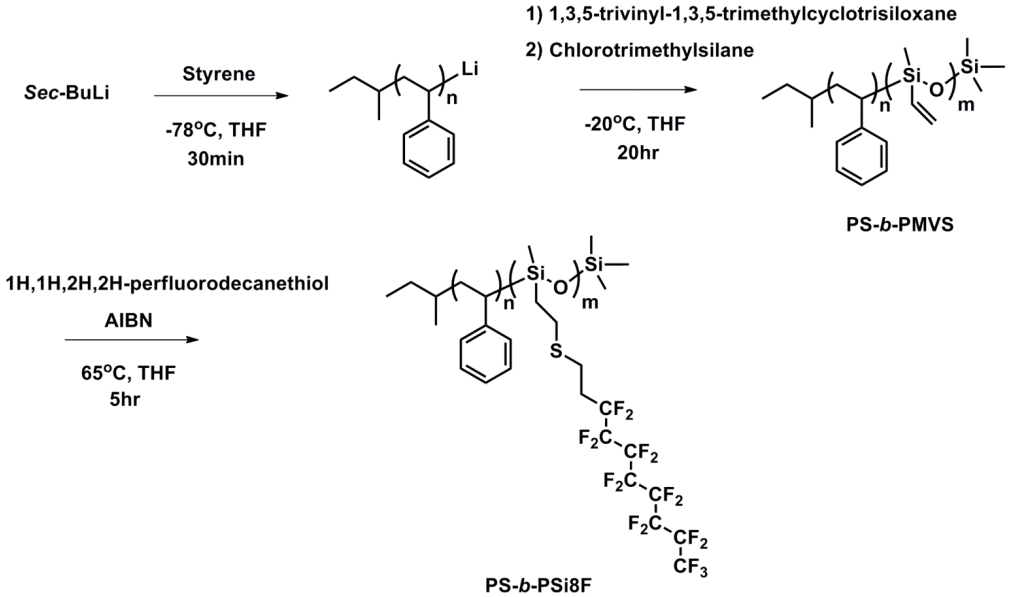


**Scheme 5-2.** Synthetic scheme of PS-*b*-PMVS precursor via sequential living anionic polymerization of styrene and cyclic siloxane-based monomer and post-functionalization with thiols.

successful synthesis of PS-*b*-PMVS. The composition of vinyl siloxane was kept at low level because of the bulky side chain introduced in next step.

### 5-3-2. Synthesis of PS-*b*-PSi8F

After the synthesis of precursor BCPs, the vinyl groups in the siloxane unit was chemically modified with 1H,1H,2H,2H-perfluorodecanethiol. In Figure 5-5(b), the disappearance of proton signals from vinyl groups and the arising of proton signals from introduced side chain indicated the complete conversion in modification reaction. The signals in $^{1}$HNMR could be well assigned to each proton in the targeted product. In the thiol-ene reaction, excessive amount of thiol were added to ensure high conversion. Accordingly, the trace of SEC was shifted to the higher $M_n$ after the modification reaction with a nearly constant dispersity, as presented in Figure 5-3. The determined $M_n$ of PS-*b*-PSi8F from SEC was in good agreement with the estimated $M_n$ based on the precursor PS-*b*-PMVS.

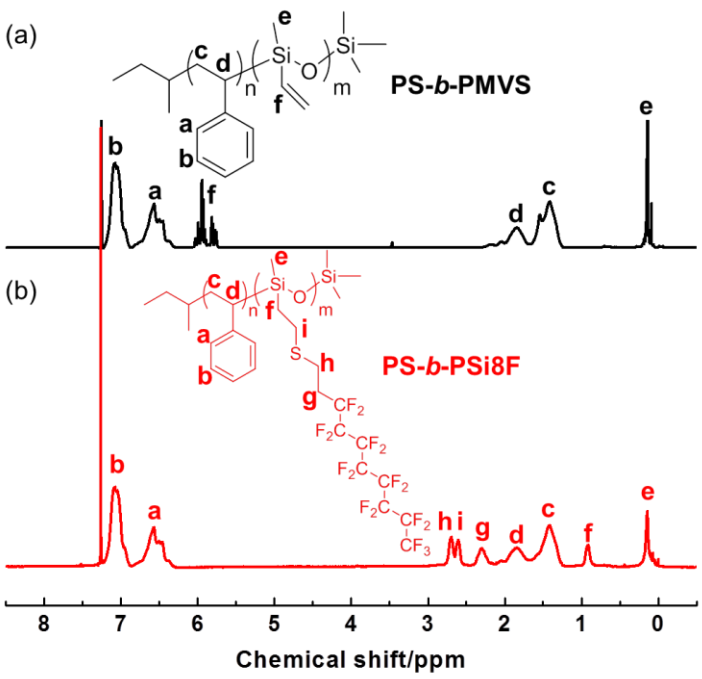


**Figure 5-5.** An illustrative $^{1}$H NMR spectra of (a) PS-*b*-PMVS (SV13.6) and (b) PS-*b*-PSi8F

### 5-3-3. Bulk Morphology

The bulk morphologies of the synthesize PS-*b*-PSi8Fs were characterized by small-angle X-ray scattering (SAXS). Additionally, as shown in Figure 5-6, differential scanning calorimetry (DSC) characterization suggested an obviously glass transition attributed to PS

segments. A transition from liquid crystal ordered phase to isotropic phase were detected below 40 ˚C, which is proportional to the molecular weight of PS-*b*-PSi8F. Compared to the isotropic transition of similar fluorinated side chain attached to poly-(methyl acrylate)-based[30] or poly-(isoprene)-based backbone[23], the transition temperature of fluorinated side chain attached to siloxane-based backbone is significantly lower, because of the intrinsic flexible polysiloxane-based backbone. As the annealing temperature for bulk sample and thin film in this study were set 160 ˚C and 180 ˚C, which is far beyond the isotropic transition temperature, the interplay between liquid crystal nano-ordering and block segregation in self-assembly under thermal annealing became negligible and merely amorphous self-assembled nano-structure was preserved. The formation of liquid crystal nanostructure from side chain was also evidenced by the SAXS result (Figure 5-7) of as-prepared SF20.8 bulk sample evaporated from THF solution at 30 ˚C, which is below the isotropic transition temperature. A significant scattering peak at $q$ of 2.0 $nm^{-1}$ indicates a liquid crystal ordering

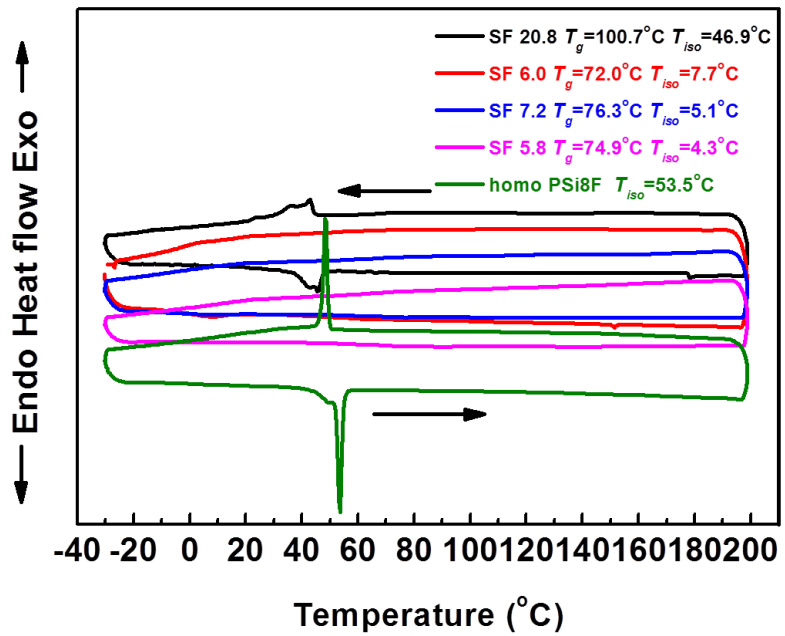


**Figure 5-6**. DSC curves of the studied PS-*b*-PSi8Fs and homo- PSi8F at a heating rate of 10 ˚C /min under nitrogen atmosphere.

of 3.14 nm, which is highly consistent with the reported ordering scale from similar fluorinated side chain in literatures[30] [23]. Besides, the SAXS profile measured in cooling process below the isotropic transition temperature (Figure 5-7(a) ) clearly reveals the appearance of scattering peak at $q$ of 2.0 $nm^{-1}$, which is attributed to the ordering of liquid crystalline side chain. Comparatively, no liquid crystalline ordering of side chains was observed in SF6.0, SF7.2 and SF5.8 in X-ray analysis at room temperature because of the observed isotropic transition temperatures below 10 ˚C in DSC analysis (Figure 5-6).

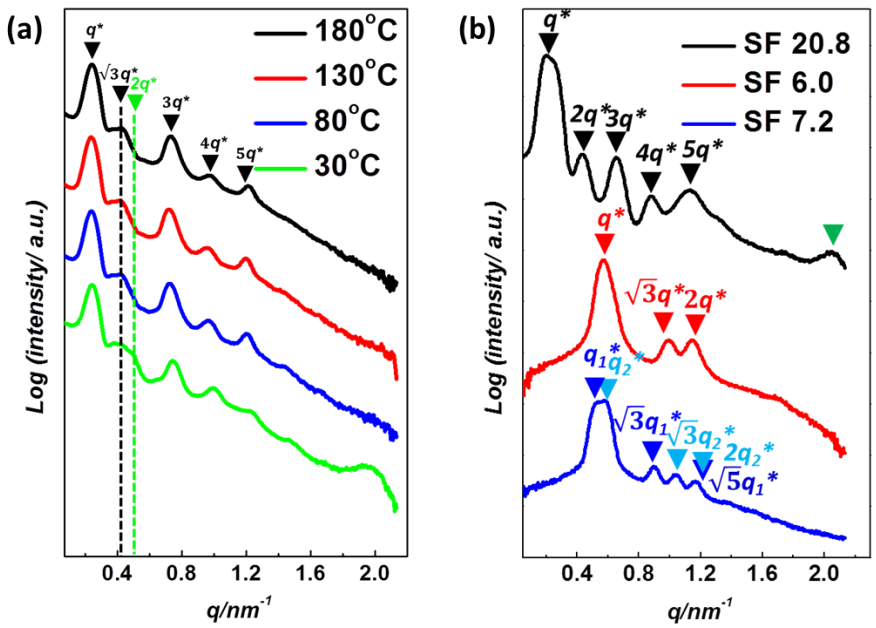


**Figure 5-7.** (a) SAXS profiles of the chemically modified SF20.8 bulk sample measured at 180 ˚C, 130 ˚C, 80 ˚C and 30 ˚C, respectively in cooling cycle. (b) SAXS profiles of the as-prepared chemically modified PS-*b*-PSi8F bulk samples. The green triangle indicates the scattering peak attributed to the LC structure of perfluoroalkyl side chain.

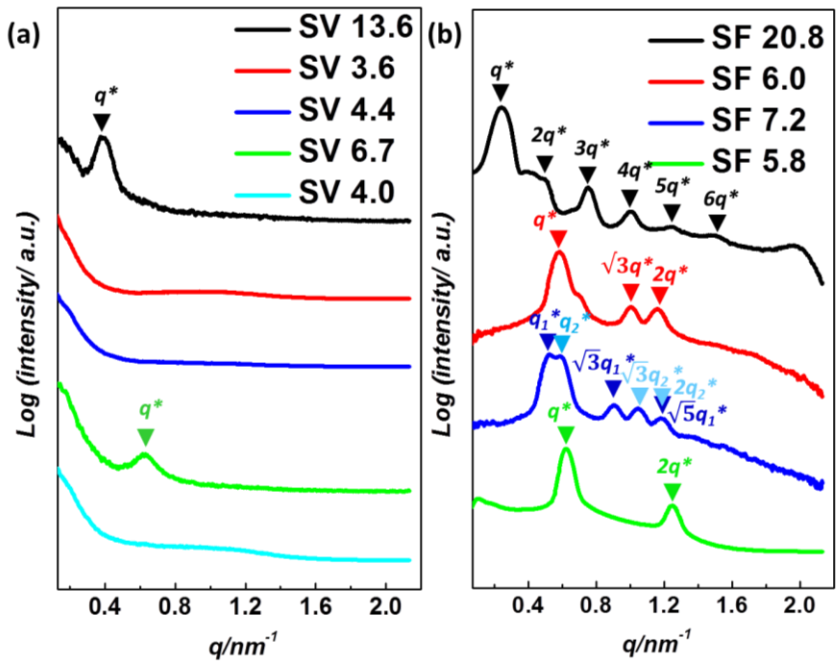


**Figure 5-8.** SAXS profiles of the synthesized (a) precursor PS-*b*-PMVS and (b) chemically modified PS-*b*-PSi8F bulk samples following thermal annealing at 160 ˚C for 24 hr.

Following thermal annealing, all chemical modified PS-*b*-PSi8Fs exhibited multiplied scattering peaks, indicating the formation of ordered self-assembly nanostructure. The domain spacing of formed nanostructure was determined by the position of the primary scattering peak and the results were summarized in Table 5-5. The self-assembly morphology of SF20.8 reveals a temperature-dependence (Figure 5-7(a) ), as a significantly enhanced broad scattering peak at $2q^*$ partially overlapped with the board peaks at $\sqrt{3}q^*$ was detected below isotropic transition temperature of LC side chain. The change in featured scattering peaks suggests a morphology transition from low-ordered hexagonally packed cylinder to the mixed type combined with lamellae as major fraction in presence of side chain liquid crystalline ordering. It's worthy to note that the periodicity or correlation length of the formed morphology resulting from SF20.8 are not long-ranged because of the observed relatively wide full width at half maximum (FWHM) of primary scattering peak, which are against the extremely high driving force ($\chi N$) for self-assembly. The reason is possibly attributed to the metastable state formed in fast annealing process. Besides, the preferential self-assembly into lamellae was also supported by the observed SAXS peak at integer ratios in SF20.8 bulk sample prepared from slow evaporation at room temperature (Figure 5-7(b) ). When $M_n$ of BCP was further reduced from 20 k to 6 k Da, the morphology exhibited a transition from low-ordered quasi-lamellae (quasi-LAM) to cylinder of two distinctive packing arrays, dependent on the specific volume fraction of block in each BCP. Comparatively, all precursors PS-*b*-PMVSs exhibited disordered morphologies and thus indicated the increment on $\chi$ parameter after chemical modification. The fact revealed the significant enhancement effect of side chain on the magnitude of segments segregation. Generally, as the periodicity of self-assembly structure was revealed by the number of scattering peak, chemical modified SF6.0 and SF7.2 exhibited multiple scattering peaks, compared to the sole primary scattering peak of precursor BCP SV6.7 with the similar molecular weight. The difference also indicated the enhanced $\chi$ parameter between blocks. Furthermore, SF7.2 reveals a deformed anisotropic hexagonally packed cylinder (aniso-HEX) structure, which is different from the mostly obtained isotropic hexagonally packed cylinder (HEX) structure in SF6.7. The TEM image in Figure 5-9 gives evidence for the formed aniso-HEX structure. The splitted primary scattering peaks at $q_1^*$ and $q_2^*$ in SAXS are obviously attributed to the deformed array. This deformed anisotropic array was thought caused by the mismatch between certain block volume fraction and bulky perfluoroalkyl side chains of high rigidity, as clearly revealed by the SCFT studies later. Owing to the similar side chain effects, a comb-coil diblock copolymer capable of forming tetragonally-packed cylinder structure was previously reported[31]. In contrast, the SAXS profile of SF5.8 with relatively more asymmetric volume fraction ($f_{PS}$=0.72) revealed a lamellar morphology with 10.1 nm domain spacing.

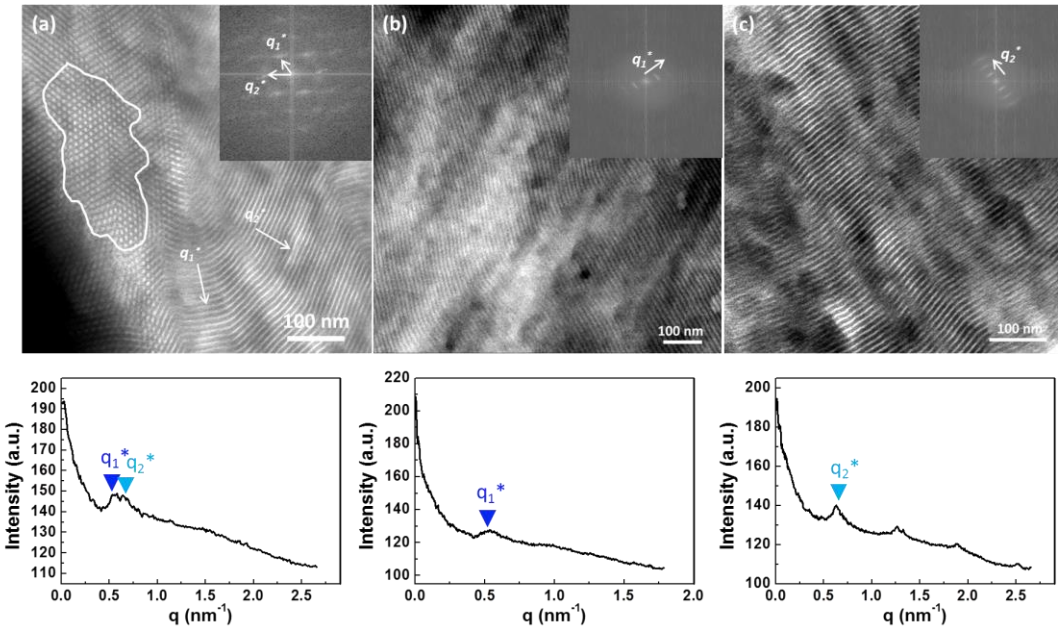


**Figure 5-9.** TEM micrograph showing the domains corresponding to the (a) top view of PSi8F cylinders in anisotropic hexagonal packing and (b)-(c) coexisted striations of two distinctive dimensions at $q_1$* and $q_2$* corresponding to the side view in SF 7.2 annealed bulk sample. The upper right inset displays the fast Fourier-transform (FFT) pattern of the real-space image (a) within the indicated white circle. The bottom profile in each TEM image displays the integration of FFT signals along the radius to the center of FFT image. Two distinctive spacings could be thus estimated $d_1$=11.8 nm ($q_1$*) and $d_2$=10.0 nm ($q_2$*), which are in response to two center-to-center distances $a_1=2/\sqrt{3}\ d_1$=13.6 nm and $a_2=2/\sqrt{3}\ d_2$=11.5 nm, respectively. The PS and PSi8F domains are seen dark and bright, respectively, because of the selective ruthenium tetraoxide staining onto PS segments.

**Table 5-4**. Characterization data of the synthesized BCPs.

| BCP | Label[a] | $M_n$[b] (kg mol$^{-1}$) | $Đ$ | $w_{PS}$[c] | $f_{PS}$[d] | $d_{spacing}$[e] (nm) | Morphology[f] | ODT[g] (°C) |
|---|---|---|---|---|---|---|---|---|
| PS-*b*-PMVS | SV13.6 | 13.6 | 1.22 | 0.83 | 0.82 | 16.1 | Disordered | - |
| | SV4.4 | 4.4 | 1.29 | 0.86 | 0.86 | - | Disordered | - |
| | SV3.6 | 3.6 | 1.20 | 0.81 | 0.80 | - | Disordered | - |
| | SV4.0 | 4.0 | 1.35 | 0.93 | 0.93 | - | Disordered | |
| | SV6.7 | 6.7 | 1.14 | 0.56 | 0.55 | 10.0 | Disordered | - |
| PS-*b*-PSi8F | SF20.8 | 20.8 | 1.18 | 0.43 | 0.54 | 26.2 | Quasi-LAM | |
| | SF7.2 | 7.2 | 1.17 | 0.49 | 0.60 | 12.0/10.7 | Aniso-HEX | |
| | SF6.0 | 6.0 | 1.16 | 0.39 | 0.50 | 10.7 | HEX | >290 |
| | SF5.8 | 5.8 | 1.28 | 0.62 | 0.72 | 10.1 | LAM | 230-240 |

[a]The labels SV and SF refer to PS-*b*-PMVS and PS-*b*-PSi8F, respectively, while the number to the right refers to the number-average molecular weight ($M_n$) of the polymer. [b] $M_n$ and dispersities ($Đ$) were obtained by SEC using THF as the eluent based on PS standards. [c] PS weight fractions ($w_{PS}$) of PS-*b*-PMVS and of PS-*b*-PSi8F were calculated via $^1$H NMR. [d] PS volume fractions ($f_{PS}$) were calculated using the bulk densities for each block (1.05 g cm$^{-3}$ for PS, 1.01 g cm$^{-3}$ for PMVS and 1.65 g cm$^{-3}$ for PSi8F). [e] The domain spacings ($d_{spacing}$) were estimated from the position of first-order scattering peak in the SAXS profile upon thermal annealing at 160 °C for 24 hr. [f] The morphologies in the bulk were determined by SAXS and TEM. [g] ODTs were determined by SAXS at varied temperatures.

**5-3-4. Estimation of $\chi_{eff}$**

To quantify the strength of the segregation before and after chemical modification of fluorinated side chain, random-phase approximation method[32] in terms of the effective Flory-Huggins interaction parameter, expressed by $\chi_{eff} = A/T + B$, where $A/T$ is the enthalpic contribution, and $B$ is the entropic contribution, was used in this study. Firstly, temperature-dependent SAXS analyses were conducted on precursor PS-*b*-PMVS (SV6.7) and chemical modified PS-*b*-PSi8F (SF5.8), starting from 240 ℃ to 160 ℃ or 290 ℃ to 210 ℃ and in 10 ℃ decrements (Figure 5-10 and Figure 5-11). The SAXS profiles of SF5.8 showed a continuous linear change in the $I_{max}^{-1}$-$T^{1}$ plot between 290-240 ℃ and a breakthrough point between 240-230 ℃, as 290-240 ℃ temperatures range is located beyond BCP order-to-disorder transition temperatures (ODTs) (Figure 5-11(b) ). Therefore, the SAXS profiles in the mean-field disordered state were then analyzed based on Leibler's mean-field theory modified to include the effects from the molecular weight dispersity and asymmetry in the segmental volume. Remarkably, as $\chi_{eff}$ is dependent on the reference volume used to calculate $N$, a common reference volume ($v_0$ = 118 Å$^3$) was utilized to compare the $\chi_{eff}$ values with other reported values. The estimated $\chi_{eff}$ value for precursor PS-*b*-PMVS was expressed by $\chi_{eff} = 1.12/T + 0.0924$ (Table 5-6 and Table 5-7). A weak temperature dependence was observed for $\chi_{PS/PDMS}$, possibly because of geometrical packing constraints on the differently shaped monomers of the two species and chain polarization/stretching effects. The estimated $\chi_{eff}$ of PS-*b*-PMVS at 160-240 ℃ was consistent with the previously reported $\chi_{eff}$ of PS-*b*-PDMS (0.108 at 160 ℃)[33 34]. The slightly lower $\chi_{eff}$ value of PS-*b*-PMVS compared to that of PS-*b*-PDMS was possibly attributed to the lower inorganic silicon composition in siloxane-based segments. According to Leibler's theory[35], self-assembly occurs dependent on the magnitude of self-assembly driving force indicator $\chi N$. Based on the estimation results, SV6.7 reveals a $\chi_{eff}N$=8.6, which falls outside the boundary condition of self-assembly ($\chi_{eff}N$ >10.5). In contrast, owing to the enhanced $\chi$ parameter after chemical modification, SF6.7 or SF7.2 of similar $N$ values, even SF5.8 with a lower $N$ value, reveals a $\chi_{eff}N$ >=10.5, which is readily above the segregation limit condition and thus the micro-phase separation occurs. The estimated $\chi_{eff}$ from chemical modified SF5.8 is expressed by $\chi_{eff} = 2.56/T + 0.163$. Compared to the precursor PS-*b*-PMVS, the introduced long fluorinated side chain obviously contributed to a higher $\chi_{eff}$ (0.169 at 160 ℃), which is almost twice of the $\chi_{eff}$ before the chemical modification at annealing temperature. The super-hydrophobic fluorinated side chain increases the hydrophobicity of siloxane segments, as indicated by the measured extremely low 5.9 mJ/m$^2$ SFE value of homo-PSi8F in comparison with the reported 20.4 mJ/m$^2$ SFE value [36] of polydimethylsiloxane at room temperatures. Besides, the SFE of counter-block polystyrene was reported being 40.7 mJ/m$^2$ [37]. Therefore, the increased

difference between SFEs of counter-blocks leads to an enhanced segregation qualified by a higher $\chi_{eff}$ parameter.

**Table 5-6.** The fixed parameters used to estimate $\chi_{eff}$ for PS-*b*-PMVS (SF6.7) and PS-*b*-PSi8F (SF5.8).

| $T$ (°C) | Estimated $\chi_{eff}$ PS-*b*-PMVS (SV6.7) | $T$ (°C) | Estimated $\chi_{eff}$ PS-*b*-PSi8F (SF5.8) |
|---|---|---|---|
| 160 | 0.09500 | 240 | 0.16814 |
| 170 | 0.09482 | 250 | 0.16806 |
| 180 | 0.09488 | 260 | 0.16798 |
| 190 | 0.09483 | 270 | 0.16789 |
| 200 | 0.09478 | 280 | 0.16779 |
| 210 | 0.09467 | 290 | 0.16769 |
| 220 | 0.09478 | | |
| 230 | 0.09462 | | |
| 240 | 0.09448 | | |

**Table 5-7.** Estimated enthalpic and entropic contributions for PS-*b*-PMVS (SF6.7) and PS-*b*-PSi8F (SF5.8).

| BCP | Label | $A/T$ | $B$ |
|---|---|---|---|
| PS-*b*-PMVS | SV6.7 | $1.12/T$ | 0.0924 |
| PS-*b*-PSi8F | SF5.8 | $2.56/T$ | 0.163 |

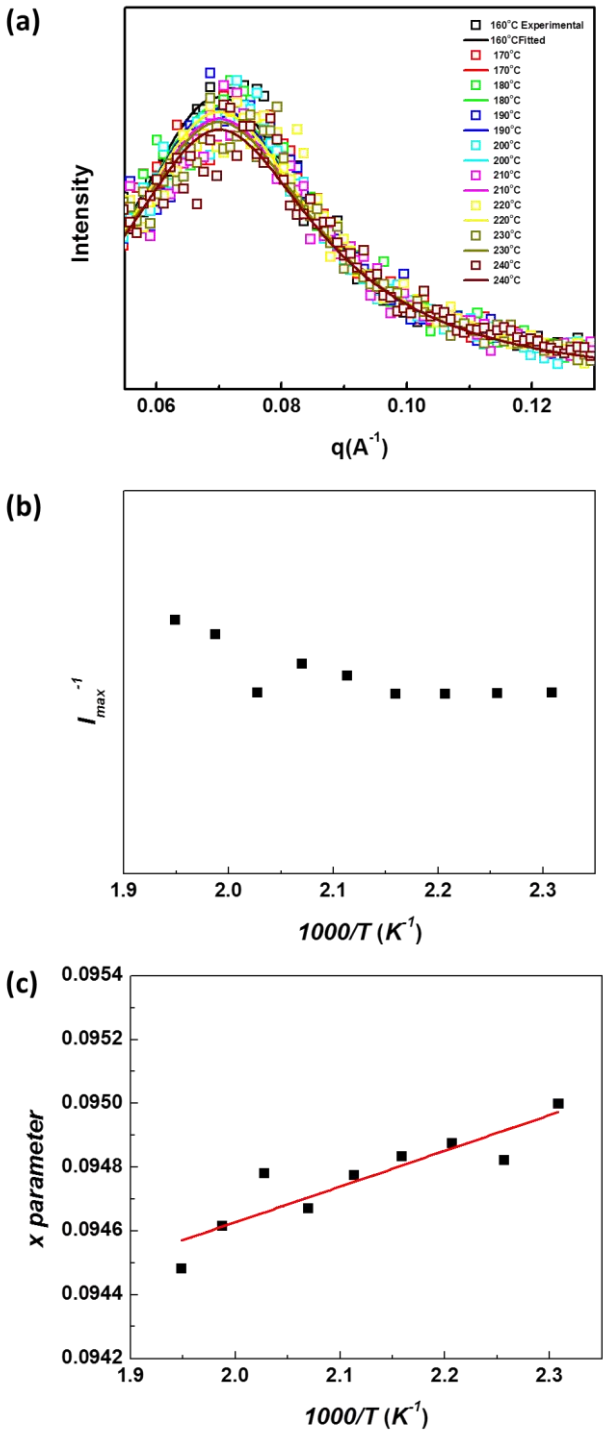


**Figure 5-10.** (a) The scattering profiles measured by SAXS in scatters at 160-240 ˚C and fitted curves at 160-240 ˚C and (b) $I_{max}^{-1}$–$T^{-1}$ plots for PS-*b*-PMVS (SF6.7) and (c) estimated χ parameter–$T^{-1}$ plots for PS-*b*-PMVS (SF6.7).

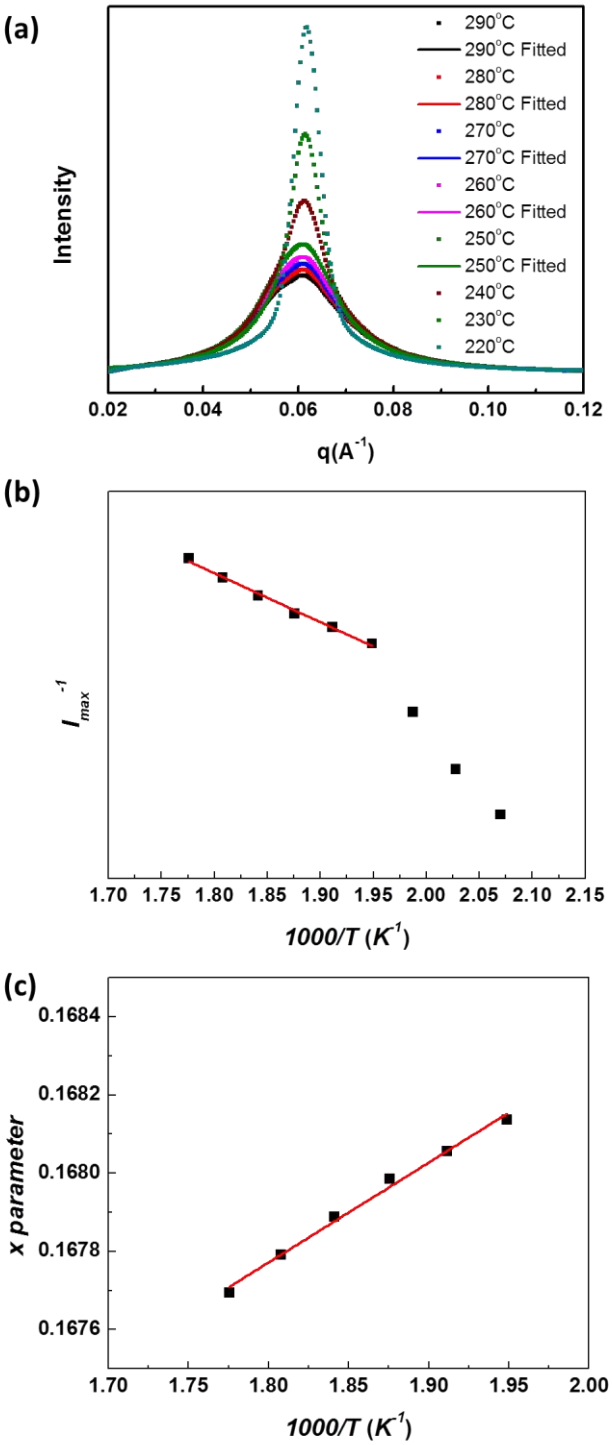


**Figure 5-11.** (a) The scattering profiles measured by SAXS in scatters at 290-220°C and fitted curves at 290-250°C and (b) $I_{max}^{-1}$–$T^{-1}$ plots for PS-*b*-PSi8F (SF5.8) and (c) estimated χ parameter–$T^{-1}$ plots for PS-*b*-PSi8F (SF5.8).

**5-3-5. Morphologies Predictions by Self-consistent field theory (SCFT)**

Briefly, an incompressible melt of AB linear diblock polymers is placed in a simulation volume $V$ where each polymer is modeled as a Gaussian chain characterized using random-walk statistics with volume fractions $f_A$ and $f_B$ with degree of polymerization $N$. The local interactions are governed by a binary interaction parameter $\chi_{AB}$=0.169 at 160 ℃ along with the incompressibility condition of $\Sigma fii$=1. The code for performing SCFT was from the reported literature[38].

The simulated polymers were assumed to be monodisperse with temperature independent densities. The statistical segment lengths of PS and PSi8F were set being 1 and 2.3 units, respectively, according to the estimation based on random-walk model, in which the end-to-end distance is governed by the root square value of molecular weight of each segment. The assumption was additionally supported by the ratio of reported 0.74 nm Gaussian segment length of polystyrene[38] over measured 1.6 nm single perfluoroalkyl side chain in SAXS, considering the semectic phase consisted of a pair of perfluoroalkyl side chains in head-to-head regularity. The statistical segment lengths of PSi8F were also set to other arbitrary units as varied inputs to mimic the rods of different rigidities. A typical grid size of 64 × 64 was used for the 2D SCFT calculations with a 100 contour steps in inner loops. The simulations were performed using the pseudo-spectral method developed by Rasmussen and Kalosakas starting from random initial conditions followed by Anderson acceleration once a stable morphology could be identified (typically at changes in the free energy $\leq 1\times10^{-10}$)[39].

SF20.8 reveals morphology consisted of randomly oriented short rods and cylinders. The extremely high driving force for self-assembly ($\chi N$) leads to the discrete aggregated domain instantly and the morphology is trapped in this metastable state even following extended annealing time, as shown in in-situ evolution of self-assembled morphology in Figure 5-12. Considering the symmetric volume fraction of counter-blocks, lamellar morphology should be expected in coil-coil model. However, the high energy barrier between metastable and stable states attributed to extremely high $\chi N$ prevents the formation of any continuous structure in SCFT prediction. The theoretical prediction is consistent with the SAXS observation of low-ordered cylinders at typical annealing temperature.

As $\chi N$ becomes lower, SF7.2 and SF6.0 of similar symmetric block volume fractions begin to reveal hexagonally packed cylindrical morphologies. In Figure 5-13 the experimentally observed isotropy and anisotropy of hexagonally packing array in SF6.0 and SF7.2 is precisely predicted by SCFT, respectively. The anisotropic packing array leads to at least two distinctive center-to-center periodic distances between adjacent PSi8F cylinders, which were in response with TEM and SAXS characterization results. The two distinctive center-to-center distances from SCFT prediction are estimated being $d_1$=1.14 units and

$d_2$=1.00 units, which are highly consistent with the experimental observation in SAXS and TEM characterizations ($d_1$=1.12 $d_2$). In contrast, a typical isotropic hexagonally packing array consistent with the experimental observation is suggest for SF6.0, which is thought possibly caused by the difference in block volume fraction. As the molecular weight is further reduced to 5.8 k Da, disordered state at 160 ℃ annealing temperature is suggested by SCFT in which two different segments are homogeneously mixed. The inconsistency between SCFT and RPA, in which RPA suggests ODT temperature of SF5.8 between 230 and 240 ℃, originates from the different assumption on BCP dispersity effects on self-assembly.

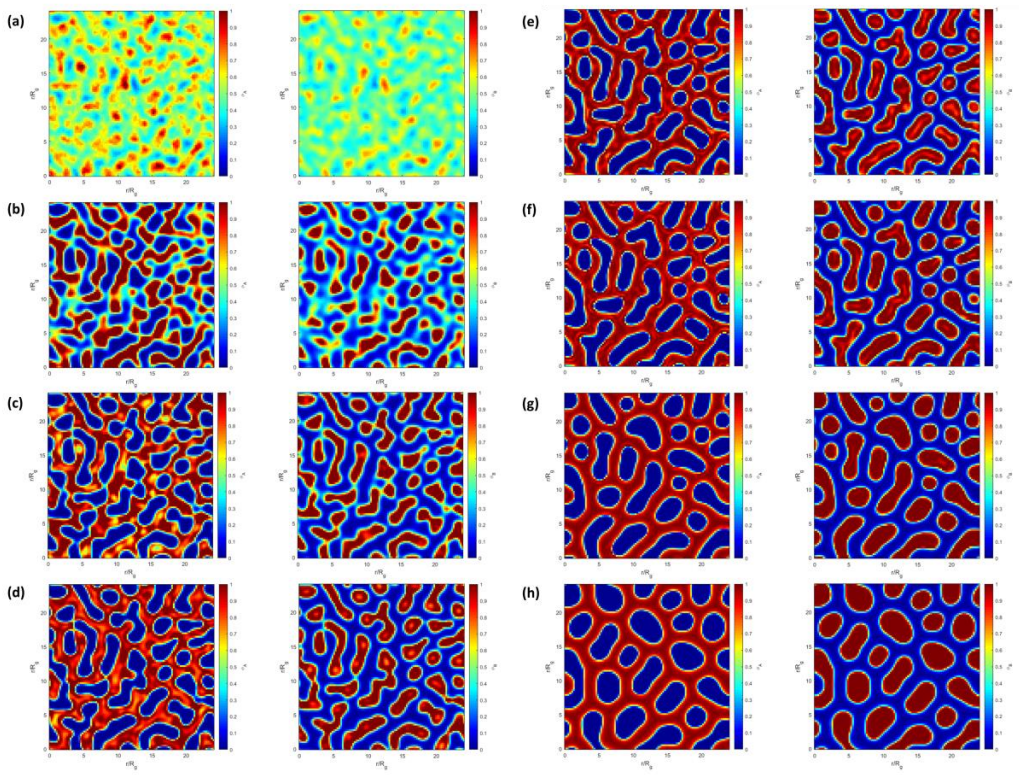


**Figure 5-12.** The in-situ evolution of 2-D morphologies calculated using SCFT for SF 20.8 using the assumptions of varied segments length (a=1; b=2.3) after running for (a) 17 steps; (b) 22 steps; (c) 33 steps; (d) 45 steps; (e) 64 steps; (f) 86 steps; (g) 195 steps; (h) 1003 steps. The red and blue colors indicate PS and PSi8F segments in left column and invert in right column. The density gradient bar for different segments is given next to each image.

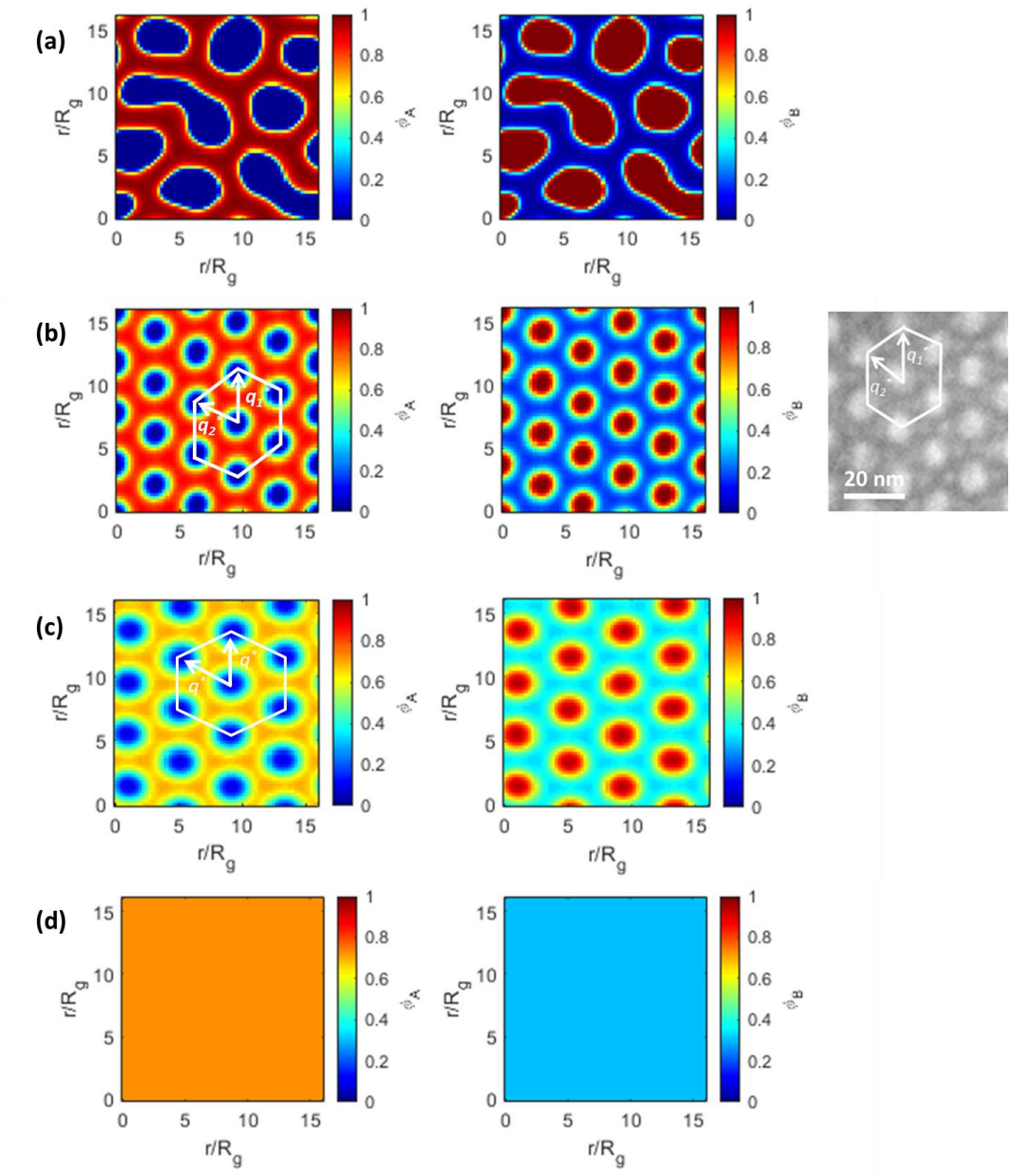


**Figure 5-13.** The predicted 2-D morphologies calculated using SCFT for (a) SF 20.8, (b) SF 7.2, (c) SF 6.0 and (d) SF 5.8. The red and blue colors indicate PS and PSi8F segments in left column and invert in right column. The density gradient bar for different segments is given next to each image. In (b) the experimental TEM image of SF 7.2 is presented at right side for comparison and two distinctive periodic distances are also marked in both simulated SCFT and experimental TEM results.

As the determined ratio of segment lengths was verified, a phase diagram for the investigated PS-*b*-PSi8F, as shown in Figure 5-14, could be further calculated using SCFT prediction. A minimal molecular weight of 6k Da with symmetric volume fraction ($\chi_{eff}N$=11.0) was predicted almost the limit for inducing self-assembly. With the increments of volume fraction $f_{PS}$, a morphology transition from hexagonally packed PS cylinders to lamellae, and a transitional hybrid type consisted of cylinder and short rod to hexagonally packed PSi8F cylinders. No axis symmetry at $f_{PS}$=0.5 was observed for the predicted morphologies in left or right half diagram, which is obviously attributed to the assumption of significantly different segment length for each block representing rigidity. Remarkably, the anisotropic hexagonally packing array was merely predicted in the vicinity of $f_{PS}$=0.6 with relatively low $M_n$, which is correlated with the reported anisotropic fluctuations of hexagonally packed cylinder mostly occurred in weakly segregated states.

To further investigate the effects of varied segments lengths on self-assembled

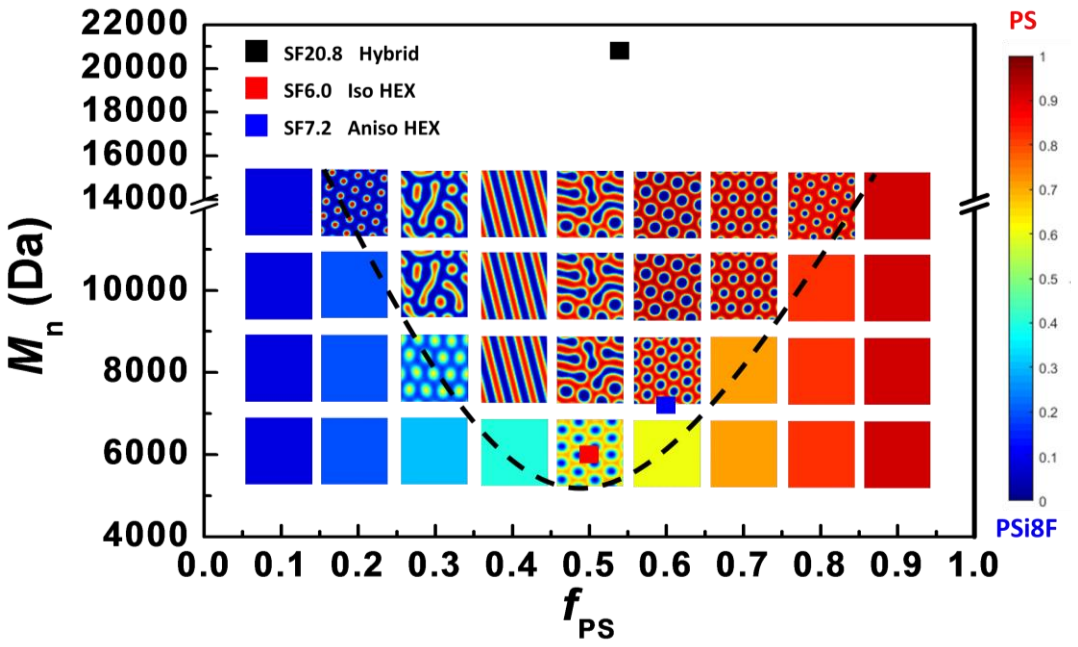


**Figure 5-14.** The predicted 2-D morphologies phase diagram calculated from SCFT using $f_{ps}$=0.1/0.2/0.3/0.4/0.5/0.6/0.7/0.8/0.9 under PS-*b*-PSi8F $M_n$ of 6000/8000/10000/14000 Da with the assumptions of varied segments length (a=1; b=2.3). The homogenous color inside the square indicates the disordered morphology. Dashed lines indicating the boundary between ordered and disordered region are meant solely as a visual aid. The red and blue colors indicate PS and PSi8F segments, respectively and the density gradient bar for the two different segments is given next to the phase diagram.

morphology, the segments length of PSi8F was tuned being 0.5, 0.75, 1.0, 1.5, 2, 3, 4 and 5 times of that of PS segment, respectively, as shown in Figure 5-15. As the segments length of PSi8F was gradually increased, a morphological transition from lamellae to hybrid, and then to hexagonal packed cylinder was revealed. The anisotropy of hexagonal packing array becomes more significant when the segments length of PSi8F is greater than 1.5 times of PS segments. The most obvious anisotropy was observed when PSi8F segments length was between 2 and 3 times of PS segment length, which is consistent with the estimated 2.3 times PSi8F/PS segments length in this study. However, as the segments length was further increased to above 3, the anisotropy of hexagonal packing array seems to diminish again. This transition clearly indicates the dependence of self-assembled morphology on the segments lengths at given block volume fraction and molecular weight.

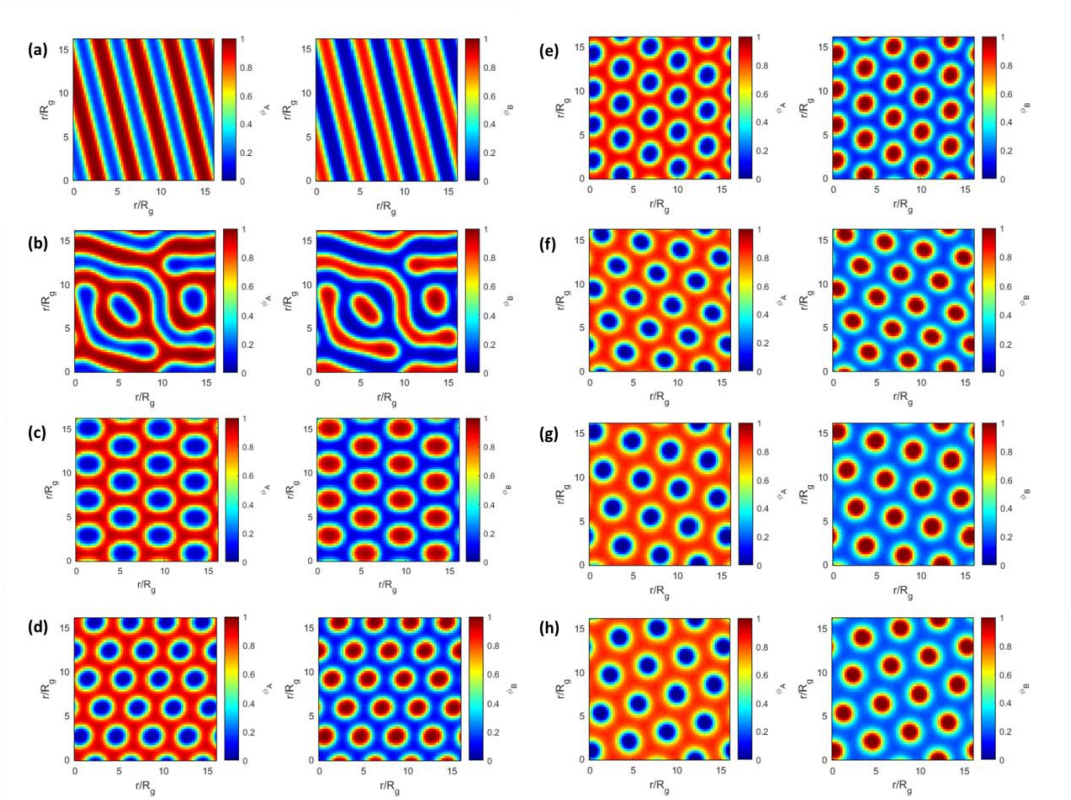


**Figure 5-15.** The predicted 2-D morphologies calculated using SCFT for SF 7.2 using the assumptions of varied segments length (a=1; (a) b=0.5; (b) b=0.75; (c) b=1; (d) b=1.5; (e) b=2; (f) b=3; (g) b=4; (h) b=5). The red and blue colors indicate PS and PSi8F segments in left column and invert in right column. The density gradient bar for different segments is given next to each image.

### 5-3-6. Perpendicular Lamellae in Thin Film

The study on the self-assembled qusai-lamellae structure of SF20.8 ($d_{spacing}$=26.2 nm determined by SAXS) was carried out in thin film. Owing to the extremely hydrophobic fluorinated siloxane blocks compared to PS, the tuning on neutral materials at both top and bottom interfaces were essential.

To address the neutralization problem at BCP bottom interfaces, Cross-linkable random copolymer poly(2,2,2-Trifluoroethyl methacrylate-*random*-methyl methacrylate-*random*-methacrylic acid) (PTFEMA-*r*-PMMA-*r*-PMAA) were used as bottom surface layer (BSL). The embedded major components PTFEMA (SFE~19 mN/m)[40] and PMMA (SFE~40 mN/m)[41] were used to generate a synthetically accessible neutral composition. Within TFEMA and dissimilar MMA monomer acts as analogous of Si-containing PSi8F and PS unit in BCP, respectively. Approximately 3 wt% PMAA was added for cross-linking with hydroxyl-rich wafer substrate under high temperature. Residual un-cross-linked random copolymers were completely rinsed off in prior to the spin coating of BCP. To evaluate the wetting in BSL, confined hole and island test was performed by using another two homopolymer materials, PS-*r*-PMAA and PMMA-*r*-PMAA, both with 3 wt% cross-linkable MAA units. The film stacks were annealed at 180 ˚C for 10 min on a hot plate and subsequently observed by an atomic force microscope.

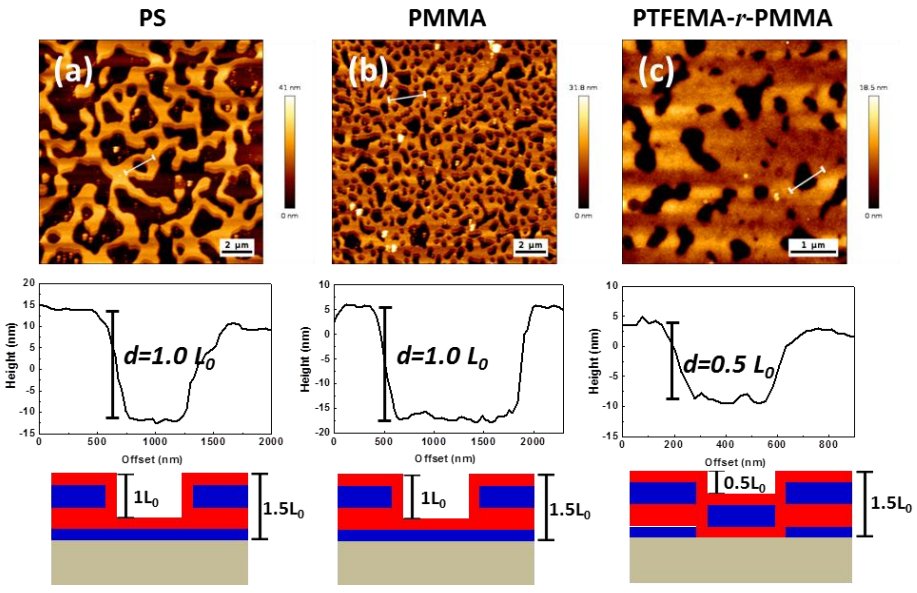


**Figure 5-16.** AFM height, height traces and block wetting of selected PS-*b*-PSi8F ($L_0$ = 26 nm) sample on (a) PS, (b) PMMA and (c) PTFEMA-*r*-PMMA bottom surface layer, annealed at 180 ˚C for 5 min. The red and blue in wetting model denotes PSi8F and PS block, respectively.

Note that according to the previous study, the BCP film thickness plays a non-negligible role in the film surface topography, therefore the BCP film thickness was kept between 1.0 $L_0$ and 1.5 $L_0$ in the test. As shown in Figure 5-16, holes were observed for all studied three BSL materials. The depth of hole for PS-*r*-PMAA and PMMA-*r*-PMAA was measured to be near 1.0 $L_0$, which was supported by the cross-section of AFM height images. Based on the observed hole topography, asymmetric wetting is implied in which less hydrophobic PS block wets BSL interface and more hydrophobic Si8F block wets the air top interface. In contrast, holes with 0.5 $L_0$ depth was observed for the random copolymer PTFEMA-*r*-PMMA-*r*-PMAA. The half hole topography indicates the equally preferential BSL for counter-blocks of ontop BCP and presence of desired neutral BSL materials was confirmed[17].

The development of top coat (TC) materials also responded to the refined hole and island test. A random copolymer consisted of equal mole of maleic anhydride (MA) and 4-tert-Butylstyrene (BSt) was used as top coat materials for test. MA acts as the essential element for polarity switch under thermal annealing and BSt is expected to be non-preferential to PS and PSi8F, which is indicated by the mediated SFE (~22 mN/m)[42] of homopolymer Poly-(4-*tert*-Butylstyrene). To better evaluate the wetting at top interface, PS-*r*-PMA was utilized as BSL as PS block is readily more preferential to the bottom surface.

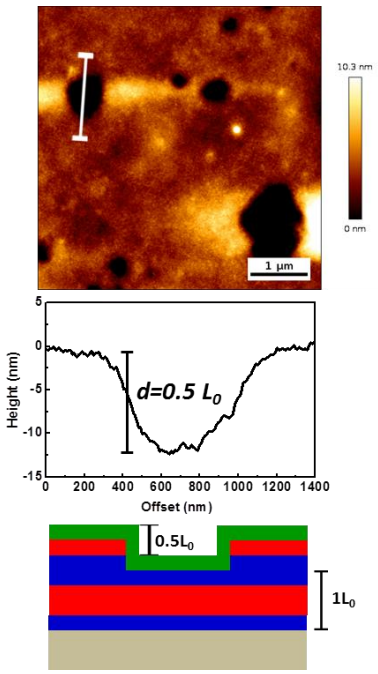


**Figure 5-17.** AFM height, height traces and block wetting of selected PS-*b*-PSi8F ($L_0$ = 26 nm) sample, confined between a top coat and a PS bottom surface layer, annealed at 180 °C for 5 min. The red, blue and green in wetting model denotes PSi8F block, PS block and TC layer, respectively.

After thermal annealing at 180 °C for 10 min, a hole topology of 0.5 $L_0$ depth was observed by AFM scanning. The fact implied the presence of neutral top coat materials at top interface.

As the two neutral materials at top and bottom interfaces were obtained, PS-*b*-PSi8F was confined between neutral interfaces and thermal annealed at 180 °C for polarity switch of TC and self-assembly of BCP. A typical featureless surface was characterized as shown in Figure 5-18, because of the coverage of approximately 17 nm thickness top coat ontop BCP. Oxygen-plasma reactive-ion etching ($O_2$-RIE) was thereby used to remove the organic compound and reveal the underlying self-assembly nanostructure of BCP.

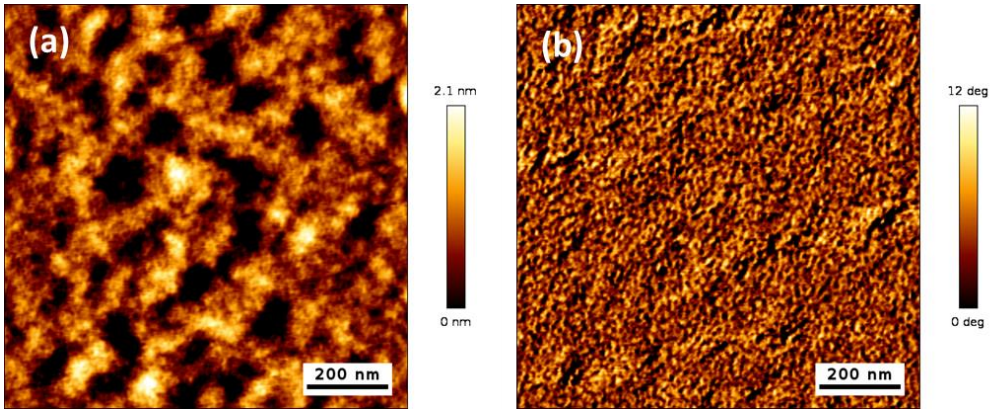


**Figure 5-18.** A typical AFM (a) height and (b) phase image of selected PS-*b*-PSi8F ($L_0$ = 26 nm) sample, confined between a neutral top coat and bottom surface layer, annealed at 180 °C for 5 min.

In theory, the perpendicular orientation of any BCP thickness become energetically favorable, however, one interface may deviate slightly from the perfect neutrality. Therefore, only a discrete BCP thickness scope can produce perpendicular orientation. Therefore, an optimization on BCP thickness becomes necessary. In the experimental, the annealing condition was fixed to 180 °C for 10 min. As shown in Figure 5-19, when BCP thickness varies from 0.5 $L_0$ to 2.2 $L_0$, perpendicular lamella with long correlation length was only achieved in vicinity of 1.0 $L_0$. In contrast, 0.5 $L_0$ exhibited a perpendicular lamellar pattern of lower orders. The domain orientation dependence on BCP thickness was revealed in previous theoretic study[20], as the used bottom surface layer or top coat may be slightly preferential to particular one block. Beneficial from the high etching resistance of Si-containing block, the domains consisted of PSi8F segments were readily identified in AFM images. The periodic length of the optimized formed pattern is averagely estimated to be 22 nm, which is located near to the region of sub-10 nm half pitch. The SEM observations (Figure 5-20) on the thin film sample with 1.0 $L_0$ BCP thickness were also consistent with the corresponding AFM image.

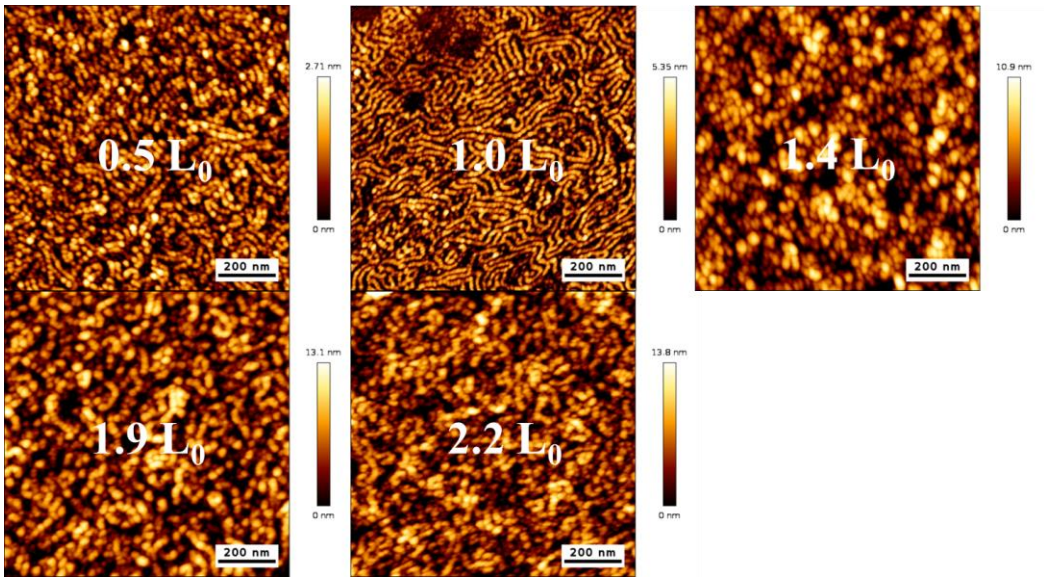


**Figure 5-19.** AFM height images of selected PS-*b*-PSi8F ($L_0$ = 26 nm) of varied film thickness, from 0.5 $L_0$ up to 2.2 $L_0$, confined between a near neutral top coat and bottom surface layer, annealed at 180 °C for 10 min and followed by $O_2$-RIE etching.

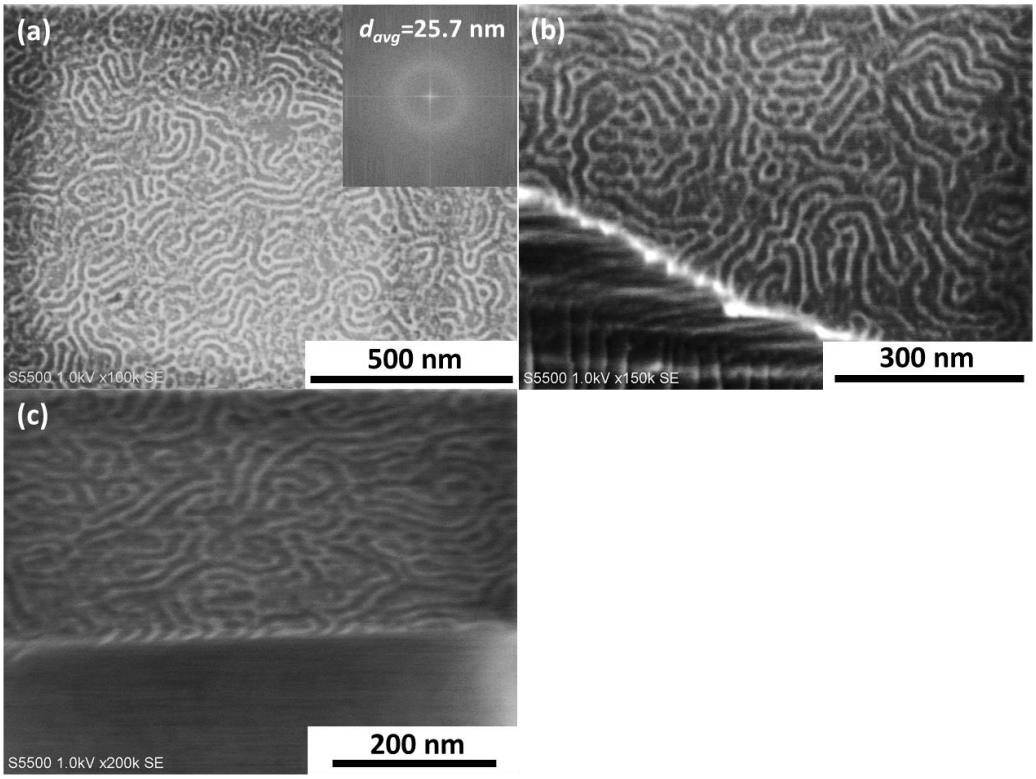


**Figure 5-20.** (a) SEM image shows the surface top-view, (b) shows the sample edge and (c) shows tilted cross-section of the annealed SF20.8 thin film after $O_2$-RIE treatment, respectively. The inset in (a) presents the FFT of the image and the number-averaged periodic length of domain is estimated from FFT.

Additionally, the impact of the annealing time on the perpendicular lamella was examined. As the annealing time is extend from initial 2 min, 5 min and ultimately 10 min, the correlation length of the observed pattern became elongated along with a gradually reduced domain length, which are evidenced by the shortened half peak width and increased *q* of primary peak based on analysis on fast Fourier transform (FFT) insets of Figure 5-21. The results are consistent with the theory and the previous experimental data, as more annealing time responds to the more stable state in thermodynamic with significantly reduced defect densities. After annealing at 180 ℃ for 10 min, the evolution of pattern becomes slow as a qusai-equilibrium state is achieved. The prompt process to well-developed self-assembly is obviously to the low friction of fluorinated side chain for segments movement. These applied annealing conditions are undoubtedly milder than those for commonly used PS-*b*-PMMA, which are typically higher than 200 ℃ or over 30 min. The feature of ultra-fast annealing entitles the investigated BCP the good compatibility with current process and economic cost in semi-conducting manufacturing industry.

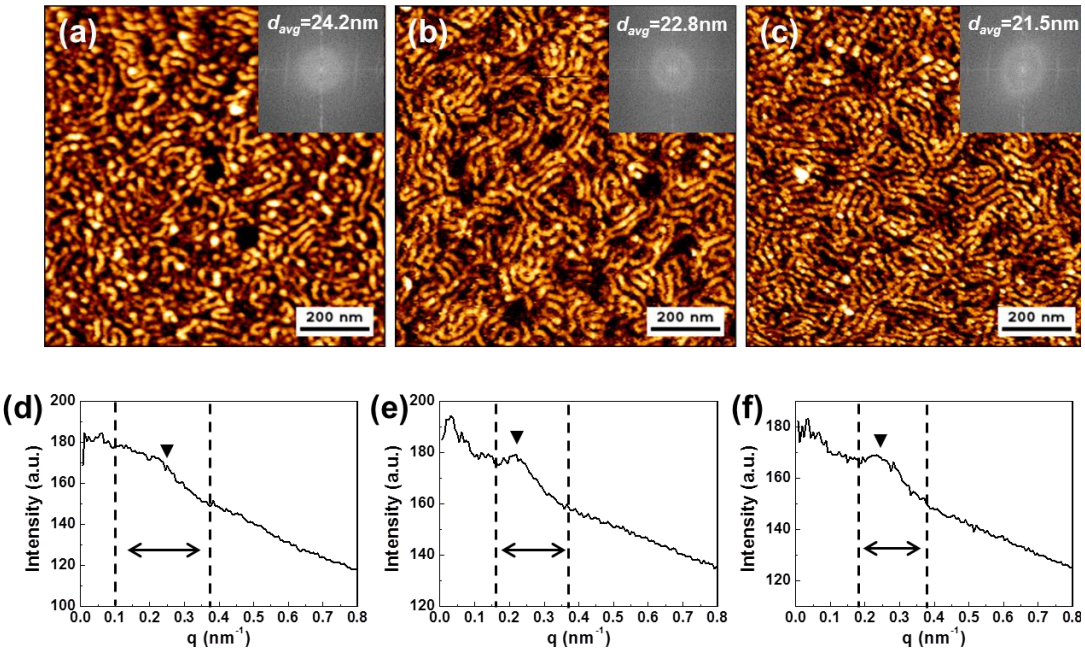


**Figure 5-21.** AFM height images of selected PS-*b*-PSi8F ($L_0$ = 26 nm) of 1.1$L_0$ film thickness, confined between a neutral top coat and bottom surface layer, annealed at 180 ℃ for (a) 2, (b) 5 and (c) 10 min, and followed by $O_2$-RIE etching. The inset presents the FFT of each image and the averaged periodic length of domain is estimated from FFT. And the 1-D integration profile of 2D FFT signals along the radius to the center of FFT inset image extracted from AFM images of the thin films annealed at 180 ℃ for (d) 2, (e) 5 and (f) 10 min. The peak attributed to the periodic length of self-assembled BCP domain is indicated and the width of peak is also marked by a pair of black dash lines.

## 5-4. Conclusion

In this study, 1H,1H,2H,2H-perfluorodecanethiol was introduced to the backbone of Si-containing polystyrene-*block*-poly(methyl vinyl siloxane) via facile thiol-ene reaction. The super hydrophilic long fluorinated is designed as a booster for the segregation between counter-blocks. The estimated χ parameter after modification reaction was expressed by $\chi_{eff} = 2.56/T + 0.163$, which is 80% percent higher than that of precursor BCP PS-*b*-PMVS at annealing temperature. The estimation results revealed the successful molecular design for a higher χ parameter and thus self-assembled domains in a minimized 10 nm-spacing were formed. Additionally owing to the ineligible rigidity of introduced perfluoroalky side chain, the synthesized coil-rod diblock copolymer could self-assemble into anisotropic hexagonal packing cylinder with two distinctive center-to-center distances. The experimental observations were further verified by the morphology prediction from self-consistent field theory (SCFT) using coil-rod model assumption. In thin film study, a confined hole and island test was utilized to exploit the neutral bottom surface layer and top coat materials for PS-*b*-PSi8F ($L_0$ =26 nm). A series of optimizations, such as BCP film thickness and annealing time were carried out. Under optimized conditions, perpendicular lamellae ($L_0$=22 nm) with were quickly produced after annealing at 180 ℃ for 5 min. Additionally, the high oxygen plasma etching resistance of Si-containing BCP readily erased the concern on over-etch problem and thus facilitated the following pattern transfer onto underlying substrate. The ultra-fast annealing feature was obviously attributed to the low friction of fluorinated side chain attached to the flexible siloxane backbone. By chemically tailoring the BCP to fulfill the minimized scale of self-assembly domain, PS-*b*-PSi8F of high effective χ parameter has proven to be a strong candidate for next-generation BCP lithography resists.

## 5-5. Reference

1. Bates, C. M.; Maher, M. J.; Janes, D. W.; Ellison, C. J.; Willson, C. G., Block Copolymer Lithography. *Macromolecules* **2014,** *47* (1), 2-12.

2. Jeong, S. J.; Kim, J. Y.; Kim, B. H.; Moon, H. S.; Kim, S. O., Directed self-assembly of block copolymers for next generation nanolithography. *Mater Today* **2013,** *16* (12), 468-476.

3. Stoykovich, M. P.; Nealey, P. F., Block copolymers and conventional lithography. *Mater Today* **2006,** *9* (9), 20-29.

4. Sunday, D. F.; Maher, M. J.; Hannon, A. F.; Liman, C. D.; Tein, S.; Blachut, G.; Asano, Y.; Ellison, C. J.; Willson, C. G.; Kline, R. J., Characterizing the Interface Scaling of High chi Block Copolymers near the Order-Disorder Transition. *Macromolecules* **2018,** *51* (1), 173-180.

5. Jung, Y. S.; Ross, C. A., Orientation-controlled self-assembled nanolithography using a

polystyrene-polydimethylsiloxane block copolymer. *Nano Lett* **2007,** *7* (7), 2046-2050.

6. Son, J. G.; Gotrik, K. W.; Ross, C. A., High-Aspect-Ratio Perpendicular Orientation of PS-b-PDMS Thin Films under Solvent Annealing. *ACS Macro Lett* **2012,** *1* (11), 1279-1284.

7. Wan, L.; Ruiz, R.; Gao, H.; Patel, K. C.; Albrecht, T. R., The Limits of Lamellae-Forming PS-b-PMMA Block Copolymers for Lithography. *ACS Nano* **2015,** *9* (7), 7506-7514.

8. Luo, Y. D.; Montarnal, D.; Kirn, S.; Shi, W. C.; Barteau, K. P.; Pester, C. W.; Hustad, P. D.; Christianson, M. D.; Fredrickson, G. H.; Kramer, E. J.; Hawker, C. J., Poly(dimethylsiloxane-b-methyl methacrylate): A Promising Candidate for Sub-10 nm Patterning. *Macromolecules* **2015,** *48* (11), 3422-3430.

9. Hirai, T.; Leolukman, M.; Jin, S.; Goseki, R.; Ishida, Y.; Kakimoto, M. A.; Hayakawa, T.; Ree, M.; Gopalan, P., Hierarchical Self-Assembled Structures from POSS-Containing Block Copolymers Synthesized by Living Anionic Polymerization. *Macromolecules* **2009,** *42* (22), 8835-8843.

10. Cushen, J. D.; Bates, C. M.; Rausch, E. L.; Dean, L. M.; Zhou, S. X.; Willson, C. G.; Ellison, C. J., Thin Film Self-Assembly of Poly(trimethylsilylstyrene-b-D,L-lactide) with Sub-10 nm Domains. *Macromolecules* **2012,** *45* (21), 8722-8728.

11. Azuma, K.; Sung, J.; Choo, Y.; Rokhlenko, Y.; Dwyer, J. H.; Schweitzer, B.; Hayakawa, T.; Osuji, C. O.; Gopalan, P., Self-Assembly of an Ultrahigh-chi Block Copolymer with Versatile Etch Selectivity. *Macromolecules* **2018,** *51* (16), 6460-6467.

12. Seshimo, T.; Maeda, R.; Odashima, R.; Takenaka, Y.; Kawana, D.; Ohmori, K.; Hayakawa, T., Perpendicularly oriented sub-10-nm block copolymer lamellae by atmospheric thermal annealing for one minute. *Sci Rep-Uk* **2016,** *6*.

13. Yamazaki, S.; Odashima, R.; Seshimo, T.; Hayakawa, T., Perpendicularly-Oriented Block Copolymers Containing Silicon-Rich Hyperbranched Polymers for High Resistance to O-2-RIE. *J Photopolym Sci Tec* **2017,** *30* (2), 191-196.

14. Lowe, A. B., Thiol-ene "click" reactions and recent applications in polymer and materials synthesis. *Polym Chem-Uk* **2010,** *1* (1), 17-36.

15. Bates, C. M.; Seshimo, T.; Maher, M. J.; Durand, W. J.; Cushen, J. D.; Dean, L. M.; Blachut, G.; Ellison, C. J.; Willson, C. G., Polarity-Switching Top Coats Enable Orientation of Sub-10-nm Block Copolymer Domains. *Science* **2012,** *338* (6108), 775-779.

16. Seshimo, T.; Bates, C. M.; Dean, L. M.; Cushen, J. D.; Durand, W. J.; Maher, M. J.; Ellison, C. J.; Willson, C. G., Block Copolymer Orientation Control Using a Top-Coat Surface Treatment. *J Photopolym Sci Tec* **2012,** *25* (1), 125-129.

17. Maher, M. J.; Bates, C. M.; Blachut, G.; Sirard, S.; Self, J. L.; Carlson, M. C.; Dean, L. M.; Cushen, J. D.; Durand, W. J.; Hayes, C. O.; Ellison, C. J.; Willson, C. G., Interfacial

Design for Block Copolymer Thin Films. *Chem Mater* **2014,** *26* (3), 1471-1479.

18. Maher, M. J.; Rettner, C. T.; Bates, C. M.; Blachut, G.; Carlson, M. C.; Durand, W. J.; Ellison, C. J.; Sanders, D. P.; Cheng, J. Y.; Willson, C. G., Directed Self-Assembly of Silicon-Containing Block Copolymer Thin Films. *ACS Appl Mater Inter* **2015,** *7* (5), 3323-3328.

19. Maher, M. J.; Mori, K.; Sirard, S. M.; Dinhobl, A. M.; Bates, C. M.; Gurer, E.; Blachut, G.; Lane, A. P.; Durand, W. J.; Carlson, M. C.; Strahan, J. R.; Ellison, C. J.; Willson, C. G., Pattern Transfer of Sub-10 nm Features via Tin-Containing Block Copolymers. *ACS Macro Lett* **2016,** *5* (3), 391-395.

20. Durand, W. J.; Carlson, M. C.; Maher, M. J.; Blachut, G.; Santos, L. J.; Tein, S.; Ganesan, V.; Ellison, C. J.; Willson, C. G., Experimental and Modeling Study of Domain Orientation in Confined Block Copolymer Thin Films. *Macromolecules* **2016,** *49* (1), 308-316.

21. Lane, A. P.; Yang, X. M.; Maher, M. J.; Blachut, G.; Asano, Y.; Soineya, Y.; Mallavarapu, A.; Sirard, S. M.; Ellison, C. J.; Willson, C. G., Directed Self-Assembly and Pattern Transfer of Five Nanometer Block Copolymer Lamellae. *ACS Nano* **2017,** *11* (8), 7656-7665.

22. Perutz, S.; Wang, J.; Kramer, E. J.; Ober, C. K.; Ellis, K., Synthesis and surface energy measurement of semi-fluorinated, low-energy surfaces. *Macromolecules* **1998,** *31* (13), 4272-4276.

23. Wang, J. G.; Mao, G. P.; Ober, C. K.; Kramer, E. J., Liquid crystalline, semifluorinated side group block copolymers with stable low energy surfaces: Synthesis, liquid crystalline structure, and critical surface tension. *Macromolecules* **1997,** *30* (7), 1906-1914.

24. Owens, D. K.; Wendt, R., Estimation of the surface free energy of polymers. *J Appl Polym Sci* **1969,** *13* (8), 1741-1747.

25. Bertolucci, M.; Galli, G.; Chiellini, E., Wetting behavior of films of new fluorinated styrene - Siloxane block copolymers. *Macromolecules* **2004,** *37* (10), 3666-3672.

26. Kim, Y.-S.; Lee, J.-S.; Ji, Q.; McGrath, J. E., Surface properties of fluorinated oxetane polyol modified polyurethane block copolymers. *Polymer* **2002,** *43* (25), 7161-7170.

27. Li, X. M.; Li, J.; Wang, C. X.; Liu, Y. Y.; Deng, H., Fast self-assembly of polystyrene-b-poly(fluoro methacrylate) into sub-5 nm microdomains for nanopatterning applications. *J Mater Chem C* **2019,** *7* (9), 2535-2540.

28. Wang, C. X.; Li, X. M.; Deng, H., Synthesis of a Fluoromethacrylate Hydroxystyrene Block Copolymer Capable of Rapidly Forming Sub-5 nm Domains at Low Temperatures. *ACS Macro Lett* **2019,** *8* (4), 368-373.

29. Fedors, R. F., A method for estimating both the solubility parameters and molar volumes

of liquids. *Polymer Engineering & Science* **1974,** *14* (2), 147-154.

30. Al-Hussein, M.; Serero, Y.; Konovalov, O.; Mourran, A.; Moller, M.; de Jeu, W. H., Nanoordering of fluorinated side-chain liquid crystalline/amorphous diblock copolymers. *Macromolecules* **2005,** *38* (23), 9610-9616.

31. Chiang, W. S.; Lin, C. H.; Yeh, C. L.; Nandan, B.; Hsu, P. N.; Lin, C. W.; Chen, H. L.; Chen, W. C., Tetragonally Packed Cylinder Structure of Comb-Coil Block Copolymer Bearing Heteroarm Star Architecture. *Macromolecules* **2009,** *42* (6), 2304-2308.

32. Yoshimura, Y.; Chandra, A.; Nabae, Y.; Hayakawa, T., Chemically tailored high-chi block copolymers for perpendicular lamellae via thermal annealing. *Soft Matter* **2019,** *15* (17), 3497-3506.

33. Andersen, T. H.; Tougaard, S.; Larsen, N. B.; Almdal, K.; Johannsen, I., Surface morphology of PS-PDMS diblock copolymer films. *J Electron Spectrosc* **2001,** *121* (1-3), 93-110.

34. Kennemur, J. G.; Yao, L.; Bates, F. S.; Hillmyer, M. A., Sub-5 nm Domains in Ordered Poly(cyclohexylethylene)-block-poly(methyl methacrylate) Block Polymers for Lithography. *Macromolecules* **2014,** *47* (4), 1411-1418.

35. Leibler, L., Theory of Microphase Separation in Block Co-Polymers. *Macromolecules* **1980,** *13* (6), 1602-1617.

36. Roe, R. J., Surface Tension of Polymer Liquids. *J Phys Chem-Us* **1968,** *72* (6), 2013-&.

37. Wu, S., Surface and interfacial tensions of polymer melts. II. Poly(methyl methacrylate), poly(n-butyl methacrylate), and polystyrene. *The Journal of Physical Chemistry* **1970,** *74* (3), 632-638.

38. Miyaki, Y.; Einaga, Y.; Fujita, H., Excluded-Volume Effects in Dilute Polymer Solutions. 7. Very High Molecular Weight Polystyrene in Benzene and Cyclohexane. *Macromolecules* **1978,** *11* (6), 1180-1186.

39. Wylie, K.; Dong, L.; Chandra, A.; Nabae, Y.; Hayakawa, T., Modifying the Interaction Parameters of a Linear ABC Triblock Terpolymer by Functionalizing the Short, Reactive Middle Block To Induce Morphological Change. *Macromolecules* **2020,** *53* (4), 1293-1301.

40. Sohn, E. H.; Ha, J. W.; Lee, S. B.; Park, I. J., Tuning Surface Properties of Poly(methyl methacrylate) Film Using Poly(perfluoromethyl methacrylate)s with Short Perfluorinated Side Chains. *Langmuir* **2016,** *32* (38), 9748-9756.

41. Extrand, C. W.; Gent, A. N., Retention of Liquid-Drops by Solid-Surfaces. *J Colloid Interf Sci* **1990,** *138* (2), 431-442.

42. Augsburg, A.; Grundke, K.; Poschel, K.; Jacobasch, H. J.; Neumann, A. W., Determination of contact angles and solid surface tensions of poly(4-X-styrene) films. *Acta Polym* **1998,** *49* (8), 417-426.

# Chapter 6

# Downsizing the Thin Film Domain of Poly-(styrene-*block*-methyl methacrylate) by Introducing Fluorine to Randomly Pre-polymerized Functional Units

## 6-1. Introduction

As discussed in Chapter 2-6, the introduction of fluorinated side chain could significantly enhance the segregation among blocks and thus effectively downsize the domain of block copolymers (BCPs) from self-assembly. However, the tremendous fluorinated side chain in one block not only lead to a high $\chi$ parameter between blocks, but also the significant hydrophilic property of extremely low surface free energy (SFE), which is usually hugely different from that of counter-block. On the other hand, for next-generation lithography applications based on thin film self-assembly BCP materials, the perpendicular orientation of BCP domain is in demand for the following pattern transferring onto underlying silicon substrate. The huge gap between surface free energies of counter-blocks requires the additional costly techniques, such as top coating[1 2 3 4], solvent annealing[5 6 7] or incorporation of liquid crystalline side chain[8 9 10 11] for achieving perpendicular orientation of domain, which are not highly compatible with the current chip-fabrication process.

Among all potential BCPs materials for next-generation lithographic application, poly(styrene-*block*-methyl methacrylate) (PS-*b*-PMMA) is the most mature and well-studied material[12 13], making it the mostly-likely candidate for trial manufacturing. Owing to the intensive studies before, a whole family technologies involving chemoepitaxy[14 15 16] and graphoepitaxy[17 18 19] guiding patterns, as well as other surface modification polymer mats and brush [14 20 21 22 23 24 25] are developed for the so-called directly self-assembly (DSA) of BCPs. As one of the advantages of PS-*b*-PMMA, both PS and PMMA block reveal the almost equal surface free energies [26]. Given the neutral wetting bottom interface, perpendicularly oriented domain of PS-*b*-PMMA will be fabricated between the bottom and top ambient interface. However, suffering from a low $\chi$ parameter ($\chi$~0.04)[27], the smallest achievable domain size is limited to 18.5-27 nm[28] with a relatively wide domain interface. Therefore, the pattern transfer will be limited to the similar large pitch size with a relatively high edge roughness. To solve the problem, instead of developing novel high $\chi$ parameter BCPs, many studies especially introducing functional units into PS/PMMA block, had been reported for improvement on existing PS-*b*-PMMA. For instance, by introducing a small number of methacrylamides of chemical modification potential[29 30] or mono/oligosaccharide moieties[31] into the PMMA block,

the hydrophilicity of PMMA block is increased and thus the segregation between segments is enhanced . On the contrary, the same target could be achieved by quantitatively incorporating a self-interacting monomer, vinylnaphthalene, into the styrenic block in PS-*b*-PMMA[32]. Another approach to increasing the χ parameter between PS and PMMA could be the introduction of hydrogen bonding [33] into block copolymer interfaces. All the above mentioned molecular designs are capable of forming perpendicular orientated thin film domain under thermal annealing because of the almost equal SFEs of blocks insignificantly affected by the minor introduced units.

Our group recently reported a high χ parameter BCP, polystyrene-*block*-poly[2-hydroxy-3-(2,2,2-trifluoroethylsulfanyl)propyl methacrylate] (PS-*b*-PHFMA)[34], which is capable of forming sub-10 nm domain. Although the fabrication of perpendicularly oriented domains of 26 nm width was successfully demonstrated in thin film, the challenge on sub-20 nm fabrication was not successful because of the unignorable gap between SFEs of PS (41 mJ $m^{-2}$) and PHFMA (33 mJ $m^{-2}$). Additionally, our group discovered that by introducing a short block of PHFMA into the interface between PS and PMMA blocks, hexagonally packed cylinder (HEX) of 15 nm domain was formed at almost symmetric volume of PS and PMMA. The self-assembly of HEX is obviously attributed to the significantly enhanced χ parameter between PS and PHFMA interface, which facilitates the high curvature in interface.

In this study, the repeating units of PHFMA are quantitatively incorporated into PMMA block as random structure to increase the χ parameter between PS and PMMA block. Therefore, in comparison with the attainable smallest domain size of PS-*b*-PMMA, the minimal domain size of newly synthesized poly(styene-*block*-(2-hydroxy-3-(2,2,2-trifluoroethylsulfanyl)propyl methacrylate-*random*-methyl methacrylate)) (PS-*b*-(PHFMA-*r*-PMMA) can be effectively reduced. By precisely control on the amount of incorporation, the dose effects are unveiled and an accordingly minimal dose could be further determined. Besides, by mixing a minimal amount of fluorinated moieties and MMA monomers in molecular levels, the almost equal SFEs of PS and modified PMMA block could be maintained for perpendicular orientation control on thin film domain.

## 6-2. Experimental Section

### 6-2-1. Materials

Lithium chloride (LiCl) was obtained from Kanto Chemical Co. Inc. and baked under a reduced pressure at 200 °C overnight before use. Styrene was washed by 0.1M sodium hydroxide (NaOH) aqueous solution three times and dried by magnesium sulfate ($MgSO_4$),

afterwards, calcium hydride ($CaH_2$) was added and stirred overnight before distillation. After the distillation, the styrene was distilled over *di-n-buty*lmagnesium ($MgBu_2$) again under Ar protection to remove any residual water and oxygen in styrene. Similarly, methyl acrylate (MMA) was firstly distilled over $CaH_2$ and subsequently distilled over *tri*octyl-aluminum again under Ar protection before usage. Glycidyl methacrylate (GMA) was distilled over $CaH_2$ and subsequently degassed under Ar. Diphenylethene (DPE) was distilled over *n-butyl* lithium and subsequently degassed under Ar. All other materials were reagent grade, purchased from Kanto Chemical Co. Inc., Tokyo Chemical Industry, FUJIFILM Wako Pure Chemical Corporation, and Sigma-Aldrich, and used as received.

### 6-2-2. Methods

$^1$H NMR spectra were recorded with a JEOL JNM-ECS400 (400 MHz) instrument using chloroform-*d* or Acetone-$d_6$ as the solvent. Size exclusion chromatography (SEC) analysis was performed on a Shodex GPC-101 instrument, which was equipped with Shodex LF804 columns. The number average molecular weights ($M_n$) and molecular weight distributions ($M_w/M_n$) were determined by SEC with polymer/tetrahydrofuran solution at a flow rate of 1.0 ml/min at 40 °C and calibrated with polystyrene. Small angle X-ray scattering (SAXS) measurements were carried out using synchrotron radiation facility at BL40B2 Spring-8 with a sample-to-detector of 2.0 meters and Bruker SAXS NanoSTAR (Output:50kV, 50mA) instrument. After monochromatic processing by a Göbel mirror, a concentrated CuKα radiation (wavelength:1.5416Å) was applied to the sample with a 1.0 m distance to the detector. Oxygen plasma etching was performed by etching instrument (SATO VAC, Inc.). The oxygen flow rate was set to 20 sccm and the applied power was 20 W with 30 Pa chamber pressure. The thin film samples were prepared using a MIKASA spin coater IH-D7, and the film thicknesses were measured by a FILMETRICS F20-EXR. AFM (NanoWizard Ultra Speed A, JPK) was used to observe the surface architectures of the BCP thin films at room temperature.

### 6-2-3. Synthesis of PS-*b*-(PGMA-*r*-PMMA)

An example of the anionic polymerization for PSGM20-13 was presented for illustrating the details. Remarkably all anionic polymerization procedures were performed under Ar. Here, 30 mL of THF and LiCl (21.2 mg, 0.500 mmol) were transferred to a 50 mL Schlenk flask and then cooled to -78 °C. *Sec*-butyllithium (*sec*-BuLi) (1.05 M hexane/cyclohexane solution) was added until the color changed to yellow. The Schlenk flask was removed from the cooling bath and warmed to room temperature until the solution became colorless. The Schlenk flask was again cooled to -78 °C and *sec*-BuLi (0.095 mL, 0.100 mmol) was added as initiator. Styrene (1.03 mL, 9.04 mmol) was added and stirred for 30 min, resulting in bright orange

color of the solution. DPE (0.088 mL, 0.50 mmol) was added, changing the color to deep red color. After 30 min of stirring, a mixture of MMA (0.96 mL, 9.00 mmol) and GMA (0.13 mL, 1.00 mmol) monomers was added, causing the color to disappear, and stirred for 30 min. Finally, 3 mL of degassed methanol (MeOH) was added to the Schlenk flask to yield proton-terminated PS-*b*-(PGMA-*r*-PMMA). The polymer was precipitated into MeOH and filtered. The product was dried under reduced pressure at 40 ℃ overnight to yield PS-*b*-(PGMA-*r*-PMMA) as a white powder (1.76 g, 88% yield).

**Characterization of PS-*b*-(PGMA-*r*-PMMA)**

The $M_n$ and dispersity ($Đ = M_w/M_n$) of the product determined by SEC were 18700 g mol$^{-1}$ and 1.24, respectively.

$^1$H NMR (400 MHz, $CDCl_3$, δ, ppm): 0.85 (s, α-$CH_3$, PMMA), 1.01 (s, α-$CH_3$, PGMA), 1.23-1.69 (br, backbone, -$CH_2$-CH-, PS), 1.74-2.02 (br, backbone, -$CH_2$-CH-, PS, br, backbone, -$CH_2$-C($CH_3$)-, PGMA and PMMA), 2.63 (s, -$CH_2$-CH($CH_2$)-O-, PGMA), 2.84 (s, -$CH_2$CH($CH_2$)-O-, PGMA), 3.21 (s, -$CH_2$-CH($CH_2$)-O-, PGMA), 3.59 (s, -$OCH_3$, PMMA), 3.79 (s, -(C=O)O-$CH_2$-, PGMA), 4.28 (d, -(C=O)O-$CH_2$-, PGMA), 6.39-6.85 (m, o-aromatic, PS) 6.91-7.42 (m, m-, p-aromatic, PS).

**6-2-4. Synthesis of PS-*b*-(PHFMA-*r*-PMMA) via thiol-epoxy reaction**

A general procedure for the functionalization of the precursor PS-*b*-(PGMA-*r*-PMMA) is given here. A 10 ml glass tube was charged with 0.2 g PS-*b*-(PGMA-*r*-PMMA) and THF (20 wt% solution) and immersed in an ice-water bath. 1 wt% lithium hydroxide (LiOH) aqueous solution (LiOH 0.05 mole equiv. per GMA unit) and 2,2,2-trifluoroethanethiol (2 mole equiv. per GMA unit) were added to the tube. After stirring for 20 min at room temperature, the reactor was set to 40 ℃ and stirred for 3 h. The crude solution was repeatedly precipitated from methanol or mixture with hexane, depending on $M_n$ and PHFMA fraction of synthesized BCPs, for several times to remove any residual reagents. The product was dried under a reduced pressure at room temperature overnight to yield a white powder.

**Characterization of PS-*b*-(PHFMA-*r*-PMMA)**

$^1$H NMR (400 MHz, Acetone-$d_6$, δ, ppm): 0.84 (s, α-$CH_3$, PMMA), 0.87 (s, α-$CH_3$, PMMA), 1.00 (s, α-$CH_3$, PMMA), 1.03 (s, α-$CH_3$, PGMA), 1.23-1.73 (br, backbone, -$CH_2$-CH-, PS), 1.75-2.23 (br, backbone, -$CH_2$-CH-, PS, br, backbone, -$CH_2$-C($CH_3$)-, PGMA and PMMA), 2.78-3.00 (d, CH(OH)-$CH_2$-S-, PHFMA), 3.40-3.77 (s, -S-$CH_2$-$CF_3$, PHFMA), 3.54-3.75 (s, -$OCH_3$, PMMA), 3.92-4.07 (d, -(C=O)O-$CH_2$-, PHFMA), 4.07-4.18 (m, -CH(OH)-, PHFMA) 4.50-4.72 (br, -CH(OH)-, PHFMA), 6.36-6.84 (m, o-aromatic, PS), 6.85-7.35 (m, m-,

p-aromatic, PS).

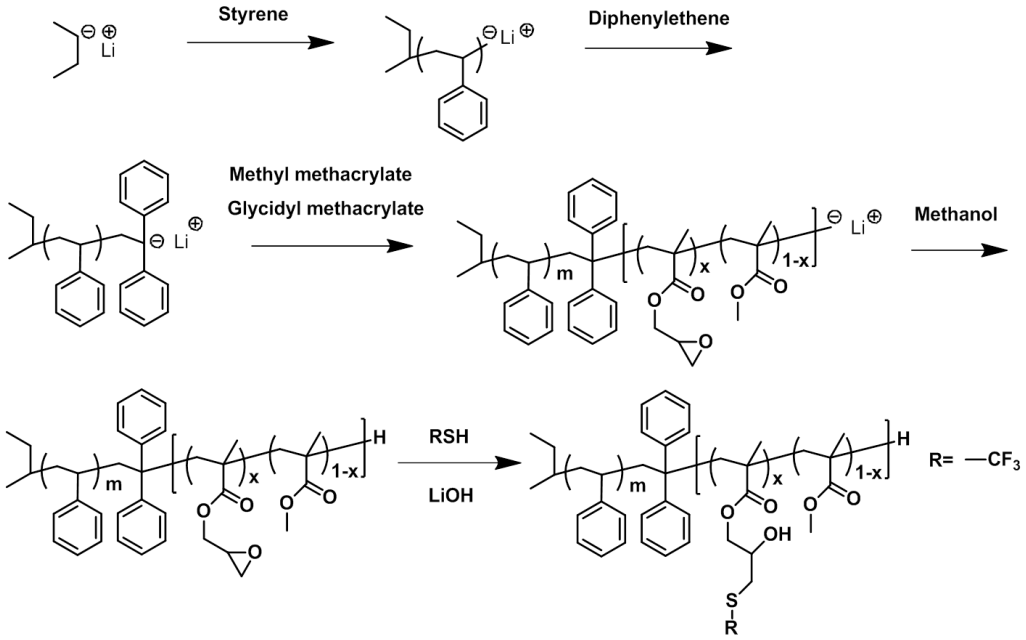


**Scheme 6-1.** Synthetic scheme of PS-*b*-(PGMA-*r*-PMMA) precursor via sequential living anionic polymerization of styrene and mixture of methyl acrylate and glycidyl methacrylate, as well as the post-functionalization with 2,2,2-trifluoroethanethiol. *x* indicates the molar ratio of GMA monomer.

### 6-2-5. Detailed information about the estimation of $\chi_{eff}$

Molten BCP samples were placed in 0.01 mm thick glass tubes and the SAXS profiles were collected at each temperature in 10 ˚C decrement in cooling cycles, at which the temperature was maintained for 30 min prior to the measurements to reach a thermally equilibrated state. The scattering function $I(q)$ from the disordered melt of the BCPs with a dispersity in the molecular weight and asymmetry in the segmental volume was summarized below, where $A_0$ is a fitting constant, $S(q)$ and $W(q)$ together are correlation functions of the BCP, $g(q)$ is a modified Debye function and $y(q)$ is a dimensionless wave vector, $r_c$ is the molar volume normalized over the degree of polymerization of the BCP, $f_X$ is volume fraction of $X$ calculated using the bulk densities for each block (1.05 g $cm^{-3}$ for PS, 1.18 g $cm^{-3}$ for PMMA, 1.43 g $cm^{-3}$ for PHFMA), $v_X$ is the molar volume of $X$. Here the averaged density and molar weight of repeating units were used for the block PHFMA-*r*-PMMA with inner randomly distributed segments. $N_X$ is the degree of polymerization normalized over a common reference volume ($v_0$ = 118 $Å^3$) for $X$, $FW$ is the formula weight of $X$, $N_A$ is Avogadro's constant, and $b_X$ is the segmental length of $X$. Here the dispersities for each homopolymer segment ($D_X$) are assumed equal and were estimated from the $M_w/M_n$ of the BCP and weight fraction of $X$ ($w_X$). Four parameters, including $b_X$ for both polymers, $A_0$ and $\chi_{eff}$, were optimized in a least-squares fit to the SAXS profiles at a certain temperature. The calculated parameters for each sample were summarized in Table 6-4. The estimation of $\chi_{eff}$ for each sample was done at temperatures higher than the order-to-disorder transition ($T_{ODT}$). The detailed equations for estimation of $\chi_{eff}$ are presented in similar parts of previous chapters.

### 6-2-6. Bulk sample preparation

The bulk samples used to investigate the bulk morphologies and domain spacings (*d*-spacing) of the microphase-separated structures were prepared by slowly evaporating a dilute BCP THF solution filtered through a 0.25 μm pore size PTFE membrane syringe filter at 30 ˚C. The as-prepared samples were dried under a reduced pressure before annealing at 180 ˚C for 24 hr, which is a typical annealing condition in previously reported studies on PS-*b*-PMMA.

### 6-2-7. Thin film preparation

Bare silicon wafers cut into 1 $cm^2$ pieces were sonicated in toluene for 3 min, and dried in a stream of nitrogen. The substrates were treated with a mixture of $H_2O_2$ (30%) and $H_2SO_4$ (70%) (*v/v*) at 80 ˚C for 40 min. The wafers were rinsed with water repeatedly and dried in a stream of nitrogen. Bottom surface layers (BSLs) were generated by spin-coating a 1.0 wt% polystyrene-*random*-poly(methyl methacrylate)-*random*-poly(glycidyl methacrylate) (PS-*r*-PMMA-*r*-PGMA) toluene solution at 3000 rpm and 30 s onto the cleaned silicon

wafers, followed by crosslinking at 160 ˚C for 24 hr. In BSL materials, 1 % molar fraction of glycidyl methacrylate (GMA) was added as the potential sites anchoring with the hydroxyl-rich silicon-oxide surface. The substrates were sonicated in toluene to remove any random copolymers that were not attached to the substrate and rinsed with fresh toluene. Furthermore, approximately 1.0 wt % solutions of the BCPs in toluene were spin-coated at 3000 rpm for 30 s onto the surface-modified silicon substrates to obtain thin films with approximately 2.0 $L_0$ thicknesses (30 nm). The thin films were then annealed at 200˚C for varied time under ambient conditions. An $O_2$-RIE treatment was conducted for a certain time (20 sccm, 20 W, 30 Pa) to selectively remove the top-covering layer and enhance the contrast between PS and PMMA-based domains.

## 6-3. Results and Discussion

### 6-3-1. Synthesis and characterization of the BCPs

Similar to the synthesis of PS-*b*-PGMAs and the subsequent post-functionalization via thiol-epoxy reaction, the syntheis of the targeted BCP PS-*b*-(PHFMA-*r*-PMMA)s is divided into two steps (Scheme 6-1).

The first step is the anionic polymerization for precursor BCP PS-*b*-(PGMA-*r*-PMMA)s. Six PS-*b*-(PGMA-*r*-PMMA)s precursor polymers (Table 6-1) were successfully synthesized via the sequential anionic polymerization of styrene and mixture of GMA and MMA using *sec*-BuLi, excess LiCl, and DPE in THF at -78 ˚C under an Ar atmosphere. Here the synthesized six BCPs were categorized into 2 batches of distinctive $M_n$ range. For all investigated BCPs, PS volume fraction ($f_{PS}$) is approximately controlled within 0.4-0.5. In the batch of 20 k $M_n$ Da, the GMA molar ratio is set to approximately 0.1, 0.2 and 0.3. Meanwhile, in the batch of less than 10 k $M_n$ Da, higher GMA ratios starting from 0.2 to 0.46 were set because of lower *N* contribution to self-assembly. Based on the integration of characteristic peaks attributed to PS aromatic rings (6.26-7.40 ppm), the epoxy moieties in GMA (a, a', b, c, and c' at 2.63, 2.84, 3.22, 3.79 and 4.29 ppm, respectively) and the pendent methoxy group in MMA (d at 3.59 ppm), the fraction of these three components were further estimated accordingly (Figure 6-1(a)).

The precursor PS-*b*-(PGMA-*r*-PMMA)s were then functionalized with 2,2,2-trifluoroethanethiol in THF with LiOH as the catalyst at 30 ˚C for 3 h to yield the targeted PS-*b*-(PHFMA-*r*-PMMA)s. The mild reaction conditions work with high efficiency as the disappearance of $^1$H NMR signals corresponding to the glycidyl moieties suggested almost 100% conversion. Instead, the characteristic proton peaks attributed to post-functionalized 2-hydroxy-3-(2,2,2-trifluoroethylsulfanyl)propyl methacrylate (D, E, A, B and C at 2.90, 3.50, 4.01, 4.10 and 4.60 ppm) were revealed in predicted ratio of peak integration (Figure 6-1(b)).

Besides, all SEC chromatography (Figure 6-2) of precursor BCPs reveal a shift towards higher $M_n$ regime following the post-functionalization reaction with almost constant narrow dispersities, which also suggests the quantitative introduction of 2,2,2-trifluoroethanethiol onto glycidyl methacrylate units in polymer chains. The volume fraction of each component was calculated using the known densities of components.

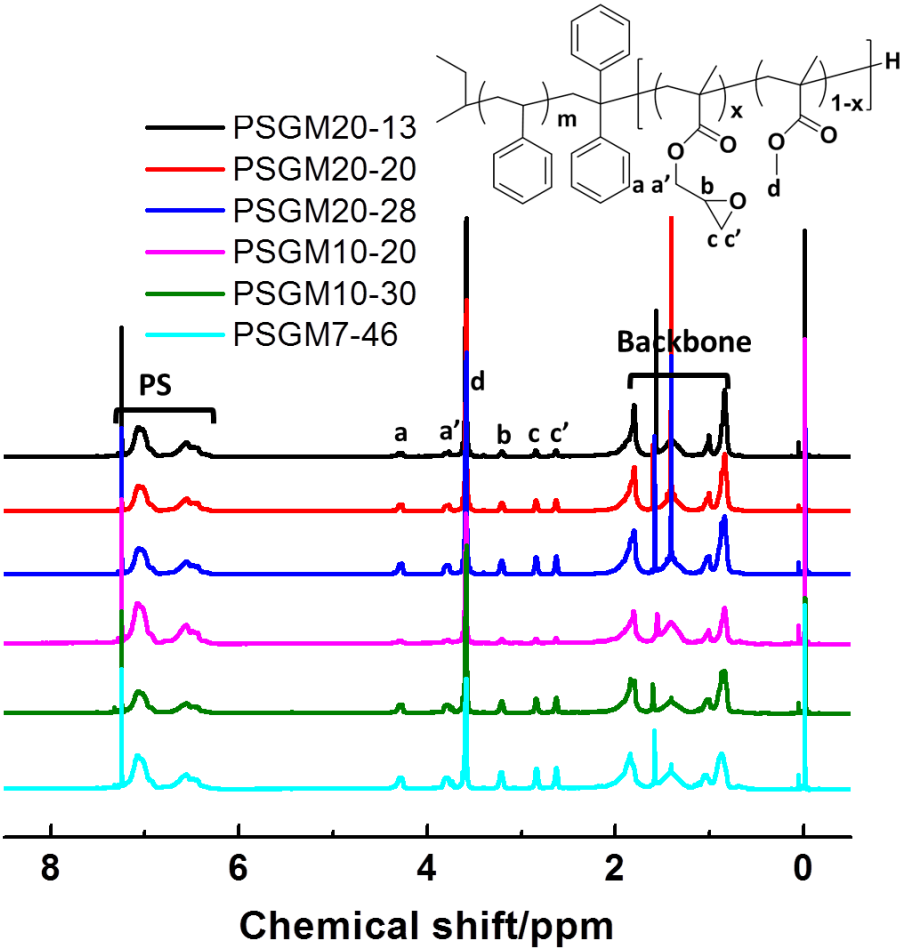


**Figure 6-1 (a).** $^1$H NMR spectra of synthesized PS-*b*-(PGMA-*r*-PMMA) (PSGM) using $CDCl_3$ as solvent. Here PS-*b*-(PGMA-*r*-PMMA) is abbreviated to PSGM and the suffixed number in XX-YY form indicates the number-averaged molecular weight in a thousand Dalton scale and GMA molar ratio in percentage.

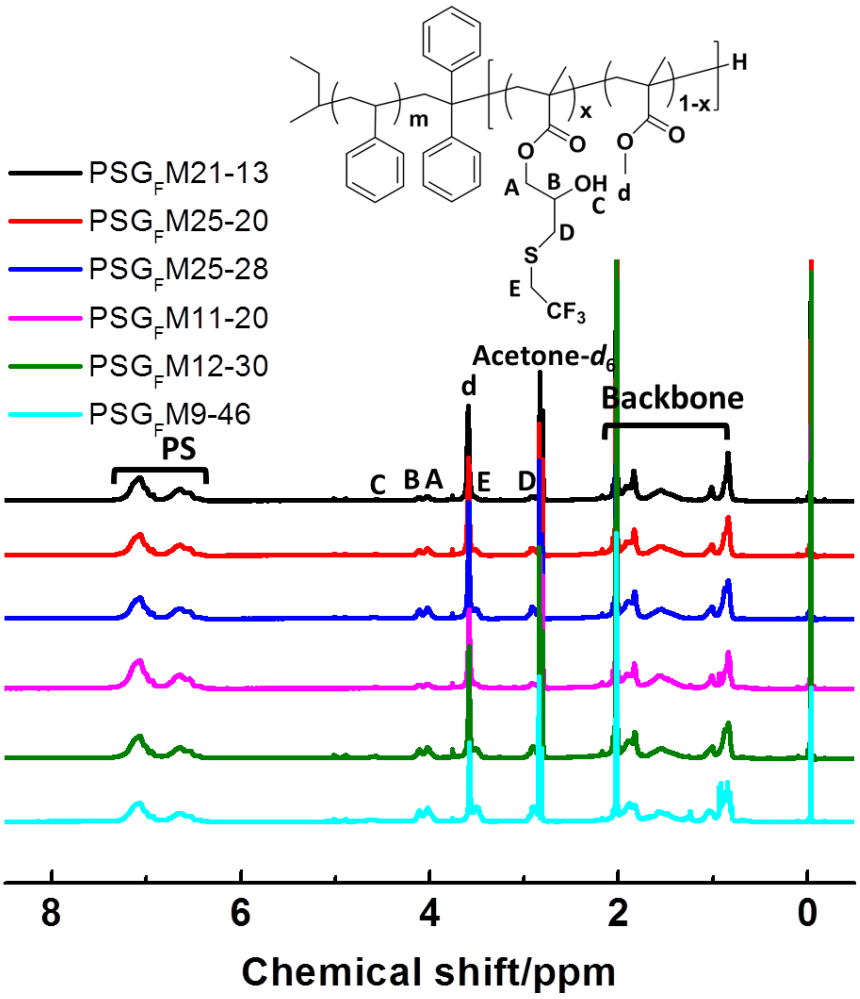


**Figure 6-1 (b).** $^1$H NMR spectra of synthesized PS-*b*-(PHFMA-*r*-PMMA) (PSG$_F$M) using acetone-$d_6$ as solvent. Here PS-*b*-(PHFMA-*r*-PMMA) is abbreviated to PSG$_F$M and the suffixed number in XX-YY form indicates the number-averaged molecular weight in a thousand Dalton scale and fluorinated GMA molar ratio in percentage.

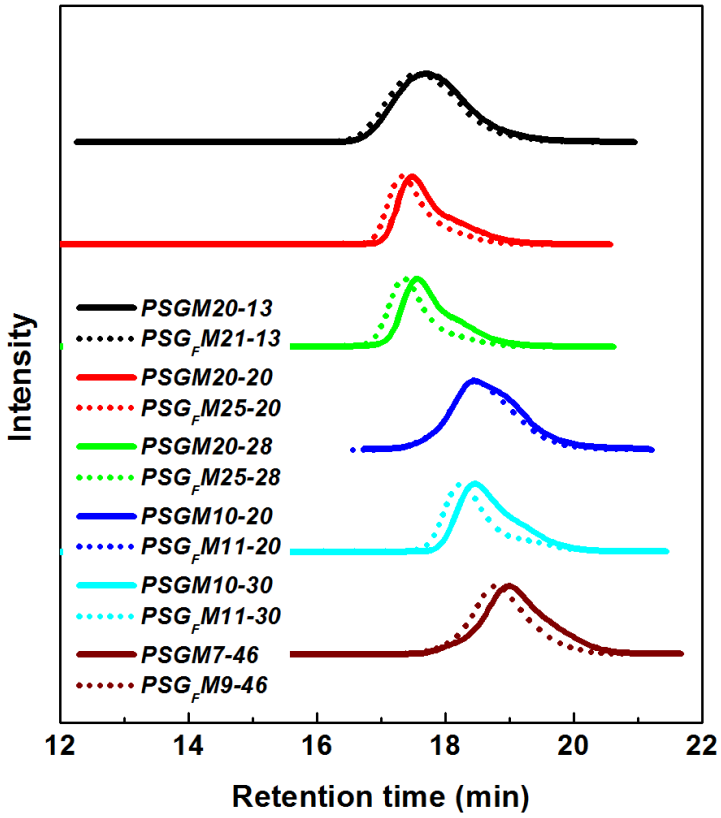


**Figure 6-2.** SEC chromatography of precursor PS-*b*-(PGMA-*r*-PMMA) (PSGM) and corresponding fluorinated PS-*b*-(PHFMA-*r*-PMMA) ($PSG_FM$) after post functionalization.

**Table 6-1**. Characterization data of the synthesized BCPs.

| BCP | Label[a] | $M_n$[b] (kg mol$^{-1}$) | $Đ$ | $f_{PS}$[c] | $f_{PGMA}$[c] | $f_{PMMA}$[c] | $n_{GMA}/(n_{GMA+}n_{MMA})$[c] | Morphology[d] | $d_{spacing}$[e] (nm) |
|---|---|---|---|---|---|---|---|---|---|
| PS-*b*-(PGMA-*r*-PMMA) | PSGM20-13 | 18.7 | 1.24 | 0.47 | 0.13 | 0.40 | 0.13 | LAM | 22.7 |
| | PSGM20-20 | 20.2 | 1.17 | 0.41 | 0.20 | 0.39 | 0.20 | LAM | 24.1 |
| | PSGM20-28 | 19.7 | 1.17 | 0.35 | 0.29 | 0.36 | 0.28 | LAM | 22.0 |
| | PSGM10-20 | 9.8 | 1.23 | 0.61 | 0.10 | 0.29 | 0.20 | Dis | - |
| | PSGM10-30 | 9.7 | 1.18 | 0.35 | 0.31 | 0.34 | 0.30 | Dis | 14.0 |
| | PSGM7-46 | 6.9 | 1.23 | 0.42 | 0.37 | 0.21 | 0.46 | Dis | 12.3 |

| BCP | Label[a] | $M_n$[b] (kg mol$^{-1}$) | $Đ$ | $f_{PS}$[c] | $f_{PGMA-F}$[c] | $f_{PMMA}$[c] | $n_{GMA}/(n_{GMA-F+}n_{MMA})$[c] | Morphology[d] | $d_{spacing}$[e] (nm) |
|---|---|---|---|---|---|---|---|---|---|
| PS-*b*-(PGMA$_F$-*r*-PMMA) | PSG$_F$M20-13 | 20.7 | 1.24 | 0.47 | 0.13 | 0.40 | 0.13 | LAM | 22.9 |
| | PSG$_F$M25-20 | 25.2 | 1.15 | 0.45 | 0.19 | 0.36 | 0.20 | LAM | 22.8 |
| | PSG$_F$M25-28 | 25.0 | 1.16 | 0.41 | 0.27 | 0.32 | 0.28 | LAM | 23.8 |
| | PSG$_F$M11-20 | 10.6 | 1.19 | 0.60 | 0.14 | 0.26 | 0.20 | LAM | 14.3 |
| | PSG$_F$M12-30 | 11.6 | 1.21 | 0.41 | 0.28 | 0.31 | 0.30 | LAM | 15.3 |
| | PSG$_F$M9-46 | 8.5 | 1.19 | 0.39 | 0.40 | 0.21 | 0.46 | HEX | 14.4 |

[a] The labels PSGM and PSG$_F$M refer to PS-*b*-(PGMA-*r*-PMMA) and PS-*b*-(PGMA$_F$-*r*-PMMA), respectively, while the number to the right refers to the number-average molecular weight ($M_n$) of the polymer and molar fraction of GMA in random (PGMA-*r*-PMMA) segments. [b] $M_n$ and dispersities ($Đ$) were obtained by SEC using THF as the eluent based on PS standards. [c] The volume fractions ($f$) of monomers were calculated via $^1$H NMR based on the densities of 1.05 g cm$^{-3}$ for PS, 0.805 g cm$^{-3}$ for PGMA, 1.18 g cm$^{-3}$ for PMMA and 1.43 g cm$^{-3}$ for PGMA$_F$. [d] The domain spacings ($d_{spacing}$) were estimated from the position of first-order scattering peak in the SAXS profile upon thermal annealing at 180 °C for 24 h. [e] The morphologies in the bulk were determined by SAXS and TEM.

**6-3-2. Estimation of $\chi_{eff}$**

Similar to the used random-phase approximation (RPA) method for $\chi_{eff}$ estimation in previous chapters, $\chi_{eff}$ of particularly one PS-*b*-(PHFMA-*r*-PMMA) ($PSG_FM11$-20) of 20% GMA molar ratio was estimated in this study. Another two diblock copolymer samples PS-*b*-PHFMA and PS-*b*-PMMA were also prepared for SAXS measurements. The temperature-dependent SAXS analyses on $PSG_FM$ were conducted starting from 290 ℃ and in 10 ℃ decrements (Figure 6-3(a)). The detected SAXS profiles showed a discontinuous change in the $I_{max}^{-1}$-$T^{-1}$ plot between 250-260 ℃, as typically observed around order-to-disorder transition (ODT). According to Hashimoto's works[35], RPA method is applicable when the measured temperature is higher than the so-called mean field temperature ($T_{MF}$), which is slightly higher ODT. The gap between ODT and $T_{MF}$ is almost negligible considering the 10 ℃ measuring interval. Similar discontinuity in $I_{max}^{-1}$-$T^{-1}$ plot were discovered for both PS-*b*-PHFMA and PS-*b*-PMMA at 180-190 ℃. Extracted from the SAXS profiles taken under varied temperatures above ODT, Flory-Huggins interaction parameter expressed by $\chi_{eff} = AT^{-1} + B$, where $AT^{-1}$ is the enthalpic contribution, and $B$ is the entropic contribution, was estimated using reference volume of 118 Å$^3$ for comparison. $\chi_{eff}$ of $PSG_FM11$-20, PS-*b*-PHFMA and PS-*b*-PMMA was expressed by $\chi_{eff} = 2.6/T + 0.057$, $\chi_{eff} = 19.4/T + 0.126$ and $\chi_{eff} = 3.4/T + 0.034$ (Table 6-5 Figure 6-5), respectively. The measured expression of $\chi_{eff}$ of PS-*b*-PHFMA[34] and PS-*b*-PMMA[27] are highly consistent with the literature. Obviously the value of measured $\chi_{eff}$ at typical annealing temperature is between those of PS-*b*-PHFMA and PS-*b*-PMMA. An analogous diblock copolymer system with randomly distributed units in one block was previously studied[36]. In that study, conversion of monomers into functionalized ones occurs randomly along the one particular block and the exact $\chi$ values between the two blocks are determined as a function of the degree of conversion of monomers. An exponential increase in the $\chi$ value was revealed by a progressive conversion. Therefore, the exact $\chi$ value seems dominated by the major component in the mixing block, which is in good agreement with our observation.

Besides, for the investigated A-*b*-(B-*r*-C) type copolymer, the theoretic $\chi_{eff}$ based on blending of homopolymer (A) and random copolymer ((B-*r*-C), is governed by the following equation[29]:

$$\chi_{eff} = \frac{r_B}{100}\chi_{A-B} + \left(1 - \frac{r_B}{100}\right)\chi_{A-C} - \frac{r_B}{100}\left(1 - \frac{r_B}{100}\right)\chi_{B-C}$$

where the subscripts of A, B, and C refer to each segment and B is the minor comonomer in the random copolymer B-*r*-C. $f_B$ refers to the molar ratio of B comonomer in B-*r*-C in

percentage. As the estimated values of $\chi_{A-B}$, $\chi_{A-C}$, and $\chi_{B-C}$ at annealing temperature are input into the equation, a positive dependence of $\chi_{eff}$ on the molar ratio of introduced fluorinated GMA is revealed (Figure 6-6).

The estimated $\chi_{eff}$ value of $PSG_FM11$-20 at 180 °C annealing temperature is more close to that of PS-*b*-PMMA, despite taking volume fraction of two components in mixing block into account (Figure 6-6). Meanwhile, the value of $\chi_{eff}$ was significantly increased by almost 60% with barely 20% molar fluorinated GMA loading into PMMA block. The enhanced $\chi_{eff}$ allows a stronger segregation under significantly lower $M_n$ of BCPs, which eventually leads to the micro-phase separation for forming sub-20 nm microdomain morphology.

To verify the temperature dependence of the characteristic scattering parameter in whole temperature range including ordered state, another PS-*b*-(PHFMA-*r*-PMMA) ($PSG_FM9$-46) of 46% GMA molar loading ratio was used in SAXS measurements (Figure 6-7). The whole measured temperature range starting from 250 °C to 200 °C all revealed ordered states, as the second and third order peaks at $\sqrt{3}q^*$ and $2q^*$ were maintained up to the highest 250 °C. The observed ordered state at high annealing temperatures are obviously attributed to the higher loading of fluorinated moieties in mixing block, which provides a higher incompatibility ($\chi_{eff}$) for segments segregation between the counter-blocks. The $d_{-spacing}$-$T^{-1}$ plot was fitted into a linear relation (Figure 6-8), which is consistent with the reported works[35]. The increment of domain spacing with reduced temperature was mainly caused by the thermal expansivity of the polymer, as the value of $\chi_{eff}$ became less dependent on the temperature in ordered state.

**Table 6-2**. The fixed parameters used to estimate $\chi_{eff}$ for BCPs.

| BCP | $r_c$ | $M_n$ (kg mol$^{-1}$) | $M_w$ (kg mol$^{-1}$) | $M_{n,PS}$[a] (kg mol$^{-1}$) | $f_{PS}$ | $f_{PHFMA}$ | $w_{PS}$ | $Đ$ |
|---|---|---|---|---|---|---|---|---|
| PS-*b*-PMMA | 250 | 19.6 | 22.0 | 9.6 | 0.52 | - | 0.49 | 1.13 |
| PS-*b*-PHFMA | 43 | 3.7 | 4.4 | 1.8 | 0.52 | 0.48 | 0.44 | 1.19 |
| $PSG_FM11$-20 | 132 | 10.7 | 12.7 | 6.0 | 0.60 | 0.14 | 0.56 | 1.19 |

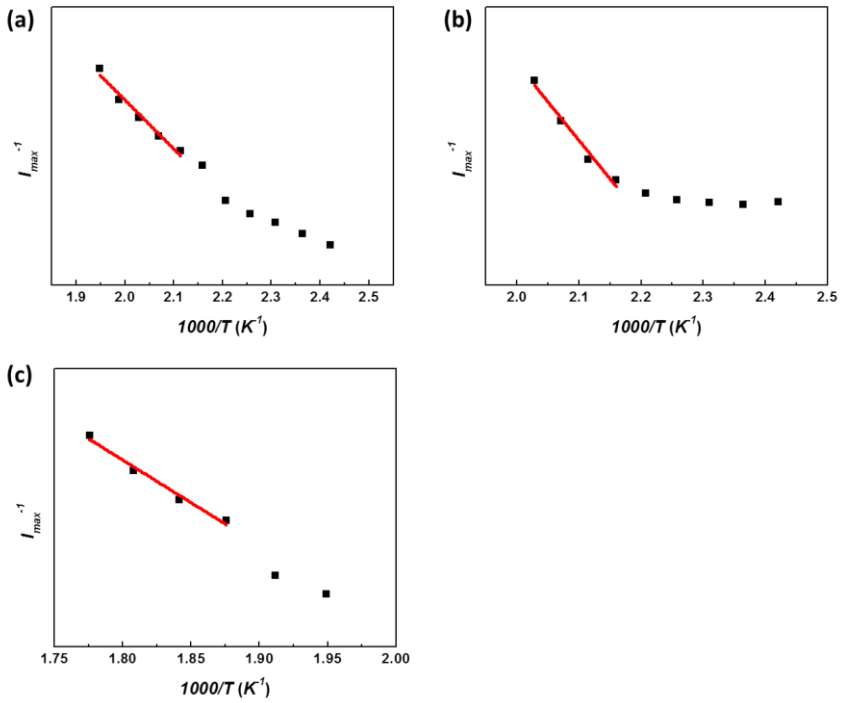


**Figure 6-3.** The $I_{max}$-$T^{-1}$ plots for (a) PS-*b*-PHFMA, (b) PS-*b*-PMMA and (c) $PSG_FM11$-20. The red line indicates the linear relation above ODTs.

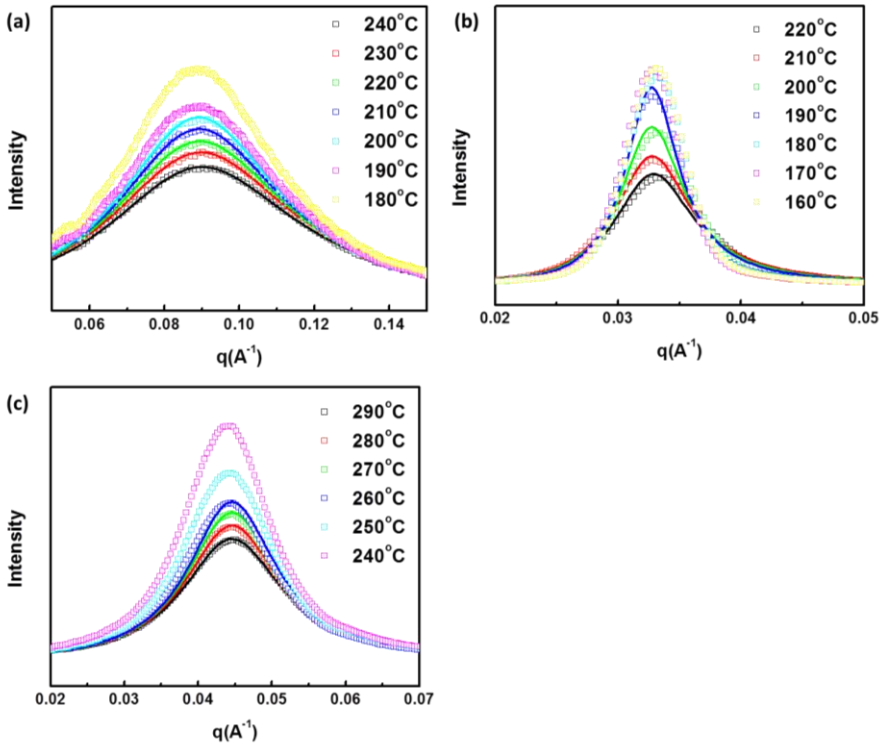


**Figure 6-4.** The scattering profiles (square scatters) measured by SAXS and the fitting profiles (smooth lines) at different temperatures for (a) PS-*b*-PHFMA, (b) PS-*b*-PMMA and (c) $PSG_FM11$-20.

**Table 6-3**. The estimated parameters $\chi_{eff}$ for BCPs at varied temperatures.

| | Estimated $\chi_{eff}$ | | | Estimated $\chi_{eff}$ |
|---|---|---|---|---|
| $T$ (°C) | PS-*b*-PHFMA | PS-*b*-PMMA | $T$ (°C) | PS-*b*-(PHFMA-*r*-PMMA) |
| 240 | 0.16410 | - | 290 | 0.06193 |
| 230 | 0.16491 | - | 280 | 0.06204 |
| 220 | 0.16575 | 0.04131 | 270 | 0.06212 |
| 210 | 0.1666 | 0.04139 | 260 | 0.06219 |
| 200 | 0.16727 | 0.04159 | | |
| 190 | - | 0.04174 | | |

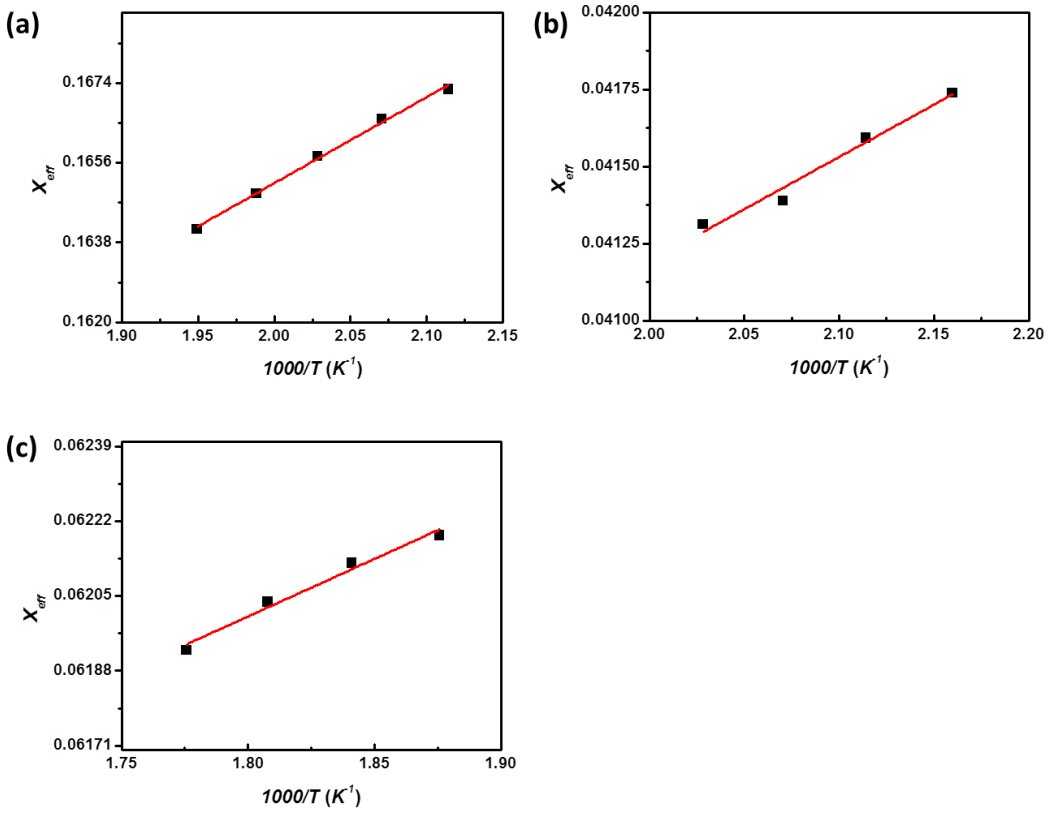


**Figure 6-5.** Temperature dependences of the effective Flory-Huggins interaction parameter for (a) PS-*b*-PHFMA, (b) PS-*b*-PMMA and (c) $PSG_FM11$-20 using a reference volume of 118 Å$^3$.

**Table 6-5.** Estimated enthalpic (*B*/*T*) and entropic contributions (*A*) for $\chi_{eff}$ of BCPs.

| BCP | *B*/*T* | *A* |
|---|---|---|
| PS-*b*-PHFMA | 19.4/*T* | 0.126 |
| PS-*b*-PMMA | 3.4/*T* | 0.034 |
| PS-*b*-(PHFMA-*r*-PMMA) | 2.6/*T* | 0.057 |

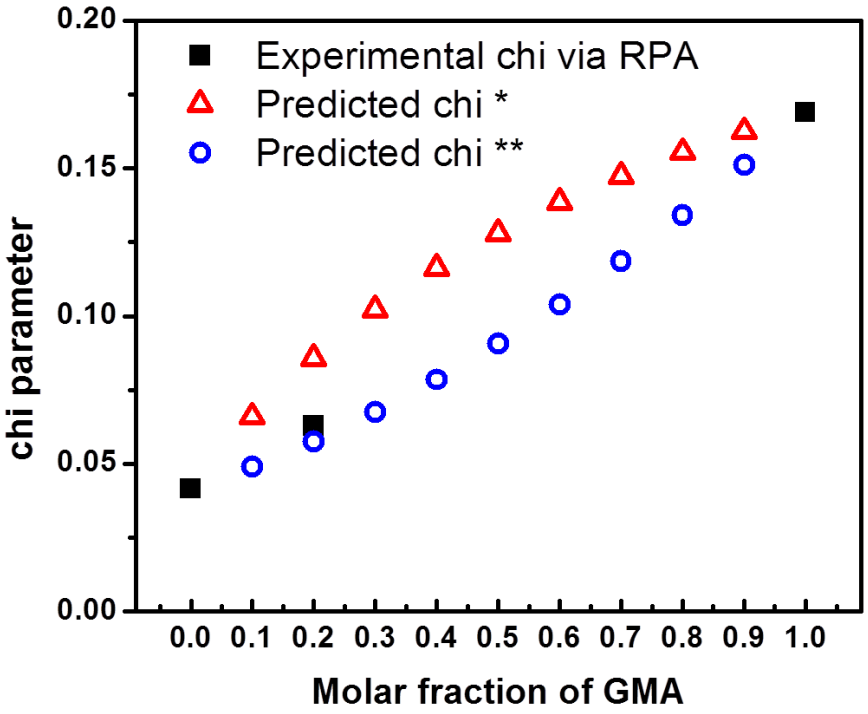


**Figure 6-6.** The measured effective Flory-Huggins interaction parameter chi from RPA-experiments, the predicted effective chi* consisted of contributors from $\chi_{PS/PHFMA}$ and $\chi_{PS/PMMA}$ scaled by the volume fraction of $GMA_F$ or MMA comonomer in the random chain and the predicted effective chi** using the theoretic equation based on blending model in relationship with the molar fraction of fluorinated GMA in $GMA_F$-*r*-MMA random chain. The predictions are carried out using the inputs of $\chi_{PS/PHFMA}$=0.169, $\chi_{PS/PMMA}$=0.041 and $\chi_{PHFMA/PMMA}$=0.059 at 180 ℃ [38].

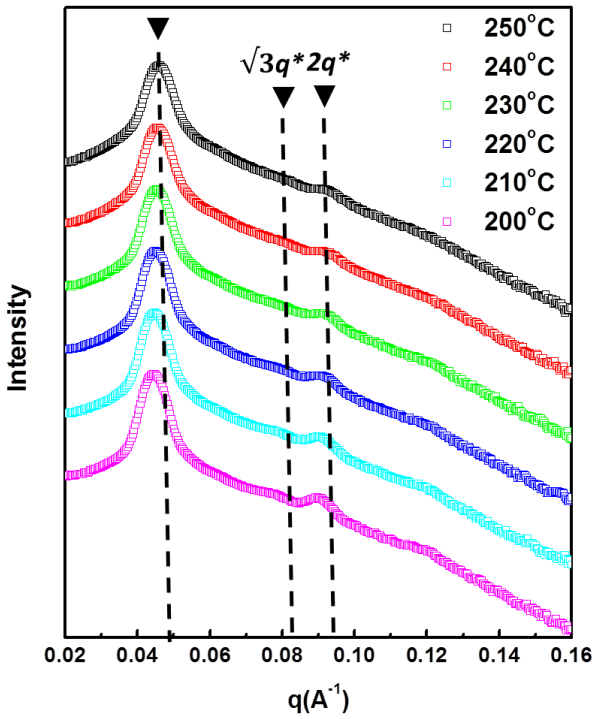


**Figure 6-7.** The scattering profiles (square scatters) measured by SAXS at different temperatures for $PSG_FM9$-46. The positions of primary, secondary and third scattering peak (marked in dash line) are all shifted towards higher *q* direction under reduced temperatures from 250 ˚C to 200 ˚C.

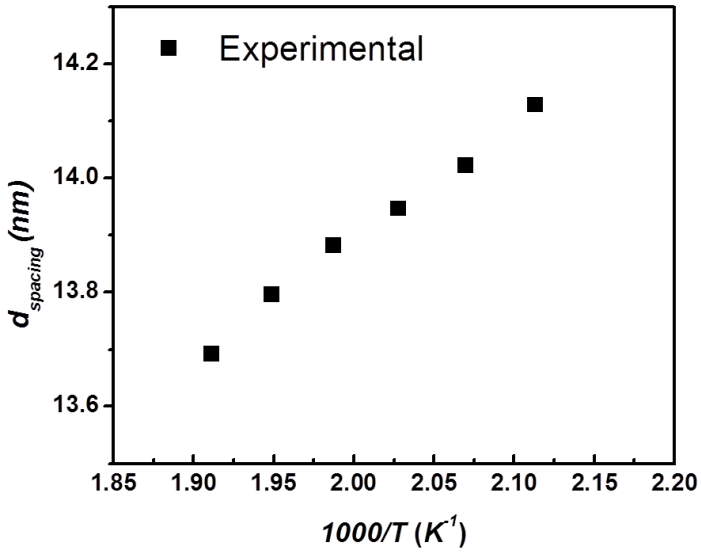


**Figure 6-8.** Temperature dependences of the estimated $d_{\text{-spacing}}$ of $PSG_FM9$-46 in ordered states.

**6-3-3. Morphologies in the bulk**

SAXS profiles of precursor PSGMs and post- functionalized $PSG_FMs$ with varied fluorinated GMA loading ratios were measured at room temperature after thermal annealing to examine the self-assembly morphologies (Figure 6-9(a)-(b)). The domain spacing of the ordered morphology was estimated by the equation $d_{\text{-spacing}}=2\pi/q^*$. Here $q^*$ denotes the position of the primary scattering peak.

For all PSGMs of approximately 20 k $M_n$, micro-phase separated lamellae (LAM) were suggested as an integer of $q^*$ ratio was revealed. The segregation limit for self-assembly of PS-*b*-PMMA is $M_n$ of at least 23 k, which is obviously higher than $M_n$ of all investigated PSGMs. The enhanced segregation among blocks was caused by the GMA loading into the PMMA block. In our previous studies, the $\chi_{eff}$ between PS and PGMA at 180 ℃ annealing was measured being $\chi_{PS/PGMA}=0.133$, which are lower than that between PS and PHFMA ($\chi_{PS/PHFMA}=0.169$), but still significantly higher than that between PS and PMMA ($\chi_{PS/PMMA}=0.041$). Therefore, the loading of randomly distributed GMA along PMMA block enhanced the $\chi_{eff}$ between counter-blocks and resulted in self-assembly morphology at lower $M_n$. The increased GMA loading ratio displayed a scattering profile of more high-order scattering peaks of higher absolute intensity, indicating a stronger micro-phase separation owing to the higher $\chi_{eff.}$ After the post-functionalization, the lamellar morphologies were kept with significantly increased intensity of multiple high order reflections. For $PSG_FM$ of the highest 28% GMA molar loading ratio, up to the sixth order ($6q^*$) scattering reflection was displayed, indicating the most intensive micro-phase separation in the assembled morphologies. More evidences are from the quantitative analysis on full width at half maximum (FWHM) and inverse of the maximum intensity ($1000/I(q^*)$) of primary scatting reflection (Figure 6-10(a)-(d)). For the particularly same type of morphology, a narrower FWHM indicates a longer correlation length or higher periodicity of the formed periodic nano-structure. Meanwhile, an increased maximum intensity indicates a higher periodicity of morphology. The only inconsistence from the FWHM results of $PG_FSM25$-30 was probably caused a change in the symmetry of the lamellar structure under massive fluorinated GAM loading into precursor BCP, as PS volume fraction of $PG_FSM25$-30 ($f_{PS}=0.41$) is significantly lower than the other two symmetric BCPs ($f_{PS}$~0.5) in the same batch.

As $M_n$ of PSGM and post-functionalized $PG_FSM$ was further reduced to around 10 k Da, PSGM of 20% GMA loading ratio revealed an absolutely disordered state, as the primary scattering reflection could hardly be detected. However, after the introduction of 2,2,2-trifluoroethanethiol, a second order peak ($2q^*$) was observed indicating the formation of lamellar morphology. The micro-phase separation driving force indicator $\chi_{eff}N$ was considered near the segregation limit because of the weak scattering signals, which is consistent with

observed disordered state at higher annealing temperature. When the fluorinated GMA molar loading ratio was further increased to 30%, a lamellar morphology of 15.3 nm domain size was detected by SAXS signals. Up to the intensive third scattering peak ($3q^*$) was displayed, indicative of the strongly micro-phase separation in the formed morphology in comparison to the weak micro-domain separation at 20 % GMA loading ratio. The corresponding precursor PSGM10-30 also revealed a relatively higher-ordered state with a detectable primary scattering signal. Therefore, by randomly introducing at least 20 % molar percentage of functional GMA into the mixing block of PMMA, the segregation between PS and mixing block interface was significantly enhanced and sub-15 nm lamellae was formed in the bulk sample.

To investigate the limit for self-assembly, the GMA loading ratio was further increased to 46 % with BCP $M_n$ lower than 9 k Da. Owing to the enhanced $\chi_{eff}$ at high degree, $PSG_FM9$-46 displayed a hexagonally packed cylinder (HEX) of 14.4 nm $d_{\text{-}spacing}$ with characteristic SAXS scattering signals at $\sqrt{3}q^*$ and $\sqrt{7}q^*$. The change to HEX from LAM was probably attributed to the lower PS volume fraction and increased $\chi_{eff}$, as an increased $\chi_{eff}$ energetically favors the micro-phase separation interface of high curvature.

In addition, the relative intensity of multiple scattering peaks to the primary one indicated the geometry of the inner domain[37]. By using Scatter (Version 2.5, 03/2011) software, all SAXS profiles of investigated $PSG_FM$ were successfully fitted by the given models of adjustable input parameter (Figure 6-11). Here the fitted peaks shape is set to Lorentzian with the assumption of equal block density and scattering contrast. The block volume fractions extracted from these fitted models are highly consistent with those estimated from $^1$H NMR.

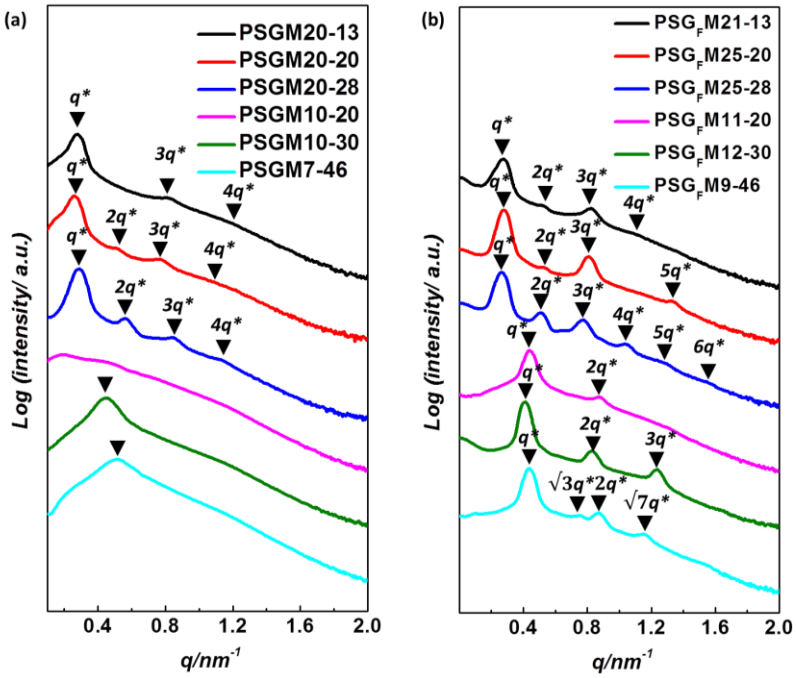


**Figure 6-9.** SAXS profiles of the synthesized (a) precursor PSGM and (b) chemically modified $PSG_FM$ bulk samples following thermal annealing at 180 ˚C for 24 hr.

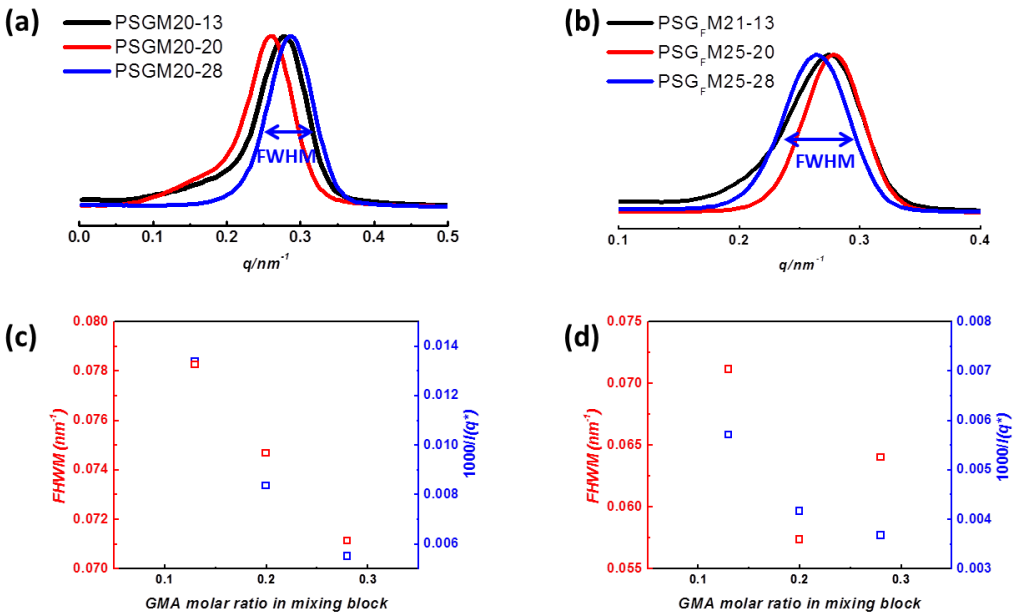


**Figure 6-10.** Normalized primary scattering signals in SAXS profiles of (a) PSGM and (b) $PSG_FM$ bulk samples following thermal annealing at 180 ˚C for 24 hr. The full width at half maximum (FWHM) was indicated. Inverse of a maximum intensity ($1000/I(q^*)$), and full width at half-maximum (FWHM) determined from the SAXS profiles of (c) PSGM and (d) $PSG_FM$ are marked at each GMA molar ratio in mixing block.

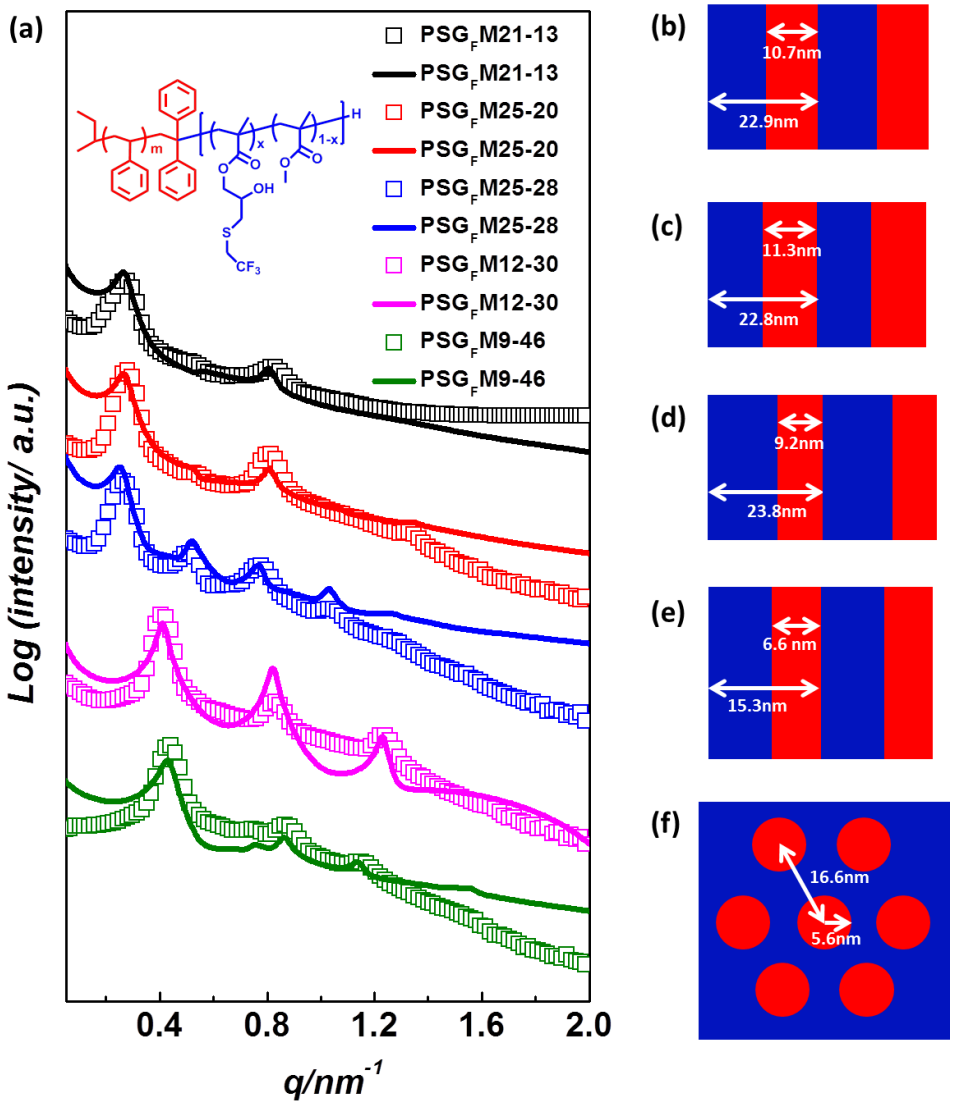


**Figure 6-11.** (a) The scattering profiles (square scatters) measured by SAXS and the fitting profiles (smooth lines) of the chemically modified PSG$_F$M bulk samples following thermal annealing at 180 ℃ for 24 hr. The fitting model represents for (b) PSG$_F$M21-13 with $f_{PS}$=0.47, (c) PSG$_F$M25-20 with $f_{PS}$=0.49, (d) PSG$_F$M25-28 with $f_{PS}$=0.39, (e) PSG$_F$M12-30 with $f_{PS}$=0.43 and (f) PSG$_F$M12-30 with $f_{PS}$=0.41. The red and navy color indicates PS and randomly mixing PHFMA-*r*-PMMA block, respectively. The characteristic distance inside domain was labeled in white double-end arrow.

**6-3-4. Morphologies Predictions by Self-consistent field theory (SCFT)**

Similar to the discussion parts on SCFT prediction in Chapter 5, an incompressible melt of AB linear diblock polymers is placed in a simulation volume $V$ where each polymer is modeled as a Gaussian chain characterized using random-walk statistics with volume fractions $f_A$ and $f_B$ with degree of polymerization $N$. The local interactions are governed by predicted interaction parameters at varied GMA molar ratios (Figure 6-6) along with the incompressibility condition of $\Sigma fii$=1. The code for performing SCFT was from the reported literature[38].

The simulated polymers were assumed to be monodisperse with temperature independent densities. The simulations were carried out at 180 °C annealing temperature and the statistical segment lengths of counter-blocks were set equal. The averaged densities of mixing blocks with varied fluorinated GMA molar ratios were estimated from the specific fractions of two components. A grid size of 64 × 64 (box in 8 $R_g$ scale) or 96 × 96 (box in 12 $R_g$ scale) was used for the 2D SCFT calculations with a 100 contour steps in inner loops. The simulations were performed using the pseudo-spectral method developed by Rasmussen and Kalosakas starting from random initial conditions followed by Anderson acceleration once a stable morphology could be identified (typically at changes in the free energy $\leq 1\times10^{-10}$).

In predictions all investigated $PSG_FMs$ revealed the morphologies in good agreements with those determined by SAXS analysis (Figure 6-12 and Figure 6-13). Disordered morphology instead of weakly segregated lamellae was suggested for $PSG_FM11$-20 because of the assumption of monodisperisity in SCFT, which is different from the dispersity approximation in RPA methods. The SCFT prediction on $PSG_FM9$-46 displayed PS domains in hexagonally packing array. More simulations using the slightly tuned values of $f_{PS}$ as inputs are carried out for exploring the morphology transition boundary (Figure 6-14). As $f_{PS}$ of $PSG_FM9$-46 was slightly increased to 0.42, a morphology transition from hexagonally packed cylinders to lamellae was observed.

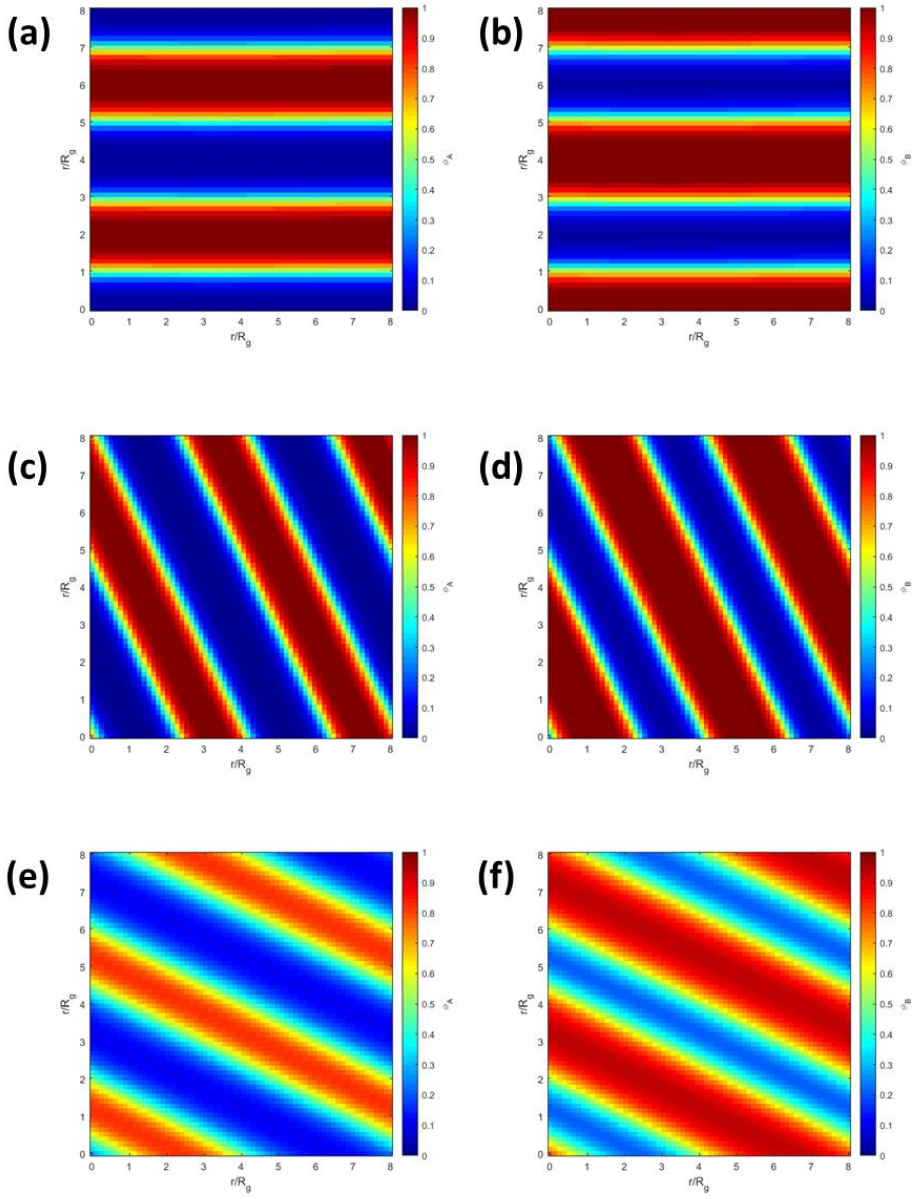


**Figure 6-12.** The predicted 2-D morphologies calculated using SCFT for (a-b) LAM $PSG_FM21$-13, (c-d) LAM $PSG_FM25$-20 and (e-f) LAM $PSG_FM25$-28. The red and blue colors indicate PS and randomly mixed PHFMA-*r*-PMMA segments in left column and invert in right column. The density gradient bar for different segments is given next to each image. The scale of rectangular box for running the simulations was set to 8 times of radius of gyration ($R_g$) of BCPs.

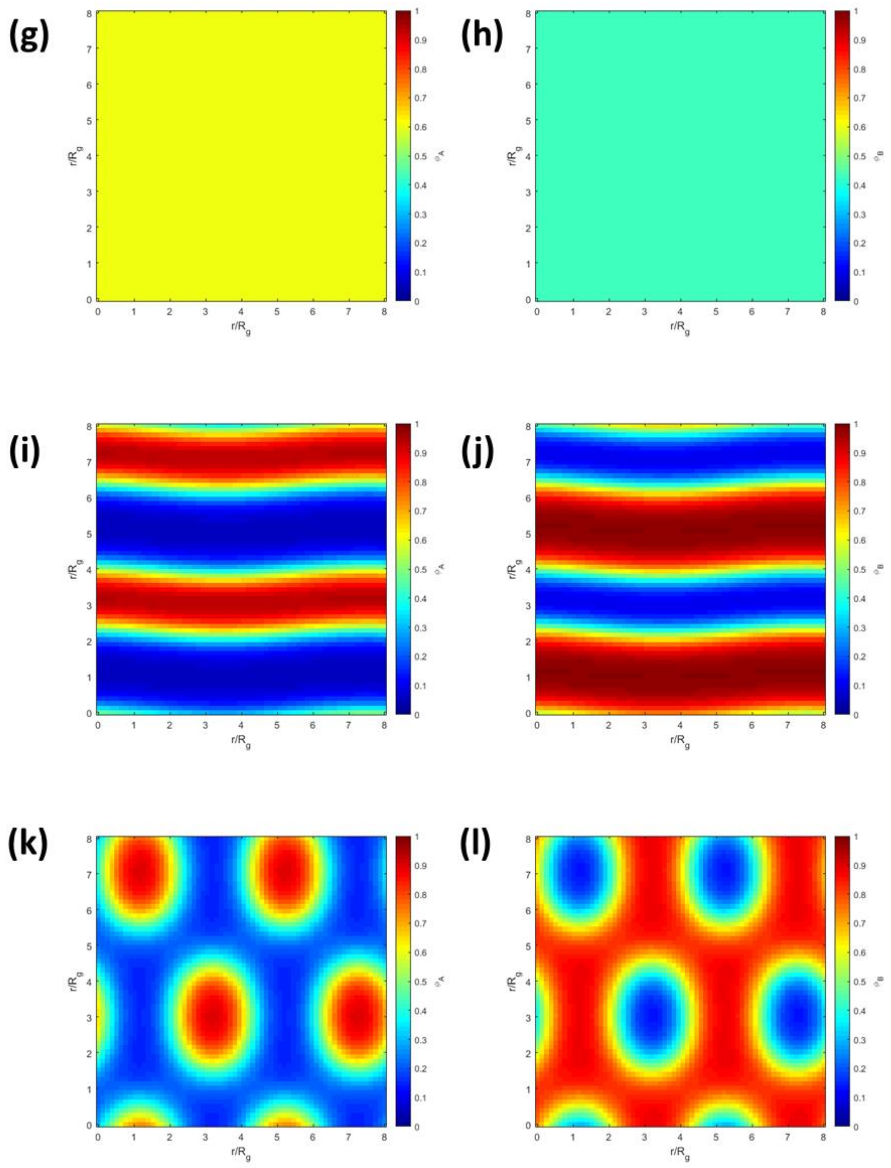


**Figure 6-13.** The predicted 2-D morphologies calculated using SCFT for (g-h) Dis $PSG_FM11$-20, (i-j) LAM $PSG_FM12$-30 and (k-l) HEX $PSG_FM9$-46. The red and blue colors indicate PS and randomly mixed PHFMA-*r*-PMMA segments in left column and invert in right column. The density gradient bar for different segments is given next to each image. The scale of rectangular box for running the simulations was set to 8 times of radius of gyration ($R_g$) of BCPs.

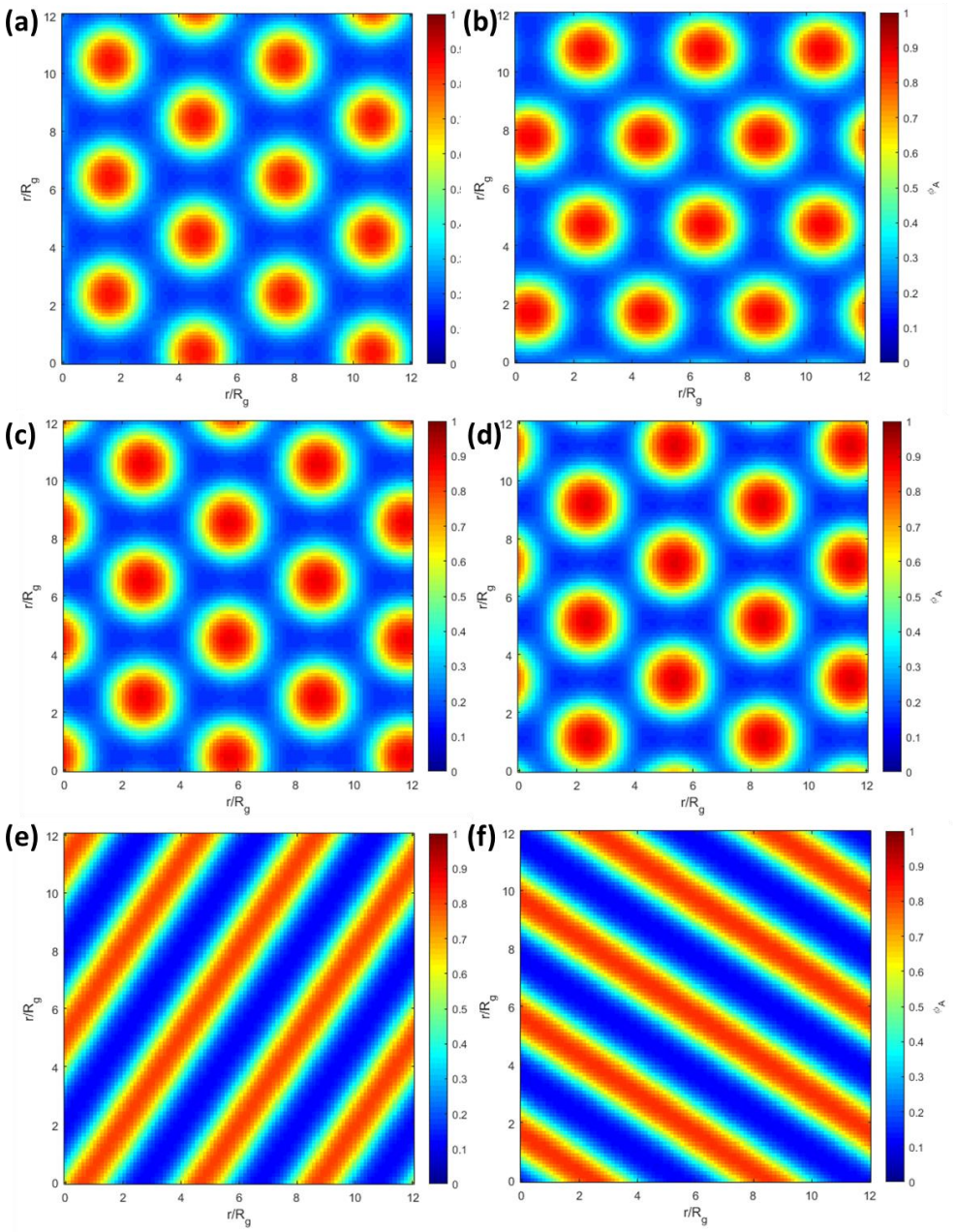


**Figure 6-14.** The predicted 2-D morphologies calculated using SCFT for $PSG_FM9$-46 using (a) $f_{PS}$=0.38, (b) $f_{PS}$=0.39, (c) $f_{PS}$=0.40, (d) $f_{PS}$=0.41, (e) $f_{PS}$=0.42 and (f) $f_{PS}$=0.43 as inputs. The red and blue colors indicate PS and randomly mixed PHFMA-*r*-PMMA segments. The density gradient bar for different segments is given next to each image. The scale of rectangular box for running the simulations was set to 12 times of radius of gyration ($R_g$) of BCPs. A morphology transition from anisotropic HEX to LAM was observed at $f_{PS}$=0.42.

**6-3-5. Perpendicular Lamellae in Thin Film**

To investigate the effects of randomly loaded fluorinated moieties into PMMA block on the self-assembly behavior in the thin films, $PSG_FM12$-30 ($f_{PS}$=0.38), which is capable of forming 15 nm lamellae in bulk, was used for preparation of thin film samples. Here the random copolymer PS-*r*-PMMA-*r*-PGMA with $f_{PS}$=0.39 was used as bottom surface layer (BSL) to neutralize any preferential affinity of the counter-blocks in $PSG_FM12$-30 onto the bottom interface. The $PSG_FM12$-30 was then spin-coated from toluene solution onto BSLs and annealed at 200 ℃ under ambient conditions. To create a higher contrast between distinctive domains in thin film, an $O_2$-RIE treatment was further conducted to selectively remove the mixed acrylated-based domain consisted of MMA and fluorinated GMA units.

Since the thin film morphology is highly dependent the thermal annealing conditions, the first optimization is focused on the annealing time. Following $O_2$-RIE treatments, fingerprint pattern was observed in all thin film samples annealed for distinctive time (Figure 6-15). The fast Fourier transform (FFT) of the AFM images indicates an increased periodicity of the observed fingerprint pattern, as the absolute intensities of primary and secondary peaks from FFT integration were both increased (Figure 6-16).. No significant difference between the FFT integrations of thin film patterns annealed at 10 min and 60 min was observed. The fact indicates that 10 mins' thermal annealing at 200 ℃ is adequate for inducing self-assembled morphology in thermodynamics stable state. The averaged periodic width of fingerprint pattern was estimated from the position of the primary peak in FFT integration. An averaged domain size ($L_0$) of almost constant 15.0 nm under varied annealing time was suggested, which is highly consistent with the domain spacing obtained in bulk sample.

Besides, the quantitative analysis[39] on the AFM phase images were further carried out. The coloring mapping (Figure 6-17) results displayed the orientation of the finger-print patterns across the entire scanning area. The cluster of the uniform color indicative of the same orientation could be defined as one specific grain. As the annealing time was extended, larger grains in response to higher periodicity were observed. One quantified parameter for evaluating the periodicity of lined pattern is correlation length ($\xi$). The quantitative analysis also gave the estimated correlation lengths of patterns under various annealing time. A short 2 min's annealing instantly produced patterns with a correlation length of 6.4 times of $L_0$. Up to 10 min's annealing, the correlation length was dramatically grown to 13 times of $L_0$ and became constant. The change of correlation length upon thermal annealing is highly correlated with the results from analysis on FFT integration profiles and color mapping. The analysis results based on an extended scanning area is also evident for the above conclusion. (Figure 6-18(a), (c) and (e)) Thus, the analysis results based on 1.0 μm × 1.0 μm scanning scale were thought representative for the whole thin film sample surface. Compared to other

reported high χ parameter BCPs[39 40] and commonly studied PS-*b*-PMMA[41 42] with a correlation length of 3~7 $L_0$ in randomly oriented thin film state, $PSG_FM12$-30 revealed an significantly improved correlation length of rarely seen 13 $L_0$ in short annealing time. The similar improved correlation length usually requires time-costly annealing of at least 72 hr[43].

Generally, the perfectly neutralized interfacial conditions were difficult to be achieved for most high χ parameter BCPs because of the frequently occurred huge SFE gap between counter-blocks. Hence, the high periodicity in bulk morphologies prepared from BCPs of high χ parameters could not be completely transferred to the thin film morphologies. Meanwhile, the relatively low χ parameter of PS-*b*-PMMA was insufficient for inducing high-ordered patterns under low $M_n$, despite the near perfectly balanced SFEs between PS and PMMA segments. However, by quantitatively introducing randomly distributed fluorinated units into PMMA blocks, the trade-off relationship between the high χ parameter and perfectly neutralized interfaces was optimized. Inherited from the combined advantages from the above mentioned two perspectives, $PSG_FM12$-30 successfully demonstrated the potential for fabrication of sub-15 nm lined patterns (7.5 nm half pitch) of super long-ranged periodicity.

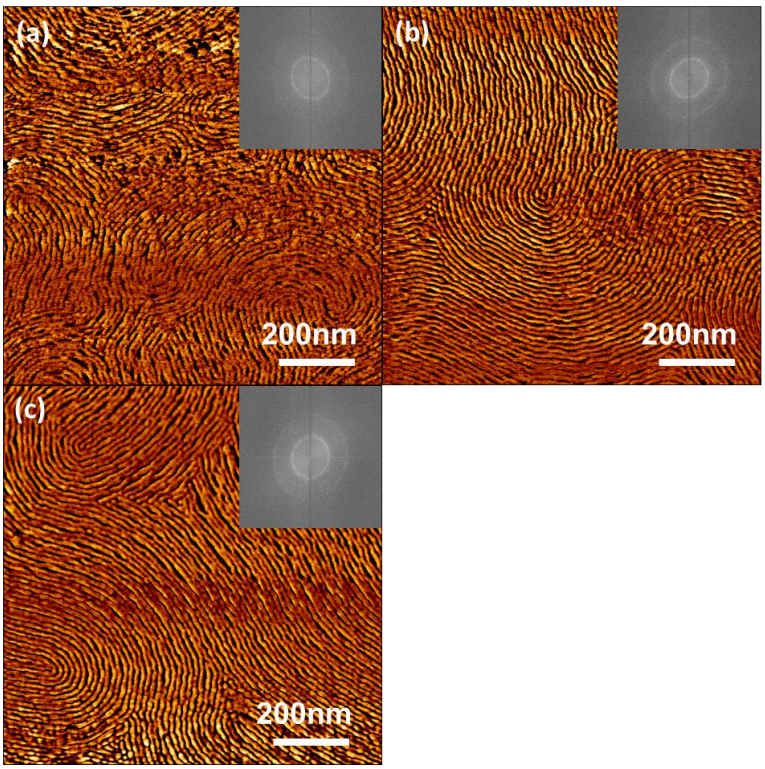


**Figure 6-15**. AFM phase images of $PSG_FM12$-30 ontop neutral BSLs following thermal annealing at 200 °C for (a) 2 min, (b) 10 min and (c) 60 min. The $O_2$-RIE treatment is carried out with exposure for 30 s. The inset in each image presents the FFT of the image.

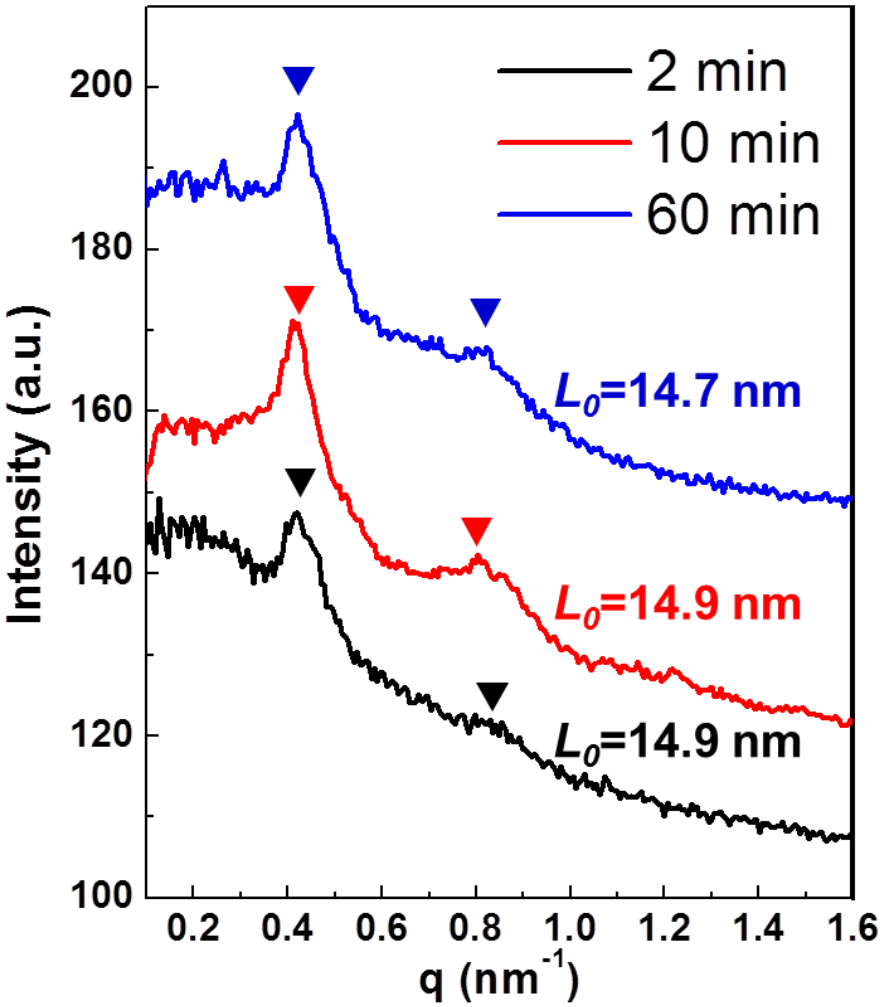


**Figure 6-16**. The 1-D integration profile of 2D FFT signals along the radius to the center of FFT inset image extracted from AFM phase images of the thin films annealed at 200 ℃ for 2, 10 and 60 min. The averaged periodic length of domain ($L_0$) is further estimated from the position of primary peak in 1-D integration profile and marked in different colors.

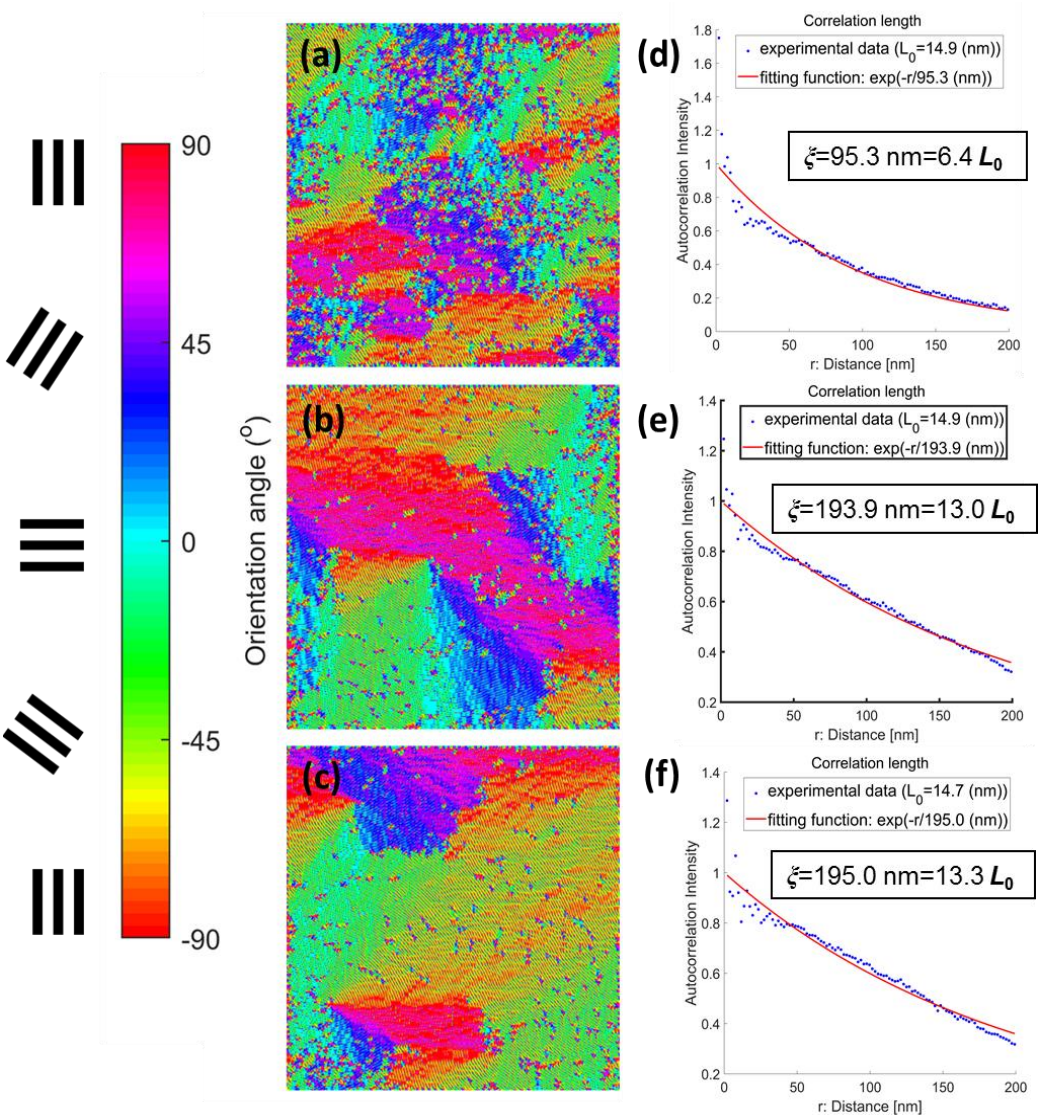


**Figure 6-17**. For the left column, the corresponding color mappings of AFM phase images of the thin films annealed at 200 ℃ for (a) 2, (b) 10 and (c) 60 min following $O_2$-RIE treatment in 1.0 μm × 1.0 μm scale. The distinctive color denotes the varied orientation angle of domain as shown in the left bar. For the right column, the autocorrelation intensity plot and fitting for correlation length ($\xi$) from corresponding AFM phase images of the thin films annealed for (d) 2, (e) 10 and (f) 60 min.

Besides the annealing time, another factor affecting the thin film morphology is the exposure time under $O_2$ RIE treatment. According to the previous study, fluorinated PHFMA and PMMA blocks both exhibited significantly higher etching rates compared to that of PS segments[34 44]. Hence, the contrast between PS and mixed acrylated-based domains will be improved by selective removal of blocks of lower etching-resistance under $O_2$ RIE treatment.

To investigate the optimized etching time, the thin film samples annealed at 200 °C for 10 min were placed under $O_2$ RIE treatment for varied time intervals (Figure 6-19). The dim fingerprint patterns were even observed on the surface of as-prepared sample. However, in some areas featureless covering layers were observed. A larger scanning area in 10 μm × 10 μm scale clearly revealed the randomly distributed covering clusters with up to a few hundred nanometers scale. The featureless surfaces were speculated caused by the aggregation of fluorinated PHFMA segments onto the free surface. Compared to the reported SFE of PS of 40.7 mJ $m^{-2}$ at 25 °C [45], the measured SFE of PHFMA is 33.3 mJ $m^{-2}$ at 25 °C [34], which is relatively lower than that of PS. Hence, the segments of lower SFE will be driven towards free surface under thermal annealing. The segments may come from some discrete and short PHFMA blocks in polymer chains, as the added MMA and GMA monomers may not be exactly simultaneously polymerized in equal kinetics. Following $O_2$ RIE treatment for merely 5 seconds, the contrast between distinctive domains became more significant. The similar quantitative analysis was applied to the observed AFM phase images, and the almost same domain spacing of 15.4 nm with a correlation length of 12.1 $L_0$ was extracted. (Figure 6-18(b), (d) and (f)). However, as the $O_2$ RIE treatment time is further extended 15 s or 30 s, the collapses of PS domains, to some extent, was observed with fused junction between neighbored domains. Meanwhile, the featureless top-coverings consisted of aggregated segments were completely removed under extended exposure to etching stream. Therefore, $O_2$ RIE treatment lasting for a few seconds is adequate for AFM observation. To fully remove the top-covering layers and complete the pattern transferring into the underlying substrate, extended etching time became essential, despite of the risk of bringing some collapsed domain structure.

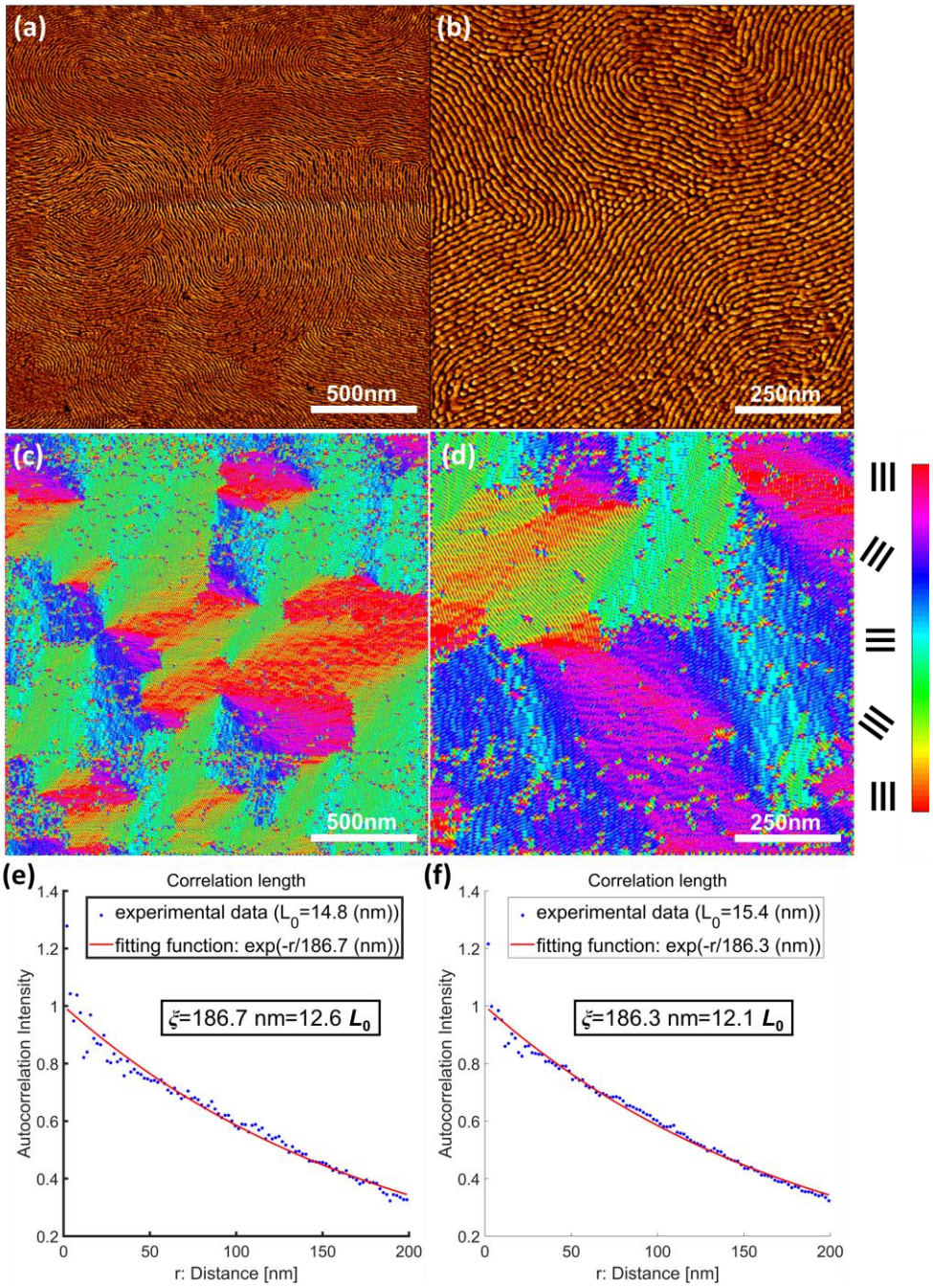


**Figure 6-18**. AFM phase images of $PSG_FM12$-30 ontop neutral BSLs following thermal annealing at 200 ˚C for 10 min and subsequent $O_2$-RIE treatment for (a) 30 s and (b) 5 s. The corresponding color mappings of AFM phase (c) and (d), autocorrelation intensity plot and fitting for correlation length ($\xi$) (e) and (f), was presented in each column, respectively. Remarkably the scanning of (a) is within a 2.0 μm × 2.0 μm scale.

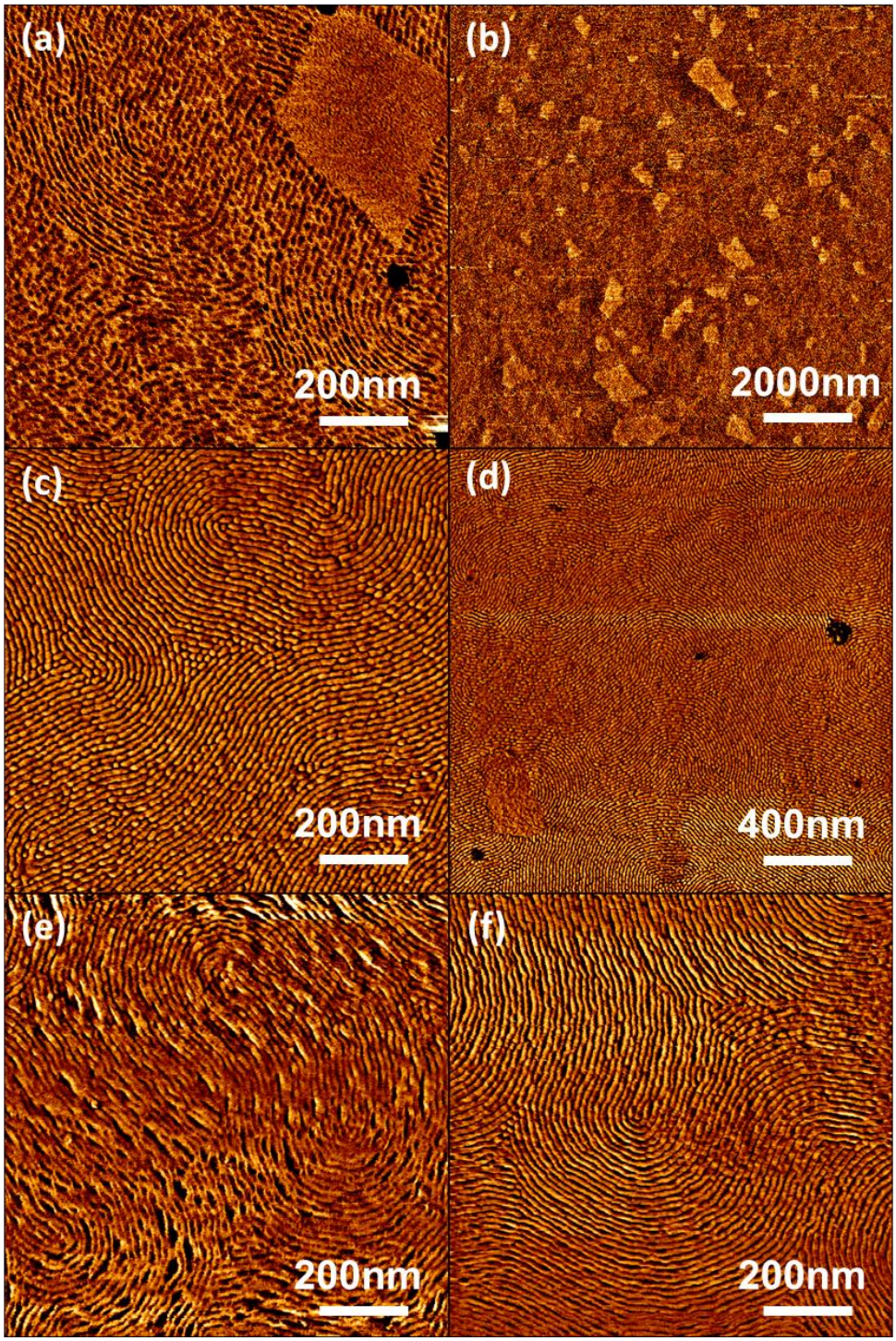


**Figure 6-19**. AFM phase images of $PSG_FM12$-30 ontop neutral BSLs following thermal annealing at 200 ˚C for 10 min (a)-(b) and subsequent $O_2$-RIE treatment for (c)-(d) 5 s, (e) 15 s and (f) 30 s.

**6-4. Conclusion**

In this study, a design concept of introducing quantitative trifluoroethyl functionalities into PMMA block in PS-*b*-PMMA for downsizing the perpendicularly oriented lamellae domain in thin film was demonstrate, which is of paramount importance to improvements on next-generation lithographic application based on PS-*b*-PMMA materials. The precursor BCPs PS-*b*-(PGMA-*r*-PMMA) were first synthesized using sequential anionic living polymerization. The ratio of two monomers in randomly mixed block was facilely tuned by the feeding ratio of glycidyl methacrylate and methyl acrylate added in living polymerization. Beneficial from the easily-handled post-functionalization reaction in mild conditions, the 2,2,2-trifluoroethanethiol was further introduced to the randomly polymerized functional glycidyl moieties in PGMA-*r*-PMMA block with high efficiency and the targeted PS-*b*-(PHFMA-*r*-PMMA) was obtained. The affinities to air from the yielded hydrophilic hydroxyl groups and hydrophobic trifluoroethyl functionalities after post-functionalization were cancelled off with each other, leading to near balanced SFEs but enhanced segregation between block interfaces. The SAXS characterization revealed a positive correlation between the introduced fluorinated GMA molar ratio and the periodicity in self-assembled morphologies. Based on the random-phase approximation and using a reference volume of 118 $Å^3$ to normalize the degree of polymerization over the volume, the temperature dependence of the effective Flory-Huggins interaction parameter of PS-*b*-(PHFMA-*r*-PMMA) at 20 % molar percentage of fluorinated GMA was estimated to be $\chi_{eff} = 2.6/T + 0.057$, and $\chi_{eff}$ was 0.063 at 180 ℃ annealing temperature. The measured $\chi_{eff}$ was slightly lower than the value estimated from the linear combination of $\chi_{PS/PHFMA}$ and $\chi_{PS/PMMA}$ according to volume fraction contribution. Owing the enhanced $\chi_{eff}$, well-ordered lamellae and hexagonally packed cylinders of sub-15 nm domain spacing were observed in bulk. SCFT simulation results were also consistent with experimentally discovered morphologies. The PS-*b*-(PHFMA-*r*-PMMA) capable of forming 15 nm lamellae domain was used in thin film studies. The AFM observation of long-ranged fingerprint patterns indicated the perpendicular lamellae of 15 nm domain spacing on surface-modified silicon wafers after thermal annealing at 200 ℃ for 10 min. The quantitative analysis on AFM images suggested a maximum correlation length of 13 times of domain spacing, which is significantly longer than other reported BCP materials. The formation of super long-ranged ordered fingerprint patterns was attributed to the combination between an increased $\chi_{eff}$ from PS-*b*-PMMA and the perfectly balanced SFEs of counter-blocks. The molecular design of adding quantitative randomly polymerized functionalities into PMMA segments in PS-*b*-PMMA enabled the formation of perpendicularly oriented lamellae domain of a minimized 15 nm-width following thermal

annealing under ambient conditions. Hence, its potential for effectively downsizing the pitch size in next-generation BCP lithographical application was successfully demonstrated.

**6-5. Reference**

1. Bates, C. M.; Seshimo, T.; Maher, M. J.; Durand, W. J.; Cushen, J. D.; Dean, L. M.; Blachut, G.; Ellison, C. J.; Willson, C. G., Polarity-Switching Top Coats Enable Orientation of Sub-10-nm Block Copolymer Domains. *Science* **2012,** *338* (6108), 775-779.

2. Maher, M. J.; Bates, C. M.; Blachut, G.; Sirard, S.; Self, J. L.; Carlson, M. C.; Dean, L. M.; Cushen, J. D.; Durand, W. J.; Hayes, C. O.; Ellison, C. J.; Willson, C. G., Interfacial Design for Block Copolymer Thin Films. *Chem Mater* **2014,** *26* (3), 1471-1479.

3. Durand, W. J.; Carlson, M. C.; Maher, M. J.; Blachut, G.; Santos, L. J.; Tein, S.; Ganesan, V.; Ellison, C. J.; Willson, C. G., Experimental and Modeling Study of Domain Orientation in Confined Block Copolymer Thin Films. *Macromolecules* **2016,** *49* (1), 308-316.

4. Lane, A. P.; Yang, X. M.; Maher, M. J.; Blachut, G.; Asano, Y.; Soineya, Y.; Mallavarapu, A.; Sirard, S. M.; Ellison, C. J.; Willson, C. G., Directed Self-Assembly and Pattern Transfer of Five Nanometer Block Copolymer Lamellae. *ACS Nano* **2017,** *11* (8), 7656-7665.

5. Son, J. G.; Gotrik, K. W.; Ross, C. A., High-Aspect-Ratio Perpendicular Orientation of PS-b-PDMS Thin Films under Solvent Annealing. *ACS Macro Lett* **2012,** *1* (11), 1279-1284.

6. Jeong, J. W.; Park, W. I.; Kim, M. J.; Ross, C. A.; Jung, Y. S., Highly Tunable Self-Assembled Nanostructures from a Poly(2-vinylpyridine-b-dimethylsiloxane) Block Copolymer. *Nano Lett* **2011,** *11* (10), 4095-4101.

7. Kim, J. M.; Hur, Y. H.; Jeong, J. W.; Nam, T. W.; Lee, J. H.; Jeon, K.; Kim, Y.; Jung, Y. S., Block Copolymer with an Extremely High Block-to-Block Interaction for a Significant Reduction of Line-Edge Fluctuations in Self Assembled Patterns. *Chem Mater* **2016,** *28* (16), 5680-5688.

8. Al-Hussein, M.; Serero, Y.; Konovalov, O.; Mourran, A.; Moller, M.; de Jeu, W. H., Nanoordering of fluorinated side-chain liquid crystalline/amorphous diblock copolymers. *Macromolecules* **2005,** *38* (23), 9610-9616.

9. Verploegen, E.; Zhang, T.; Jung, Y. S.; Ross, C.; Hammond, P. T., Controlling the Morphology of Side Chain Liquid Crystalline Block Copolymer Thin Films through Variations in Liquid Crystalline Content. *Nano Lett* **2008,** *8* (10), 3434-3440.

10. Qu, T.; Guan, S.; Zhang, C.; Zheng, X. X.; Zhao, Y. B.; Chen, A. H., Liquid crystalline moiety-assisted perpendicular orientation of cylindrical domains within P4VP-b-PMA(Az) films with high aspect ratio. *Soft Matter* **2018,** *14* (35), 7107-7112.

11. Jiang, X. Q.; Zhao, R. Y.; Chang, W. Y.; Yin, D. X.; Guo, Y. C.; Wang, W.; Liang, D. H.; Yang, S.; Shi, A. C.; Chen, E. Q., Highly Ordered Sub-10 nm Patterns Based on Multichain

Columns of Side-Chain Liquid Crystalline Polymers. *Macromolecules* **2019,** *52* (13), 5033-5041.

12. Wan, L.; Ruiz, R.; Gao, H.; Patel, K. C.; Albrecht, T. R.; Yin, J.; Kim, J.; Cao, Y.; Lin, G., The Limits of Lamellae-Forming PS-b-PMMA Block Copolymers for Lithography. *ACS Nano* **2015,** *9* (7), 7506-7514.

13. Sinturel, C.; Bates, F. S.; Hillmyer, M. A., High χ–Low N Block Polymers: How Far Can We Go? *ACS Macro Lett* **2015,** *4* (9), 1044-1050.

14. Liu, C. C.; Han, E.; Onses, M. S.; Thode, C. J.; Ji, S. X.; Gopalan, P.; Nealey, P. F., Fabrication of Lithographically Defined Chemically Patterned Polymer Brushes and Mats. *Macromolecules* **2011,** *44* (7), 1876-1885.

15. Delgadillo, P. A. R.; Thode, C. J.; Nealey, P. F.; Gronheid, R.; Wu, H.; Cao, Y.; Neisser, M.; Somervell, M. H.; Nafus, K., Implementation of a chemo-epitaxy flow for directed self-assembly on 300-mm wafer processing equipment. *Journal of Micro/Nanolithography, MEMS, and MOEMS* **2012,** *11* (3), 031302.

16. Gronheid, R.; Delgadillo, P. R.; Pathangi, H.; Van den Heuvel, D.; Parnell, D.; Chan, B. T.; Lee, Y.-T.; Van Look, L.; Cao, Y.; Her, Y. In *Defect reduction and defect stability in IMEC's 14nm half-pitch chemo-epitaxy DSA flow,* Alternative Lithographic Technologies VI, International Society for Optics and Photonics: 2014; p 904905.

17. Tsai, H.; Pitera, J. W.; Miyazoe, H.; Bangsaruntip, S.; Engelmann, S. U.; Liu, C.-C.; Cheng, J. Y.; Bucchignano, J. J.; Klaus, D. P.; Joseph, E. A., Two-dimensional pattern formation using graphoepitaxy of PS-b-PMMA block copolymers for advanced FinFET device and circuit fabrication. *ACS Nano* **2014,** *8* (5), 5227-5232.

18. Xiao, S.; Yang, X.; Edwards, E. W.; La, Y.-H.; Nealey, P. F., Graphoepitaxy of cylinder-forming block copolymers for use as templates to pattern magnetic metal dot arrays. *Nanotechnology* **2005,** *16* (7), S324.

19. Han, E.; Kang, H.; Liu, C. C.; Nealey, P. F.; Gopalan, P., Graphoepitaxial assembly of symmetric block copolymers on weakly preferential substrates. *Adv Mater* **2010,** *22* (38), 4325-4329.

20. Han, E.; Gopalan, P., Cross-linked random copolymer mats as ultrathin nonpreferential layers for block copolymer self-assembly. *Langmuir* **2010,** *26* (2), 1311-1315.

21. Han, E.; Stuen, K. O.; Leolukman, M.; Liu, C.-C.; Nealey, P. F.; Gopalan, P., Perpendicular orientation of domains in cylinder-forming block copolymer thick films by controlled interfacial interactions. *Macromolecules* **2009,** *42* (13), 4896-4901.

22. Ham, S.; Shin, C.; Kim, E.; Ryu, D. Y.; Jeong, U.; Russell, T. P.; Hawker, C. J., Microdomain orientation of PS-b-PMMA by controlled interfacial interactions. *Macromolecules* **2008,** *41* (17), 6431-6437.

23. Han, E.; Stuen, K. O.; La, Y.-H.; Nealey, P. F.; Gopalan, P., Effect of composition of substrate-modifying random copolymers on the orientation of symmetric and asymmetric diblock copolymer domains. *Macromolecules* **2008,** *41* (23), 9090-9097.

24. Guo, R.; Kim, E.; Gong, J.; Choi, S.; Ham, S.; Ryu, D. Y., Perpendicular orientation of microdomains in PS-b-PMMA thin films on the PS brushed substrates. *Soft Matter* **2011,** *7* (15), 6920-6925.

25. Lee, W.; Park, S.; Kim, Y.; Sethuraman, V.; Rebello, N.; Ganesan, V.; Ryu, D. Y., Effect of grafting density of random copolymer brushes on perpendicular alignment in PS-b-PMMA thin films. *Macromolecules* **2017,** *50* (15), 5858-5866.

26. Ryu, D. Y.; Ham, S.; Kim, E.; Jeong, U.; Hawker, C. J.; Russell, T. P., Cylindrical microdomain orientation of PS-b-PMMA on the balanced interfacial interactions: composition effect of block copolymers. *Macromolecules* **2009,** *42* (13), 4902-4906.

27. Zhao, Y.; Sivaniah, E.; Hashimoto, T., SAXS Analysis of the Order−Disorder Transition and the Interaction Parameter of Polystyrene-block-poly(methyl methacrylate). *Macromolecules* **2008,** *41* (24), 9948-9951.

28. Wan, L.; Ruiz, R.; Gao, H.; Patel, K. C.; Albrecht, T. R., The Limits of Lamellae-Forming PS-b-PMMA Block Copolymers for Lithography. *ACS Nano* **2015,** *9* (7), 7506-7514.

29. Yoshida, K.; Tian, L.; Miyagi, K.; Yamazaki, A.; Mamiya, H.; Yamamoto, T.; Tajima, K.; Isono, T.; Satoh, T., Facile and Efficient Modification of Polystyrene-block-poly(methyl methacrylate) for Achieving Sub-10 nm Feature Size. *Macromolecules* **2018,** *51* (20), 8064-8072.

30. Isono, T.; Yoshida, K.; Mamiya, H.; Miyagi, K.; Yamazaki, A.; Satoh, T. In *Post-polymerization modification of PS-b-PMMA for achieving directed self-assembly with sub-10nm feature size*, Advances in Patterning Materials and Processes XXXVI, International Society for Optics and Photonics: 2019; p 109600U.

31. Yoshida, K.; Tanaka, S.; Yamamoto, T.; Tajima, K.; Borsali, R.; Isono, T.; Satoh, T., Chain-End Functionalization with a Saccharide for 10 nm Microphase Separation: “Classical” PS-b-PMMA versus PS-b-PMMA-Saccharide. *Macromolecules* **2018,** *51* (21), 8870-8877.

32. Zhou, S. X.; Janes, D. W.; Kim, C. B.; Willson, C. G.; Ellison, C. J., Designing Intrablock Attractions To Increase the χ Parameter of a Symmetric Diblock Copolymer. *Macromolecules* **2016,** *49* (21), 8332-8340.

33. Lee, K. S.; Lee, J.; Kwak, J.; Moon, H. C.; Kim, J. K., Reduction of Line Edge Roughness of Polystyrene-block-Poly(methyl methacrylate) Copolymer Nanopatterns By Introducing Hydrogen Bonding at the Junction Point of Two Block Chains. *ACS Appl Mater Inter* **2017,** *9* (37), 31245-31251.

34. Yoshimura, Y.; Chandra, A.; Nabae, Y.; Hayakawa, T., Chemically tailored high-chi block copolymers for perpendicular lamellae via thermal annealing. *Soft Matter* **2019,** *15* (17), 3497-3506.

35. Sakamoto, N.; Hashimoto, T., Order-Disorder Transition of Low Molecular Weight Polystyrene-block-Polyisoprene. 1. SAXS Analysis of Two Characteristic Temperatures. *Macromolecules* **1995,** *28* (20), 6825-6834.

36. Yu, D. M.; Mapas, J. K. D.; Kim, H.; Choi, J.; Ribbe, A. E.; Rzayev, J.; Russell, T. P., Evaluation of the Interaction Parameter for Poly(solketal methacrylate)-block-polystyrene Copolymers. *Macromolecules* **2018,** *51* (3), 1031-1040.

37. Chatterjee, J.; Jain, S.; Bates, F. S., Comprehensive phase behavior of poly(isoprene-b-styrene-b-ethylene oxide) triblock copolymers. *Macromolecules* **2007,** *40* (8), 2882-2896.

38. Wylie, K.; Dong, L.; Chandra, A.; Nabae, Y.; Hayakawa, T., Modifying the Interaction Parameters of a Linear ABC Triblock Terpolymer by Functionalizing the Short, Reactive Middle Block To Induce Morphological Change. *Macromolecules* **2020,** *53* (4), 1293-1301.

39. Nakatani, R.; Chandra, A.; Uchiyama, T.; Nabae, Y.; Hayakawa, T., Dynamic Ordering in High-chi Block Copolymer Lamellae Based on Cross-Sectional Orientational Alignment. *ACS Macro Lett* **2019,** *8* (9), 1122-1127.

40. Murphy, J. N.; Harris, K. D.; Buriak, J. M., Automated Defect and Correlation Length Analysis of Block Copolymer Thin Film Nanopatterns. *PLOS ONE* **2015,** *10* (7), e0133088.

41. Ceresoli, M.; Volpe, F. G.; Seguini, G.; Antonioli, D.; Gianotti, V.; Sparnacci, K.; Laus, M.; Perego, M., Scaling of correlation length in lamellae forming PS-b-PMMA thin films upon high temperature rapid thermal treatments. *J Mater Chem C* **2015,** *3* (33), 8618-8624.

42. Ferrarese Lupi, F.; Giammaria, T. J.; Volpe, F. G.; Lotto, F.; Seguini, G.; Pivac, B.; Laus, M.; Perego, M., High Aspect Ratio PS-b-PMMA Block Copolymer Masks for Lithographic Applications. *ACS Appl Mater Inter* **2014,** *6* (23), 21389-21396.

43. Black, C. T.; Forrey, C.; Yager, K. G., Thickness-dependence of block copolymer coarsening kinetics. *Soft Matter* **2017,** *13* (18), 3275-3283.

44. Ting, Y.-H.; Park, S.-M.; Liu, C.-C.; Liu, X.; Himpsel, F.; Nealey, P. F.; Wendt, A. E., Plasma etch removal of poly (methyl methacrylate) in block copolymer lithography. *Journal of Vacuum Science & Technology B: Microelectronics and Nanometer Structures Processing, Measurement, and Phenomena* **2008,** *26* (5), 1684-1689.

45. Wu, S. In *Calculation of interfacial tension in polymer systems*, Journal of Polymer Science Part C: Polymer Symposia, Wiley Online Library: 1971; pp 19-30.

# Chapter 7
# General Conclusions

Diblock copolymers (BCPs) of high χ parameter had been widely studied, due to the potential application in perspective lithographic technologies. In specific, to meet the requirements for these applications, the desired diblock copolymers materials were at least expected to exhibit a high etching selectivity, a facile perpendicular orientation control on thin film domains assisted by compatible thermal annealing process and of course a high χ parameter. Based on previous theoretic and experimental studies, a high χ parameter will provide the strong microphase separation driving force and afford a small self-assembly domain spacing, which satisfies the demand for minimized line with of pattern in current lithographic industry.

Fluorinated BCPs are reported to reveal high χ parameters because of their intrinsic low surface energy, which is extremely incompatible with organic segments. Therefore, recently BCPs with facile introduction of fluorinated side chains are considered as a promising category of candidate materials for fabrication of minimized pattern size (e.g. sub-5 nm) in next-generation lithography of semiconductor manufacturing.

In this thesis, the author discussed the molecular design on novel high χ parameter BCPs with semi-fluorinated liquid crystalline or amorphous side chains and essential efforts to satisfy these above mentioned requirements in thin film for next-generation lithographic application, such as for BCP domain orientation control.

In Chapter 1, the background of BCPs self-assembly, especially those focused on high χ parameter, was firstly described. Meanwhile, the early studies on BCPs with fluorinated side chains were concentrated on the surface structure for understanding the reason for causing super-hydrophilic properties, which were of paramount importance to applications such as antifouling coating or surface patterning. Another application as polymer resist is also widely studied because of the high transparency of fluorinated BCPs under photolithographic wavelength. In these studies, liquid crystalline (LC) semi-fluorinated side chains were widely used and the LC side chain mesogens were observed tilted at certain angle to the air surface. The surface structure and LC phase of side chain is found highly dependent on the length of fluorinated side chain and environment. In self-assembly studies, in prior to the thin film self-assembly, the earlier micelles self-assembly in preferential solvents was firstly reviewed because of the high correlation between these two fields. In thin film studies, as some literatures used the BCPs of LC fluorinated side chain, a hierarchy nanostructure with different self-assembly scales of BCP domain and LC ordering was revealed by X-ray characterization. Besides, the LC ordering was reported to have an impact on the orientation of BCP domain in

thin film. Furthermore, the simulation works on side chain liquid crystalline BCPs were introduced as theoretical supports. Due to the competing self-assembly driving forces from segregation and liquid crystal organizing, a hierarchical self-assembly in the system occurs and a phase diagram enormously different from that derived from flexible coil model was obtained. The situation in thin film even becomes more complex and the relevant theory is developing till now. An outline of this thesis was given in the last part of Chapter 1.

Chapter 2 focused on side chain liquid crystalline (SCLC) fluorinated functionalities capable of forming minimal spacing and controlling the orientation of the BCP domains in thin film. By introducing 1H,1H,2H,2H-perfluorodecanethiol onto a PS-*b*-PGMA precursor polymer to obtain a novel BCP with a $C_8F_{17}$-containing LC side chain, a high $\chi$ parameter ($\chi$ =0.244 at 25 °C) and strong LC side chain ordering enabled the formation of BCP domain in 6.3-36.3 nm scale. For the studied SCLC diblock copolymers of basically symmetric volume fraction, a morphology transition from lamellae to cylinder was observed with reduced molecular weight and enhanced contribution on self-assembly from side chain LC ordering. A co-existed 3.6 nm periodicity from lamellar smectic phase of SCLC was also verified in all synthesized BCPs of varied $M_n$ by comprehensive characterizations of small (SAXS) and wide angle X-ray scattering (WAXS), differential scanning calorimetry (DSC) and polarized optical microscopy (POM). The quantitative analysis on images obtained from atomic force microscopy (AFM) of the thin films revealed the formation of fingerprint patterns with increased correlation length and reduced width/edge roughness when the $d_{spacing}$ of the BCP is closer to the periodicity of the smectic structures. The LC side chain ordering enabled the perpendicularly-oriented lamellar or parallel-oriented cylindrical domain of a minimized 12 nm length in thin film, which is among the smallest scale observed to date. The facile approach to sub-5 nm striation pattern of BCPs in thin film provides a new insight into the role of LC side chain on thin film BCP domain orientation and ordering control.

In Chapter 3, the self-assembly morphology in hierarchical ordering of particularly one BCP with a minimal spacing in thin film was further investigated. Because of the confinement from smectic LC structures with 3.6 nm periodicities, anisotropic hexagonally packed PS cylinder domains with an averaged periodicity of 11.5 nm were characterized by transmission electron microscopy (TEM) and small angle X-ray scattering (SAXS). Owing to the anisotropic array, two striations of distinctive dimensions ($a_1$=10.9 nm and $a_2$=12.7 nm) from side view of the array were observed, which are in response to two distinctive domain spacings between adjacent PS cylinders ($d_1=2/\sqrt{3}a_1$=11.9 nm and $d_2=2/\sqrt{3}a_2$=13.9 nm). To better investigate the role of LC structures in this hierarchical self-assembly system, the effects of side chain length were investigated by introducing semi-fluorinated side chains of varied lengths (CF3, C4F9, C6F13 and C8H17) into a fixed precursor PS-*b*-PGMA. The $M_n$ and

volume fraction of all synthesized copolymers are basically similar with each other. As the fluorinated side chain is elongated from C4F9 to C6F13, the side chain LC ordering starts to appear in bulk. Accordingly, a morphology transition from lamellae to circular cylinder in isotropic hexagonal packing array, and further to elliptical cylinder in anisotropic hexagonal packing array was observed with gradually elongated fluorinated side chain, despite the similar symmetric volume fraction and block segregation intensity ($\chi N$). The morphology studies on BCPs of varied fluorinated side chains reveals the significant role of LC side chain ordering with highly-ordered smectic phase on this unique anisotropic feature of hierarchical self-assembly morphology.

Owing to the observed anisotropic array of self-assembly morphology in bulk, the potential for tailoring domain size and domain orientation in thin film was firstly indicated in Chapter 3. Therefore, in the following Chapter 4, a facile approach of domain orientation control in thin film was demonstrated by employing a certain BCP with liquid crystalline semifluroinated side chains through tuning the composition of the copolymers of the bottom surface layer (BSL). Following the synthetic routine in Chapter 2 and Chapter 3, 1H,1H,2H,2H-Perfluorodecanethiol was attached onto a precursor polymer, polystyrene-*block*-poly(glycidyl methacrylate) (PS-*b*-PGMA), to obtain a novel BCP with a C8F17-containing liquid crystal (LC) side chain (PS-*b*-P8FMA). Statistical/random copolymers Poly(methyl methacrylate-*random*-2,2,2-trifluoroethyl methacrylate-*random*-methacrylic acid)s (PMMA-*ran*-PTFEMA-*ran*-PMAA)s were used as BSLs in the study. The surface free energy (SFE) of BSL was tailored by changing the major composition of PMMA and PTFEMA. Atomic force microscopy (AFM) enabled the investigation of the patterns formed in the thin films. Perpendicularly oriented PS domains in anisotropic hexagonally packed array were obtained by using a non-preferential neutral BSL. Besides, as the composition of BSL is tuned from PS-preferential to P8FMA-preferential, a dimension transition of striation pattern from $d_1$ ($d_1$=11.9 nm) to a wider $d_2$ ($d_2$=13.9 nm) is revealed, in which two distinctive dimensions of patterns are in response to non-tilted and tiled PS cylinders in parallel orientation to the substrate. This transition is thought related to the preferential wetting of PS or P8FMA blocks onto BSL. Therefore, the fine orientation control on BCP domains was successfully achieved by precisely tuning on SFE of BSLs. Accordingly both type and dimension of long-ranged patterns could be easily tailored in thin films partially owing to the anisotropic feature of packing array. The anisotropic array can be reasonably explained by the scale-confined effects from significant LC side chain ordering on self-assembly nanostructures, as evidenced by the previous bulk morphology study on BCPs of distinctive fluorinated side chains of CF3, C4F9 and C6F13 with similar $M_n$ and block volume fractions in Chapter 3. The thin film study in Chapter 4 using BCPs of varied side

chain lengths also reveals the essential role of intensive LC ordering for successful orientation control on BCP domain in long-range orders.

Moving to Chapter 5, semi-fluorinated side chain was further introduced to silicon-backbone BCP via click chemistry because of the well-known advantages of inorganic silicon-based hybrid BCPs, including high χ parameter and enormous etching contrast. In Chapter 5, a high χ parameter diblock polymer, Polystyrene-*block*-poly(methyl ethyl(3,3,4,4,5,5,6,6,7,7,8,8,9,9,10,10,10-heptadecafluorodecyl)sulfane siloxane) (PS-*b*-PSi8F), was synthesized by post-polymerization functionalization of its precursor polystyrene-*block*-poly(methyl vinyl siloxane) (PS-*b*-PMVS) with 1H,1H,2H,2H-perfluorodecanethiol via a thiol-ene reaction. The χ parameter was increased after the incorporation of super-hydrophobic of fluorinated side chain and the χ value at 160 °C was estimated to be 0.095 and 0.179 for precursor PS-*b*-PMVS and PS-*b*-PSi8F, respectively. This in turn resulted in enhanced segregation strength between blocks, giving a potential of minimization in the domain spacing of the block copolymer and thus self-assembled domains in minimal 10 nm-scale spacing were formed. The observed self-assembled morphologies were later found mutually consistent with the modified self-consistent field theory (SCFT) prediction developed for coil-rod structure, in which the rod and coil represents rigid PSi8F and flexible PS segments, respectively, at high annealing temperatures. Additionally, PS-*b*-PSi8F copolymer exhibited ultra-fast self-assembly within 5 minutes' thermal annealing, which is significantly faster than days accounting annealing at similar temperatures for the classical polystyrene-*block*-polydimethylsiloxane (PS-*b*-PDMS), and this was attributed to the low friction of fluorine atoms. A lamellar-forming PS-*b*-PSi8F was further studied in thin films. To overcome the preferential segregation due to the surface energy difference, the PS-*b*-PSi8F thin film (thickness = 28 nm) was sandwiched between both neutral top and bottom interfaces, where the top coat involved a polarity switch and the bottom coat involved a cross-linking process. Perpendicular orientation of lamellae was successfully achieved in thin film with $L_0$ = 22 nm. A pattern consisted of silicon oxide was subsequently obtained after removing organic components via oxygen plasma etching.

In Chapter 6, different from the molecular designs based on the typical diblock copolymer in Chapter 2-5, controlled amounts of randomly polymerized glycidyl methacrylate were incorporated into the PMMA block in poly(styrene-*block*-methyl methacrylate) (PS-*b*-PMMA). In all reported BCP materials for lithographical application, PS-*b*-PMMA is the most widely studied BCP due to its ability to form perpendicularly oriented features when simply heated on an energetically non-preferential substrate. However, the desired smallest attainable pattern size prepared from PS-*b*-PMMA is limited to a full pitch of 24 nm, because of the relatively weak segregation between segments. In this chapter, 2,2,2-trifluoroethanethiol was

quantitatively introduced into the randomly distributed preset reactive sites in PMMA-based block. By merely introducing 20 % molar percentages of 2,2,2-trifluoroethanethiol into the PMMA-based block, the effective χ parameter is significantly increased by 60 %, resulting in BCPs capable of forming sub-15 nm domains. The existed neutralized interfacial conditions for inducing perpendicular PS-b-PMMA domains are still efficient for the newly synthesized poly(styene-*block*-(2-hydroxy-3-(2,2,2-trifluoroethylsulfanyl)propylmethacrylate-*random*-met hyl methacrylate)) (PS-*b*-(PHFMA-*r*-PMMA)), and super long-ranged ordered 15 nm-lamellae can be vertically oriented in the thin film with short-time thermal annealing.

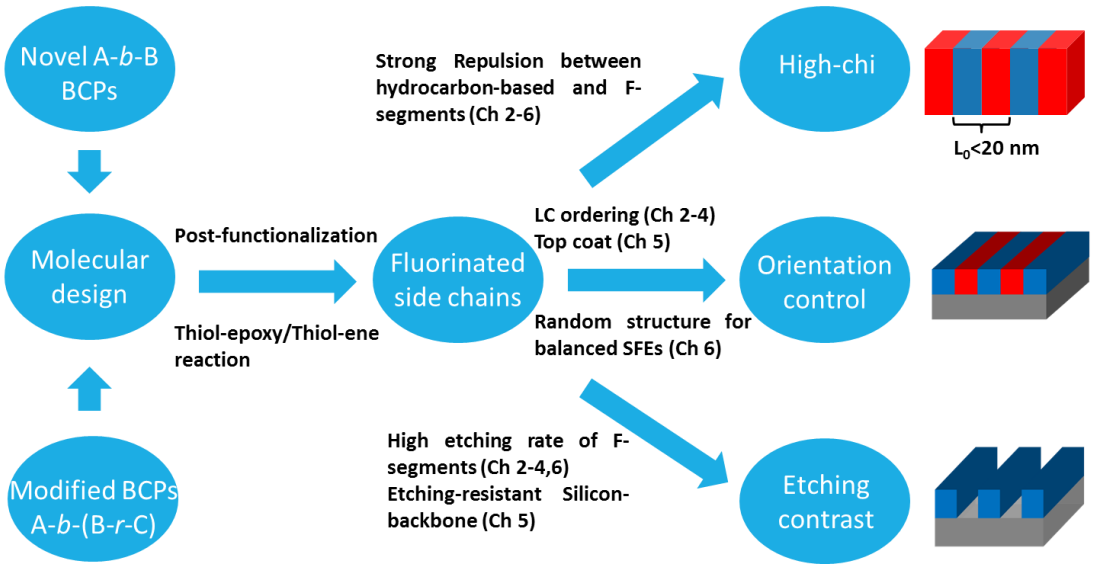


The newly designed high χ parameter BCPs with long semi-fluorinated liquid crystalline side chains reveal the potential for fabrication of long-ranged ordered sub-5 nm dimension (half pitch) pattern in thin film. And the easily performed orientation control technology enable the precise controllable preparation of diverse types of patterns using the same BCP simultaneously. Thus, this novel combination between strong block segregation and LC side chain ordering for achieving long-ranged orders of smaller features are attractive for next-generation lithographic nano-fabrication. Besides, a practical improvement on existed PS-*b*-PMMA lithography materials was achieved by quantitatively introducing short fluorinated functionalities into PMMA blocks as randomly distributed units. The relatively low molar loading ratio of fluorinated functionalities significantly enhanced the segregation intensity and the minimal thin film domain of chemically modified PS-*b*-PMMA was significantly scaled down. Hence, the usage of fluorinated side chains, regardless of being short ones as random units or being pendent rods along the integrated block, is proven highly effective for enhancing segregation intensity and pushing forward the smallest line-width limit in BCPs lithography.

# List of Publications and Presentations

**Publications based on this dissertation**

[1] **L. Dong**, Chandra, A.; Wylie, K.; Nabae, Y.; Hayakawa, T., "The Role of Liquid Crystalline Side Chains for Long-range Ordering in the Block Copolymer Thin Films". *J Photopolym Sci Tec* **2020,** *33* (5), 529-536.

[2] **L. Dong**, Chandra, A.; Wylie, K.; Nabae, Y.; Hayakawa, T., "Adjusting Thin Film Domain Spacings of Side-Chain Liquid Crystalline Semi-fluorinated Block Copolymers with Elliptical Cylinders with Anisotropic Hexagonal Packing". (Under Submission)

**International and Domestic Presentations based on this dissertation**

[1] **L. Dong**, A. Chandra, Kevin. L. Wylie, Y. Nabae, Teruaki Hayakawa, "Asymmetric Hexagonally Packed Cylinder Morphology in a Diblock Copolymer with Liquid Crystalline Semifluorinated Side Chains and Its Domain Orientation Control in Thin Films". **2019** Korea-Japan Joint Symposium on Polymer Science 2019, Seoul, South Korea **(Best Poster Award)**

[2] **L. Dong,** A. Chandra, K. Wylie, Y. Yoshimura, Y. Nabae, Teruaki Hayakawa, "Liquid Crystalline Side Chains for Orientation Control and Long-Range Hierarchical Ordering in 5.5 nm Stirations". **2019** Japan-Taiwan Bilateral Polymer Symposium, Matsue, Japan **(Poster)**

[3] **L. Dong,** A. Chandra, K. Wylie, Y. Nabae, Teruaki Hayakawa, "Asymmetric Hexagonally Packed Cylinder Morphology in a Diblock Copolymer with Liquid Crystalline Semifluorinated Side Chains and Its Domain Orientation Control in Thin Films". **2019** Prep. Itnl. Student WS on Arom. Func. Polym, Tokyo, Japan. (**Oral**)

[4] **L. Dong**, K. Wylie, R. Nakatani1, Y. Nabae, T. Hayakawa, T. Dazai, K. Miyagi, T. Mori, Daisuke Kawana, "Downsizing the Thin Film Domain of Poly(styrene-*block*-methyl methacrylate) by Introducing Fluorine to Randomly Pre-polymerized Functional Units". **2020** 69th Symposium on Macromolecules, Iwate (online), Japan. **(Oral)**

**Related publications**

[1] **Dong, L**.; Odashima, R.; Seshimo, T.; Nabae, Y.; Hayakawa, T., Synthesis and Morphology Studies of Polysiloxane-based Triblock Copolymers. *J Photopolym Sci Tec* **2020,** *32* (6), 817-822.

[2] Wylie, K.; **Dong, L**.; Chandra, A.; Nabae, Y.; Hayakawa, T., Modifying the Interaction Parameters of a Linear ABC Triblock Terpolymer by Functionalizing the Short, Reactive Middle Block To Induce Morphological Change. *Macromolecules* **2020,** *53* (4), 1293-1301.

[3] Wylie, K.; **Dong, L.**; Nabae, Y.; Hayakawa, T., Poly (Styrene-block-Glyicdyl Methacrylate-block-Methyl Methacrylate) as a Versatile Platform for Exploring the Phase Diagram of Linear Triblock Copolymers. *Bulletin of the American Physical Society* **2020**.

[4] Yamazaki, A.; Kawana, D.; Seshimo, T.; Hayakawa, T.; **Dong, L.**; Odashima, R., Block copolymer and method of producing the same, and method of producing structure containing phase-separated structure. Google Patents: 2019.

# Acknowledgements

The studies presented in this dissertation were carried out under the supervision of Professor Teruaki Hayakawa at the Department of Materials Science and Engineering, School of Materials and Chemical Technology, Tokyo Institute of Technology between 2017 and 2020. The dissertation focused on the studies of high-χ parameter diblock copolymers with fluorine-containing side chains, perfluoroalkyl in particular, for next generation lithographic nano-fabrication.

Here I would like to express my utmost appreciation to Professor Teruaki Hayakawa for his invaluable guidance and warm encouragement throughout the study, as well as to Assistant Professor Yuta Nabae for their helpful suggestion. I am also extremely grateful to Prof. Toshiaki Ougizawa, Prof. Hidetoshi Matsumoto, Associate Prof. Tsuyoshi Michinobu, and Associate Prof. Masatoshi Tokita for their valuable suggestions on reviewing this dissertation.

In addition, the administrative assistance from Secretary Ms. Chisae Kambe was highly appreciated. Besides, I would like to express my sincere gratitude to all members of Hayakawa group for their precious advice and discussion, especially the helps from two main collaborators Dr. Kevin Wylie and Dr. Alvin Chandra. The 2D morphology simulation codes based on self-consistent field theory were developed and shared by Dr. Kevin Wylie and the codes for quantitative analysis on AFM images were developed and shared by Mr. Ryuichi Nakatani.

Besides, I would like to extend my uttermost appreciation to Associate Professor Christopher J. Ellison, Department of Chemical Engineering and Materials Science, University of Minnesota, Twin Cities, U.S., who kindly accepted me as visiting student from Aug. 2019 to Nov. 2019. The top coat techniques used in this dissertation was learned from Ellison group under Professor Christopher J. Ellison's generous permission and relevant funding support. Especially, warm thanks are also sent to Dr. Kailong Jin and Dr. Sung-soo Kim for their supports on research during my stay in Ellison group.

I wish to thank Mr. Ryohei Kikuchi (Center for Advanced Materials Analysis, Tokyo Institute of Technology) for his indispensable assistance with the TEM and cross-sectional SEM observations. Additionally, I would like to thank Assistant Professor Tomoyasu Hirai (Department of Applied Chemistry, Graduate School and Faculty of Engineering, Osaka Institute of Technology), Director Noriyosu Hayashizaki and Associate Professor Satoru Tomita (Tokyo instituite of technology Radiation Research and Management Center) for their helps on usage of Spring-8 synchrotron radiation facility affiliated to Japan Synchrotron Radiation Research Institute. The atomic force microscopy experiments were supported by the New Energy and Industrial Technology Development Organization (NEDO) in Japan under the

EIDEC project. Besides, I would like to thank Prof. Yuji Wada of the Tokyo Institute of Technology for support with the SEM measurements.

The work in Chapter 6 was included as a part of collaboration project with TOKYO OHKA KOGYO CO., LTD. (TOK), Japan. The author would like to express the gratitude for the helpful discussions and technical supports from Mr. Takahiro Dazai, Mr. Ken Miyagi, Mr. Takayoshi Mori and Mr. Daisuke Kawana from Advanced Material Development Div.1, TOK.

Furthermore, the financial support provided by Ministry of Education, Culture, Sports, Science, and Technology (MEXT), Japanese Government for living cost from Sept. 2017 to Sept. 2020, was highly appreciated as well.

Last but not the least, I would like to thank to my family for their faithful love and support, financially and emotionally, throughout my overseas study in Japan.

DONG LEI

July 13th, 2020